

# **Inkjet printing and electrocatalysis**

**Thèse N° 9795**

Présentée le 24 octobre 2019

à la Faculté des sciences de base

Laboratoire d'électrochimie physique et analytique

Programme doctoral en chimie et génie chimique

pour l'obtention du grade de Docteur ès Sciences

par

**Victor COSTA BASSETTO**

Acceptée sur proposition du jury

Prof. K. Sivula, président du jury

Prof. H. Girault, Dr A. S. Lesch, directeurs de thèse

Prof. A. E Russell, rapporteuse

Prof. M. Arenz, rapporteur

Prof. R. Buonsanti, rapporteuse

2019



ÉCOLE POLYTECHNIQUE  
FÉDÉRALE DE LAUSANNE



# Acknowledgements

I could not start this section in a different way than acknowledging the one person that made this thesis possible, my thesis supervisor Prof. Hubert Girault. You are one of the great scientists I have ever met, extremely motivated, dedicated and enthusiastic regarding the science and education. I cannot thank you enough for opening me the doors of your group and giving me the opportunity to develop my PhD. The lessons taught in these years will be certainly carried for life.

I would like to thank Dr. Andreas Lesch for co-supervising this thesis. I have learned immensely with you! Thank you for your scientific contribution, dedication and profound questioning to your resilience and hardworking example. Thank you for the dedication shared during the course of this thesis.

I would like to complement and express the honour that was to have in my Jury Professor Andrea Russell, Professor Matthias Arenz and Professor Rafaella Buonsanti and the jury president Professor Kevin Sivula. Thanks for all for the wonderful discussion of my work and great insights in the thesis structure and future application of the work here developed.

How to acknowledged LEPA and its members? LEPA is not only one of the most successful research units I have ever had the chance to meet, it is a great family. Throughout the years in this group I have been blessed to work with a number of amazing researchers, that I will be shy on mentioning to avoid leaving important ones out of the list. The structure of the group and staff made it one of the most fruitful places for science! I'm blessed to have the chance to experience what it is to do research in this environment and hopefully to have contributed my share for the success of this group.

One cannot forget a PhD is not a solo activity. Throughout the years spent to execute the research a lot of interaction is done to make the projects that are presented in this thesis possible to be executed. In this section I would like to thank all EPFL staff with whom I had have contact and contributed immensely, each in their area, to make each single detail presented here possible. EPFL is a top university, above it all, because of all the minds that here work/study! A sincere thank you for all of those who made this possible!

For last I thank the Swiss National Science Foundation for the financial support provided during the project Ambizione Energy Project No. 154297.

Nesta seção dedico agradecimentos a todas as pessoas, talvez injustamente esquecendo de algumas – com as quais me desculpo de imediato, que contribuíram de diversas formas para o desenvolvimento desta tese. Primeiramente, como nunca poderia deixar de ser, agradeço a minha família e seu incondicional apoio em todos os momentos. Mesmo sem entender o conteúdo aqui descrito em sua plenitude, apoiaram minha decisão de, aqui na Suíça, desenvolver essa parte da minha carreira, e juntos vivemos as alegrias desta decisão e sofremos das saudades e das consequências que só quem escolhe viver distante sabe.

Agradeço enormemente o carinho, apoio e suporte daquela que começou esta tese como uma amiga e termina como minha amada esposa, MSc Sabrina Gracia dos Santos. Sem seu apoio, com certeza, os esforços aos longos dos anos dispendidos para a realização deste trabalho teriam sido impossíveis. Desculpe a distância – está já acabou.

Agradeço também a família que ganhei com o LEPA. Muito mais que só colegas de trabalho, a/o Dra. Milica Jovic, MSc. Aleksandar Cvetkovic, Dra. Natalia Gasilova, Prof. Dr. Mathieu Soutrenon, Dra. Alexandra Bondarenko e Dr. Christopher Dennison, Dra. Justyna Piwek. Sra Katie Moon

e Dr. Wanderson Oliveira da Silva. Obrigado pelo apoio, compreensão e acima de tudo ao maravilhoso exemplo que me deram ao longo destes anos.

Não posso deixar aqui de agradecer ao meu grande mentor, Prof. Dr. Lauro Tatsuo Kubota. Não seria possível chegar aonde cheguei se o professor não tivesse aberto a primeira porta. Hoje chego a esse patamar dentro da ciência pelo exemplo e ensinamentos que aprendi com você.

Aos meus grandes amigos do Brasil que ao longo dessa caminhada me incentivaram e me ajudaram: Dr. Ronaldo Adriano Timm, Sra. Bruna Duarte, MSc Marina Dessotti Cortez, Dr. Waldemir Paschoalino, MD Douglas de Alencar, MD Caroline Neves, MSc Paula Bolrin e Dra. Mariana Massafera.

Por fim, nesta sessão mais familiar e, porque não, tupiniquin, não posso deixar de agradecer aos brasileiros (uns nem tanto) que encontraram tempo de em suas caminhadas e permitiram que andássemos juntos pelos cantos deste país. Ao Sr. Victor Augusto da Silva, Sra. Priscila Yuri Yazawa, Prof. Dra. Cecilia Silva, Dra. Emilia Nery, Dr. Carlos Alberto Mestrimer, Sr. Rogerio Teles e a família Cook, que entre visitas e risadas fizeram esses 4 anos muito mais leves.

A todos vocês, sem sua participação, cada um de sua forma, essa tese jamais teria acontecido.

Obrigado!

## Acknowledgements

---

# Abstract

The transition in energy matrix, from fossil to renewable energy sources, will require the utilization of grid levelling alternatives to cope with the intermittent characteristic of renewable energy. Advanced electrochemical energy conversion and storage devices, ranging from batteries to fuel cells, play a crucial role in that process. Many of these electrochemical devices are based on the oxidation and reduction reactions of oxygen and water respectively, compounds that can conveniently be taken from air/moisturized air and released to the environment. However, the sluggish kinetics of the oxygen reactions at current electrode materials require the synthesis and study of more efficient and stable electrocatalysts and catalyst layers made thereof.

This thesis focuses on combined drop-on-demand inkjet printing coupled with pulsed light sintering for the fabrication of catalyst layers containing advanced electrocatalyst materials. Inkjet printing allowed the precise control of the material loading inside the catalyst layers and the pulsed light-induced post-processing enabled rapid drying and even material functionalization, such as changing the oxidation state of the metal oxide-based catalyst for improved electrochemical performance. The electrocatalysts were in particular studied for their activity and stability towards the oxygen reduction reaction (ORR) and oxygen evolution reaction (OER).

First, an ink with an advanced non-precious metal-based catalyst, nitrogen-doped reduced graphene oxide supported cobalt oxide nanoparticles (*i.e.*,  $\text{Co}_3\text{O}_4/\text{N-rGO}$ ), was prepared and inkjet printed in form of a catalyst layer on large glassy carbon electrodes. The application of the flash lamp reduced in a rapid, non-equilibrium thermal process, the oxidation state of cobalt within a short high intensity light pulse and modified the catalytic properties for the ORR. The electrocatalyst

properties are discussed in detail in Chapter III and compared with catalyst layers that were prepared by using equilibrium thermal processing in a furnace.

In Chapter IV, the application of inkjet printing and flash light processing for the synthesis of nanoparticles from printed dissolved metal precursors is presented. This concept was recently introduced as "Print-Light-Synthesis" and was herein applied to fabricate Pt nanostructures on glassy carbon substrates. The process is based on the light-induced thermal decomposition of the Pt precursor. It represents a promising, low material consumption process and highly controllable alternative to standard wet chemical synthesis of nanoparticles in reactors.

Based on Print-Light-Synthesis, Chapter V describes the development of mixed NiFe nano-composites with well-defined material ratios and loadings in the corresponding inks. Catalyst layers of the composites were fabricated as OER electrocatalysts. A support layer of carbon-nanotubes was used as "light-to-heat-absorber" and alcohols in the ink as reducing agents for the efficient decomposition of the chloride-based Ni and Fe precursors.

The last section of this thesis presents future perspectives of the current work. The possibilities in which this research can engender will be discussed. Focus will be drawn to possible industrial applications of the proposed and developed techniques presented in this thesis. Mainly it is demonstrated the possibility of having, through the combination of inkjet printing and flash light processing as two state-of-art techniques the possibility of fabricating in an easily-up scalable way catalyst layers for implementation in a wide range of electrochemical energy conversion and storage devices.

**Keywords :** Inkjet printing, Print-Light-Synthesis, oxygen reduction reaction, oxygen evolution reaction, electrocatalyst.



# Résumé

La transition énergétique des énergies fossiles vers les énergies renouvelables nécessitera l'utilisation d'alternatives de nivellement du réseau énergétique pour faire face au caractère intermittent des productions d'énergie renouvelable. Dans ces dispositifs de nivellement du réseau énergétique, les systèmes avancés de conversion d'énergie ou de stockage électrochimique, des batteries aux piles à combustibles, jouent un rôle important. Beaucoup de ces dispositifs sont basés sur l'oxydation et la réduction d'oxygène et de eau, un composé qui peut être pris dans l'air et rejeté dans l'environnement. Cependant, la cinétique lente de ces réactions d'oxygène sur les matériaux d'électrodes actuels nécessite la synthèse et l'étude d'électrocatalyseurs et de couches de catalyseurs réalisés avec ces matériaux.

Cette thèse se focalise sur l'utilisation combinée de l'impression jet d'encre et du frittage par pulsations pour la fabrication de couches de catalyseurs contenant des matériaux électrocatalyseurs avancés. L'impression jet d'encre permet le contrôle précis de la charge du matériel à l'intérieur des couches de catalyseurs et le post-traitement par l'utilisation de lumière pulsée permet un séchage rapide et même une fonctionnalisation des matériaux, telle que modifier le degré d'oxydation de métaux pour améliorer leur performance électrochimique. Les électrocatalyseurs ont en particulier été étudiés pour leur activité et leur stabilité en vue des réactions de réduction d'oxygène (RRO) et d'évolution d'oxygène (REO).

Premièrement, une encre avec un catalyseur métallique avancé, basé sur un métal non précieux, c'est-à-dire les nanoparticules d'oxyde de cobalt supportées par l'oxyde du graphène réduit dopé à l'azote ( $\text{Co}_3\text{O}_4/\text{N-rGO}$ ), a été préparée et imprimé par jet d'encre sous la forme d'une couche

de catalyseur sous la forme d'une couche de catalyseur sur de grandes électrodes de carbone vitreux. L'application de la lumière pulsée a réduit, dans un processus rapide et donc thermique non-équilibré, le degré d'oxydation du cobalt au cours d'une impulsion lumineuse de forte intensité et a modifié ses propriétés catalytiques pour les RRO. Les propriétés d'électrocatalyseur sont détaillées dans le Chapitre III et la comparaison est faite avec les couches de catalyseurs qui ont été préparées dans le four en utilisant un processus thermique équilibré dans le four.

Dans le Chapitre IV, l'application de l'impression jet d'encre et du traitement par la lumière pulsée pour la synthèse des nanoparticules à partir des précurseurs métalliques dissous et imprimés, est présentée. Ce concept a été introduit récemment comme "Print-Light-Synthesis" a été appliqué ici pour fabriquer des nanostructures de platine sur un substrat de carbone vitreux. Le procédé est basé sur la décomposition thermique du précurseur de platine par la lumière. Il représente une alternative intéressante à la synthèse chimique de nanoparticules par réactions standards en phase liquide dans des réacteurs.

Basé sur le concept « Print-Light-Synthesis », le Chapitre V décrit le développement des nano-composites de NiFe avec les ratios et la charge des matériaux bien définis dans les encres correspondantes fabriquées sous forme de catalyseurs REO. Une couche de support de nanotubes de carbone sur du carbone vitreux a été utilisée comme un absorbeur de lumière-en-chaaleur et des alcools dans l'encre ont servi d'agents réducteurs pour les précurseurs de Ni et Fe à base de chlorure.

La dernière section de cette thèse présente les perspectives futures de ce travail en cours. Les possibilités dans lesquelles cette recherche peut engendrer sont discutées. L'accent est mis sur les applications industrielles possibles des techniques développées et présentées dans cette thèse. Cela est principalement démontré par la combinaison de l'impression à jet d'encre et du traitement à la lumière pulsée comme deux techniques de pointe, la possibilité de fabriquer des couches de catalyseur

d'une manière facilement évolutive pour une mise en œuvre dans une large gamme de dispositifs de conversion et de stockage d'énergie électrochimiques.

**Mots-clés:** Impression jet d'encre, Print-Light-Synthesis, réaction de réduction d'oxygène et d'évolution d'oxygène, électrocatalyseur.

# List of abbreviations

---

2D	Two dimensions
3D	Three dimensions
AFC	Alkaline fuel cell
CA	Chronoamperometry
CE	Counter electrode
CL	Catalyst layer
CNT	Carbon nanotubes
CV	Cyclic voltammetry
DMFC	Direct methanol fuel cell
DOD	Drop-on-demand
DSA	Dimensionally stable anodes
EDX	Energy-dispersive X-ray
EHD	electrohydrodynamic
EIS	Electrochemical Impedance Spectroscopy

---

---

ETD	Everhart-Thornley detector
FeMeOH	Ferrocenemethanol
GC	Glassy Carbon
IJP	Inkjet printed
IPA	Isopropanol
ITO	Indium Tin Oxide
MCFC	Molten carbonate fuel cell
N-rGO	Nitrogen doped reduced graphene oxide
OER	Oxygen evolution reaction
ORR	Oxygen reduction reaction
PAFC	Phosphoric acid fuel cell
PEMFC	Proton-exchange membrane fuel cell/ Polymer electrolyte membrane fuel cell
PET	Polyethylene terephthalate
PLS	Print-Light-Synthesis
PVP	Polyvinylpyrrolidone
RDE	Rotating disk electrode
RE	Reference electrode

---

---

RHE	Reversible hydrogen electrode
SECM	Scanning Electrochemical Microscopy
SEM	Scanning electron microscopy
SOFC	Solid Oxide Fuel Cell
STEM	Scanning transmission electron microscopy
TEM	Transmission electron microscopy
TGA	Thermogravimetric analysis
UV	Ultraviolet
WE	Work electrode
XPS	X-ray photoelectron spectroscopy
XRD	X-ray diffraction spectroscopy
SEM	Scanning electron microscopy
SOFC	Solid Oxide Fuel Cell
STEM	Scanning transmission electron microscopy
TEM	Transmission electron microscopy
TGA	Thermogravimetric analysis
UV	Ultraviolet
WE	Work electrode

---

List of abbreviations

---

XPS

X-ray photoelectron spectroscopy

XRD

X-ray diffraction spectroscopy

---

# List of symbols

Symbol	Symbol meaning	Unit
$A$	Area	$\text{cm}^2$
$c$	Concentration	$\text{mol}\cdot\text{m}^{-3}$
$D$	Diffusion coefficient	$\text{m}^2\text{s}^{-1}$
$F$	Faraday constant	C
$i$	Current	A
$n$	Number of electrons	None
$R$	Ohmic resistance	$\Omega$
$\rho$	Density	$\text{g}\cdot\text{cm}^3$
$d$	Diameter	m
$\gamma$	Surface tension	$\text{N}\cdot\text{m}^{-1}$
$v$	Velocity	$\text{m}\cdot\text{s}^{-1}$
$\eta$	Viscosity	$\text{Pa}\cdot\text{s}$
$eV$	Electron volt	eV
$E$	Potential	V
$E^0$	Standard potential of an electrode or a couple	V



List of symbols

---

$\Delta G$	Gibbs free energy change in a chemical process	kJ, kJ/mol
$j$	Current density	A/cm <sup>2</sup>
$j_k$	Diffusion-limited current density	A/cm <sup>2</sup>
$\nu$	Kinematic viscosity	Pa·s

---



# Contents

<b>Acknowledgements .....</b>	<b>vi</b>
<b>Abstract.....</b>	<b>x</b>
<b>Résumé .....</b>	<b>xii</b>
<b>List of abbreviations .....</b>	<b>xv</b>
<b>List of symbols .....</b>	<b>xix</b>
<b>Contents .....</b>	<b>xxii</b>
<b>List of Figures .....</b>	<b>xxv</b>
<b>List of Tables.....</b>	<b>33</b>
<b>Chapter 1      Introduction.....</b>	<b>35</b>
1.1 The role of electrochemical energy storage and conversion devices in the current and future power grids.....	35
1.2 Electrochemical energy storage/conversion based on oxygen evolution and reduction half-cell reactions .....	38
1.3 Oxygen reduction reaction catalysts.....	41
1.3.1 ORR at platinum group metals.....	47
1.3.2 ORR at non-precious, low cost catalyst materials.....	50
1.4 Oxygen evolution reaction catalysts.....	50
1.5 Interpretation of the electrocatalytic activities for ORR and OER.....	55
1.6 Catalyst layer structure .....	56
1.6.1 Fabrication techniques for catalyst deposition .....	57
1.6.2 Ink/substrate interaction and post-printing processing .....	63
1.7 Inkjet printing of electrocatalysts combinatorial libraries .....	64
1.7.1 Printing of catalyst layers.....	64
1.7.2 Pulsed Light Sintering .....	65
1.8 Thesis outline .....	70

<b>Chapter 2</b>	<b>Experimental part.....</b>	<b>71</b>
2.1	Chemicals.....	71
2.1.1	Commercial Chemicals.....	71
2.1.2	Synthesized Chemicals .....	72
2.2	Equipment.....	73
2.2.1	Electrochemistry.....	73
2.2.2	Inkjet printers .....	75
2.2.3	Ink and printed wet pattern characterization tools .....	77
2.3	Ink Formulation.....	80
2.3.1	Nanoparticulated inks formulation.....	82
2.3.2	Precursor inks.....	83
2.4	Post processing.....	83
2.4.1	UV .....	83
2.4.2	Thermal.....	84
2.4.3	Photonic Curing.....	84
2.5	Pattern and catalyst layer characterizations .....	84
2.5.1	Microscopy.....	84
2.5.2	Spectroscopic characterization.....	84
2.5.3	Electrochemical characterization.....	85
<b>Chapter 3</b>	<b>Inkjet printing of Co<sub>3</sub>O<sub>4</sub>/N-rGO electrocatalyst forming high activity catalyst layers for oxygen reduction reaction.....</b>	<b>86</b>
3.1	Abstract.....	86
3.2	Introduction.....	87
3.3	Results and discussion .....	91
3.3.1	Optical and microscopic characterization.....	91
3.3.2	Ink characterization and printability.....	93
3.4	Conclusions .....	111

<b>Chapter 4</b>	<b>Print-Light-Synthesis of noble metal nano-electrocatalysts.....</b>	<b>114</b>
4.1	Abstract.....	114
4.2	Introduction.....	115
4.3	Results and Discussion .....	118
4.4	Conclusion.....	126
<b>Chapter 5</b>	<b>Print-Light-Synthesis of Ni and NiFe-nanoscaled electrodes for oxygen evolution reaction.....</b>	<b>129</b>
5.1	Abstract.....	129
5.2	Introduction.....	130
5.3	Results and discussion .....	133
5.4	Conclusion.....	157
<b>Chapter 6</b>	<b>Conclusions and Perspectives.....</b>	<b>160</b>
6.1	Conclusions .....	160
6.2	Perspectives.....	161
<b>References</b>	<b>.....</b>	<b>165</b>

# List of Figures

<b>Figure 1-1.</b> Energy production based on different sources in Germany in March 2019. Source: Fraunhofer <sup>13</sup> .....	36
<b>Figure 1-2</b> Schematic representation of a) a polymer electrolyte membrane (PEM) fuel cell, b) PEM electrolyzer and c) a metal air battery (discharging). .....	39
<b>Figure 1-3</b> Proposed oxygen reduction pathways on noble metals. "ad" indicates adsorbed species, while "aq" indicates solvated species in water.....	41
<b>Figure 1-4</b> Theoretical free energy diagram for Pt <sub>3</sub> Y(111) with 25% Y in the subsurface layer data obtained from DFT calculation. Original citation <sup>34</sup> – Published by The Royal Society of Chemistry.....	44
<b>Figure 1-5</b> Examples of simulated volcano plots extracted from literature. Diagram of activity enhancement and overpotential versus oxygen binding energy. From Stephens <i>et al.</i> <sup>34</sup> Published by The Royal Society of Chemistry.....	45
<b>Figure 1-6</b> Theoretical overpotential for oxygen evolution <i>vs</i> the difference between the standard Gibbs energy of two subsequent intermediates of several binary oxides. Figure extracted from reference <sup>91</sup> Reprinted with permission for AAAS. ....	52
<b>Figure 1-7</b> Free energy diagram for the oxygen evolution reaction on Co-C <sub>3</sub> N <sub>4</sub> and IrO <sub>2</sub> surfaces. Figure adapted with permission from. <sup>99</sup> Copyright (2017) American Chemical Society. ....	55
<b>Figure 1-8.</b> Scheme representing a catalyst layer (membrane electrode assembly (MEA)). The catalyst layer is presented as "Cathode/Anode Material" and located between the "Conducting support/Gas diffusion layer" and "Membrane" ...	56

**Figure 1-9** Schematic representation of the three-phase boundary inside the catalyst layer.....57

**Figure 1-10** Schematic representation of continuous inkjet printing. ....60

**Figure 1-11.** Schematic representation of drop-on-demand inkjet printing. a) Piezoelectric generated droplets. b) Thermally generated droplets. c) Electrohydrodynamic droplets formation.....61

**Figure 1-12.** Emission spectrum of a Xenon flash lamp with 750 V of bank voltage and 220  $\mu$ s pulse length. Raw data kindly provided by Rob Hendriks from Novacentrix.....66

**Figure 2-1.** a) Electrochemical cell composed of the three main components: Bottom part with WE contact plate (left), liquid reservoir/cell cover (middle) and lid (right). b) Electrochemical cell partially assembled with a GC electrode kept at the bottom of the cell and hold in place with an O-ring (green) inserted into the liquid reservoir. c) Electrochemical cell, fully assembled with lid and screws for fixation and sealing the cell. ....73

**Figure 2-2.** RDE setup a) Working electrode connector with individual parts identified. b) Assembled RDE with GC rod position and connector to the rotator identified.....74

**Figure 2-3.** a) Dimatix DMP-2850 inkjet printer. b) Dimatix ink cartridge movement during printing of nanoparticulated carbon-based ink over GC substrates with 3 mm thickness.....76

**Figure 2-4.** Ceradrop X-Serie inkjet printer coupled with a PulseForge 1300 photonic curing system. a) Overview of the printer setup combined with the photonic curing system. b) View of the inside on the printer featuring the areas of photonic curing. ....77

**Figure 2-5.** Viscometer utilized to determine the viscosity of the developed inks. ....78

**Figure 2-6.** Drop shape analyser utilized to determine the surface tension of the developed inks in pending droplet mode and to measure the contact angle of a sessile droplet on a substrate.....79

- Figure 2-7** Coordinate system defined by the Reynolds and Weber number to define the printability of an ink. Extracted with permission from Derby<sup>155</sup>. ..... 81
- Figure 3-1** Characterization of as-synthesized  $\text{Co}_3\text{O}_4/\text{N-rGO}$ . a) BF-TEM image, and b) corresponding SAED pattern (left semicircle). Simulated electron diffraction pattern (ring sampling diffraction planes) of cubic  $\text{Co}_3\text{O}_4$  is shown to the right of the SAED pattern. c) Rietveld refinement plot of powder XRD pattern. .... 92
- Figure 3-2.** High-resolution IJP of  $\text{Co}_3\text{O}_4/\text{N-rGO}$ -based CLs. a) Photograph of the  $\text{Co}_3\text{O}_4/\text{N-rGO}$  ink. b) Four droplets ejected from four parallel nozzles. c) 25 IJPL as a  $25 \text{ mm}^2$  CL on glassy carbon before and after photonic curing with the  $(10.60 \pm 0.19) \text{ J}\cdot\text{cm}^{-2}$  pulse. d) Inkjet-printed and photonic-cured  $1 \text{ mm}^2$  patterns of  $\text{Co}_3\text{O}_4/\text{N-rGO}$  with different numbers of printed layers on a glassy carbon substrate. .... 94
- Figure 3-3.** UV Vis absorption spectrum of an as-printed PVP- $\text{Co}_3\text{O}_4/\text{N-rGO}$  layer on quartz glass (red curve) compared with a typical lamp emission spectrum (black curve; kindly provided by Novacentrix, same spectrum as in ref<sup>116</sup>). ..... 95
- Figure 3-4.** Schematic representation of Soft-Probe-SECM using soft carbon microelectrodes in contact mode over catalyst layers printing on glassy carbon. Similar currents are expected over conductive surfaces (polymer-free catalyst layer and glassy carbon). Lower currents are expected due to the presence of polymers (e.g. PVP) slowing down the electrode kinetics at the substrate or even insulating the substrate (the latter means no regeneration reaction). ..... 96
- Figure 3-5.** Soft-Probe-SECM feedback mode image of the catalyst patterns using a soft carbon microelectrode in contact mode. An exemplary line scan was extracted. Identical currents over the CLs demonstrate their homogeneous conductivity similar to bare glassy carbon. Exp. conditions: 2 mM FcMeOH and 0.1 M  $\text{KNO}_3$ , Potential at the microelectrode: 0.4 V, sample was unbiased, step size in  $x$ - and  $y$ -direction  $25 \mu\text{m}$ , probe translation rate  $25 \mu\text{m}\cdot\text{s}^{-1}$ , scan direction from left to right. The SECM data were plane-fitted using two margins in order to compensate for slight solvent evaporation effects during the experiment. ... 98
- Figure 3-6.** BF-TEM images (upper panels) and corresponding SAED patterns (lower panels) of the raw catalyst material, after different photonic curing pulses and after oven curing. To the right of each SAED pattern, the simulated electron



diffraction pattern (ring sampling diffraction planes) is shown. Reddish rings indicate  $\text{Co}_3\text{O}_4$ , blueish rings  $\text{CoO}$ ..... 99

**Figure 3-7.** Intensity profiles measured on the SAED patterns of inkjet-printed  $\text{Co}_3\text{O}_4/\text{N-rGO}$ -based CLs without curing (raw material), photonic-cured with the low, medium, and high pulse (solid curves). Simulated intensity profiles for  $\text{Co}_3\text{O}_4$  and  $\text{CoO}$  are presented as dashed lines. Red curves correspond to  $\text{Co}_3\text{O}_4$ , blue curves to  $\text{CoO}$  and magenta represents a transition state. .... 102

**Figure 3-8.** Removal of PVP through thermal post-processing. FT-IR spectra of a) raw  $\text{Co}_3\text{O}_4/\text{N-rGO}$  (black), b) non-cured inkjet-printed PVP-  $\text{Co}_3\text{O}_4/\text{N-rGO}$  pattern (red), c) oven-cured inkjet-printed PVP- $\text{Co}_3\text{O}_4/\text{N-rGO}$  pattern (blue), d) med pulse photonic-cured inkjet-printed PVP-  $\text{Co}_3\text{O}_4/\text{N-rGO}$  pattern (green), e) high pulse photonic-cured inkjet-printed PVP-  $\text{Co}_3\text{O}_4/\text{N-rGO}$  pattern (orange) and f) PVP (purple). Asterisks and colored rectangles in the background indicate recognizable peaks throughout all spectra. Peaks marked by purple asterisks and rectangles correlated with selected peaks in bare PVP. Green asterisks correlate with degradation products of PVP. .... 104

**Figure 3-9.** Stationary LSVs for the ORR of inkjet-printed and post-processed CLs of  $\text{Co}_3\text{O}_4/\text{N-rGO}$  (LSVs not  $iR$ -corrected). a) Comparison of oven-cured and photonic-cured CLs using different pulses. b) Reproducibility of three different CLs that were identically printed and post-processed (high pulse) on three GC substrates. c) Comparison of the ORR performance of a typical  $\text{Co}_3\text{O}_4/\text{N-rGO}$  CL (low pulse) with two Pt/C-based CLs made with different Pt content. Experimental conditions: Oxygen-saturated 0.1 M KOH, scan rate  $5 \text{ mV s}^{-1}$ ..... 108

**Figure 3-10.** Koutecky-Levich plots for oven-cured and photonic-cured CLs. Left inset LSVs at 1600 rpm for the ORR of inkjet-printed and post-processed CLs of  $\text{Co}_3\text{O}_4/\text{N-rGO}$  (LSVs not  $iR$ -corrected). Right inset, RDE after measurement with the low pulse CL, demonstrating material removal. Oven cured (black), low pulse (green), medium pulse (red) and high pulse (blue). Experimental conditions: Oxygen-saturated 0.1 M KOH, scan rate  $5 \text{ mV}\cdot\text{s}^{-1}$  ..... 111

**Figure 4-1** Schematic representation of Print-Light-Synthesis of Pt nanoparticles and nanostructures on a glassy carbon electrode. .... 117

**Figure 4-2** a) Droplets of the Pt precursor ink generated from seven exemplary parallel nozzles. b) Photograph of the Pt precursor ink. c) Printed Pt precursor ink in the shape of a circle (5 mm diameter) on a GC plate before (left) and after (right) a 330  $\mu\text{s}$  flash lamp pulse with  $(3.52\pm 0.03) \text{ J/cm}^2$ . Please note that heterogeneity in the layer appearance is due to the GC plate surface. d) Laser scanning micrograph of a Pt nanostructure on GC, obtained by drop casting and photonic curing (330  $\mu\text{s}$  pulse,  $(3.52\pm 0.03) \text{ J/cm}^2$ ). ..... 119

**Figure 4-3** a) 30 inkjet-printed squares of Pt precursor salt (1  $\text{mm}^2$ ) on indium-coated borosilicate glass after printing with 5 min drying time at 54  $^\circ\text{C}$  (left) and after photonic curing using a 330  $\mu\text{s}$  short light pulse with  $(3.52\pm 0.03) \text{ J/cm}^2$  shot energy density (right). b) Absorption spectra of bare borosilicate glass slide (black), ITO-coated borosilicate glass slide (blue) and Pt ink on ITO-coated borosilicate glass slide (green) prior to photonic curing. Photographs and data kindly provided by Dr. Andreas Lesch. .... 121

**Figure 4-4** a) Scanning electron microscopy – energy dispersive x-ray (SEM-EDX) spectroscopy analysis of inkjet-printed Pt precursor ink before (left) and after (right) photonic curing. Substrate: Indium tin oxide-coated glass slide. b) Bragg Brentano X-ray diffractometry (BBXRD) patterns of bare ITO glass substrate (grey) and the Pt nanostructures (blue) on the ITO-coated glass. Peaks marked with an asterisk correspond to ITO. c) X-ray photoelectron spectroscopy (XPS) spectra of the Pt nanostructures on the ITO-coated glass slide, focus is on Cl 2p and Pt 4f. Data were kindly provided by Dr. Andreas Lesch and published in reference <sup>116</sup>. .... 122

**Figure 4-5.** Soft-Probe-SECM feedback mode image of the catalyst patterns using a soft carbon microelectrode in contact mode. Experimental conditions: 2mM FcMeOH and 0.1 M  $\text{KNO}_3$ , Potential at microelectrode: 0.4 V, sample was unbiased, step size in  $x$ - and  $y$ -direction 25  $\mu\text{m}$ , probe translation rate 25  $\mu\text{m}\cdot\text{s}^{-1}$ , scan direction from right to left. .... 125

**Figure 4-6.** Electrochemical characterization of the Pt/GC electrode obtained by Print-Light-Synthesis. a) 42 activation cycles, 50 mV/s. b) Activated Pt/GC electrode, 50 mV/s. All experiments were carried out in 0.1 M  $\text{HClO}_4$ . ... 126

**Figure 5-1** Schematic representation of Print-Light-Synthesis to create nanostructured electrodes with a combined inkjet-printing and flash light irradiation

step to induce the thermal decomposition of electrocatalyst precursors following either a direct and indirect precursor heating mechanism. A layer of CNTs act, as light absorber and local heat generator..... 133

**Figure 5-2** Single droplet development during different periods after droplet ejection. Micrographs of inkjet-printed and flash light-irradiated separated (b) and overlapping (c)  $\text{Ni}_{0.45}\text{Fe}_{0.55}$  precursor ink droplets on a CNT layer on GC. d) Absorption spectra of Fe (red),  $\text{Ni}_{0.45}\text{Fe}_{0.55}$  (orange) and Ni precursor wet films and CNT ink wet film (blue) on a quartz glass slide. Emission spectrum of the Xe flash lamp (pulse condition 750 V, 200  $\mu\text{s}$ , green). ..... 135

**Figure 5-3** Thermogravimetric analysis (TGA) of the iron, nickel and iron:nickel 0.45:0.55 molar ratio salts. Temperature scan with 10  $^{\circ}\text{C}/\text{min}$  heating ramp at air. Number in the plot indicate the number of the decomposition reaction steps for each compound. .... 136

**Figure 5-4** Simulated temporal temperature profiles of the two applied flash light pulses for the water removal/complete solvent evaporation ("water removal pulse") and material conversion ("conversion pulse") on the GC surface. The effect of the presence of a CNT layer could not be simulated due to a lack of known physical constants required for the simulation. The measured shot energy densities given in the main text consider the entire pulse duration. .... 139

**Figure 5-5** Bright field (a) and dark field (b) STEM of  $\text{Ni}_{0.45}\text{Fe}_{0.55}$  NPs formed on CNTs. The area indicated in (b) by the white rectangle was used for particle size distribution analysis (c). The dashed line in (c) indicates the lower cut-off value that was set for the image-based particle size analysis. .... 140

**Figure 5-6** X-ray photoelectron spectroscopy (XPS) characterization of Fe (a-c) and Ni (d-f) precursor patterns, printed on CNT/GC substrates, before (black) and after flash light irradiation (red). Lines for Ni2p (a), Fe2p (b), Cl2p (b, e) and O1s (c, f) are shown. Note: all spectra were normalized considering the base line and the main peak height, thus the spectra before and after flash light irradiation do not represent quantitative comparisons. .... 141

**Figure 5-7** Normalized XPS spectra of mixed  $\text{Ni}_{0.45}\text{Fe}_{0.55}$  precursor ink printed on CNT/GC (left) and GC (right) substrates before (black) and after flash light irradiation (red). Lines for Ni 2p (a,d), Fe 2p (b,e) and Cl 2p (c,f) are shown. Note:

all spectra were normalized considering the base line and the main peak height, thus the spectra before and after flash light irradiation do not represent quantitative comparisons. .... 143

**Figure 5-8** Flash light irradiation of Ni, Fe and NiFe-precursor salt wet layers with (top) and without (bottom) sacrificial electron donor, *i.e.*, alcohol. .... 145

**Figure 5-9** Scanning electron micrographs with four different magnifications of Ni/CNT/GC substrates before (a) and after (b) flash light sintering. .... 146

**Figure 5-10.** Scanning electron microscopy of Ni/GC before (a) and after (c) flash light sintering and of Fe/GC before (b) and after (d) flash light sintering. 147

**Figure 5-11** Excerpts of cyclic voltammograms of  $\text{Ni}_x\text{Fe}_{(1-x)}$  on CNT/GC and on GC. a)  $\text{Ni}_{0.50}\text{Fe}_{0.50}/\text{CNT}/\text{GC}$  (dashed line), Ni/CNT/GC (solid line) and Fe/CNT/GC (point line). b)  $\text{Ni}_{0.45}\text{Fe}_{0.55}/\text{GC}$  (dashed line), Ni/GC (full line) and Fe/GC (point line). c) Comparison between different  $\text{Ni}_x\text{Fe}_{(1-x)}/\text{CNT}/\text{GC}$ . Electrolyte 0.1 M KOH, scan rate 50 mV/s, cycle number 20, vertex potentials 0.25 and 1.70 V. Not *iR*-corrected. .... 149

**Figure 5-12** 20 cyclic voltammograms of a) Ni/CNT/GC, b)  $\text{Ni}_{0.45}\text{Fe}_{0.55}/\text{CNT}/\text{GC}$ , c) Fe/CNT/GC and d) excerpts of Ni,  $\text{Ni}_{0.88}\text{Fe}_{0.12}$ ,  $\text{Ni}_{0.71}\text{Fe}_{0.29}$ ,  $\text{Ni}_{0.45}\text{Fe}_{0.55}$ ,  $\text{Ni}_{0.22}\text{Fe}_{0.78}$ , Fe. a) Main figure shows the CV excerpt between 1.0 and 1.6 V while the insert shows the full potential range. With cycling, the peak currents increased until reaching a stable behaviour. b) Main figure shows the CV excerpt between 1.0 and 1.6 V while the left insert shows the full potential range. Right insert presents a zoomed view of the oxidation reduction wave. With cycling, the peak currents increased until reaching a stable behaviour. c) Main figure shows the CV excerpt between 1.0 and 1.6 V while the insert shows the full potential range. d) Excerpts of cyclic voltammograms of Ni,  $\text{Ni}_{0.88}\text{Fe}_{0.12}$ ,  $\text{Ni}_{0.71}\text{Fe}_{0.29}$ ,  $\text{Ni}_{0.45}\text{Fe}_{0.55}$ ,  $\text{Ni}_{0.22}\text{Fe}_{0.78}$ , Fe printed on CNT/GC. Electrolyte 0.1 M KOH, scan rate 50 mV/s. .... 150

**Figure 5-13** 20 cyclic voltammograms of a) Ni/GC, b)  $\text{Ni}_{0.45}\text{Fe}_{0.55}/\text{GC}$ , c) Fe/GC and d) excerpts of Ni,  $\text{Ni}_{0.88}\text{Fe}_{0.12}$ ,  $\text{Ni}_{0.71}\text{Fe}_{0.29}$ ,  $\text{Ni}_{0.45}\text{Fe}_{0.55}$ ,  $\text{Ni}_{0.22}\text{Fe}_{0.78}$ , Fe. a) Main figure shows the CV excerpt between 1.0 and 1.6 V while the insert shows the full potential range. With cycling, the peak currents increased until reaching a stable behaviour. b) Main figure shows the CV excerpt between 1.0 and 1.6 V while the left insert shows the full potential range. Right insert presents a zoomed view of the

List of Figures

oxidation reduction wave. With cycling, the peak currents increased until reaching a stable behaviour. c) Main figure shows the CV excerpt between 1.0 and 1.6 V while the insert shows the full potential range. d) Excerpts of cyclic voltammograms of Ni, Ni<sub>0.88</sub>Fe<sub>0.12</sub>, Ni<sub>0.71</sub>Fe<sub>0.29</sub>, Ni<sub>0.45</sub>Fe<sub>0.55</sub>, Ni<sub>0.22</sub>Fe<sub>0.78</sub>, Fe printed on GC. Electrolyte 0.1 M KOH, scan rate 50 mV/s.<sup>284</sup> ..... 151

**Figure 5-14** *iR*-corrected first (black) and twentieth (red) forward half cycles of CVs of Ni<sub>x</sub>Fe(1-x)/CNT/GC with x = 0 (a), 0.22 (b), 0.45 (c), 0.71 (d), 0.88 (e) and 1 (f) (red). Electrolyte 0.1 M KOH, scan rate 50 mV/s..... 152

**Figure 5-15** *iR*-corrected polarization curves (a, b), average overpotentials at 0.1, 5, 10 and 20 mA/cm<sup>2</sup> (N = 3; c, d) with dashed connection lines as guides to the eye and Tafel slopes (e, f) of Ni<sub>x</sub>Fe(1-x) on CNT/GC (left) and GC (right) with x = 0, 0.22, 0.45, 0.71, 0.88 and 1. Electrolyte 0.1 M KOH, scan rate 5 mV/s and rotation rate 3200 rpm. .... 154

**Figure 5-16.** Comparison of the *iR*-corrected first (black) and twentieth (red) forward half cycles of CVs of Ni/CNT/GC electrode, prepared using Print-Light-Synthesis and using the CV vertex potentials 0.25 V and 1.70 V (solid lines in all plots) with a) Ni/CNT/GC (Print-Light-Synthesis) and lower CV vertex potential (0.9 V) avoiding cathodic currents (dashed), b) Ni/CNT/GC (Print-Light-Synthesis), lower CV vertex potential (0.9 V) for 20 cycles and then 20 CV cycles with vertex potentials 0.25 and 1.70 V (dashed) and c) Ni/CNT/GC (electrodeposited).157

# List of Tables

<b>Table 1-1.</b> Fuel cell market for stationary, transport and portable applications. Overview of installed units and Megawatts per year. <sup>14</sup> .....	37
<b>Table 1-2</b> Leading technologies in fuel cell market data. <sup>14</sup> Installed units and Megawatts per year. ....	38
<b>Table 1-3.</b> Three possible mechanisms for oxygen reduction reaction on Pt (111) surface. Adapted from Nilekar <i>et al.</i> <sup>31</sup> . Mechanism obtained by DFT calculations. Species that are adsorbed at the active sites on the electrode surface are represented as * .....	42
<b>Table 1-4.</b> Process of the ORR under different reaction conditions. Adapted from Zhang <i>et al.</i> <sup>38</sup> .....	47
<b>Table 1-5</b> Possible mechanisms for OER in alkaline media. (* – activated surface site). ....	52
<b>Table 1-6</b> Possible mechanisms for OER in acid media. (* – activated surface site). ....	53
<b>Table 1-7.</b> Methods of depositing catalyst layers over membranes. ....	58
<b>Table 2-1.</b> Commercial chemicals utilized. ....	71
<b>Table 3-1.</b> Particle sizes after different post-processing conditions. ....	100
<b>Table 3-2</b> Transfer electron number for different electrode preparation methods. ....	110
<b>Table 5-1</b> Assumed steps for the thermal decomposition of $\text{FeCl}_2 \cdot 4\text{H}_2\text{O}$ in air following references <sup>269,270</sup> .....	137
<b>Table 5-2</b> Assumed steps for the thermal decomposition of $\text{NiCl}_2 \cdot 6\text{H}_2\text{O}$ in air following references <sup>270,271</sup> .....	137

<b>Table 5-3.</b> Onset potential, overpotential, Tafel slope and TOF numbers after 20 CV cycles.....	156
---	-----





# Chapter 1 Introduction

## 1.1 The role of electrochemical energy storage and conversion devices in the current and future power grids

Due to the global increase in energy consumption and higher environmental awareness, cleaner sources of energy, such as wind and solar, in the power grid composition has been gaining importance.<sup>1</sup> However, the renewable technologies still have the down side of intermittent energy generation.<sup>2</sup> The challenge of levelling the grid, variable fed with intermittent sources, can be addressed by developing smart grids with a clean energy power system.<sup>3</sup> Among the various possibilities of energy storage, flywheel storage,<sup>4</sup> compressed air storage,<sup>5</sup> pumped storage,<sup>6</sup> battery storage,<sup>7</sup> supercapacitor storage<sup>8</sup> and hydrogen storage<sup>9,10</sup> are the most discussed ones. Harnessing energy from renewable sources and accumulating it in electrical energy storage systems for electrical power supply have been widely considered as being the one of optimal solutions for future smart power grid systems.<sup>11</sup>

Germany has made much progress in the integration of renewable energy sources. It can be taken as an example of the future energy mix in many countries. As a matter of fact, the German electricity grid cannot be totally compared with Switzerland one. As Switzerland lacks a seacoast for extensive wind turbines installations, but the electricity market is internationally connected and both countries decided to shut down all their nuclear power plants: Germany by 2022 and Switzerland by 2034<sup>12</sup>. Furthermore, the energy production and consumption are well documented in Germany and made public. The contribution of renewable energy sources, such as wind and sun, can clearly be seen in **Figure 1-1**, which shows the German energy mix during the month of March 2019, and its effects and requirements are briefly introduced in the following text.

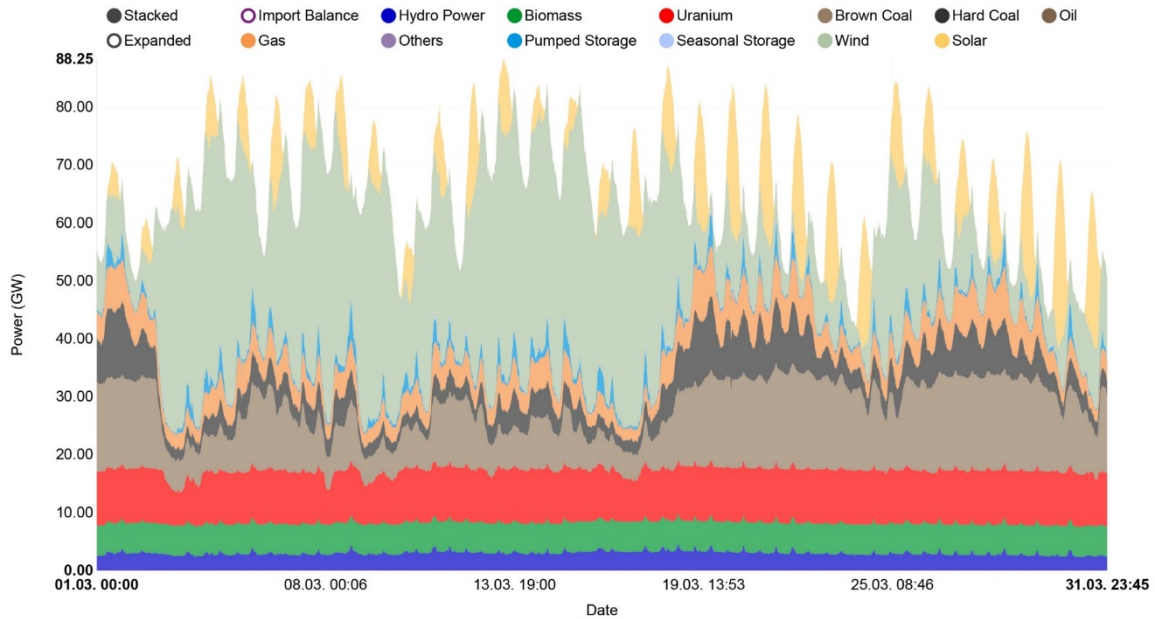


**Figure 1-1.** Energy production based on different sources in Germany in March 2019. Source: Fraunhofer<sup>13</sup>.

Power plants based on hydropower, nuclear power, biomass, and brown coal, for instance, can be considered as steady energy producers in the time domain of one month, while other forms of electricity generation, some based on their availability, others on the suitability, such as wind, solar, hard coal and gas, show variations on a daily or even hourly basis. The reasons for these variations are distinct. For wind and solar energy, the production oscillation is mainly due to weather conditions, while for hard coal and gas energy production the fluctuation is intentional, as they are used to control the total amount of energy produced in the day by adjusting the production to the consumption. Considering these facts, two lines can be traced to explain this behavior in the electricity generation in Germany. The first point to be considered is related to the flexibility of the technologies deployed. The generation of energy must be able to supply enough electricity as needed by the consumers as well as respond in the adequate time frame to variations in demand. Considering, on the one hand, nuclear power plant electricity generation (red in **Figure 1-1**), it is challenging to fast tune the energy generation to supply the needs of an individual day or particular situation. On the other hand, the absence of wind in one specific day requires alternative energy sources to compensate for it. For

instance, rapid reactivity and flexibility are essential to keep the energy supply constant and predictable even with intermittent energy sources.

Taking fuel cells as an example a succinct market analysis is present in **Table 1-1** and **Table 1-2**. From the data set, that comprehends the worldwide market of fuel cells, it is possible to analyse the fact that, in the last 5 years, the number of units installed per year has doubled for stationary applications while quadrupled for transport. Moreover, the installed capacity (in Megawatts) has doubled for stationary applications while in transport it has increased by 10 times. Such data supports the growing interest in fuel cell development and application. Moreover, it is demonstrated that the fuel cell technology is becoming more available and more powerful.

**Table 1-1.** Fuel cell market for stationary, transport and portable applications. Overview of installed units and Megawatts per year.<sup>14</sup>

<i>Year</i>	<i>Stationary</i>		<i>Transport</i>		<i>Portable</i>	
	<b>10<sup>3</sup> units</b>	<b>Megawatts</b>	<b>10<sup>3</sup> units</b>	<b>Megawatts</b>	<b>10<sup>3</sup> units</b>	<b>Megawatts</b>
<i>2012</i>	24.1	124.9	2.7	41.3	18.9	0.5
<i>2013</i>	51.8	186.9	2.0	28.1	13.0	0.4
<i>2014</i>	39.5	147.8	2.9	37.2	21.2	0.4
<i>2015</i>	47.0	183.6	5.2	113.6	8.7	0.9
<i>2016</i>	51.8	209.0	7.2	307.2	4.2	0.3
<i>2017</i>	55.7	213.5	12.0	455.7	4.9	0.5

The two leading fuel cell technologies in terms of installed capacity are the proton exchange membrane fuel cell (PEMFC) and the solid oxide fuel cell (SOFC). Other technologies, such as the direct methanol fuel cell (DMFC), phosphoric acid fuel cell (PAFC), molten carbonate fuel cell

(MCFC) and alkaline fuel cell (AFC) are compiled under “other technologies”. In **Table 1-2**, a summary of the units sold and installed capacity per year is presented. It is possible to analyse two distinct scenarios. First, even though the number of PEMFC units installed has been kept roughly constant, the capacity installed has increased almost by 10 times. However, while SOFC units installed increased by 10 times in 5 years, the installed capacity has only tripled. Such distinct increase in capacity of PEMFCs in comparison to SOFCs indicates a bigger market interest in the PEMFCs and the energy requirement for the technology. Moreover, the rapid increase in PEMFCs energy per unit is seen as well.

**Table 1-2** Leading technologies in fuel cell market data.<sup>14</sup> Installed units and Megawatts per year.

<i>Year</i>	<i>PEMFC</i>		<i>SOFC</i>		<i>Other technologies</i>	
	<b>10<sup>3</sup> units</b>	<b>Megawatts</b>	<b>10<sup>3</sup> units</b>	<b>Megawatts</b>	<b>10<sup>3</sup> units</b>	<b>Megawatts</b>
<i>2012</i>	40.4	68.3	2.3	26.9	3.0	71.5
<i>2013</i>	58.7	68	5.5	47.0	2.6	100.4
<i>2014</i>	58.4	72.7	2.7	38.2	2.5	74.5
<i>2015</i>	53.5	151.8	5.2	53.3	2.2	93.0
<i>2016</i>	44.5	341.0	16.2	62.9	2.5	112.6
<i>2017</i>	45.5	486.8	24	76.4	3.1	106.5

## 1.2 Electrochemical energy storage/conversion based on oxygen evolution and reduction half-cell reactions

In this work, the focus was made on electrochemical energy storage and conversion devices based on oxygen half-cell reactions, including fuel cells, electrolyzers and metal-air batteries. The basic structure of a PEMFC is shown schematically in **Figure 1-2 (a)**. In a typical arrangement, the fuel (*e.g.* H<sub>2</sub>) fed to the anode while the oxidant (*e.g.* O<sub>2</sub>) is fed to the cathode. The chemical reaction

at the electrodes (oxidation of the fuel and reduction of the oxidant) is the source of electrons in the electric circuit connecting the anode and cathode. On the contrary a PEM electrolyzer (**Figure 1-2 (b)**) utilizes electrical energy to drive the chemical reaction (*e.g.* decomposition of the electrolyte in  $H_2$  and  $O_2$ ). Finally, the third device for energy storage considered in this discussion are the metal-air battery (**Figure 1-3 (c)**). All these devices have in common the oxygen reaction in one half cell, either oxygen reduction (*i.e.* fuel cells and metal-air batteries) or oxygen evolution (*i.e.* electrolyzer). A deeper discussion in the oxygen reduction reaction will be presented further in this chapter.

Considering grid levelling applications, reversible fuel cells (switching between fuel cell and electrolyzer mode), or fuel cell in tandem with an electrolyzer are an interesting alternative to transform electricity into chemical energy or *vice versa*. However, from the three examples, secondary batteries are the most commonly used grid levelling device. Different types of batteries were developed throughout the years, from the lead-acid battery, which was first described by Gaston Panté in 1859<sup>15</sup>, to recent redox flow battery<sup>16</sup>.

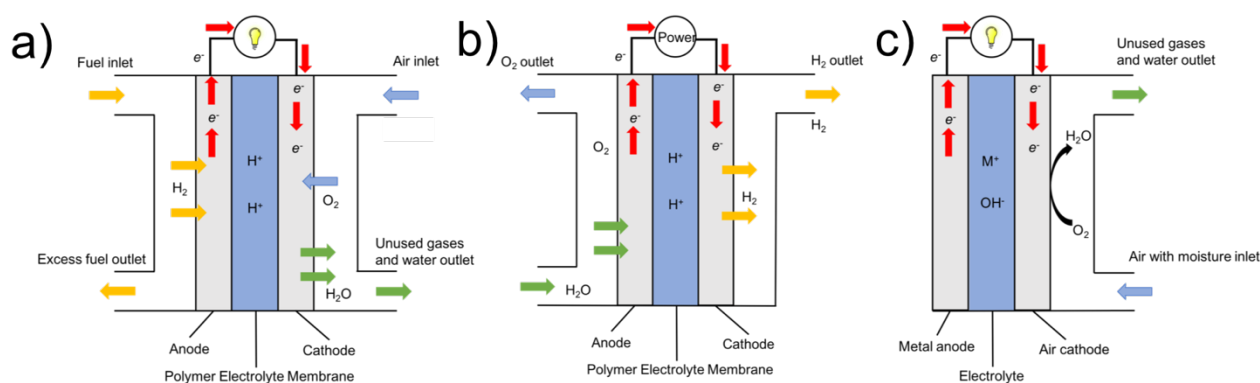
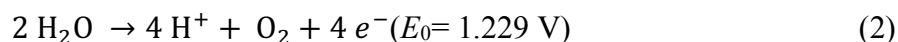
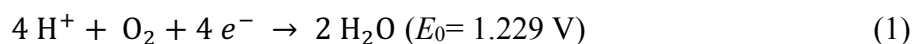


**Figure 1-2** Schematic representation of a) a polymer electrolyte membrane (PEM) fuel cell, b) PEM electrolyzer and c) a metal air battery (discharging).

In addition, with metal-air batteries, for instance the Li air battery (**Figure 1-2 (c)**), electricity is generated through a redox reaction between a metal and oxygen in air. The metal is the anode, thus being oxidized and releasing electrons to the external circuit during discharging. In the other half of the electrochemical cell, air diffuses to the cathode where  $O_2$  is reduced to oxygen containing species,

such as  $\text{Li}_2\text{O}_2$ <sup>17</sup>. Several advantages of metal air batteries are related to the operation conditions. As the metal-air battery is operated with air, the need to have a second electrolyte, in case of redox flow batteries the electrolyte would have to be stored in a tank, is suppressed by the simple fact that air is abundant, and then a compressor would be enough to supply it.

The reaction occurring in the cathode of a PEMFC is the oxygen reduction reaction (ORR), where  $\text{O}_2$  is to  $\text{H}_2\text{O}$  (Eq. 1) in aqueous systems. In PEM electrolyzer  $\text{O}_2$  is generated through the electrochemical oxidation of  $\text{H}_2\text{O}$  (Eq. 2). This reaction is known as the oxygen evolution reaction (OER).



For both reactions, electrocatalysts are required to overcome the sluggish kinetics of the ORR<sup>18</sup> and OER<sup>19</sup>. Considering state-of-the-art electrocatalysts, 0.3 V and 0.25 V overpotential are present for the ORR and OER, respectively.<sup>20</sup> This accounts for losses in energy conversion efficiency, decreasing the power density of the devices that employ this technology.

To better understand the origins of this overpotential and ways to overcome it, first one must look at the reaction mechanisms: The mechanisms for ORR and OER are not as simple as Eq. 1 and Eq 2 indicate. Various intermediate steps can take place on different routes to transfer the four electrons. Depending on the catalyst and electrolyte, the pathways the reaction may take could vary. The current understanding and propositions of the ORR and OER are discussed in the further sections with a closer view on state-of-the-art and alternative catalyst materials.

### 1.3 Oxygen reduction reaction catalysts

The ORR is a multi-electron reaction with two main competing pathways, which are a direct 4-electron reduction of  $O_2$  to  $H_2O$  and the 2-electron pathway that generates  $H_2O_2$  as a product or intermediate.<sup>21</sup> **Figure 1-3** shows a general simplified scheme for ORR pathways according to Wroblowa.<sup>22</sup>

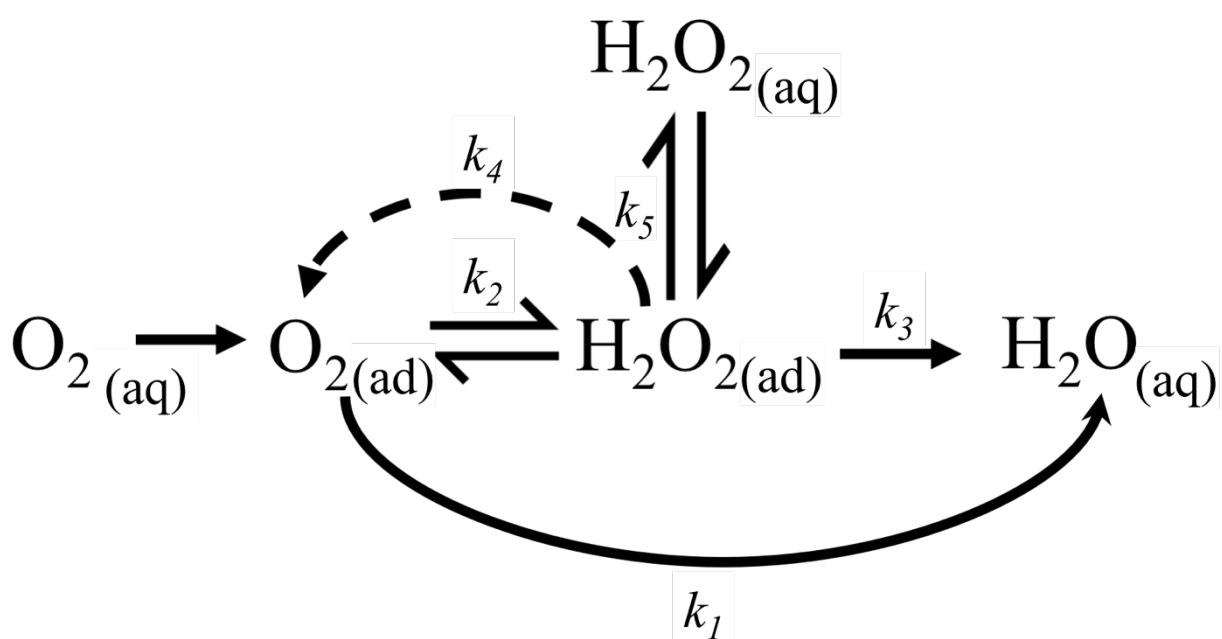


**Figure 1-3** Proposed oxygen reduction pathways on noble metals. "ad" indicates adsorbed species, while "aq" indicates solvated species in water.

The 4-electron pathway (reaction  $k_1$ ) is more interesting due to highest energy efficiency, where 4-electrons are extracted from each adsorbed  $O_2$  molecule. However, the 2-electron pathway can occur (reactions  $k_2$  and  $k_3$ ), or intermediate reactions with combinations of the 2 and 4 electron pathways (reactions  $k_2 + k_3$ ). Moreover, it is possible to have the catalytic decomposition of  $H_2O_2$  to  $O_2$  (reaction  $k_4$ ) and finally the desorption of  $H_2O_2$  from the electrode (reaction  $k_5$ ). Intermediate reactions, expect reaction  $k_1$ , are extremely relevant factors regarding catalyst stability, since not only

the 2-electron pathway will achieve half of the energy efficiency but also the generation of H<sub>2</sub>O<sub>2</sub> can cause catalyst and catalyst layer degradation. Specially the formation of radical species which degrade the polymer on the catalyst layer.<sup>23</sup> A vast literature is available on the detrimental effects of H<sub>2</sub>O<sub>2</sub> to catalyst particles, and catalyst layer components such as binder (*i.e.* Nafion) and catalyst support (*i.e.* carbon black).<sup>24–29</sup> The ORR generally passes through a series of intermediate species that are adsorbed at the active sites on the electrode surface (active sites are represented as \* in Table 1-3). Recently, a 3-electron reduction pathway had been reported, which resulted in the concurrent formation of OH•(aq)<sup>30</sup>. The authors reported that such pathway is exclusive to the Pt surfaces and it is an unexpected process, despite the OH•(aq) production to be envisaged during ORR in the Haber–Weiss reaction. However, such mechanism could be a consequence of their experimental conditions. This may suggest that more efficient radicals are produced in the diffusion layer between the microelectrode tip and the sample rather than on the electrode surface, and that only a small fraction of the produced reactive oxygen species reach the surface.

**Table 1-3.** Three possible mechanisms for oxygen reduction reaction on Pt (111) surface. Adapted from Nilekar *et al.*<sup>31</sup>. Mechanism obtained by DFT calculations. Species that are adsorbed at the active sites on the electrode surface are represented as \*.

<b>1. Oxygen dissociation</b>	<b>2. Peroxyl dissociation</b>	<b>3. Hydrogen peroxide dissociation</b>
$O_2 + * \rightarrow O_2^* \text{ (3)}$		
$O_2^* + * \rightarrow O^* + O^* \text{ (4)}$	$O_2^* + H^+ + e^- \rightarrow OOH^* \text{ (5)}$	
$OOH^* + * \rightarrow O^* + OH^* \text{ (7)}$		$OOH^* + H^+ + e^- \rightarrow H_2O_2^* \text{ (6)}$
$O^* + H^+ + e^- \rightarrow OH^* \text{ (9)}$		$H_2O_2^* \rightarrow OH^* + OH^* \text{ (8)}$
$OH^* + H^+ + e^- \rightarrow H_2O + * \text{ (10)}$		



It is important to point out that many discussions in order to elucidate the ORR are based on Density Functional Theory (DFT) calculations<sup>32</sup>. According to Nilekar *et al.*<sup>31</sup>, the ORR can possibly be explained by three mechanisms, as presented in **Table 1-3**. Each mechanism relies, fundamentally, on an O-O bond scission step and a series of protonation steps. The main difference among the three mechanisms of **Table 1-3** lies in the O-O\* bond cleavage step. In the oxygen dissociation mechanism, the O-O\* bond scission step is only preceded by the O<sub>2</sub> adsorption on the surface. In the peroxy mechanisms, the O-O\* bond scission occurs through the dissociation of O-OH\* into O\* and OH\* consecutive to a preceding O<sub>2</sub>\* protonation step. Finally, in the hydrogen peroxide dissociation mechanism, O-OH\* is further protonated to form H<sub>2</sub>O<sub>2</sub> and then the scission of the O-O bond occurs to form two adsorbed OH\*.

Generally, the mechanism depends on the presence of a catalyst that allows the intermediate steps to occur. Therefore, one of the main challenges for the ORR is to overcome the overpotential applied to surpass the kinetics of the intermediate steps. Nørskov *et al.*<sup>33</sup> discussed this intermediates stabilization as the origin of the overpotential for the ORR reaction. The overpotential was shown to be linked directly to the proton transfer to the adsorbed oxygen or hydroxide, being strongly bonded to the surface of the electrocatalyst at the electrode potential where the overall cathode reaction is at equilibrium. Presented in **Figure 1-4** is a diagram of the effects of overpotential to modulate the free energy  $\Delta G$  in order to facilitate the intermediate steps of the ORR. For instance, at the equilibrium potential in the exemplary case of Pt<sub>3</sub>Y (1.23 V vs RHE),  $\Delta G_1$  (Eq. 5) and  $\Delta G_4$  (Eq. 10) are positive, indicating the non-spontaneous path for the reaction. To compensate the activation energy required to drive the ORR downhill in energy an overpotential is added. However, at -0.42 V of overpotential, all the intermediate steps of the ORR have a negative  $\Delta G$ .

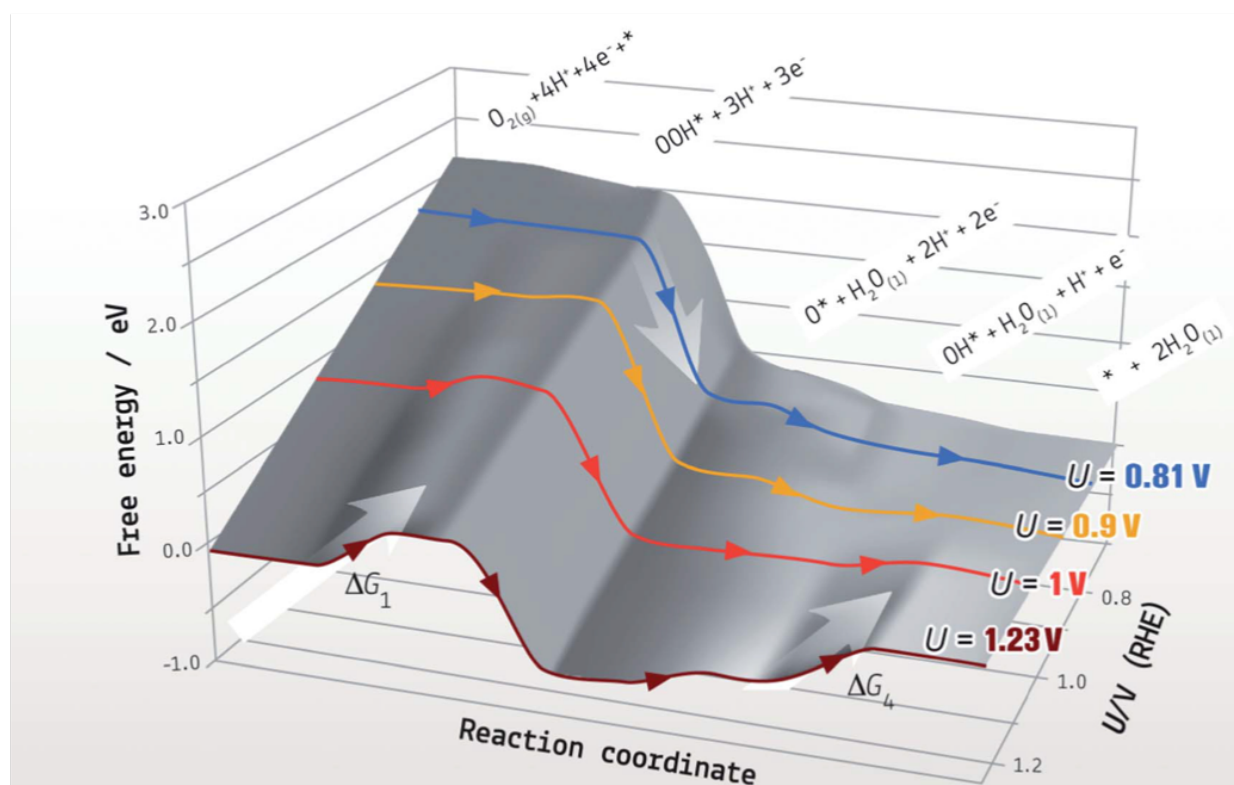


**Figure 1-4** Theoretical free energy diagram for Pt<sub>3</sub>Y(111) with 25% Y in the subsurface layer data obtained from DFT calculation. Original citation <sup>34</sup> – Published by The Royal Society of Chemistry.

Such analysis was confirmed by the work of Hansen *et al.*<sup>35</sup>, in which the limiting step, on the basis of thermodynamic analysis, is the reduction of OH\* to H<sub>2</sub>O (Eq. 10). Therefore, one way to compensate this limitation is to weaken the binding energy of O\* or OH\*. However, from the kinetic point of view, the bottleneck of the ORR is the first electron transfer reaction ( $\Delta G_1$ ), as seen in **Figure 1-4**, due to the highest activation energy from all the intermediate reactions of the ORR.

The activity of a material towards the ORR can be presented as a volcano plot, where the relative activity enhancement is plotted against the hydroxyl binding energy (**Figure 1-5**), as well as the required overpotential to all intermediate reactions to have negative free energy. By analysing the volcano plot, it is possible to identify the following regions: The top of the volcano represents the theoretically most active catalyst relative to Pt (111). Catalysts on the left side of the thermodynamic plot have as limiting step the reduction of OH\* to H<sub>2</sub>O, while on the right leg the activation of O<sub>2</sub> as

OOH\* is limited. In the kinetic model, the first electron transfer reaction for the reduction of O<sub>2</sub> is discussed as the rate limiting step.<sup>34</sup>

For instance, as demonstrated by Stephens *et al.*,<sup>34</sup> the most active catalyst for the ORR reaction should exhibit a slightly weaker binding energy than Pt to some of the intermediates, such as O\*, HO\* and HOO\*. Moreover, recent studies focused on optimizing the size, shape and composition of nanoparticles to increase further the catalytic activity.<sup>36</sup> Multiple compositions have been tested, such as Pt<sub>3</sub>Ni (111), Pt<sub>3</sub>Ti, Pt/Pd (111) and the overall activity can be seen in **Figure 1-5**. The dashed lines represent the theoretical boundaries that determine the step in which the overpotential is originated, while the red line represents different near-surface alloys for Cu/Pt(111). In this scenario, Pt<sub>3</sub>Ni (111) presents the highest activity compared to Pt, while Pt<sub>3</sub>Ti and Pt/Pd (111) present similar activity. However, the overpotential origin is defined in different steps in the ORR for Pt<sub>3</sub>Ti it is  $\Delta G_1$  while for Pt/Pd it is  $\Delta G_4$ .<sup>37</sup>

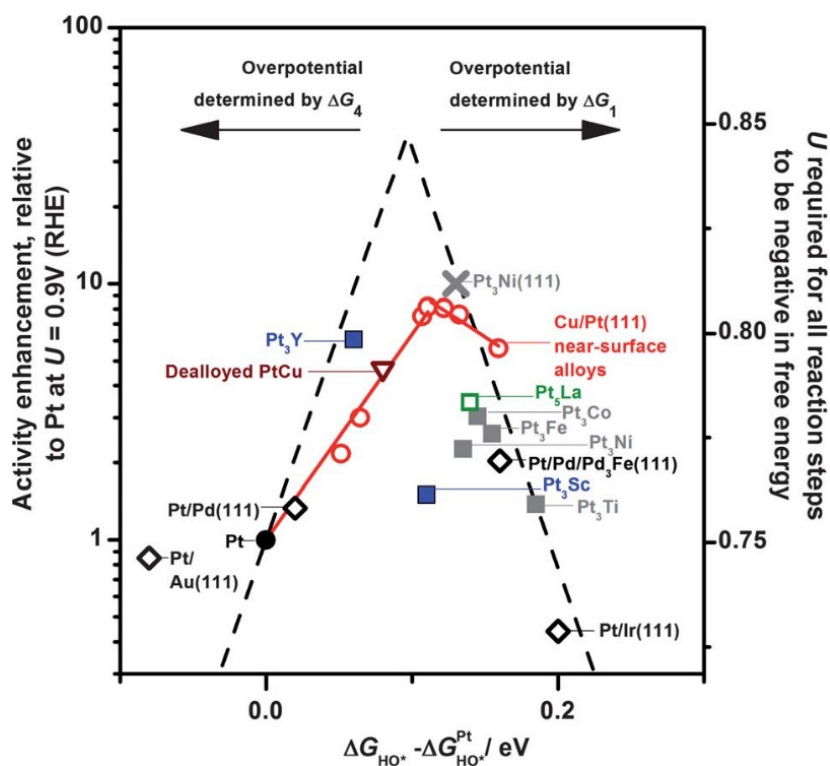


**Figure 1-5** Examples of simulated volcano plots extracted from literature. Diagram of activity enhancement and overpotential versus oxygen binding energy. From Stephens *et al.*<sup>34</sup> Published by The Royal Society of Chemistry.

The main characterization tools for understanding the 4-electron reaction pathway are based on the determination of the Gibbs energy for all the steps of the ORR (**Figure 1-4**). The relation of different binding energies to each limiting step, and the overpotential, is presented in each side of the volcano. Therefore, it is possible to compare different materials, for example: Pt alloys such as Pt<sub>3</sub>Y and Pt<sub>3</sub>Ni (111). Pt<sub>3</sub>Y has the overpotential determined by the  $\Delta G_4$ , while Pt<sub>3</sub>Ni (111) has the overpotential determined by  $\Delta G_1$ . Finally, having the overpotential and coverage relationship, it is possible to understand which species are predominating at the electrode surface at a given potential and predict, based on the reaction pathway, how the reaction will proceed. Moreover, it is possible to determine the Tafel plot for the reaction. For instance, in the work of Hansen<sup>35</sup>, it was determined, through DFT calculations for Pt (111), that between potentials 0.75 and 0.95 V *vs* RHE the Tafel slope is of 59 mV/dec, while for potentials above 0.95 V *vs* RHE the Tafel slope decreases to 30 mV/dec. Such variation is due to the change in the predominant species adsorbed on the surface of Pt (111). At potentials above 0.95 V *vs* RHE, the surface coverage is dominated by O\*. At potentials between 0.95 and 0.75 V *vs* RHE, the surface coverage is mainly of OH\*, and at potentials below 0.75 V *vs* RHE most surface sites are free.

Finally, one more point of discussion is the influence of the pH and solvent on the pathway (**Table 1-4**). Depending on the pH of the electrolyte the ORR will proceed to a different pathway. For instance, in alkaline aqueous solutions, the reaction pathway will follow Eq. 11 – 13, while in acid aqueous solution Eq. 14 – 16, and in aprotic solvents the reaction will follow the pathway presented in Eq. 17.

**Table 1-4.** Process of the ORR under different reaction conditions. Adapted from Zhang *et al.*<sup>38</sup>

Reaction Condition	Reaction	Potential (V vs. SHE)
Alkaline aqueous solution	$O_2 + H_2O + 4 e^- \rightarrow 4OH^-$ (11)	0.401
	$O_2 + H_2O + 2 e^- \rightarrow HO_2^- + OH^-$ (12)	-0.065
	$HO_2^- + H_2O + 2 e^- \rightarrow 3OH^-$ (13)	0.897
Acidic aqueous solution	$O_2 + 4 H^+ + 4 e^- \rightarrow 2H_2O$ (14)	1.229
	$O_2 + 2 H^+ + 2 e^- \rightarrow H_2O_2$ (15)	0.700
	$H_2O_2 + 2 H^+ + 2 e^- \rightarrow 2H_2O$ (16)	1.760
Aprotic solvent	$O_2 + 2 e^- \rightarrow 2O_2^{2-}$ (17)	

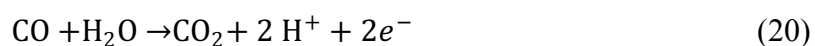
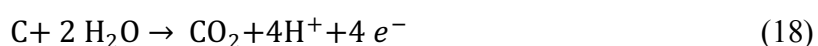
Moreover, according to Fang *et al.*<sup>39</sup>, it can be inferred that, for the ORR at Pt(111) in solutions with pH between 1 and 13, the reaction pathway followed will not interfere in the kinetic and kinetic-mass transport mixed-control regions for ORR. The ORR will be located in the same potential region for Eq. 13 and 16 and both ORR and OH<sup>•</sup> adsorption/desorption display similar pH independence.

### 1.3.1 ORR at platinum group metals

The most common and studied materials for the ORR are mainly noble metal particles, especially platinum.<sup>38</sup> At the current stage, Pt and Pt-alloys are the most practical catalysts used for the ORR. Despite the discussions presented above been obtained from Pt based systems the exact mechanisms of the ORR are still under debate<sup>40</sup>. Moreover, the limited availability (concentration of 5 ppb in Earth's crust<sup>41</sup>) of platinum and its high cost of 27.83 USD per gram (price consulted in 06.05.2019<sup>42</sup>), lead to many efforts been done to reduce the platinum loading while increasing the Pt utilization<sup>43</sup>. For instance, early fuel cell vehicles contained 100 g of platinum for a 90 kW fuel cell, which was already reduced to 30 g per vehicle<sup>44</sup>. In order to keep the power density of the devices and yet reduce the amount of Pt utilized, Pt nanoparticles are usually supported on carbonaceous

materials, such as carbon black, carbon nanotubes (CNTs) and, more recently, graphene. This symbiosis allows high-catalyst surface areas at low-catalyst loadings.

However, at the down side, carbon supported catalysts are susceptible to catalyst particle agglomeration.<sup>26</sup> Another major drawback of high-performance, low-loaded electrodes resides in the thermodynamic instability of carbon under PEMFC cathode conditions. Above 0.207 V *vs* NHE carbon can be oxidized to carbon dioxide following reactions (Eq. 18 and Eq. 20) or oxidized to carbon monoxide (Eq. 19).<sup>26</sup> The oxidation of the carbon support – generally referred to as carbon corrosion – can lead to a performance decrease due to accelerated loss of active surface area and alteration of pore morphology and pore surface characteristics.<sup>26</sup>



At typical operating conditions (*e.g.* temperature of 80 °C and current density of 1A/cm<sup>2</sup>) of a PEMFC,<sup>45</sup> carbon is susceptible to corrosion. In general terms, it is postulated that a Pt nanoparticle catalyzes the support corrosion by the transfer of O and/or OH radicals to the carbon, generating CO<sub>2</sub>. Likewise, been a parasitic reaction, carbon corrosion in the nanoparticle support increases the electrode resistance, leading to a decrease in the efficiency of the device, and a higher overpotential will be required to achieve the same values of current. Different attempts have been employed to reduce carbon support corrosion specially at high overpotentials.<sup>46–51</sup> As standard practice, either the carbon

black support is modified or substituted to nanostructured thin film catalysts (NSTF), or highly graphitised carbon blacks. In addition, alternative supports *e.g.* metal oxides, borides or carbides can be used.<sup>52</sup> Graphitised carbon blacks have been used to reduce carbon corrosion.<sup>52 53</sup>

A second strategy to decrease the total amount of Pt in a fuel cell is the utilization of alloys<sup>54</sup>. A major advantage of alloys over their corresponding pure metal counterparts is their broad range of composition and adjustable properties<sup>55</sup>. In the case of Pt alloys, a less noble metal would be unstable at the surface under certain operating conditions (*i.e.* extreme pH). However, it has been demonstrated that, for instance, Cu/Pt(111) near-surface alloys are able to achieve a higher position in the volcano plot than pure Pt (**Figure 1-5**).<sup>34,56</sup> Such performance is attributed to the surface reactivity tuning. It is possible to change the interatomic distance of Pt atoms forming a monolayer over a Cu surface, affecting the stabilization of the adsorbed species in the Pt surface. Such changes will allow the shift of the overpotential coming from either  $\Delta G_1$  or  $\Delta G_4$ , leading to a compromise between them to achieve a lower overpotential for the ORR.<sup>57</sup>

Therefore, it is possible to tune finely the composition of nanoparticles in order to improve the catalytic activity.<sup>58</sup> Peng *et al.*<sup>59</sup> presented a comprehensive study of the platinum-based nanoparticle properties such as shape, alloy composition, and nanostructure. The variation of these parameters will influence the overall surface area ratio, as well as the dependency of the binding strength between Pt atoms and adsorbed species<sup>36</sup>. However, platinum based catalysts for the ORR suffer from a limited durability, *e.g.* by Pt dissolution during operation.<sup>60</sup>

More recent works approach the use of platinum-based core-shell particles. These particles can be synthesized with different materials such as Pt@Cu,<sup>61</sup> Pt@Fe<sub>2</sub>O<sub>3</sub>,<sup>62</sup> Pd@Pt.<sup>63</sup> According to Oezaslan *et al.*<sup>64</sup> the Pt shell thickness is a key parameter for controlling the activity of core-shell nanocatalysts. Strong ORR activity enhancements were specially observed for Pt shells of single to few atomic

layers. Stability, on the other hand, is a more complex subject since it does not only depend on the thickness of the shell layer and core size, but on the interaction of this particle with the support.<sup>64</sup>

### 1.3.2 ORR at non-precious, low cost catalyst materials

Catalyst materials based on non-precious oxidized metals, such as cobalt (*e.g.* cobalt oxides, cobalt sulfides, cobalt corroles and other cobalt compounds), are known since decades<sup>65</sup> to show activity towards the ORR.<sup>65,66</sup> Other non-noble catalyst materials, besides cobalt-based, are normally carbon-supported transition metals<sup>67</sup>. Within the transition metals used, the most commons are Fe,<sup>68</sup> Co,<sup>69</sup> Ni<sup>70</sup> and Cu.<sup>71</sup> Recent works in the field describe CoO<sup>72</sup> and MnO<sub>2</sub><sup>73</sup> as alternatives to platinum as well as N-doped carbonaceous nanomaterials, such as carbon nanotubes,<sup>74</sup> graphene<sup>75</sup> and graphite.<sup>76</sup> Finally, another group of non-precious oxidized metals worth mentioning is the nitrogen coordinated metal inserted on a carbon matrix (M-N-C), with catalyst materials such the Dodelet<sup>77</sup> type Fe-N-C and FeCo-N-C.<sup>78</sup>

Co<sub>3</sub>O<sub>4</sub> adopts a normal spinel structure, with Co<sup>2+</sup> ions in tetrahedral interstices and Co<sup>3+</sup> ions in octahedral interstices, in which the peculiar crystal structure enables a readily accessible Co<sub>3</sub>O<sub>4</sub> and provides high environmental stability.<sup>79</sup> However, this material usually suffers from dissolution in acidic conditions, during normal operation conditions<sup>80</sup> and, due to this fact, supporting this material on another one for stabilization, while keeping or enhancing the catalytic activity, is of great interest.

## 1.4 Oxygen evolution reaction catalysts

The oxygen evolution reaction (OER) is the second reaction of interest, considering electrolyzers and rechargeable metal air batteries.<sup>20</sup> However, in case of reversible systems, the overpotential is related to the sum of both reactions. Therefore, decreasing the global overpotential of the electrochemical energy conversion device, requires the use of OER catalysts.<sup>81</sup> The great majority of OER electrocatalyst materials are metal oxides (*i.e.* IrO<sub>2</sub>, RuO<sub>2</sub>, PtO<sub>2</sub>, SrCoO<sub>3</sub>, NiFe), being IrO<sub>2</sub> and RuO<sub>2</sub>



the most active electrocatalysts<sup>82</sup>. However, the scarcity and high cost of some metals, such as iridium (*i.e.* iridium is 10 times less abundant than Pt and 22.15 USD/gram – 06.05.2019), has a limiting effect in the large-scale production of such electrocatalysts. Alternative OER electrocatalysts are widely investigated to substitute precious metals by tuning the structures and components of materials based on transition metals<sup>83</sup>, such as Ni doping with Fe and Co, for OER<sup>84-87</sup>. In such group, we have metal oxides, phosphates, chalcogenides and metal-carbon materials<sup>40</sup>. As presented in **Figure 1-6**, similar to the ORR, it is possible to develop volcano type plots for OER electrocatalysts. The principle is the same, *i.e.*, after the determination of the binding energies of the intermediate reactions, it is possible to compare different material activities at a fixed parameter, such as a given overpotential. In such case one can consider the top of the volcano as the position of the most active material (the one that requires less overpotential to overcome the kinetic limiting steps). The descriptor presented in **Figure 1-6** is the  $\Delta G$  for  $O^*$  and  $OH^*$  adsorption. According to Frydendal,<sup>88</sup> these theoretically predicted overpotentials relate to a thermodynamic allowance of the reaction. Moreover, the comparison to experimental current densities is not straightforward. However, the trends found from such analyses are in good agreement with experiments and, in fact, the overpotential needed to drive 10 mA/cm<sup>2</sup> at surfaces match to the theory within 0.1-0.2 mV for most materials<sup>81,89</sup>. In the case of the OER, Ir or IrO<sub>2</sub> are known as state-of-art catalyst materials. However, at the current state of research, materials such as NiFeO<sub>x</sub> and NiCoO<sub>x</sub> are more active towards the OER than Ir or IrO<sub>x</sub>. Still, stability is a big issue for non-noble metals oxides.<sup>90</sup>

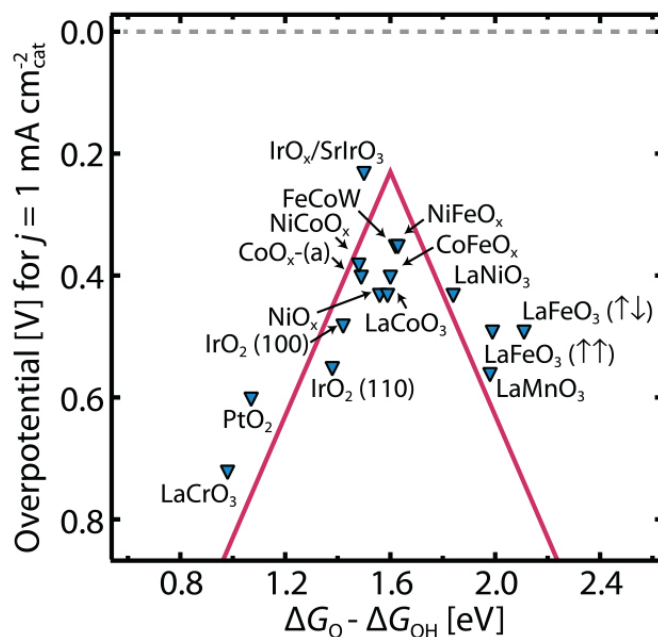


**Figure 1-6** Theoretical overpotential for oxygen evolution vs the difference between the standard Gibbs energy of two subsequent intermediates of several binary oxides. Figure extracted from reference<sup>91</sup> Reprinted with permission for AAAS.

Several OER mechanisms are presented in the literature. The differences arise from the electrolyte pH and possible intermediate species formed during the catalytic reaction. Common to all pathways (*i.e.* electrochemical oxide, oxide, Krasil'shchikov and Yeager's paths) is the formation of a metal hydroxide bond that is broken, prior to the release of O<sub>2</sub> from the electrocatalyst surface. **Table 1-5** and **Table 1-6** show the mechanism based on reactions for the OER, with electrochemical oxide and oxide path in alkaline and acid electrolyte, respectively.

**Table 1-5** Possible mechanisms for OER in alkaline media. (\* – activated surface site).

Reaction path	Reaction process
Electrochemical oxide <sup>92</sup>	$* + \text{OH}^- \rightarrow * \text{OH} + e^-$ (21)
	$* \text{OH} + \text{OH}^- \rightarrow * \text{O} + \text{H}_2\text{O} + e^-$ (22)
	$2 * \text{O} \rightarrow 2 * + \text{O}_2$ (23)
Oxide <sup>92</sup>	$* + \text{OH}^- \rightarrow * \text{OH} + e^-$ (24)
	$2 * \text{OH} \rightarrow * \text{O} + * + \text{H}_2\text{O}$ (25)
	$2 * \text{O} \rightarrow 2 * + \text{O}_2$ (26)
Krasil'schchikov <sup>93</sup>	$* + \text{OH}^- \rightarrow * \text{OH} + e^-$ (27)

	$*\text{OH} + \text{OH}^- \rightarrow * \text{O}^- + \text{H}_2\text{O}$ (28)
	$* \text{O}^- \rightarrow * \text{O} + e^-$ (29)
	$2 * \text{O} \rightarrow * \text{S} + \text{O}_2$ (30)
Bockri's <sup>94</sup>	$* + \text{OH}^- \rightarrow * \text{OH} + e^-$ (31)
	$* \text{OH} + \text{OH}^- \rightarrow * \text{H}_2\text{O}_2 + e^-$ (32)
	$* \text{H}_2\text{O}_2 + \text{OH}^- \rightarrow * \text{O}_2\text{H}^- + \text{H}_2\text{O}$ (33)
	$* \text{H}_2\text{O}_2 + * \text{O}_2\text{H}^- \rightarrow \text{H}_2\text{O} + \text{OH}^- + \text{O}_2$ (34)
Yeager's <sup>93</sup>	$* + \text{OH}^- \rightarrow * \text{OH} + e^-$ (35)
	$* \text{ZOH} \rightarrow * \text{Z}^{+1}\text{-OH} + e^-$ (36)
	$2 * \text{Z}^{+1}\text{OH} + 2 \text{OH}^- \rightarrow 2 * + 2 \text{H}_2\text{O} + \text{O}_2$ (37)

**Table 1-6** Possible mechanisms for OER in acid media. (\* – activated surface site).

Reaction path	Reaction process
Electrochemical oxide <sup>92</sup>	$* + \text{H}_2\text{O} \rightarrow * \text{OH} + \text{H}^+ + e^-$ (38)
	$* \text{OH} \rightarrow * \text{O} + \text{H}^+ + e^-$ (39)
	$2 * \text{O} \rightarrow 2 * + \text{O}_2$ (40)
Oxide <sup>92</sup>	$* + \text{H}_2\text{O} \rightarrow * \text{OH} + \text{H}^+ + e^-$ (41)
	$2 * \text{OH} \rightarrow * \text{O} + * + \text{H}_2\text{O}$ (42)
	$2 * \text{O} \rightarrow 2 * + \text{O}_2$ (43)
Krasil'schchikov <sup>93</sup>	$* + \text{H}_2\text{O} \rightarrow * \text{OH} + \text{H}^+ + e^-$ (44)
	$* \text{OH} \rightarrow * \text{O}^- + \text{H}^+$ (45)
	$* \text{O}^- \rightarrow * \text{O} + e^-$ (46)
	$2 * \text{O} \rightarrow 2 * + \text{O}_2$ (47)
Wade and Hackerman's <sup>95</sup>	$2 * + 2 \text{H}_2\text{O} \rightarrow * \text{O} + * \text{H}_2\text{O} + 2 \text{H}^+ + 2e^-$ (48)
	$* \text{O} + 2 * \text{OH}^- \rightarrow 2 * + * \text{H}_2\text{O} + \text{O}_2 + 2e^-$ (49)

Considering the energy diagram, when the potential is shifted beyond 1.23 V vs RHE (more anodically), the overpotential starts to shift the energy profile to negative  $\Delta G$  (**Figure 1-7**)<sup>96</sup>. Still, not all of the four steps are favored. In fact, to get all steps downhill in the energy diagram it is

required the application of potentials above 1.60 V according to Frydendal<sup>88</sup>. For the ideal catalyst, all steps would require low overpotential beyond 1.23 V to have  $\Delta G < 0$ . However, the formation of adsorbates on the surface do not allow such to be feasible. In such diagram, the reaction path for the OER is presented as only downhill in energy. To obtain such a condition, the authors present an overpotential for the reaction of  $\eta = 0.35$  V. Even at this condition  $\Delta G_3$  of **Figure 1-7** is uphill in energy. Moreover, the authors utilize the energy diagram to compare the activity of state-of-the-art IrO<sub>2</sub> catalyst with Co-C<sub>3</sub>N<sub>4</sub>. This comparison allows the researchers to identify that the intermediates have a stronger interaction with the electrocatalyst surface. Finally, it is possible to interpret from **Figure 1-7** that the overpotential applied to Co-C<sub>3</sub>N<sub>4</sub> could be smaller to reach the same  $\Delta G < 0$  as IrO<sub>2</sub>.

In commercial electrolyzers, due to the formation of the intermediates and the high overpotential applied to the electrocatalyst, to achieve the desired current densities<sup>97</sup> (in the range of 10'000 A/m<sup>2</sup>) the catalyst suffers corrosion. Therefore, the study of new materials for the OER have to face two main challenges: First, to decrease the overpotential required to drive the OER. Second, to synthesize materials that can withstand the harsh conditions (*e.g.* 6 M KOH electrolyte) and maintain stability (*e.g.* no particle aggregation and material corrosion) for hundreds of hours<sup>98</sup>.

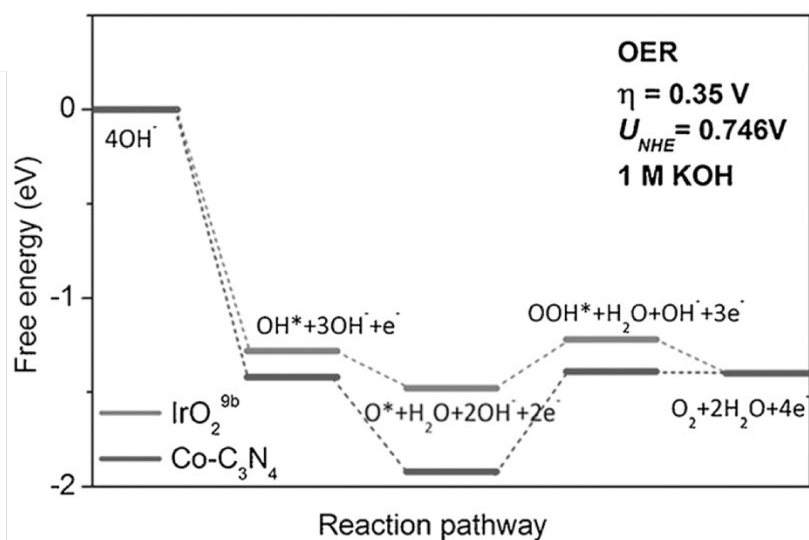


**Figure 1-7** Free energy diagram for the oxygen evolution reaction on Co-C<sub>3</sub>N<sub>4</sub> and IrO<sub>2</sub> surfaces. Figure adapted with permission from.<sup>99</sup> Copyright (2017) American Chemical Society.

## 1.5 Interpretation of the electrocatalytic activities for ORR and OER

In the case of the ORR, the most commonly used parameter for catalytic activity comparison is the kinetic current at 0.9 V (*vs* RHE). According to Stephens *et al.*<sup>34</sup>, an ideal catalyst should exhibit high current densities (1.5 A/cm<sup>2</sup>) for the ORR with a low overpotential from the thermodynamic limit (1.17 V). For such to happen, all the intermediate reactions following the scheme presented in Figure 1-4, should have a  $\Delta G$  equal or lower than 0. However, the  $\Delta G$  of adsorption of intermediates formed during the reaction pathway cannot be varied independently. Therefore, in the overall reaction, to overcome the activation energy of the formation of HOO\* ( $\Delta G_1$ ) and reduction of HO\* ( $\Delta G_4$ ) the potential must be shifted more from equilibrium than 0.2 V. In addition, Stephens *et al.*<sup>34</sup> discussed that, if  $\Delta G_1 + \Delta G_4$  has a minimum value of 0.8 eV, in an ideal catalyst, the potential for both reactions is divided equally. Hence, the minimum overpotential one can expect for a catalyst is of  $\sim 0.4$  V. This shift from equilibrium would be enough to grant that all steps from the reaction would have a  $\Delta G$  lower than 0. Considering the equilibrium potential and the shift of 0.4 V of overpotential, we achieve the potential of 0.9 V, where the comparison of catalysts is made.

For OER, according to Fabbri *et al.*<sup>19</sup>, the common parameter to describe the activity of electrocatalysts is the Tafel slope. Other parameters such as current density at a defined potential, potential at a defined current density and exchange current density can be allied to the Tafel slope to define the activity of the electrocatalysts. The irreversibility of the OER limited the reliability of exchange current density calculation. Moreover, for the other parameters presented above, the values are intrinsically related to the measuring conditions (*i.e.* scan rate and potential sweep direction). In the case of the Tafel slope, it is described that the catalytic current increases as a function of the applied overpotential.

## 1.6 Catalyst layer structure

In several electrochemical energy conversion devices, the electrodes contain so-called catalyst layers (CLs). A catalyst layer is the active component in the energy conversion device for the electrochemical reaction<sup>100</sup> and represents a porous three dimensional network to achieve high surface area of the catalyst, high electronic conductivity and transport channels for all reactants and products in liquid as well as gaseous form, normally mounted as a membrane electrode assembly (MEA) (**Figure 1-8**). Conventional catalyst layers in fuel cells contain  $0.2 \text{ mg}_{\text{Pt}}/\text{cm}^2$  in the cathode<sup>101</sup> with a thickness of  $1\text{--}3 \text{ }\mu\text{m}$ .<sup>102</sup> The catalyst phase is supported as nanoparticles of diameter  $2\text{--}5 \text{ nm}$  on carbon particles of  $20\text{--}50 \text{ nm}$ .<sup>26</sup>

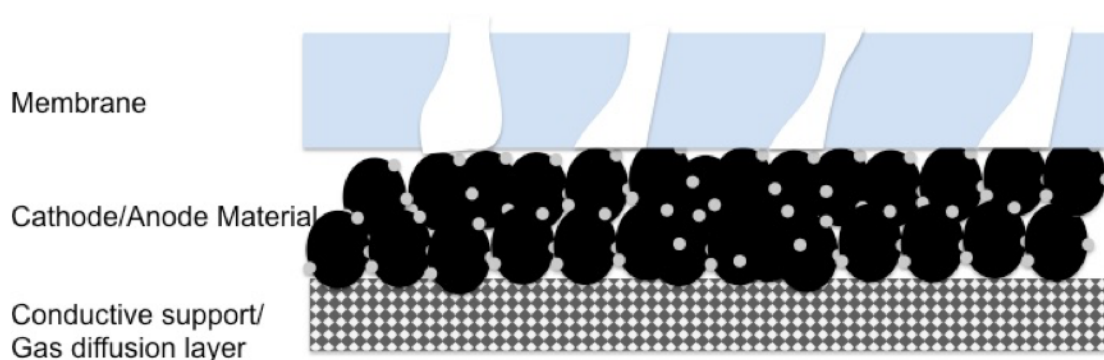


**Figure 1-8.** Scheme representing a catalyst layer (membrane electrode assembly (MEA)). The catalyst layer is presented as "Cathode/Anode Material" and located between the "Conducting support/Gas diffusion layer" and "Membrane".

The catalyst layer (CL) contains further an ion-conducting phase, usually Nafion (a sulfonated tetrafluoroethylene polymer, generally shown as fibers), generating porosity and proton conductivity. Nafion forms the electrolyte in wet condition, and provides the transportation of protons coming from the anode side through a Nafion membrane placed in-between the anode and cathode. A three-phase boundary (inset in **Figure 1-9** for the ORR) is formed around a catalyst nanoparticle (solid) where  $O_2$  (gas) is reduced, in the presence of  $H^+$  (aq) (liquid). The electrons reach the active sites through the electron conducting pathway in the CL (mainly connected carbon nanoparticles, but also Pt).

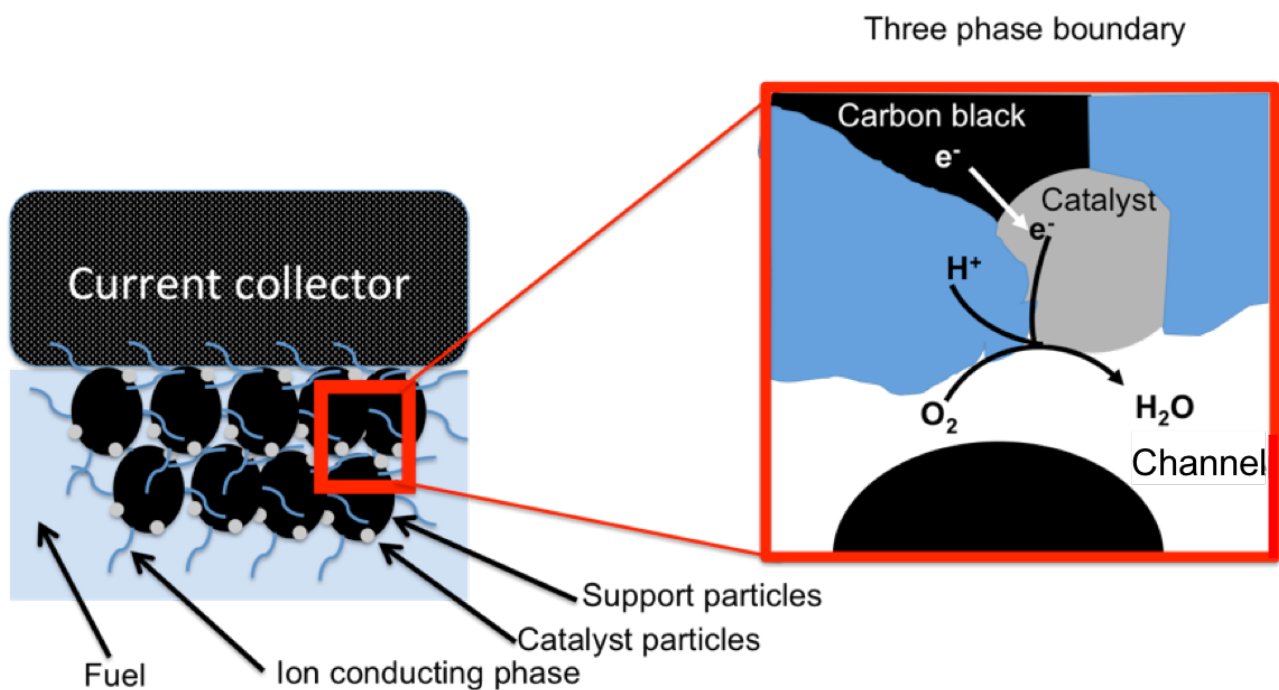


**Figure 1-9** Schematic representation of the three-phase boundary inside the catalyst layer.

### 1.6.1 Fabrication techniques for catalyst deposition

Catalyst layers are normally engineered in a manner that the catalyst particles are kept in contact with the membrane, electrolyte and current collector, as shown in **Figure 1-9**. In case of membrane electrode assemblies (MEAs), as applied in fuel cells and electrolyzers, various fabrication

methods have been developed to deposit particles either directly on the membrane (catalyst coated membrane – CCM) or on the gas diffusion layer (catalyst coated electrode – CCE).

The catalyst layer itself needs to hold enough catalyst material and needs to create as much active surface area (three-phase boundary) as possible. Furthermore, the fabrication techniques used need to provide stable and reproducible CLs for the reliable performance on the industrial level. Traditionally, catalyst layers are deposited on the membranes by a series of methods as listed in **Table 1-7**. Each method is characterized by certain properties, such as cost (equipment and running), speed, reproducibility, simplicity and equipment dimensions. For instance, inkjet printing can fabricate catalyst layers in minutes or in hours depending on the size and throughput of the machine, yet maintaining reproducibility. While spray gun aerolizing can produce rapidly CLs, but with low reproducibility and high wastage of material.

**Table 1-7.** Methods of depositing catalyst layers over membranes.

<b>Form of application</b>	<b>Technology</b>	<b>Reference</b>
<b>Solid</b>	Dry spraying	103
	Decal method	104
<b>Emulsion application</b>	Spreading of pastes	105
	Painting ink	106
	Screen printing	107
	Inkjet printing	108
<b>Application of Aerosol</b>	Spray gun aerosolizing	109
	Sonicated spray	109
	Spray under irradiation	110
<b>Vapor phase deposition</b>	Magnetron sputtering	111
	Chemical vapor deposition	112
<b>Electrode assisted deposition</b>	Electrodeposition	113
	Electro spraying	114
	Electrophoretic deposition	115
<b>Application in precursor state</b>	Electron beam reduction	109



	Impregnation reduction	109
	Print-Light-Synthesis	116

Most of these methods, such as decal method, spray gun and screen printing, are multistage and require large volumes of starting material (*e.g.* hundreds of mL). Some methods, such as screen-printing and spray deposition, have the disadvantage of requiring masks to produce the desired shape of the deposited pattern, which can result in significant losses of the scarce and expensive catalyst material. Other methods, such as electron beam reduction and sonicated spraying, require specialized and high cost equipment for the process<sup>117</sup>.

Four different criterions for the industrial CL fabrication are generally considered: i.) the reduction of processing steps, ii.) the adaptability to fabricate different CL designs (*e.g.* dimensions), iii.) the possibility to control the quality of the manufacturing process within the required parameters and iv.) manufacturing time. One process recently gaining interest and fulfilling most of these criterions is inkjet printing.

Inkjet printing as a fabrication tool has attracted attention due to its versatility, as it is a maskless, digital fabrication technique<sup>108</sup> with accurate control of the deposition of droplets from one up to thousands of individually addressable nozzles within a single printhead. The advantage of using digital droplet deposition techniques are: i.) the precise control of the materials deposition by the number of droplets per area, and ii.) the decrease in material waste, as no masks are required where ink gets stuck, and by depositing material only where requested (drop-on-demand, *vide infra*). These advantages are specially interesting concerning costs and labour in the case of catalyst materials handling.<sup>118</sup> Inkjet printing has a long history in the field of printed graphics. Recent further developments of printheads, printer hardware components and software has led to a wider application in the field (*e.g.*, from small prototypes to large-scale devices). This includes the fabrication of a broad range of

solid and flexible devices (known as printed electronic devices),<sup>119</sup> such as humidity sensors on plastic substrates<sup>120</sup>, radio-frequency identification (RFID) labels<sup>121</sup>, as well as energy storage and conversion devices<sup>108</sup>. However, being a relatively new alternative technique for industrial production of devices with functional nanomaterials, inkjet printing is currently mainly employed in research units to develop new inks and processes that could in the future replace or act as complementary tools for screen-printing and other established methods.

Inkjet printing can be divided into two main operation modes: continuous inkjet printing (CIJ) and drop-on-demand (DOD) inkjet printing. CIJ printing (**Figure 1-10**) is based on the continuous formation of charged droplets being ejected from a biased nozzle. If it is necessary to interrupt the flux of droplets towards the substrate, due to a desired blank substrate area, the droplets are diverted by a charged deflector and collected in an ink collector well. One advantage of this technique is that nozzles suffer less from possible blockages by dried ink at the nozzle orifice. The disadvantage is the excessive use of ink, with great quantities being jetted. Despite the collected ink can be filled back to the ink tank for reuse, such approach is prone to contamination and requires control of ink composition, pH and precipitate removal.

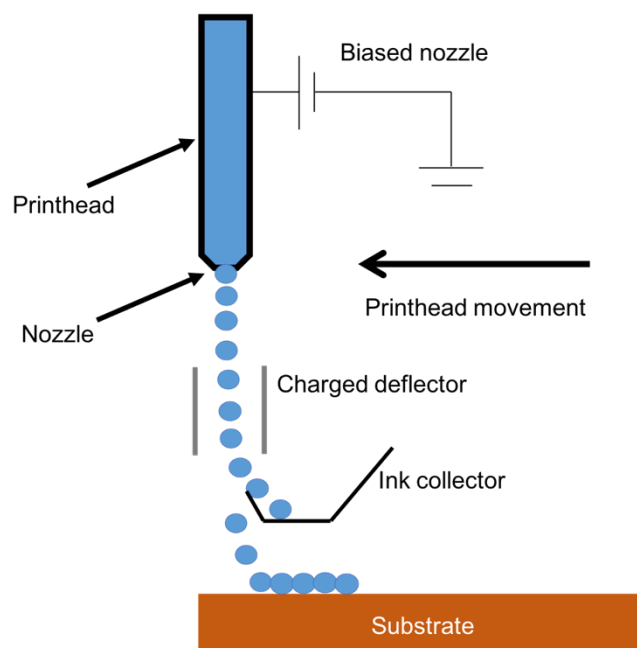


**Figure 1-10** Schematic representation of continuous inkjet printing.

Drop-on-demand generates droplets according to an accurately provoked pressure perturbation in the ink inside the nozzle. The three major DOD concepts are piezoelectric, thermal, and electrohydrodynamic (EHD) inkjet printing (**Figure 1-11**). After a droplet is generated and expelled from the nozzle, the nozzle chamber is refilled with the ink from the reservoir and the process is repeated.

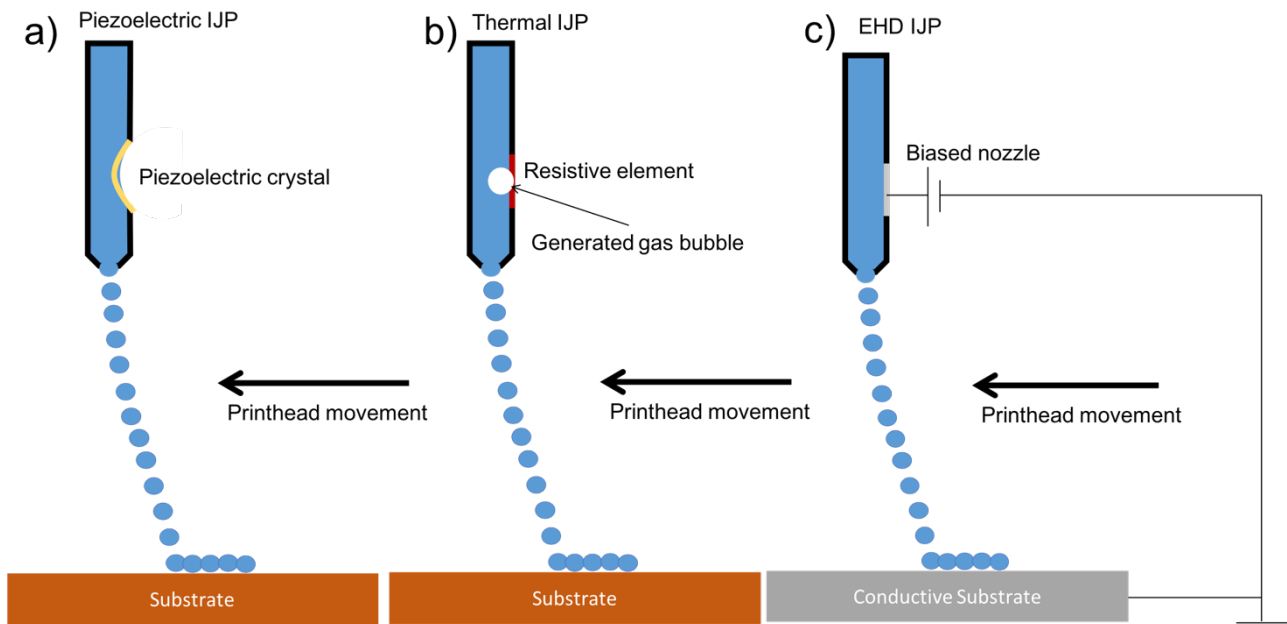


**Figure 1-11.** Schematic representation of drop-on-demand inkjet printing. a) Piezoelectric generated droplets. b) Thermally generated droplets. c) Electrohydrodynamic droplets formation.

The printhead of piezoelectric DOD (**Figure 1-11a**) systems consists of a piezoelectric element close to the nozzle and an inlet of ink on the opposite side of the nozzle. The piezoelectric component deforms inside the channel based on an applied voltage pulse and generates a pressure wave inside the printhead close to the nozzle. The pressurized ink column inside the nozzle chamber expels the ink through the nozzle orifice. Because only a local pressure change is generated, it can affect the properties of the ink solvents causing local changes in the physical properties of the ink components therefore, particle precipitation or agglomeration can occur locally. Still, piezoelectric DOD inkjet printing is currently the most suitable, commercially available inkjet printing made for nanoparticulate inks, because of a wider range of solvents to be utilized in the ink, less possibility of material thermal degradation and higher control of the generated droplets (*i.e.* due to the control of

the physical properties of the ink). For the fabrication of catalyst layers, drop-on-demand piezoelectric jetting devices are in fact mostly used.<sup>108</sup> However, a disadvantage is related to the local pressure gradient created, which could interfere in inks with non-Newtonian behaviour, leading to particle aggregation, phase separation or no droplets.<sup>122</sup>

Thermal DOD inkjet printers (**Figure 1-11b**) contain a resistive element close to the nozzle that is rapidly heated, causing an evaporation of the ink solvents, which eventually results in a bubble. This bubble leads to an increase of pressure in the nozzle channel and consequently a droplet is expelled. However, depending on the ink solvent mixture, the temperatures that the ink might achieve can induce changes in the catalyst particles dispersed in it, as well as lead to premature drying of the ink, which culminate in particle aggregation and nozzle blockage.

Finally, the electrohydrodynamic (EHD) inkjet printing (**Figure 1-11c**) is based on a potential difference that is applied between the ink and the substrate. When large enough, the charge is accumulated at the droplet air interface, the droplet starts to deform (*i.e.* deviate from the shape caused by the surface tension) and because of the effect of the electric field, it is possible to overcome the surface tension of the liquid. Therefore, at a given charging threshold, the charged droplets are expelled from the nozzles and attracted by the oppositely charged substrate. The main drawback of this technique is that both substrate and ink must be conductive to enable the electrohydrodynamic process. A big advantage is that the droplet size can be much smaller than the nozzle orifice, leading to higher pattern resolution compared to piezoelectric and thermal IJP. EDH formed the basis of ultra-fine inkjet printing known as “super-inkjet”.<sup>123</sup>

All these DOD based inkjet printing techniques are characterized by the precise control of the droplet position as well as the quantity of ink spent for each fabrication. Considering printing of scarce and costly catalyst containing inks, minimizing material losses is an important advantage. Drop-on-demand piezoelectric jetting devices are mostly used for the fabrication of catalyst layers.

## 1.6.2 Ink/substrate interaction and post-printing processing

Inkjet printing of precisely defined structures, *i.e.* with micrometer resolution, is critical for the realization of a broad range of applications<sup>118</sup>. The interaction between the ink and the substrate must be well understood, as the spreading of the ink droplet on the substrate plays a key role for the achievable pattern resolution. Factors that influence the droplet spreading are the speed of the droplet when impacting the substrate, wettability of the substrate by the ink, substrate porosity and substrate temperature. In addition, dispersed nanoparticles, polymers and solvents in the ink will interact with the substrate surface. This liquid/solid interface changes throughout time in terms of solvent evaporation, solidification of a nanoparticle layer, gelling of a polymer or a chemical reaction, such as radical polymerization. In case of insufficient interaction, printed layers can spread or contract leading to unresolved patterns as well as patterns with holes.

After printing, the ink must be brought from the liquid form to a solid usually by solvent evaporation, nanoparticle densification and even sintering. Several so-called post-printing processes can be performed in order to promote the curing of the printed ink and materials. Thermal curing is the most used method, which is executed in furnaces with temperature ramps or by using photonic curing systems that are described in detail in Section 1.7.2. There is a class of monomer and cross-linker inks, which can be cured using UV photopolymerization leading to polymeric layers.<sup>124</sup> This is in particular of interest to create dielectric layers.

The thermal properties of the substrate can limit the intensity of the post-processing techniques. For instance, polymeric substrates, such as PET, do not withstand temperatures higher than 150 °C. Even polyimide can only withstand temperatures up to 400 °C. For higher curing temperatures, ceramic substrates and glass can be used. Photonic curing (also known as light sintering or pulsed light sintering) is a light-based non-equilibrium heating technique. A xenon flash lamp irradiates light, which is absorbed by the printed layer (*e.g.* nanoparticle layer) for intense and localized thin layer heating on the millisecond time frame. While the lower absorption of the irradiated energy

by transparent plastic generates lower temperatures in the substrate. For instance, a commercially available process is the fabrication of conductive lines of copper over thermally sensitive materials such as paper.<sup>125</sup> A deeper discussion on this technique is presented in Section 1.7.2.

## 1.7 Inkjet printing of electrocatalysts combinatorial libraries

Combinatorial libraries are one of the areas in which inkjet printing, as well as dispensing in general, is a leading fabrication tool. This leadership can be attributed to the fact that inkjet printing is a digital technique, thus it is possible to place the droplets in precise positions offering also the possibility to create binary and ternary material combinations on the substrate<sup>126</sup>. The principle behind the combinatorial libraries approach was first described by Reddington *et al.*<sup>127</sup>. In this work, the materials printed were Pt, Ru, Os, and Ir based halide salts. After the printing process, quaternary Pt-Ru-Os-Ir compositions were synthesized by chemical reduction, using borohydride as reducing agent. When applied as anode in fuel cells, the addition of small amounts of Os and Ir lead to a significant increase in activity. Bard and co-workers, in the same trend, prepared a library of Pt and Ru for the ORR<sup>128</sup>. More recently, Seley *et al.* developed a combinatorial library of substrates to investigate metal oxides towards the OER<sup>129</sup>. In Chapter IV the possibility of hyphenating inkjet printing with white light sintering for the *in-situ* fabrication of libraries of catalysts will be demonstrated taking the example of NiFe mixtures.

### 1.7.1 Printing of catalyst layers

As an application related to Section 1.6, applying inkjet printing for the fabrication of catalyst layers is gaining attention.<sup>130</sup> This can be attributed to the characteristic presented for both the requirements of CLs and the wide choice of materials and techniques that can be employed in the fabrication of a CL for an electrochemical energy conversion device. As the catalyst materials employed in the CL are costly and rare, the low wastage of material is one feature of great interest. For instance, Yazdanpour *et al.*<sup>47</sup> demonstrated the effect of different post processing conditions in the

overall performance of the inkjet-printed CL. Karan *et al.*<sup>131</sup> discussed the advantages of inkjet printing, in order to fabricate thin CLs (1 – 5  $\mu\text{m}$ ) maximizing the surface area in a CL. Moreover, they were able to fabricate CLs with ultra-low loading of Pt (0.02 – 0.12  $\text{mg}_{\text{Pt}}/\text{cm}^2$ ) that achieved higher Pt utilization than samples prepared with conventional methods and higher Pt loadings (0.4  $\text{mg}_{\text{Pt}}/\text{cm}^2$ ) and thicker CLs. In a recent work, Shukla *et al.*<sup>132</sup> demonstrated that it is possible to obtain even 10 times more catalyst mass activity for inkjet-printed CLs when comparing to spray coated CLs. The authors attributed this fact to the increase in the transport of oxygen and protons through the three-dimensional pores of the catalyst layer deposited on the membrane.

Still, the main bottleneck for applying inkjet printing towards the fabrication of CLs, specially membrane electrode assemblies, is developing inks which contain the nanoparticulated catalyst material.<sup>133</sup> Therefore, there is still a vast field of opportunities to find alternative ink formulation and methodologies to print electrocatalyst materials.

## 1.7.2 Pulsed Light Sintering

Pulsed Light Sintering (PLS), intense pulsed light sintering<sup>134</sup>, photonic curing<sup>135</sup> and flash light sintering<sup>136,137</sup> are common nomenclatures in literature to describe the utilization of an intense light pulse, generated utilizing a Xenon flash lamp, to promote rapid heating and sintering of thin films. The first and still most used application of this technique is for printed electronics with the sintering of Ag<sup>124,138–140</sup> and Cu<sup>136,137,141–143</sup> nanoparticles to fabricate conductive tracks on thermally sensitive substrates. PLS is a contactless form of rapid heating based on material specific absorption of energy, emitted by a broad-spectrum source (*i.e.* 190 – 1100 nm) as micro- to millisecond pulses (**Figure 1-12**). Meanwhile, the energy density varies as a function of the applied voltage (reaching up to 30  $\text{J}/\text{cm}^2$  per light pulse).

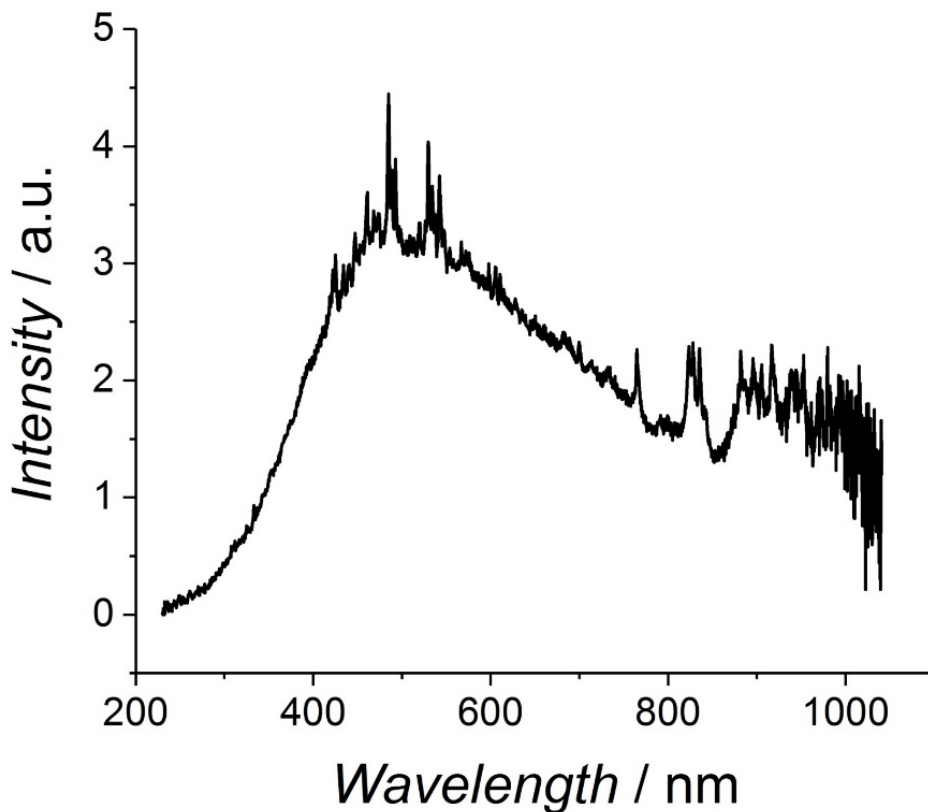


**Figure 1-12.** Emission spectrum of a Xenon flash lamp with 750 V of bank voltage and 220  $\mu\text{s}$  pulse length. Raw data kindly provided by Rob Hendriks from Novacentrix.

Druffel *et al.*<sup>144</sup> discussed that the conversion of electrical to optical radiation is at least of 30 % in a broad spectrum, over a large area without any sophisticated optics. In addition to energy density, it is possible to control the number and frequency of pulses. The fundamental principle of operation of PLS is the light absorption by metal-based thin films, more precisely the promotion of electrons from the valence to conduction band. Electrons with energies larger than the conduction band edge release their excess energy in an attempt to fill the many available band states near the conduction band edge<sup>145</sup>. The excess energy is released as phonons leading to localized heating of the material. This process is considered an instantaneous event (period of  $10^{-10}$  s) in relation to the total processing time ( $10^{-3}$  to  $10^{-6}$  s). The thermal energy generated is a consequence of the light absorbed and it is dictated by two factors: *i*) absorptivity of the film and *ii*) film thickness. Taking into consideration the substrate characteristic, first, substrates are in general much thicker than the layer to be



sintered, second, normally are made of polymeric (*e.g.* PET) or insulating materials (*e.g.* glass). In the first case, the heat generated in the thin film is distributed in the substrate and negligible heat can be detected due to the dimension difference, while in the second case the energy gap between the valence and conduction band is further apart than in conductive materials. Thus, the transition of electrons is more difficult with no phonons and less heating being generated.

One of the most relevant application of PLS is the sintering of nanoparticles. Due to the high surface to volume ratio the melting temperature required to sinter the nanoparticles, is inversely proportional to the diameter. Such relation makes it attractive to use PLS<sup>146</sup> for nanoparticle sintering and nanoparticle based films development. The relation between dimension and melting temperature is presented in Eq. 50:

$$T_m = T_0 \left(1 - \frac{4}{\rho_s L d}\right) \left[\gamma_s - \gamma_l (\rho_s - \rho_l)^{\frac{2}{3}}\right] \quad (50)$$

where  $T_m$  is the melting temperature of the metal nanoparticles,  $T_0$  is the melting temperature of the bulk metal,  $\rho_s$  is the density of the metal in the solid state,  $\rho_l$  is the density of the metal in the liquid state,  $\gamma_s$  is the surface tension of the metal in the solid state,  $\gamma_l$  is the surface tension of the metal in the liquid state,  $L$  is the latent heat of fusion, and  $d$  is the diameter of the metal nanoparticle. Moreover, with deep knowledge of the material absorption characteristics, curing parameters (*i.e.* energy density, pulse frequency and pulse number) can be tuned to improve the absorption leading to the highest efficiency in conversion.

As briefly presented above, the concept of PLS is based on the light absorption in metal based thin films and electron excitation from valence to conduction band. Such is valid for nanoparticulated based thin films. Yet in this thesis we approach chemical synthesis utilizing the principle of PLS. Herein, a more detail mechanistic analysis can be described to explain PLS. The hot-electron phenomena have been well described in literature, for other systems than PLS, however it presents

similarities which could fit the curing process with PLS. The term hot-electron is given to those electrons which have an elevated effective temperature and are described by the Fermi function. One manner to induce the generation of hot-electrons is to irradiate a given material with highly energetic photons. Normally it is done with lasers in femtosecond or picosecond time, still in the case of the current study, radiation is emitted from a Xenon flash lamp for a duration of ms.

As described by Bauer et. al<sup>147,148</sup> nascent non-thermal electrons are created upon the absorption of a femtosecond energy pulse. The excess of energy caused by the femtosecond pulse is then dissipated within free electrons via an electron-electron scattering mechanism. This process is known as thermalization as it leads to the formation of a hot electron gas with a well-defined electronic temperature. In case of a system composed of the metal nanoparticle or nanoparticle/adsorbate, the electron-molecular vibration scattering occurs via a bidirectional inelastic electron tunneling into adsorbates. Hence, immediately after the absorption of the energy pulse a nonequilibrium distribution of nascent nonthermal electrons is created. The non-equilibrium electron is temporarily transferred into an empty electronic level, in the adsorbate (*e.g.* alcohol), with an energy, leading to the creation of an intermediate negative ion state. The electron then could scatter back with an energy into the metal conduction band or induce chemical transformations in the adsorbate molecule (*i.e.* reduction).

Therefore, employing this theory in our system one can infer the following: *i*) the substrates chosen for the conversion of precursor salts to metallic nanoparticles, play a crucial role in the thermal degradation, *ii*) the ink formulation components are photodegraded and initiate the degradation of the precursor salt to nanoparticles. The substrate plays an important role in the degradation of the adsorbates, besides the convection of heat as a consequence of light absorption. The chosen substrates, which in our case are semiconductors and not metals, promote initial generation of the hot-electrons. This effect has been described in literature by Clavero<sup>149</sup>. If the substrates would be uncoated the hot-electrons would decay in the material and only a local temperature heat would be generated still, in the case of the current work, the substrates chosen (*i.e.* glassy carbon Chapter III and Chapter V, CNT

– Chapter V and ITO – Chapter IV), are coated with our precursor salts. Therefore, during the excitation/generation hot-electrons enter the LUMO of the adsorbate molecule (*i.e.* alcohol) and decay inside the adsorbate energy level before returning to the initial state in the substrate. Such can lead to the generation of heat in the precursor molecule and initiate the thermal degradation step of the precursor. The initial degradation will lead to a cascade of events, where, after the first cluster of metallic nanoparticles is generated, the reaction will expand as now a metallic nanoparticle can induce as well the generation of hot-electrons. Despite the short period of existence of the hot electrons it is at least 1000 times shorter than the total processing time under irradiation. Such mechanism can explain the initial degradation of the precursor salts in the surrounding areas of the coating material.

Moreover, more than one mechanism could explain the degradation of precursor salts subjected to PLS. Besides the generation of hot-electrons and the above described cascade of events a second possibility is regarding the photodegradation of several ink formulation components. As described by Hwang *et. al*<sup>150</sup> the UV component of the irradiated light degrades the PVP coating on Cu nanoparticles to alcohol, leading to the reduction of the copper oxide shell surrounding the copper nanoparticles. We observed a similar effect on our work described in Chapter III, where Co<sub>3</sub>O<sub>4</sub>/N-rGO gets reduced during curing. Initially the photooxidation of alcohol utilized in the ink formulation, or alcohol generated as a product of polymer degradation, induces the photodegradation (*i.e.* reduction) of the precursor salts to nanoparticles. However, it has to be noted that the described findings, differently than in this thesis, are obtained with metallic particles that were already formed and deposited in the substrate prior to exposure to the white light irradiation. In the similar direction, Lesch has demonstrated that it is possible to convert a platinum containing salt into Pt nanoparticles even over completely insulating and with low absorption substrates such as quartz glass.

In the results presented in this thesis it is postulated to have a mixed mechanism. Utilizing the energy irradiated by the Xenon flash lamp, first it initially induces the photoreduction of the precursor salts, in the presence of alcohols and subsequently particles growth as described by Hwang *et.*

*al*<sup>150</sup> and Lesch<sup>116</sup>. Yet due to the presence of semiconductor substrates and the first clusters are formed the reaction proceeds through a similar mechanism as the hot-electron mechanism. In such mechanism photons irradiated during the excitation of the substrate (*i.e.* CNT, ITO, GC) and the first formed particles continue the process of thermal degradation of adsorbates increasing the conversion from precursor salts to nanoparticles.

## 1.8 Thesis outline

The objective of the work presented in this thesis introduces and discusses possible new applications of inkjet printing as a fabrication methodology in the field of electrochemical energy conversion devices. Inkjet printing is explored as versatile technique to obtain electrodes and electroactive materials. In Chapter III, the challenges of the development of nanoparticulated inks with electrocatalyst material is presented and a broad discussion on the effects of the interaction between ink components and the processing of nano-electrocatalysts with activity towards the oxygen reactions is investigated. In Chapter IV, the utilization of the Print-Light-Synthesis to fabricate noble metal electrocatalyst particles for ORR is presented. Finally, in Chapter V, the application of the Print-Light-Synthesis for the fabrication of bi-metallic electrocatalyst nano-composites as OER electrocatalysts is explored.

# Chapter 2 Experimental part

## 2.1 Chemicals

### 2.1.1 Commercial Chemicals

All chemicals presented in **Table 2-1** were of analytical grade and used as received. Deionized (DI) water was produced with a Milli-Q plus 185 model (Merck Millipore). O<sub>2</sub> cylinders (purity 99.9%) were purchased from Carbagas. Platinum NPs supported on carbon black with 10% Pt (wt.% dry basis) and 40% Pt were purchased from Sigma-Aldrich (product number 205958) and Johnson Matthey (product number 599003), respectively. Iridium NPs supported on carbon black with 40% Ir (wt.% dry basis) were purchased from PK Catalyst (product number 3151637). A carbon nanotube (CNT) dispersion was purchased from Brewer Science. UV curable inks EMD 6200 and EMD 6415 (SunChemical -USA) were utilized to print insulating layers. Glassy carbon (GC) Sigradur K plates (12.5×12.5 mm<sup>2</sup>) and rods (5 mm in diameter) (HTW) were used as substrates due to their high conductivity, smoothness and the possibility to polish their surface reproducibly. The GC substrates were mechanically polished using alumina particles of 0.05 μm size (Buehler). After polishing to a mirror-like surface, the GC rods and plates were sonicated in isopropanol for 30 min and dried with the aid of a stream of Ar. For the work presented in Chapter IV, a CNT layer was inkjet-printed onto the GC based on previous reports<sup>138,151</sup>.

**Table 2-1.** Commercial chemicals utilized.

<b>Chemical</b>	<b>Formula</b>	<b>Purity</b>	<b>Supplier</b>
<b>1,2 propanediol</b>	C <sub>3</sub> H <sub>8</sub> O <sub>2</sub>	99.5%	Sigma-Aldrich
<b>2-methyl- 1,3-propanediol</b>	CH <sub>3</sub> CH(CH <sub>2</sub> OH) <sub>2</sub>	99%	abcr
<b>Chloroplatinic acid hexahydrate</b>	H <sub>2</sub> PtCl <sub>6</sub> ·6H <sub>2</sub> O	37.5% Pt basis	Sigma Aldrich
<b>Ethyl cellulose</b>	-	48-49.5%	Sigma-Aldrich
<b>Ethylene glycol butyl ether</b>	C <sub>6</sub> H <sub>14</sub> O <sub>2</sub>	99.5%	Sigma-Aldrich

<b>Ferrocenemethanol</b>	$C_{11}H_{12}FeO$	97%	Sigma-Aldrich
<b>Iron(II) chloride tetrahydrate</b>	$FeCl_2 \cdot 4H_2O$	97%	Sigma Aldrich
<b>Isopropanol IPA</b>	$C_3H_8O$	PA	Sigma-Aldrich
<b>Nafion solution D2020 (20 wt. %)</b>	$C_7HF_{13}O_5S \cdot C_2F_4$	-	Ion Power
<b>Nafion solution D520 (5 wt.%)</b>	$C_7HF_{13}O_5S \cdot C_2F_4$	-	Ion Power
<b>Nickel(II) chloride hexahydrate</b>	$NiCl_2 \cdot 6H_2O$	99%	Sigma Aldrich
<b>Polyvinylpyrrolidone PVP; MW 10'000</b>	$(C_6H_9NO)_n$	-	Sigma-Aldrich
<b>Potassium chloride</b>	KCl	99%	Sigma-Aldrich
<b>Potassium hydroxide</b>	KOH	85%	Fluka and Sigma Aldrich
<b>Potassium nitrate</b>	$KNO_3$	99%	Sigma Aldrich
<b>Terpineol</b>	$C_{10}H_{18}O$	96%	Sigma-Aldrich

## 2.1.2 Synthesized Chemicals

$Co_3O_4/N$ -rGO (cobalt oxide supported on nitrogen doped reduced graphene oxide) powder was synthesized by Liu and co-workers adapting a previous protocol<sup>152</sup>. In brief, 112.8 mg graphene oxide sheets of 50 to 200 nm lateral dimension (Nanjing XianFeng Nano Material Technology Co. Ltd.) and 110.4 mg cobalt (II) acetate were mixed in 14.4 mL ethanol and 14.4 mL DI water, and sonicated for 40 min to achieve a suspension. Ammonia solution was added and the dispersion was stirred at 80 °C for 12 h. The reaction mixture was then transferred into an autoclave, in which a hydrothermal reaction was carried out at 150 °C for 3 h to grow  $Co_3O_4$  nanocrystals (NCs) of ~7 nm diameter on the N-GO sheets and to reduce the sheets to N-rGO. Afterwards, the product was separated from the reaction medium by centrifugation and successively washed with ethanol and DI water, followed by vacuum drying.

## 2.2 Equipment

### 2.2.1 Electrochemistry

All electrochemical measurements were performed in the 3-electrode arrangement with one working, one counter and one reference electrode (WE, CE and RE, respectively). For static measurements, *i.e.* in unstirred solution, a customized cell was manufactured in which the WE (*i.e.* a glassy carbon plate) was placed at the bottom of the cell and pressed against a copper plate below the cell that acted as electric contact **Figure 2-1**. The geometric electroactive electrode area was determined either by using an O-ring (10 mm diameter) implemented into the cell cover or by depositing a dielectric layer on top of the WE. The lid contained holes for electrolyte filling, gas filling/purging, CE and RE. Parafilm was used to seal the cell. The copper bottom plate had a screw inserted for electrical contact.

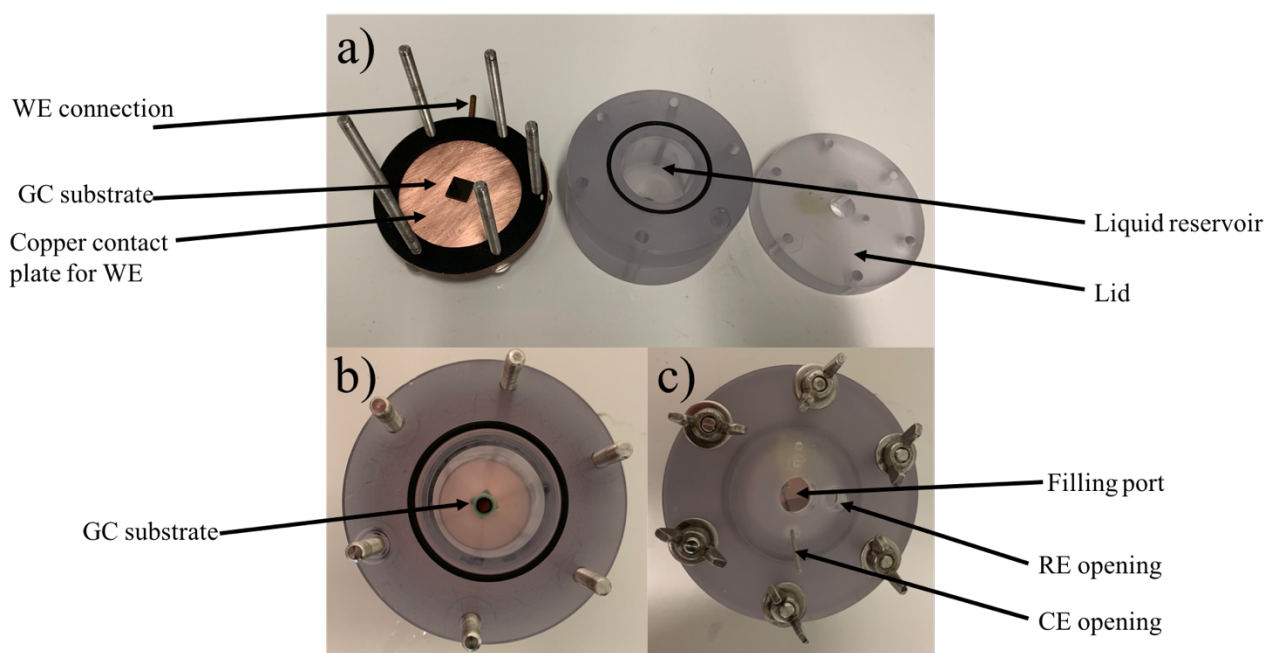


**Figure 2-1.** a) Electrochemical cell composed of the three main components: Bottom part with WE contact plate (left), liquid reservoir/cell cover (middle) and lid (right). b) Electrochemical cell partially assembled with a GC electrode kept at the bottom of the cell and hold in place with an O-ring (green) inserted into the liquid reservoir. c) Electrochemical cell, fully assembled with lid and screws for fixation and sealing the cell.

For rotating-disk electrode (RDE) measurements, an RDE system from Metrohm (Switzerland) was utilized combined with a custom-made holder (**Figure 2-2**) for fixing and replacing the GC rods. This system allowed the inkjet printing of CLs on a large number of GC rods and electrochemical characterization of the printed layers in short time by rapid rod exchange (Chapters 3 to 6). The electrochemical cell for RDE measurements was purchased from Pine Research and contained a water jacket for temperature control (part number: RRP310).

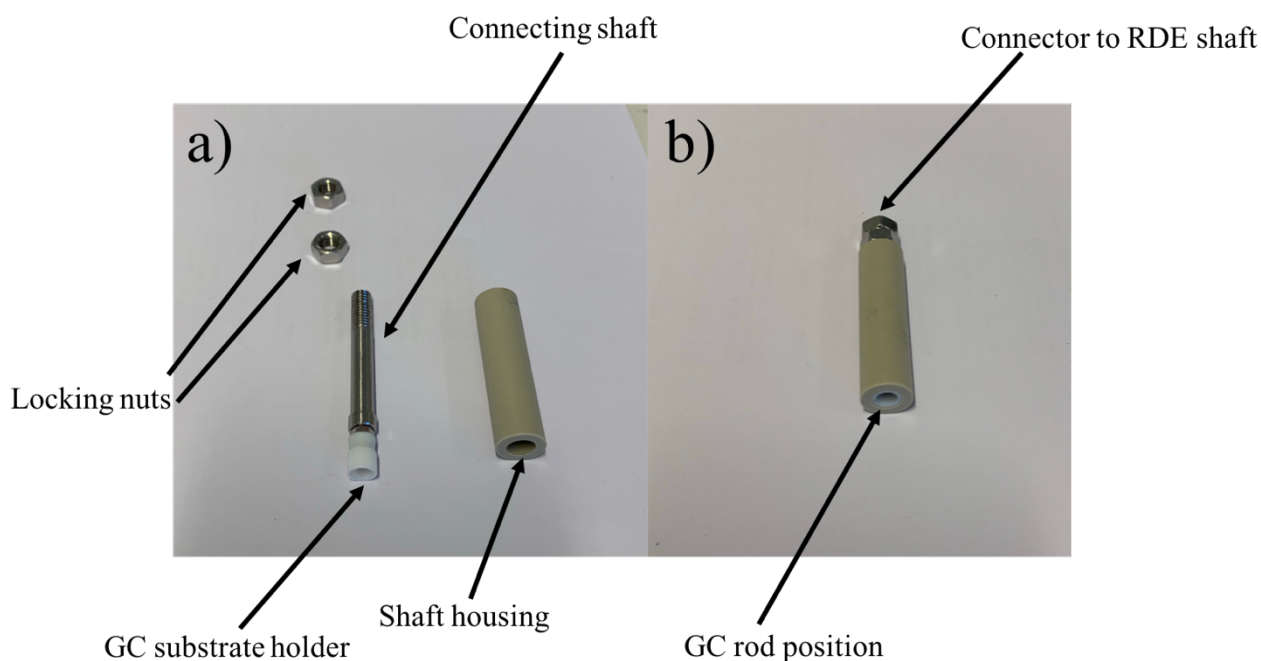


**Figure 2-2.** RDE setup a) Working electrode connector with individual parts identified. b) Assembled RDE with GC rod position and connector to the rotator identified.

Potentiostats used in this work were all from Autolab and were models PGSTAT204, 128 and 302N. Ag|AgCl in 1 M KCl reference electrodes (part number: CHI111) were from CH-Instruments (USA), Ag|AgCl in 4 M KCl (part number: RREF0024) from Pine Research (USA) and the RHE electrode was from Gaskatel (Germany). Platinum mesh (part number: 219810) and Pt coil (part number: AFCTR5) counter electrodes were from Ametek (USA) and Pine Research (USA), respectively.



Soft-Probe-scanning electrochemical microscopy (Soft-Probe-SECM) was carried out using the VersaSCAN from Ametek-Princeton Applied Research with a soft carbon microelectrode (VersaSCAN Stylus probes). The carbon paste working electrode area was  $\sim 450 \mu\text{m}^2$ . A fresh active electrode surface was obtained by a single razor blade cut. Feedback mode imaging in contact mode was performed using the VersaSCAN "Engage mode" that enables gentle contact-mode brushing of rough, curved and tilted substrates keeping a constant working distance ( $\sim 3\text{-}5 \mu\text{m}$ ) between the carbon microelectrode and the substrate surface. A tilt correction of the substrate is not required. SECM feedback mode experiments were carried out in 2mM ferrocenemethanol (FcMeOH) and 0.1 M  $\text{KNO}_3$  solution. Experimental SECM data were analyzed and plotted using the software MIRA (G. Wittstock, University of Oldenburg, Germany) or VersaScan (Princeton Applied Research).

In case indicated in the experimental procedure or figure captions, *iR* drop correction was done utilizing the impedance spectra obtained with a FRA32M module from Autolab. The impedance spectra was done with an amplitude of 10 mV at the open circuit potential with frequencies between 0.01 to 100.000 Hz. The solution resistance values utilized were extracted from the Nyquist plot. After measuring, the recorded curves were were *iR*-drop-corrected using the software NOVA 1.11.

## 2.2.2 Inkjet printers

Two drop-on-demand (DOD) material deposition inkjet printers were used, *i.e.*, a Fujifilm Dimatix DMP-2850 (**Figure 2-1**) and an X-Serie Ceraprinter from Ceradrop (**Figure 2-2**). In both machines, disposable Dimatix cartridges (DMC-11610) were used containing 16 individually addressable, parallel nozzles, generating nominally 10 pL droplets based on piezoelectric actuation. The X-Serie Ceraprinter has the possibility of utilizing industrial printheads, which comprise 256 nozzles and have nominal droplet volumes between 10 and 80 pL (depending on the printhead model). A

PulseForge 1300 photonic curing system (Novacentrix), based on a Xe flash lamp, was integrated into the Ceraprinter for in-line thermal post-processing.

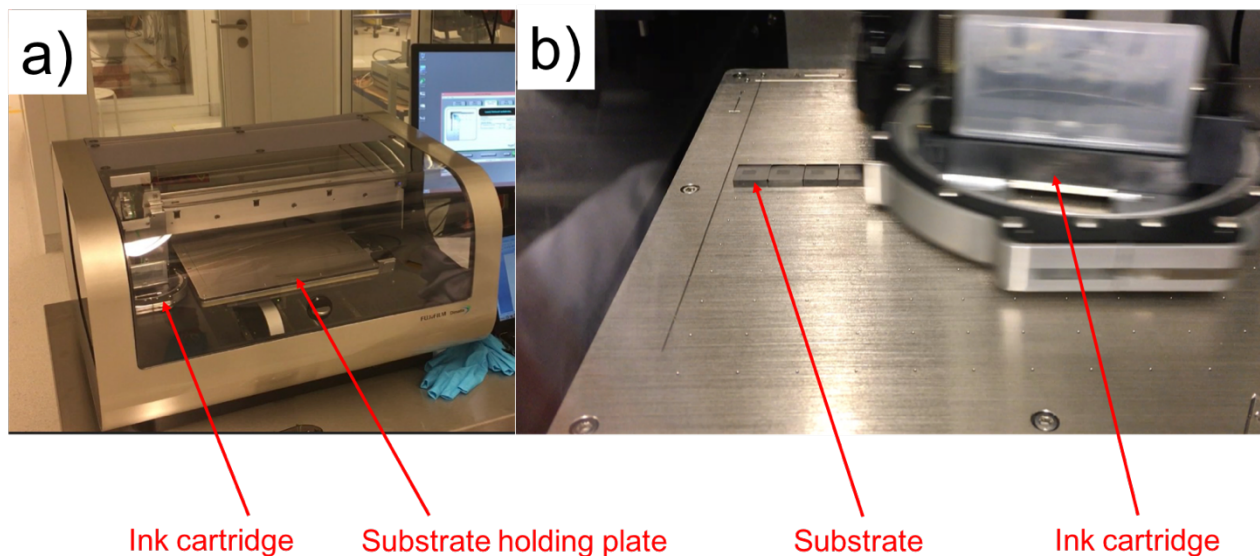


**Figure 2-3.** a) Dimatix DMP-2850 inkjet printer. b) Dimatix ink cartridge movement during printing of nanoparticulated carbon-based ink over GC substrates with 3 mm thickness.

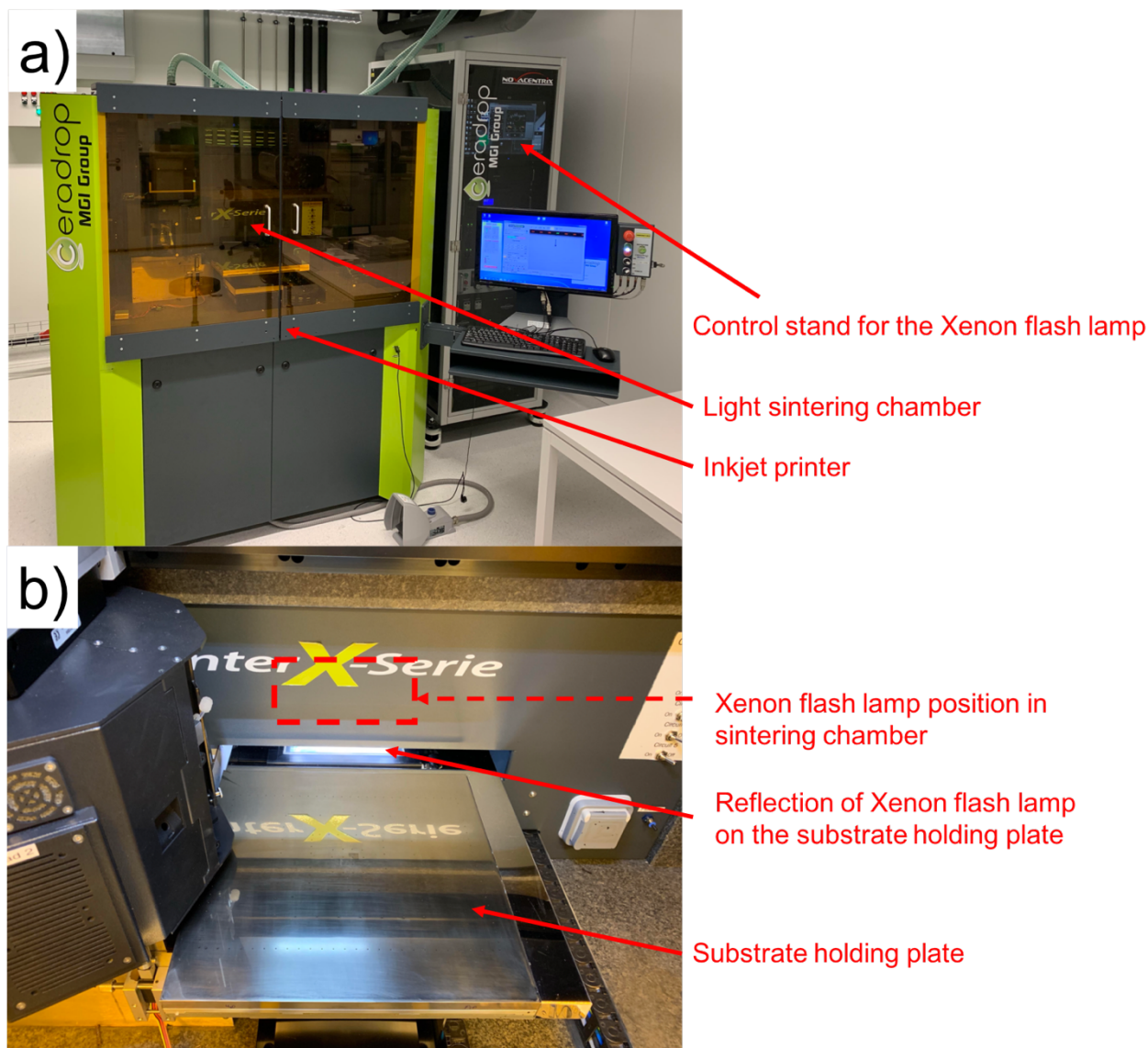


**Figure 2-4.** Ceradrop X-Series inkjet printer coupled with a PulseForge 1300 photonic curing system. a) Overview of the printer setup combined with the photonic curing system. b) View of the inside on the printer featuring the areas of photonic curing.

### 2.2.3 Ink and printed wet pattern characterization tools

The viscosity of the inks was measured with a SV-10 A series digital viscometer (A&D Instruments Limited) that utilized the current values necessary to maintain two parallel sensor plates in a tuning fork arrangement resonating at 30 Hz with an amplitude of less than 1 mm (**Figure 2-5**). As the driving force to resonate the sensor plates is proportional to the viscosity of the liquid in the surrounding of plates the electric current utilized to maintain a constant vibration amplitude can vary proportionally in different liquids, enabling thus to calculate after calibration the viscosity of a liquid

sample. Prior to the measurement the equipment is calibrated by measuring purified water. As the inks analyzed in this thesis had viscosities in the same range of water the only one-point calibration was sufficient. The system has a temperature sensor incorporated, which is important, as the viscosity is temperature-dependent. In order to perform the viscosity measurement 1.5 mL of the ink was placed in a vial in which the plates were inserted.

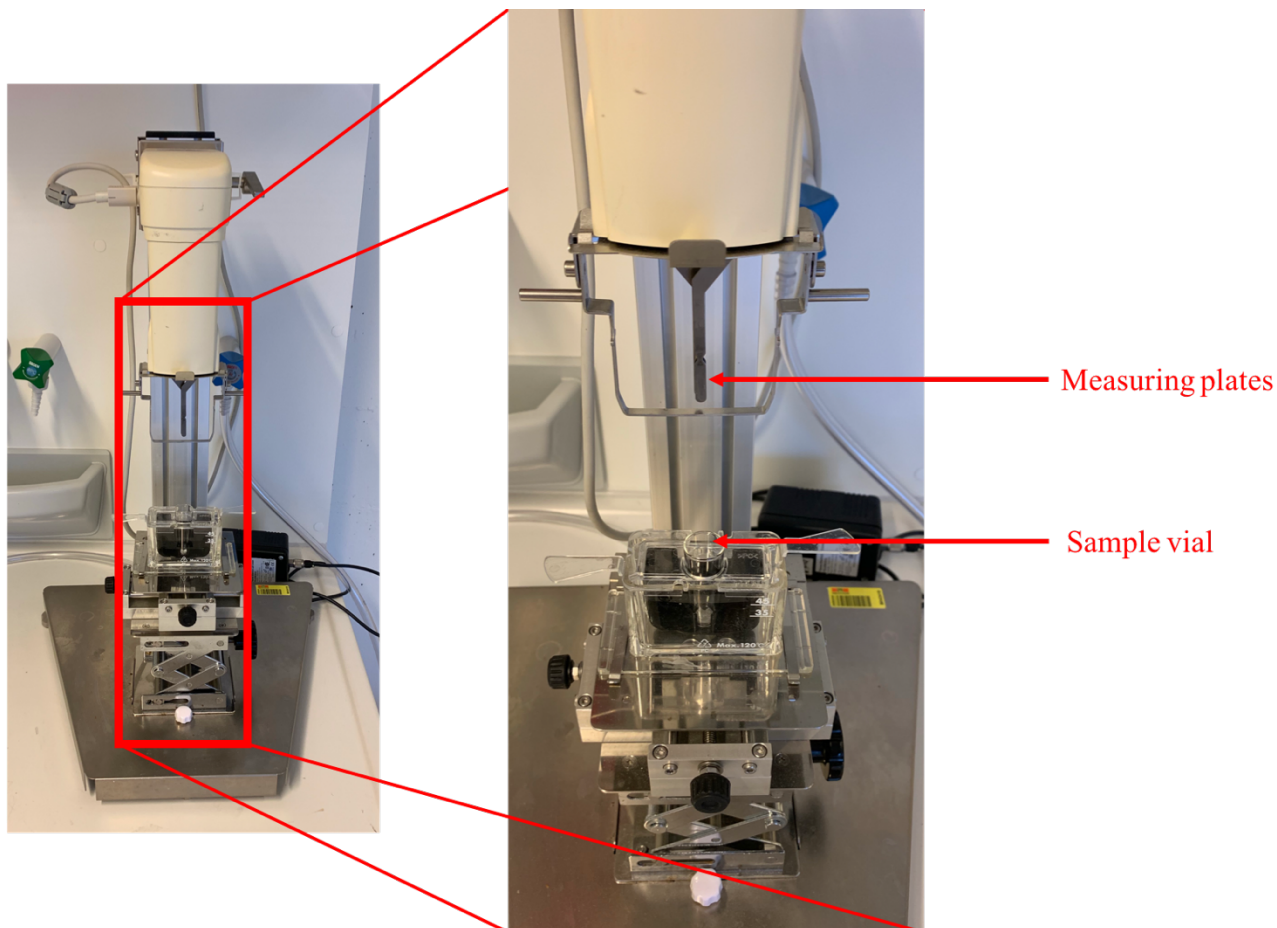


**Figure 2-5.** Viscometer utilized to determine the viscosity of the developed inks.

For surface tension analysis of the inks a drop shape analyzer DSA-30 (Krüss) was utilized. In this measurement it was analyzed the dynamic interfacial tension between the droplets of a liquid formed hanging from the tip of a capillary and the surrounding phase, in our case air (**Figure 2-6**). The pendant droplet is formed as a consequence of the gravity, the variation of shape of the droplet from a sphere is used to calculate the surface tension. For this calculation the curvature of the droplet

is fitted to the theoretical droplet shape using the Young-Laplace equation providing the surface tension.

The equipment was also employed to measure the contact angle of the droplets with the substrate as a measure of the wettability. This measurement is based on analyzing the angle of the interface generated between a liquid and a solid phase. For this, a droplet of 2  $\mu\text{L}$  was deposited on a substrate and the contact angle, of the outline of the contact surface, was calculated based on the Young's equation.

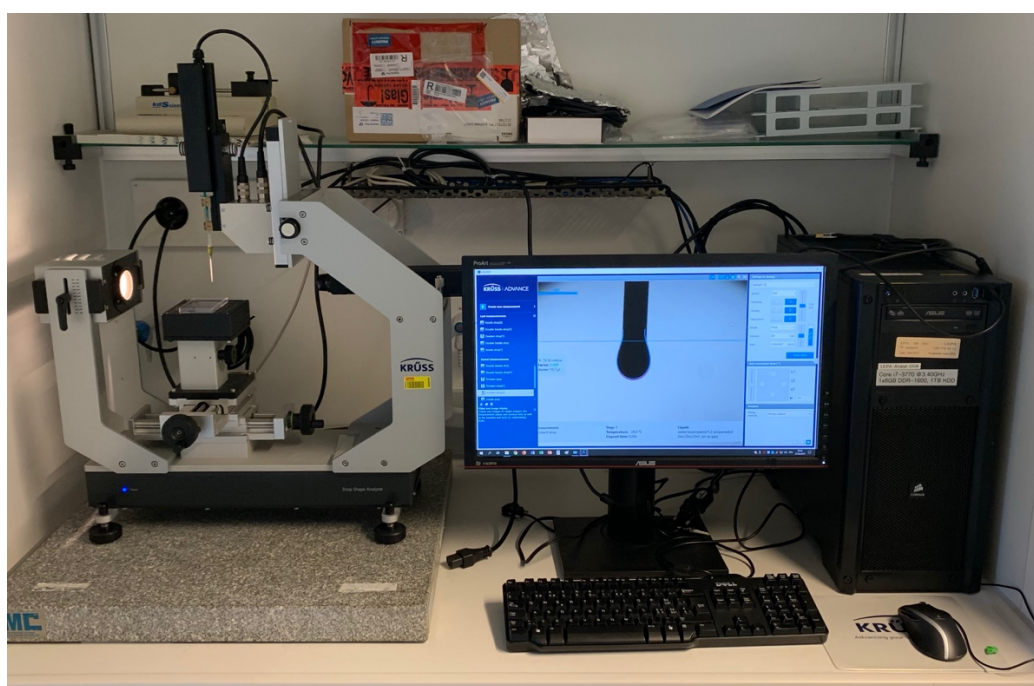


**Figure 2-6.** Drop shape analyser utilized to determine the surface tension of the developed inks in pending droplet mode and to measure the contact angle of a sessile droplet on a substrate.

Particle sizes were measured based on dynamic light scattering utilizing a Zetasizer Nano ZS90 (Malvern Panalytical). Dynamic light scattering measures the fluctuation of the scattered light intensity due to the particles in solution. After the measurement the scattering values are processed with an autocorrelation function in order to obtain the size of the particles in solution as hydrodynamic radius of a sphere. FT-IR measurements were performed with a Spectrometer Spectrum Two (Perkin Elmer). Printed patterns were analyzed with the cameras implemented in the used inkjet printers.

UV–Vis absorption spectra were recorded using an 8453 UV–Vis spectroscopy system (Agilent Technologies, Germany) on quartz glass.

## 2.3 Ink Formulation

According to Nallan *et al.*<sup>153</sup> catalyst ink formulation is yet still more empirical work than scientific, mainly due to the difficulties in finding stable, aggregate-free dispersions of nanoparticles and the interplay of several physical parameters. Some constraints have been studied and relations of these parameters have been developed<sup>154</sup>. Yet, no uniform protocol has been developed for general catalyst ink preparation. This is a serious limitation, especially now, where interest in the development of inks containing nanoparticles is continuously growing.

Catalyst ink formulations, containing the catalyst, an electrolyte (ionomer), polymers and certain solvents, are the liquid precursors of the catalyst layers. When preparing an ink, the contents of each component forming the desired pattern is usually considered first, followed by the addition of further compounds to adjust specific ink properties such as uniformity, viscosity and surface tension. The behavior of droplets in a DOD printing system is a complex process. For the ink characterization, a series of dimensionless relations of physical constants can be used. Been the most useful within the vast possibilities of dimensionless relations the Reynolds (Re) (51), Weber (We) (52) and Ohnesorge (Oh) (53) numbers. A graphical representation is presented in **Figure 2-7**. In this representation one can understand the effects of varying the physicochemical properties of the ink in the formation of the droplets. In this case it is possible to, based on  $Z$ , observe areas where satellite droplets would be generated or where the viscosity of the ink would be too high to generate droplets. Satellite droplets formation is related to the viscosity of the ink and surface tension. Low viscosity and high surface tension inks will have a higher formation of satellite droplets. On the opposite direction, too viscous inks will not be jetted due to the difficulty of the liquid to flow within the small microfluid channels inside of the printhead. The dimensionless numbers can be defined from physical values from the fluids used as ink and from the printing process and are presented in equations:

$$Re = \frac{v\rho\alpha}{\eta} \quad (51)$$

$$We = \frac{v^2\rho\alpha}{\gamma} \quad (52)$$

$$Oh = \frac{\sqrt{We}}{Re} \quad (53)$$

Where:  $\rho$ ,  $\eta$ , and  $\gamma$  are the density, dynamic viscosity, and surface tension of the fluid, respectively,  $v$  is the velocity, and  $\alpha$  is a characteristic length<sup>155</sup>.

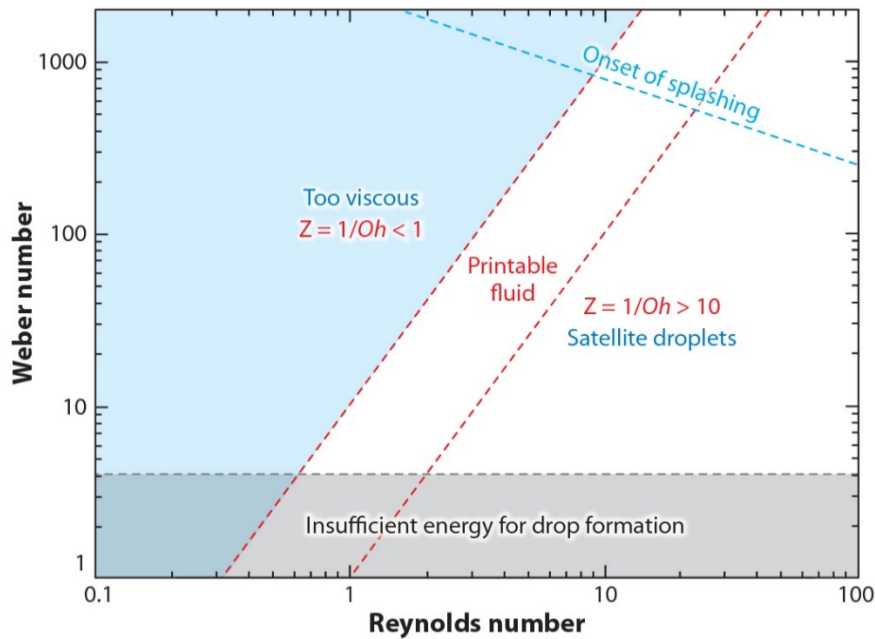


**Figure 2-7** Coordinate system defined by the Reynolds and Weber number to define the printability of an ink. Extracted with permission from Derby<sup>155</sup>.

Moreover, the process used in order to achieve the desired ink is of great importance<sup>153</sup>. Normally, the standard procedure for achieving a stable catalyst ink formulation based on nanoparticles relies on some important and critic steps. One of them is to disperse the catalyst particles using various tools including sonication or milling and, even if during the process the particles and the particle aggregates are usually well dispersed in solution, they tend to re-aggregate when the sonication or milling is stopped. Therefore, functionalizing the nanoparticle surface *e.g* with polymers is necessary to decrease the attracting interaction between the particles avoiding aggregation and keeping the solution uniform. Nafion is one widely used example of a polymer that can act as stabilizer in

the dispersion and as a proton conductor. However, Nafion has a disadvantage: this polymer degrades when intensely sonicated<sup>156</sup>. It is necessary to find polymers that can withstand the sonication process, stabilize the particles and improve, or at least maintain, the ink properties.

Inks with a very high nanoparticle content are more susceptible to have the formation of aggregates blocking the nozzles/printheads. On the other hand, with a very low content of particles, multiple printed layers of the ink might be required in order to achieve the required compactness in the desired patterns, and, consequently, a good conductivity.

Another important parameter is the particle and aggregate size. Considering a uniform ink, *i.e.* without aggregates, the particle size of the catalyst must be within a printable range. The rule of thumb for the maximum particle size is that the particles and particle aggregates in the ink should be 100 to 400 times smaller than the nozzle diameter. Taking for example a nozzle diameter of 21  $\mu\text{m}$ , which is the diameter of the nozzles in the commercial disposable cartridges used in this work, the size of the nanoparticles in the ink should be around 50 to 200 nm. Printhead nozzles are a more complex structure than a simple orifice where the ink has to pass through, the printhead has complex channels with  $\mu\text{m}$  dimension with moving part (*i.e.* piezoelectric). Therefore, the combination of aggregates and particles loading is of great relevance for the reproducibility of the printed patterns.

Ink additives, such as polymers (*e.g.* Nafion and polyvinylpyrrolidone-PVP), are not only used for stabilizing the dispersion but also to tune the surface tension and the viscosity of the ink. The same counts for the carrier solvents such isopropanol, that is one of the most commonly used solvents for inks formulation. One advantage of using this alcohol as solvent is the low evaporation temperature, *i.e.* 83 °C, which allows the rapid, but crack-free drying of the printed pattern.

### 2.3.1 Nanoparticulated inks formulation

**Co<sub>3</sub>O<sub>4</sub>/N-rGO ink.** 3 mg of Co<sub>3</sub>O<sub>4</sub>/N-rGO and 50 mg of PVP were added to 1 mL of a water:isopropanol (3:1) mixture and sonicated in 2 mL Eppendorf tubes for 180 min at 35% amplitude



with on/off cycles of 5 s, using a Sonics Vibra Cell 505 in "Cup horn" arrangement. The final dispersion reached the concentration of  $3 \text{ mg}\cdot\text{mL}^{-1}$  of  $\text{Co}_3\text{O}_4/\text{N-rGO}$ . Afterwards, the dispersions were centrifuged at 13'000 rpm for 20 min in an Eppendorf 1310 centrifuge. The supernatant was removed to separate freely suspended PVP from the PVP-modified catalyst particles. Thereafter, the PVP-modified catalyst sediment was re-dispersed in 1 mL of a 1,2-propanediol-based mixture containing 10% terpineol and 0.5% EC.

**Pt/C ink.** Pt/C was formulated with the following protocol: 3 mg of the catalyst material were added to 500  $\mu\text{L}$  of a water:isopropanol (1:1) mixture with 10 wt.% (calculated based on the solids) of Nafion and sonicated in 2 mL microtubes for 15 minutes at 30% amplitude with on/off cycles of 5 s, using a Sonics Vibra Cell 505 in the "Cup horn" arrangement. After the initial dispersion, 500  $\mu\text{L}$  and 10 wt.% (calculated based on the solids) of Nafion were added to reach  $3 \text{ mg}\cdot\text{mL}^{-1}$  with  $0.6 \text{ mg}\cdot\text{mL}^{-1}$  of Nafion. After the addition, the ink was stirred in a vortex agitator for full homogenization.

### 2.3.2 Precursor inks

The precursor salt of choice (*e.g.* iron or nickel chloride) was dissolved in an isopropanol:1,2-propanediol mixture to reach for instance  $0.5 \text{ mg}\cdot\text{mL}^{-1}$  of salt concentration. This was done with the assistance of a magnetic stirrer. Chloroplatinic acid based precursor ink was prepared with a ternary mixture of water:isopropanol:1,2 propanediol and  $50 \text{ mg}\cdot\text{mL}^{-1}$  of salt concentration.

## 2.4 Post processing

### 2.4.1 UV

The UV curable dielectric ink was simultaneously printed and photo-polymerized with a UV LED lamp (FireEdge FE300 380–420 nm; Phoseon Technology) integrated into the according print-head slot of the CeraPrinter.

## 2.4.2 Thermal

Substrates with printed layers were treated in a Heraeus K-114 furnace with adjustable heating/cooling ramps. More information on the ramps are provided in the respective chapters.

## 2.4.3 Photonic Curing

The PulseForge 1300 photonic curing system (Novacentrix) was utilized in-line as the thermal post-processing. The parameters for the photonic curing process (*i.e.* pulse time, pulse intensity and number of pulse repetitions) were adjusted for each process. The resulting shot energy densities were measured with a BX-100 Bolometer (Novacentrix). The distance between the flash lamp and the Bolometer was identical to the distance between GC substrates and the lamp during printing (6 mm).

## 2.5 Pattern and catalyst layer characterizations

### 2.5.1 Microscopy

The rapid characterization of freshly fabricated patterns was directly performed by using substrate inspection cameras inside the CeraPrinter and DMP-2850. A more detailed analysis of the printed structures was made using a Keyence VK 8700 laser scanning microscope. A scanning electron microscope (SEM) from FEI, model Teneo, was utilized. The SEM is equipped with an Everhart-Thornley detector (ETD) for secondary electrons, two in-column detectors for backscattered electrons and an energy-dispersive X-ray spectroscopy detector from Bruker. Finally, for microscopy characterization, two transmission electron microscopes (TEM) from FEI were utilized a Tecnai Spirit at 120 kV and a FEI Tecnai Osiris at 80 to 200 kV for STEM images.

### 2.5.2 Spectroscopic characterization

A Bruker D8 Advance X-ray diffractometer (XRD) was used, applying the Cu-K $\alpha$  emission profile, measurement angles between 20° and 70° (515 steps), and a rotation of 10.000°/min. For

XPS, a monochromatic Al K $\alpha$  X-ray source of 24.1 W power, with a beam size of 100  $\mu\text{m}$  directed into the center of 1  $\text{mm}^2$  printed squares, was used. The spherical capacitor analyzer was set at 45° take-off angle with respect to the sample surface. The pass energy was 46.95 eV, yielding a full width at half maximum of 0.91 eV for the Ag 3d 5/2 peak. Physical electronics VersaProbe II X-ray photoelectron spectroscope (XPS) a monochromatic Al K $\alpha$  X-ray source operated at 200 W power with a beam size of  $\sim$ 200  $\mu\text{m}$  directed into the centre of 1  $\text{mm}^2$  printed squares was used. The spherical mirror analyzer was set at 45° take-off angle with respect to the sample surface.

### 2.5.3 Electrochemical characterization

The electrochemical characterization of the electrodes is described in detail in each chapter of the thesis. In general terms, potential sweep techniques were utilized for electrocatalyst activation and long term electrochemical analysis. Electrochemical impedance spectroscopy (EIS) was performed in order to obtain and correct for the uncompensated resistance. Finally, chrono-methods were utilized to assess long-term stability of the electrodes.

# Chapter 3 Inkjet printing of $\text{Co}_3\text{O}_4/\text{N-rGO}$ electrocatalyst forming high activity catalyst layers for oxygen reduction reaction

This chapter is based on the work adapted from: Victor Costa Bassetto, Jingjing Xiao, Emad Oveisi, Véronique Amstutz, Baohong Liu, Hubert H. Girault, Andreas Lesch, Applied Catalysis A, General 563 (2018) 9–17, in which Victor Costa Bassetto contributed with the ink formulation, inkjet printing and curing procedures. He further conducted the XRD experiments and, together with Dr. Emad Oveisi, was responsible for the TEM/SAED characterization.

## 3.1 Abstract

The accurate and reproducible large-scale production of catalyst layers containing low-cost and abundant electrocatalysts have been gaining importance. Herein, pivotal factors are discussed as they need to be considered when using a combined inkjet printing and photonic curing platform as a promising fabrication method for catalyst layers based on a model low-cost catalyst, *i.e.*, nitrogen-doped reduced graphene oxide supported cobalt oxide nanosheets ( $\text{Co}_3\text{O}_4/\text{N-rGO}$ ), specifically prepared to formulate an inkjet ink. The ink is stable for weeks and can reproducibly be printed with piezoelectric printheads. Ink composition and printing parameters are optimized to achieve high-resolution printing and good adhesion on glassy carbon substrates. Polyvinylpyrrolidone and ethyl cellulose are used as catalyst stabilizers in the ink, and must be removed through thermal post-processing to avoid a decrease of the electrical conductivity of the catalyst layer and a degradation of the catalytic activity of the  $\text{Co}_3\text{O}_4$  nanocrystals. Conventional slow oven curing (*i.e.*, hours) and photonic curing with a Xe flash lamp (seconds) are compared to generate temperatures above 400 °C under ambient conditions. Both techniques can increase the size of the  $\text{Co}_3\text{O}_4$  nanocrystals from  $\sim 7$  nm up to  $\sim 15$

nm. Photonic curing with pulses above  $2 \text{ J}\cdot\text{cm}^{-2}$  shot energy density initiates the reduction of the oxidation states of cobalt from (II,III) to (II). Residues and side products of polymeric stabilizers can still be found using photonic curing pulses below  $10 \text{ J}\cdot\text{cm}^{-2}$ . This chapter highlights the advances made in digital printing and post-processing for catalyst layer production, thereby demonstrating the importance of proper design of the ink, the printing and the post-processing for the large-scale production of catalyst layers for the ORR based on low-cost materials. The findings can be transferred to other metal and mixed metal oxide nano-catalysts.

## 3.2 Introduction

Electrochemical energy conversion devices, such as polymer electrolyte membrane fuel cells (PEMFCs), rely on the one hand on the catalytic activity and stability of electrocatalysts inside three-dimensional Catalyst Layers (CLs), and on the other hand on reliable large-scale fabrication methods of such mesoporous films. Spray coating and screen printing are among the large area techniques that are widely applied to fabricate square centimetre sized Membrane Electrode Assemblies (MEAs), which are usually composed of two CLs coated on both sides of a Nafion membrane. However, new catalyst materials are first tested in laboratories with fair loadings on smaller electrode areas, usually few millimetres in diameter.

Typically, catalysts are drop-casted and/or spin-coated resulting in catalyst coatings that can be significantly different from those obtained by large-scale fabrication techniques. One technique that could provide a bridge between small and large-scale production is inkjet printing (IJP), where picoliter droplets from tens to hundreds of parallel nozzles of micrometer-size are ejected with up to kHz jetting frequency<sup>108,157</sup>. Inkjet printing requires the use of inks of well-defined properties in terms of viscosity, surface tension and particle size<sup>123</sup>. Ideally, the nominal size of the particles and their aggregates is  $\sim 100\times$  smaller than the nozzle diameter, which is typically in the range of  $20 \mu\text{m}$ .

The formulation of an agglomerate-free dispersion is typically the bottleneck of a successful printing process. Catalyst loadings can be controlled by the number of printed layers and by defining the overlap of adjacent droplets on the substrate. For instance, platinum nanoparticles (NPs) supported on carbon black are used as state-of-the-art electrocatalysts in PEMFCs for the oxygen reduction reaction (ORR) at the cathode and hydrogen oxidation reaction at the anode. Recently, IJP has demonstrated its suitability to produce square centimeter-sized MEAs for PEMFCs<sup>132,133</sup>. Due to the efforts that are generally required to obtain stable inkjet inks containing a broad range of new catalyst materials, IJP of nanoparticulate inks has rarely been used to print NP dispersions on a smaller scale for batch characterization.

However, it must be noted that IJP is frequently used to deposit metal/metal oxide precursors that, after thermal post-processing, decompose into the solid catalyst used to generate combinatorial material libraries for screening applications<sup>158–160</sup>. Nonetheless, the synthesis of promising catalyst NPs, suitable for electrochemical energy conversion devices and supported on carbonaceous materials, inside reactors under very controlled synthesis conditions in solution, is currently without feasible alternative<sup>161</sup>. Therefore, IJP is, in fact, attractive to prepare prototype CLs with controllable catalyst loadings by the printing parameters on both small and large-scale<sup>162–164</sup>. Platinum is expensive and scarce, and much research has been contributing to identify an alternative, low-cost material with similar or equal properties<sup>165</sup>.

All dropping techniques have in common that, after deposition both the ink solvents and ink additives, *e.g.* polymeric stabilizers, the materials deposited need to be thermally removed. Advanced inkjet printers include post-processing techniques, such as near infrared or flash lamps for rapid thermal post processing<sup>138</sup>. In particular, photonic curing (also known as intense pulsed light irradiation) is attractive, irradiating with a Xenon flash lamp in milli-seconds slightly dried films of inks containing light absorbing and heating materials<sup>166–168</sup>, with energy densities of several  $\text{J}\cdot\text{cm}^{-2}$  emitted within fractions of a second. Depending on the absorption properties of the ink and substrate, printed

NPs and their coatings heat directly or indirectly (the last meaning through a heat transfer from light absorbing substrate materials or ink additives) up to several hundred degrees. This can result in the complete removal of the ink additives, sintering of the NPs, including the reduction of metal oxides<sup>169–172</sup>, and an improved adhesion of NPs on plastic<sup>124</sup>. Recently, photonic curing of metal precursors was proposed as a rapid methodology to synthesize metal nanostructures<sup>134,173</sup>, a concept that, when combined with IJP, is called Print-Light-Synthesis<sup>116</sup>.

In this chapter, nitrogen-doped reduced graphene oxide nanosheets, coated with cobalt oxide nanocrystals ( $\text{Co}_3\text{O}_4/\text{N-rGO}$  NCs), were synthesized as an example of a non-platinum catalyst for the ORR, and the effects of combined IJP and photonic curing were analyzed. Cobalt oxide is considered as one promising low-cost and abundant electrocatalyst material. The price of cobalt is in the order of  $20\times$  below that of platinum at the commodity market, whereas the price of cobalt oxide nanopowder is more than  $500\times$  cheaper than platinum nanopowder. NCs of spinel-type  $\text{Co}_3\text{O}_4$  supported on graphene derivatives, in particular, have shown considerable activity for the ORR and Oxygen Evolution Reaction (OER)<sup>174,175</sup>, and cobalt oxides are preferably used in alkaline media due to stability and activity issues in acidic media. Synergetic effects between the  $\text{Co}_3\text{O}_4$  and reduced mildly oxidized graphene oxide (rmGO) have shown to improve the catalytic activity in comparison to  $\text{Co}_3\text{O}_4$  alone, as it suffers from low electrical conductivity<sup>176,177</sup>. In addition, nitrogen-doping of the graphene derivatives induces anchor groups for the nucleation of cobalt oxide NCs. As a result, small  $\text{Co}_3\text{O}_4$  NCs in the range of 4–8 nm can be synthesized, showing the highest activity for the ORR<sup>176,177</sup>.

In this system, improvements in the catalytic activity for the ORR can be achieved by optimizing either the catalyst (micro/nanostructuring, mixing with hybrids, composition, porosity) or the carbon-based material (doping, mesoporosity, type: graphene, carbon nanotubes)<sup>174,175</sup>. For instance, for the former,  $\text{MCoxO}_y$  ( $M = \text{Ni}$  or  $\text{Mn}$ ) spinels or  $\text{M-CoO}$  ( $M = \text{Co}$  or  $\text{Ni}$ ) hybrids have been reported to promote the ORR<sup>178–180</sup>. For the latter option, nitrogen-doped mesoporous graphene has recently been shown to improve the ORR of  $\text{Co}_3\text{O}_4$  most likely due to the high active surface area,

porosity and intrinsic conductivity<sup>152,181,182</sup>. Nitrogen and boron-doping together have recently shown further improvements for the ORR, mainly by uneven charge distributions<sup>183</sup>. Doped graphene derivatives have also been considered as ORR catalysts alone<sup>184,185</sup>. However, although big progress has been made, cobalt oxide-based electrocatalysts are still inferior to platinum-based NPs, in particular to stability. In addition, graphene-based materials are currently more expensive than traditionally used carbon black as catalyst support, *i.e.*, more than 100 ×. However, its superior material properties need to be considered. Furthermore, the current progress being made in the synthesis of these materials is expected to significantly lower production costs.

Inkjet-printed graphene derivatives were frequently reported for several applications, including their use as conductive layers in flexible electronics<sup>167,186–189</sup>, as electrodes in micro-supercapacitors<sup>190,191</sup>, solar cells<sup>192</sup>, or when mixed with polymers as electrodes in electroanalytical sensors<sup>193</sup>. To the best of my knowledge, IJP of graphene derivatives coated with cobalt oxide NPs has not been reported elsewhere. To achieve printability, a Co<sub>3</sub>O<sub>4</sub>/N-rGO ink containing polyvinylpyrrolidone (PVP) and ethyl cellulose (EC) as stabilizers was formulated and fully characterized. IJP parameters for generating reproducible patterns on glassy carbon substrates were optimized using piezoelectric drop-on-demand IJP. Subsequently to printing, photonic curing and oven curing were separately applied on identically printed patterns with the aim to evaporate the ink solvents, to remove the stabilizers and to achieve well-adhered, catalytically active CLs. Three photonic curing pulses from a Xenon flash lamp integrated into one of the two employed inkjet printer platforms were applied using three different flash intensities. The removal of the polymeric stabilizers and structural changes of the Co<sub>3</sub>O<sub>4</sub> NCs were investigated using light and electron microscopy, as well as, spectroscopic and electrochemical methods.



## 3.3 Results and discussion

### 3.3.1 Optical and microscopic characterization

The bright-field (BF) TEM image of the as-synthesized  $\text{Co}_3\text{O}_4/\text{N-rGO}$  particles shows that  $\text{Co}_3\text{O}_4$  nanocrystals (NCs) were successfully deposited on the N-rGO sheets of various hundred nanometers in lateral dimension (**Figure 3-1a**). Software-based analysis of the shown TEM image using ImageJ<sup>194</sup> indicates a particle size of  $(6.9 \pm 1.1)$  nm. The distribution of the  $\text{Co}_3\text{O}_4$  NCs was homogeneous with some areas showing accumulation of NCs. However, it is unclear whether these NCs grew closely together or if a partial folding of the sheets at the sheet edges resulted in the higher concentration of NCs in certain areas.

A selected area electron diffraction (SAED) pattern was acquired to investigate the crystal structure of the NCs (**Figure 3-1b**, left semicircle) and the ring pattern corresponds to  $\text{Co}_3\text{O}_4$  with a cubic structure (Fd3 m space group) as easily seen when compared to the simulated pattern (right semicircle). This is in accordance with the powder XRD pattern shown in **Figure 3-1c**. The XRD data confirm that the catalyst is crystalline and the characteristic XRD peaks (022), (113), (004), (224), (115) and (044) correspond to  $\text{Co}_3\text{O}_4$  with face-centered-cubic (fcc) structure. The simulated XRD pattern of  $\text{Co}_3\text{O}_4$  is shown for reference. The particle size and the XRD patterns are in accordance with recent literature reports<sup>176</sup>.

In order to formulate an inkjet printable ink, the highly aggregated powder of the as-synthesized  $\text{Co}_3\text{O}_4/\text{N-rGO}$  sheets had to be dispersed and stabilized in solution. The resulting dispersion must furthermore fulfill certain fluid characteristics, such as viscosity and surface tension, in order to allow the stable ejection of picoliter-sized droplets at 1–5 kHz jetting frequency. In addition, the droplets need to cover homogeneously and with high spatial resolution the target substrate. PVP and EC were used as ink stabilizers (PVP for the  $\text{Co}_3\text{O}_4$  and EC for the N-rGO), which must be sufficiently

removed from the printed pattern, after the printing process, together with the solvents terpineol and 1,2-propanediol to avoid a deactivation of the catalyst for the ORR.

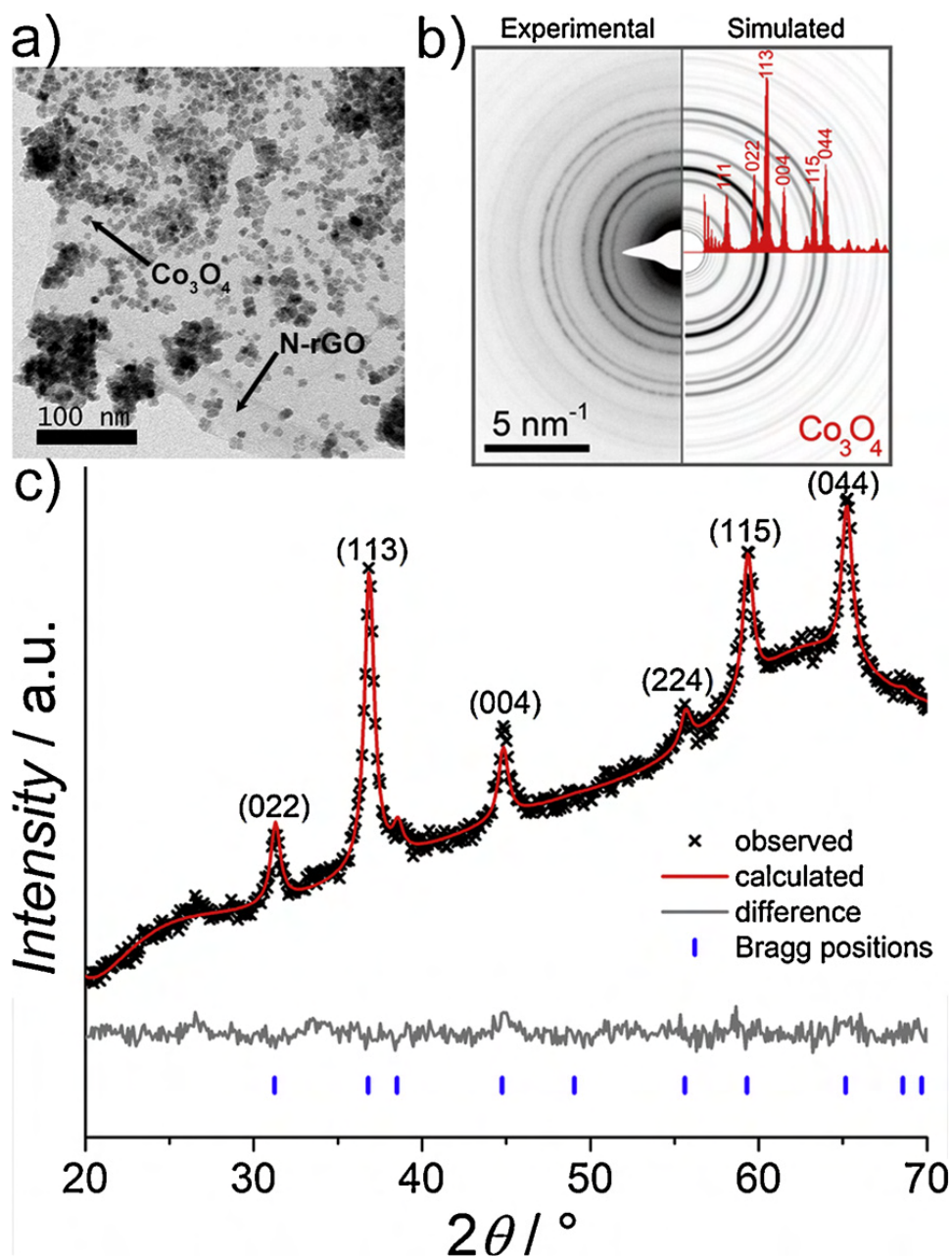


**Figure 3-1** Characterization of as-synthesized  $\text{Co}_3\text{O}_4/\text{N-rGO}$ . a) BF-TEM image, and b) corresponding SAED pattern (left semicircle). Simulated electron diffraction pattern (ring sampling diffraction planes) of cubic  $\text{Co}_3\text{O}_4$  is shown to the right of the SAED pattern. c) Rietveld refinement plot of powder XRD pattern.

### 3.3.2 Ink characterization and printability

The final Co<sub>3</sub>O<sub>4</sub>/N-rGO ink (**Figure 3-2a**) with 3 mg of particles in equal proportions of isopropanol:1,2-propanediol and water had a surface tension  $\gamma = (27.6 \pm 1.97) \text{ mN}\cdot\text{m}^{-1}$  and viscosity  $\eta = 4.3 \text{ m Pa}\cdot\text{s}$ , resulting in a printability parameter  $Z = 5.3$ , which fits well into the printability range generally defined as  $1 < Z < 10^{155}$ . The  $Z$  parameter is the reciprocal of the Ohnesorge number  $Oh$  and is given by  $Z = 1/Oh = (\gamma\rho a) / \eta$  where  $\rho$  represents the density of the ink ( $\rho = 0.8 \text{ g}\cdot\text{mL}^{-1}$ ) and  $a$  characteristic length (here the nozzle diameter with  $a = 21.5 \text{ }\mu\text{m}$ ). **Figure 3-2a** shows a picture of the formulated ink. The dark, non-transparent appearance indicates a reasonable loading, *i.e.*,  $3 \text{ mg}\cdot\text{mL}^{-1}$ , of Co<sub>3</sub>O<sub>4</sub>/N-rGO.

Ejected droplets had a tail that shortened during the flight but remained attached until the droplets landed on the substrate (**Figure 3-2b**). **Figure 3-2c** shows a printed CL of 25 inkjet-printed layers (IJPLs, refers to the number of printing passes and not to the number of monolayers of the catalyst) achieving a catalyst loading of  $5.1 \text{ }\mu\text{g}\cdot\text{mm}^{-2}$  (referred to Co<sub>3</sub>O<sub>4</sub>/N-rGO). After photonic curing with a  $(10.6 \pm 0.2) \text{ J}\cdot\text{cm}^{-2}$  pulse, the CL became solid and appeared brighter in the microscopic image. A library of Co<sub>3</sub>O<sub>4</sub>/N-rGO-based CLs with different IJPLs were printed and photonic-cured with the same  $(10.6 \pm 0.2) \text{ J}\cdot\text{cm}^{-2}$  pulse for screening purposes (**Figure 3-2d**). 5, 10, 25 and 50 IJPLs were deposited resulting in catalyst loadings of 0.05, 0.11, 0.27 and  $0.54 \text{ }\mu\text{g}\cdot\text{mm}^{-2}$ . These loadings were precisely calculated by knowing the number of deposited droplets (software parameter), droplet volume (droplet image analysis) and Co<sub>3</sub>O<sub>4</sub>/N-rGO catalyst loading in the ink (known from the ink preparation).

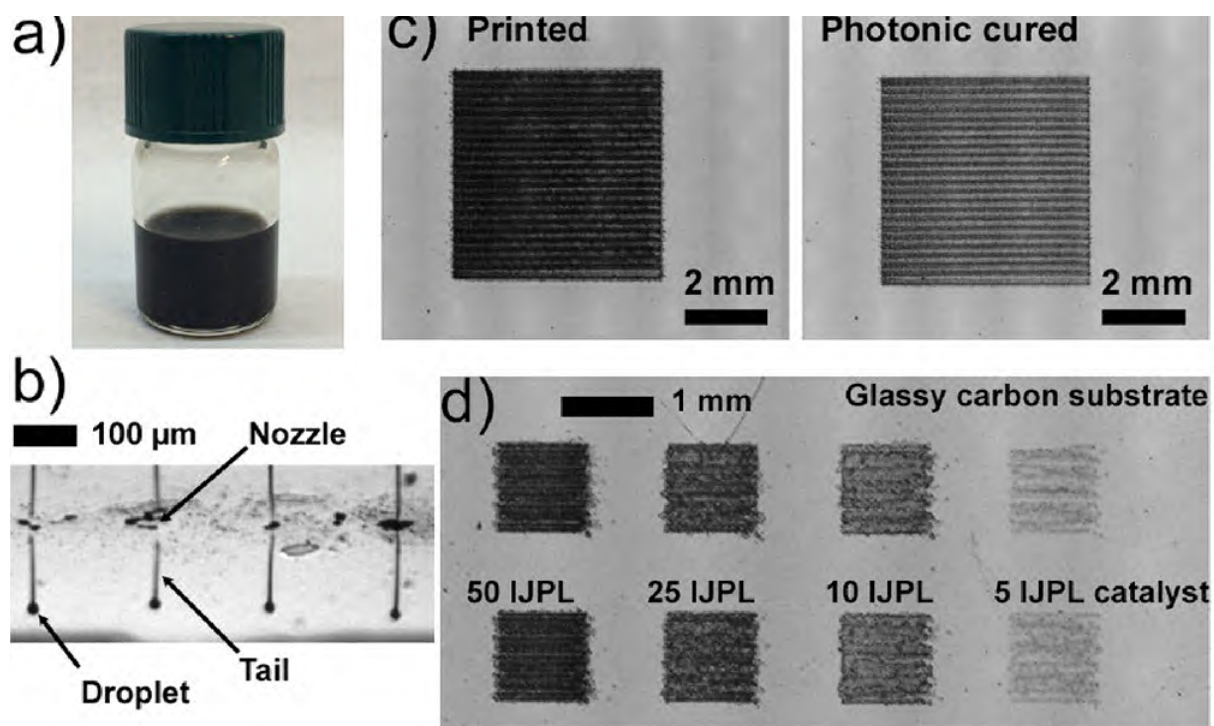


**Figure 3-2.** High-resolution IJP of  $\text{Co}_3\text{O}_4/\text{N-rGO}$ -based CLs. a) Photograph of the  $\text{Co}_3\text{O}_4/\text{N-rGO}$  ink. b) Four droplets ejected from four parallel nozzles. c) 25 IJPL as a  $25 \text{ mm}^2$  CL on glassy carbon before and after photonic curing with the  $(10.60 \pm 0.19) \text{ J}\cdot\text{cm}^{-2}$  pulse. d) Inkjet-printed and photonic-cured  $1 \text{ mm}^2$  patterns of  $\text{Co}_3\text{O}_4/\text{N-rGO}$  with different numbers of printed layers on a glassy carbon substrate.

It was verified with UV–vis spectroscopy that the absorbance of a printed PVP- $\text{Co}_3\text{O}_4/\text{N-rGO}$  layer overlaps with the emission of the Xenon flash lamp (**Figure 3-3**). This guaranteed sufficient, yet not complete, solvent evaporation and nanoparticle densification. Notably, after printing and flash light irradiation, the CLs remained attached to the GC even after rinsing with aqueous as well as organic solvents.

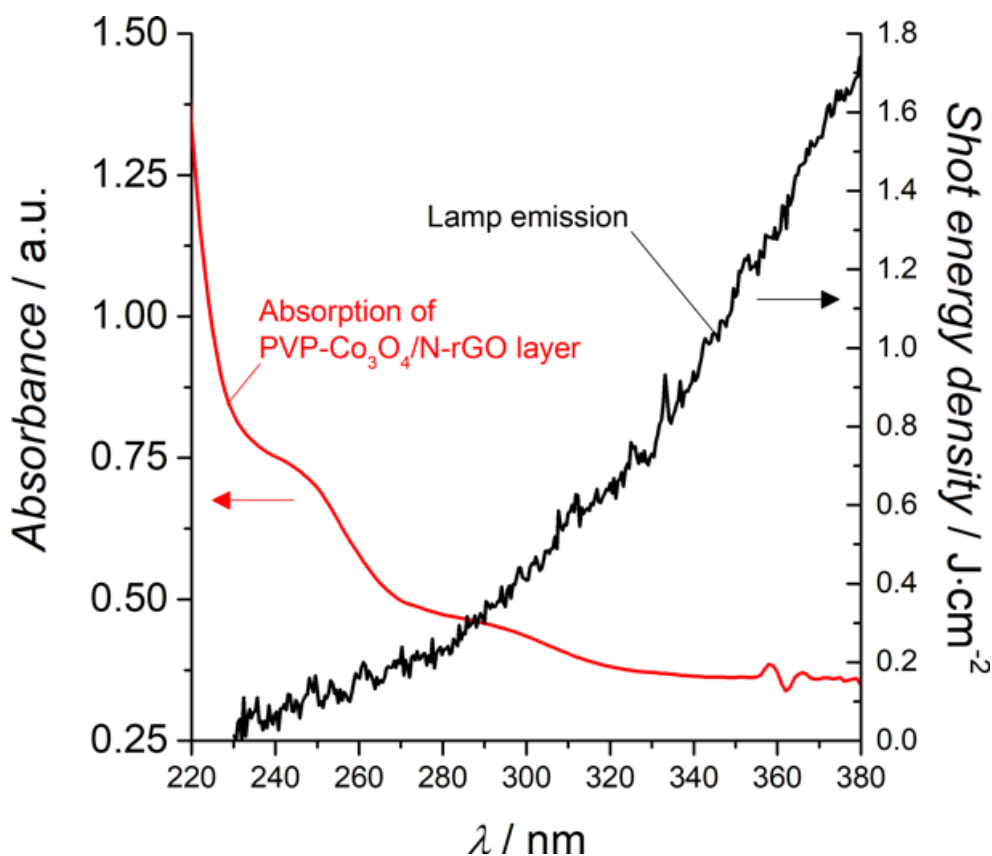


**Figure 3-3.** UV Vis absorption spectrum of an as-printed PVP-Co<sub>3</sub>O<sub>4</sub>/N-rGO layer on quartz glass (red curve) compared with a typical lamp emission spectrum (black curve; kindly provided by Novacentrix, same spectrum as in ref<sup>116</sup>).

Soft-Probe-SECM feedback mode imaging (**Figure 3-4**) was performed to investigate whether the printed and post-processed catalyst layers were conductive and well adhered to the substrate. SECM is a scanning probe microscopy technique where microelectrodes, typically metallic disk electrodes (radius  $r \leq 12.5 \mu\text{m}$ ) encapsulated in a solid insulating sheath, are laterally scanned over flat and smooth surfaces. The optimum working distance is significantly smaller than the disk radius<sup>195</sup>. This makes it challenging to scan rough and tilted substrates, which requires the operation of the scanning tip in a constant distance mode. In order to achieve this, a broad range of scanning probe microscopies that operate with a distance control, such as atomic force microscopy or ion conductance microscopy, have been combined with SECM.<sup>196–198</sup> As the hyphenating approach requires modified and often nano-sized tips as well as additional hardware, soft SECM probes have recently been suggested as simple to prepare and operate, but however powerful, constant distance mode tips.

Soft probes are made of flexible materials with embedded microelectrodes made of carbon paste or platinum and brush in a gentle contact mode on the sample keeping thus a constant working distance. The forces exerted onto the surface are weak enough to leave even biological tissue undamaged by the contact mode scanning.<sup>199–202</sup> These positive points make this technique particularly useful for investigating CLs that are rough and that can be printed with varying controlled thicknesses.

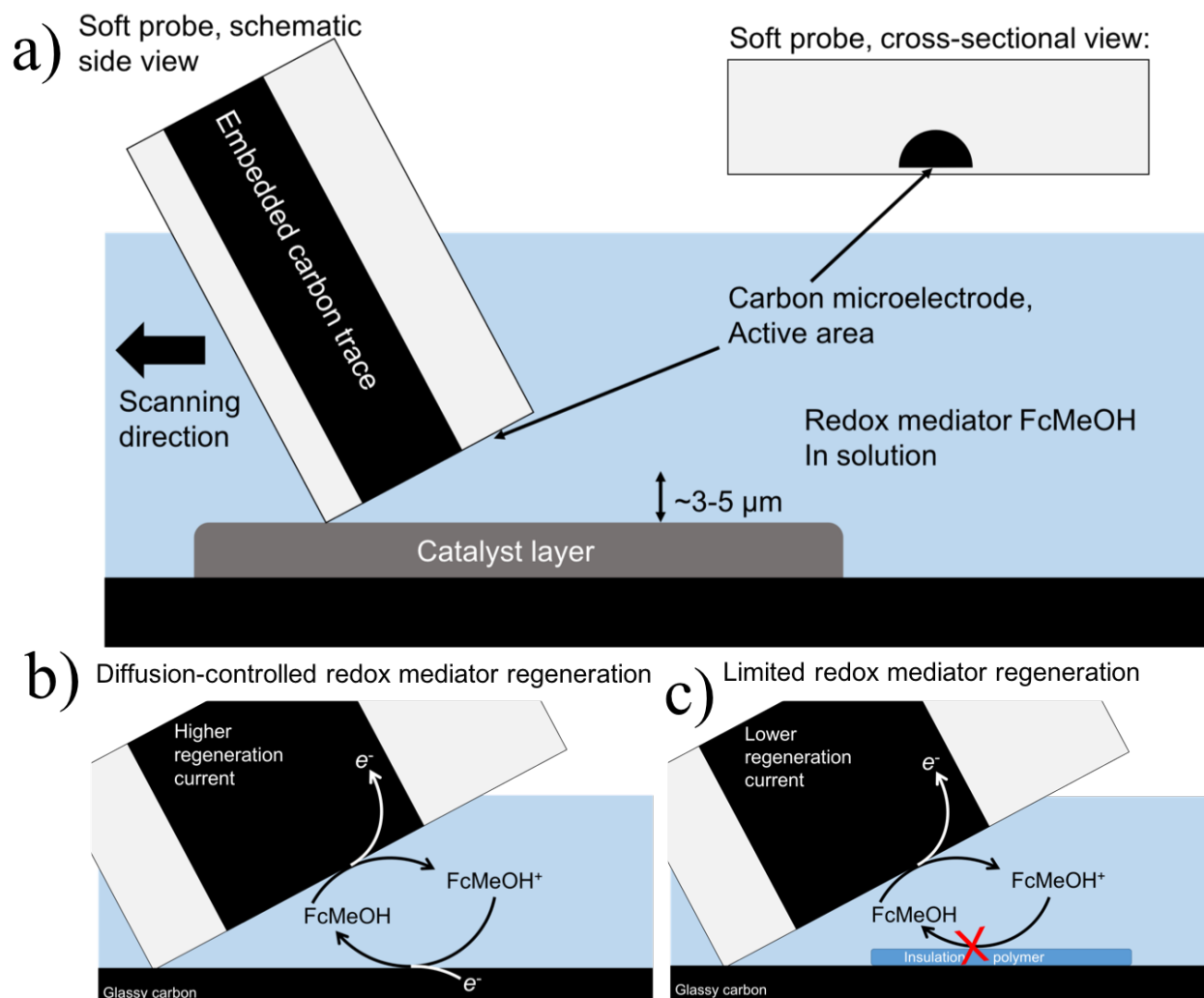


**Figure 3-4.** Schematic representation of Soft-Probe-SECM using soft carbon microelectrodes in contact mode over catalyst layers printing on glassy carbon. Similar currents are expected over conductive surfaces (polymer-free catalyst layer and glassy carbon). Lower currents are expected due to the presence of polymers (*e.g.* PVP) slowing down the electrode kinetics at the substrate or even insulating the substrate (the latter means no regeneration reaction).

Different SECM modes exist, from which the feedback mode is the most common one. Herein, ferrocene methanol (FcMeOH), a ferrocene derivate, was electrochemically oxidized to

FcMeOH<sup>+</sup> at the soft microelectrode and diffused to the substrate, where it was regenerated to FcMeOH by an electron transfer from the CL/GC, in case the substrate directly below the soft probe was conductive. This regeneration resulted in an increased flux of FcMeOH to the SECM probe. The FcMeOH regeneration reaction is fast at reactive surfaces while it is slow or absent at less reactive or insulating materials. Thus, the recorded current at the microelectrode provides information about local surface reactivity of the sample. The feedback mode SECM image of the Co<sub>3</sub>O<sub>4</sub>/N-rGO patterns (**Figure 3-5**) reveals a homogeneous surface reactivity of all printed patterns. Because feedback currents over the CLs were similar to bare glassy carbon, the printed CLs on GC were as conductive as bare GC, giving a first indication that PVP and EC were successfully removed. Only at the edges of the printed patterns slightly lower currents were recorded, most likely due to the presence of some polymeric residues that might have accumulated in those areas during ink drying, as a consequence of coffee ring effect. Another important result of the SECM imaging with the soft brushing probe is that the CL was not mechanically removed, demonstrating certain stability and adhesion. Furthermore, this experiment exemplifies the applicability of Soft-Probe-SECM for the screening of libraries of catalyst materials, offering new opportunities for soft probes.

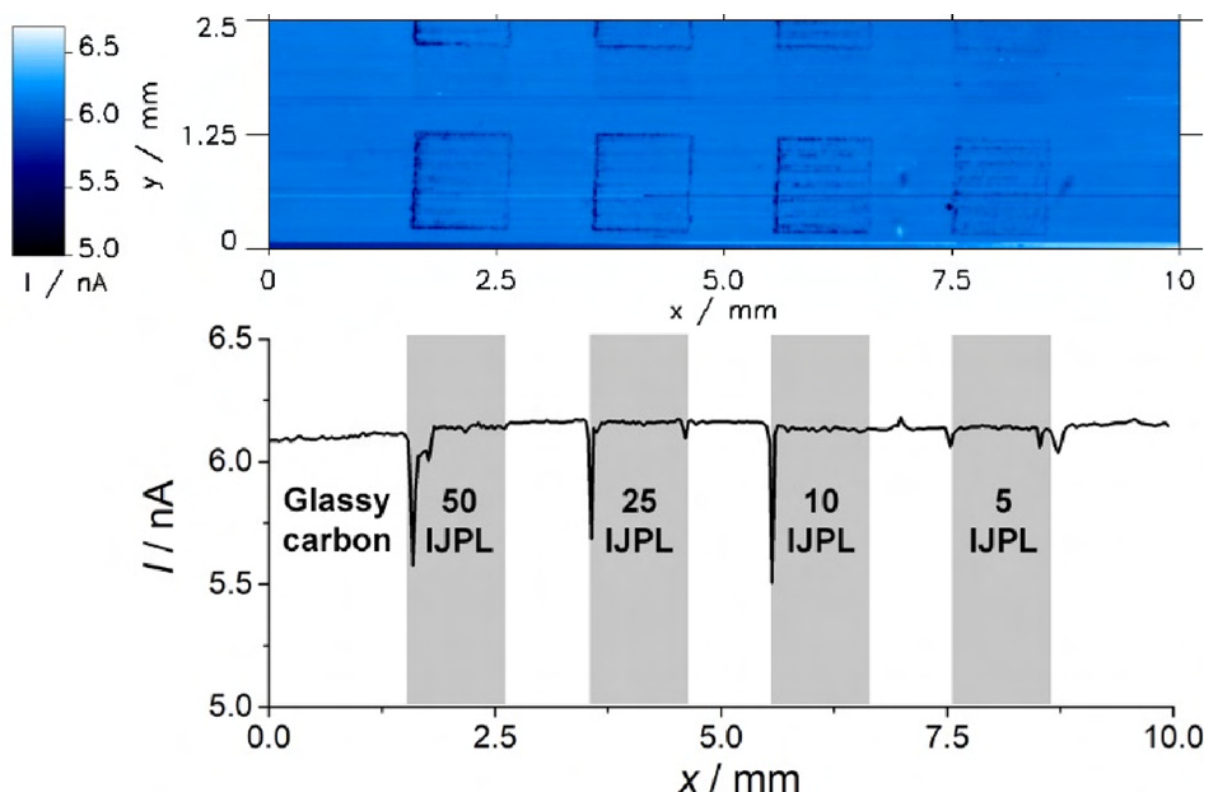


**Figure 3-5.** Soft-Probe-SECM feedback mode image of the catalyst patterns using a soft carbon microelectrode in contact mode. An exemplary line scan was extracted. Identical currents over the CLs demonstrate their homogeneous conductivity similar to bare glassy carbon. Exp. conditions: 2 mM FcMeOH and 0.1 M KNO<sub>3</sub>, Potential at the microelectrode: 0.4 V, sample was unbiased, step size in *x*- and *y*-direction 25 μm, probe translation rate 25 μm·s<sup>-1</sup>, scan direction from left to right. The SECM data were plane-fitted using two margins in order to compensate for slight solvent evaporation effects during the experiment.

Photonic curing is a powerful but critical process: On the one hand, it can reduce thermal post processing times from hours to seconds, especially when the flash lamp is installed inside the printer. A combined IJP and photonic curing platform allows further in a convenient way layer-by-layer printing with intermediate curing. On the other hand, temperatures of several hundred degrees, generated within a fraction of a second, can not only cause the evaporation of ink solvents and additives, but can also affect the properties of the processed material due to the generated heat. For instance, metal oxide reduction to the metal can occur in presence of reducing compounds<sup>171,172</sup>. To analyse this process and the required parameters, and to compare the effects of slow oven-curing and non-equilibrium photonic curing, inkjet-printed Co<sub>3</sub>O<sub>4</sub>/N-rGO-based CLs before and after thermal



post-processing were mechanically removed from the GC substrates with a scalpel and, after re-dispersion in an alcoholic solvent, were deposited on a TEM grid with carbon support. From the TEM images, it can be seen that thermal curing above a certain temperature with both techniques resulted on the one hand in larger  $\text{Co}_3\text{O}_4$  NCs that further changed their shape from cubic to roundish (**Figure 3-6**).

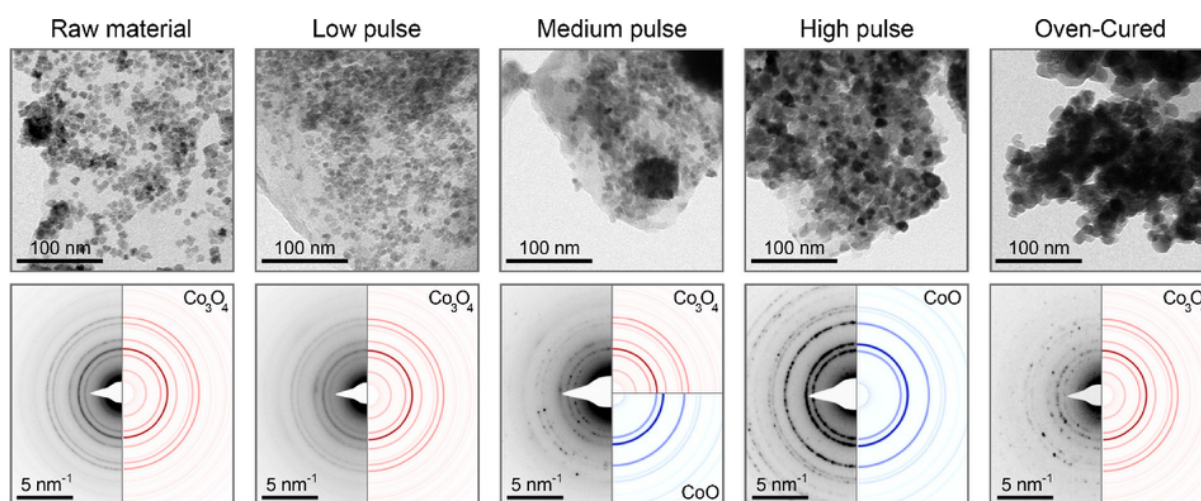


**Figure 3-6.** BF-TEM images (upper panels) and corresponding SAED patterns (lower panels) of the raw catalyst material, after different photonic curing pulses and after oven curing. To the right of each SAED pattern, the simulated electron diffraction pattern (ring sampling diffraction planes) is shown. Reddish rings indicate  $\text{Co}_3\text{O}_4$ , blueish rings CoO.

On the other hand, N-rGO sheets might have been folded or size-reduced as they appear less clear in the TEM images. The biggest changes in size and shape for  $\text{Co}_3\text{O}_4$  NCs were observed for the oven-cured sample (cured at 400°C in air (final particle size ( $14.9 \pm 3.6$ ) nm)), but also for the photonic-cured samples a gradual increase in  $\text{Co}_3\text{O}_4$  NC size was obtained with increasing flash light intensities (**Table 3-1**). Only for the low photonic curing pulse ( $(2.03 \pm 0.02) \text{ J} \cdot \text{cm}^{-2}$ , in the following "low pulse"), the cobalt oxide NCs kept their original size and shape (particle size ( $7.1 \pm 1.2$ ) nm). It has also been shown by other studies that post-thermal treatment in air of  $\text{Co}_3\text{O}_4$  nanoparticle-decorated graphene derivatives increased the catalyst particle size and porosity<sup>203</sup>. Furthermore, the N-

rGO sheets were still clearly visible. Applying the highest photonic curing pulse, *i.e.*,  $(10.6 \pm 0.2)$   $\text{J}\cdot\text{cm}^{-2}$  = "high pulse", the rings in the SAED pattern converted more into dots and the new  $\text{Co}_3\text{O}_4$  NP size was  $(14.8 \pm 4.0)$  nm, which was nearly the same as for oven curing. The samples cured with  $(5.27 \pm 0.02)$   $\text{J}\cdot\text{cm}^{-2}$  = "med (medium) pulse" demonstrate the presence of a transition zone, because two domains with two different particle sizes were identified, cubic  $(6.7 \pm 1.2)$  nm and roundish  $(13.1 \pm 2.3)$  nm. This suggests a heterogeneous heating by the medium pulse and, to elucidate the evolution of the structure with heating, a detailed analysis on the SAED pattern was performed.

**Table 3-1.** Particle sizes after different post-processing conditions.

Sample	Raw material	Low pulse	Med pulse	High pulse	Oven-cured
Particle size (nm)	$6.9 \pm 1.1$	$7.1 \pm 1.2$	$6.7 \pm 1.2/ 13.1 \pm 2.3$	$14.8 \pm 4.0$	$14.9 \pm 3.6$
Shape	Cubic	Cubic	Cubic/round	Round	Round

The clear change of the SAED pattern for the high pulse compared to the raw material can be interpreted as a change of cobalt oxidation state from Co(II,III) in  $\text{Co}_3\text{O}_4$  to Co(II) in CoO. The SAED patterns in **Figure 3-6** were divided into the measured (left semi-circle) and simulated patterns (right semi-circle/quadrant). On the contrary, the oxidation states of Co(II,III) in the CLs that were oven-cured did not change, which can be expected for thermal equilibrium curing under ambient conditions at 400 °C. It is known from calculated phase diagrams that  $\text{Co}_3\text{O}_4$  decomposes at elevated temperatures into CoO and  $\text{O}_2$  only with a partial oxygen pressure below 1 atm<sup>204</sup>. In fact, inert or reducing atmospheres (*e.g.*, hydrogen atmosphere) are usually applied inside furnaces to promote the reduction of  $\text{Co}_3\text{O}_4$ . Recently, Lee *et al.* have reported that high intensity light pulses between 18 and 24  $\text{J}\cdot\text{cm}^{-2}$  as 10 ms pulses ( $\sim 350\text{--}410$  °C) reduced nano- and microflakes of  $\text{Co}_3\text{O}_4$  supported on carbon fiber first to CoO and then at pulses above 26  $\text{J}\cdot\text{cm}^{-2}$  ( $\sim 510$  °C) to metallic Co(0)<sup>205</sup>. The authors suggested that a carbothermal reduction mechanism took place where the carbon acts as reducing agent forming carbon dioxide (Eq. 54). In this work, N-rGO, PVP and other carbon sources

in the ink (including solvent residues) could have acted as reducing agents<sup>206</sup>, identified as “C” in Eq. 54. However, an experimental proof is missing and further investigations are required. For instance, the generated temperature during the photonic curing pulses is unknown in this study. Still in literature it is discussed the effects of the UV component of the irradiated light to have an effect in the degradation of PVP as capping agents for nanoparticles.<sup>168</sup> In such case one of the product of the decomposition are alcohols which can act as reducing agents during the sintering process.<sup>134</sup>

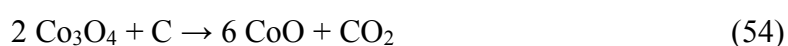


**Figure 3-7** shows intensity profiles measured on the SAED patterns of the raw material, of the CL cured with the low pulse and of a CL cured with the medium pulse in comparison to the simulated profiles for  $\text{Co}_3\text{O}_4$  (Fd-3 m) and  $\text{CoO}$  (Fm-3 m). Similar to the XRD data shown in Fig. 1c, the intensity profile of the raw material corresponds well to cubic  $\text{Co}_3\text{O}_4$  (Fd-3 m space group). For the low pulse, identical peaks were identified, demonstrating that the oxidation state of cobalt did not change. On the contrary, additional peaks corresponding to  $\text{CoO}$  (space group Fm-3 m) were identified for the CL specimen that was post-processed with the med pulse (appears in magenta on **Figure 3-7**).

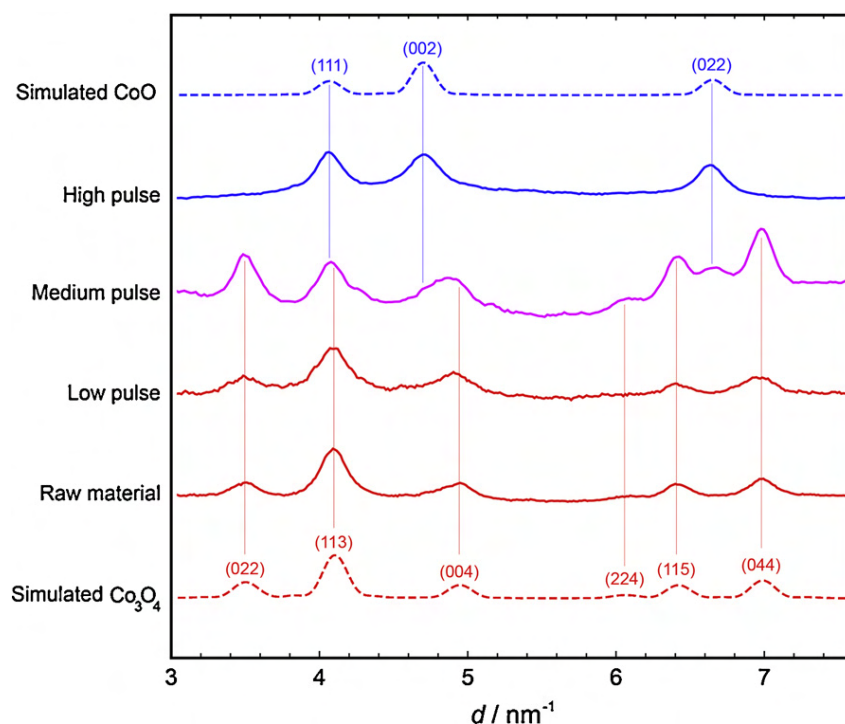


**Figure 3-7.** Intensity profiles measured on the SAED patterns of inkjet-printed  $\text{Co}_3\text{O}_4/\text{N-rGO}$ -based CLs without curing (raw material), photonic-cured with the low, medium, and high pulse (solid curves). Simulated intensity profiles for  $\text{Co}_3\text{O}_4$  and  $\text{CoO}$  are presented as dashed lines. Red curves correspond to  $\text{Co}_3\text{O}_4$ , blue curves to  $\text{CoO}$  and magenta represents a transition state.

This pulse represents a transition zone before the complete reduction of  $\text{Co(II,III)}$  to  $\text{Co(II)}$  takes place. NCs of both spinel face-centered-cubic (fcc)-  $\text{Co}_3\text{O}_4$  (space group  $\text{Fd-3 m}$ ) and fcc- $\text{CoO}$  (space group  $\text{Fm-3 m}$ ) have been identified in the same CL, but in different regions (small cubic versus larger roundish cobalt NPs, respectively), demonstrating that the heat generated by the photonic curing was not affecting the CL homogeneously. The incomplete reduction to  $\text{CoO}$  could be attributed to the mesoporous, three-dimensional structure of the CL resulting in heterogeneous light absorption. Particles at the bottom or embedded within multilayered sheets might be slightly blocked for the flash light. In addition, the mesoporous structure of the CL filled with air could have a cooling effect, leading to lower local temperatures. Furthermore, local variations in catalyst loading, the degree of folding of the N-rGO sheets and local differences in the PVP and EC loading could also influence the local generation of heat. A fast heat transfer from the CL into the glassy carbon could play a role as well in the incomplete reduction of  $\text{Co}_3\text{O}_4$  to  $\text{CoO}$ .

FT-IR spectroscopy was performed to analyse the removal of PVP by thermal post-processing (Fig. 3-7). Six characteristic peaks for bare PVP (**Figure 3-8f**, purple) have been identified to follow the presence, degradation and removal of PVP, which include sharp peaks at  $1660\text{ cm}^{-1}$  (C=O stretching/vibration),  $1420\text{ cm}^{-1}$  (C-H<sub>2</sub> bending) and  $1280\text{ cm}^{-1}$  (C-N vibration). The FT-IR spectrum of the as-synthesized Co<sub>3</sub>O<sub>4</sub>/N-rGO (**Figure 3-8a**, black) shows characteristic peaks for N-rGO at  $1570\text{ cm}^{-1}$  (sharp) and  $1220\text{ cm}^{-1}$  (broad). Furthermore, two major peaks for Co<sub>3</sub>O<sub>4</sub> can be identified at  $658\text{ cm}^{-1}$  and  $560\text{ cm}^{-1}$ . The FT-IR spectrum of the as-printed and dried PVP- Co<sub>3</sub>O<sub>4</sub>/N-rGO ink (**Figure 3-8b**, red) shows the characteristic peaks of PVP as marked by violet asterisks. In addition, a broad peak at around  $2920\text{ cm}^{-1}$  for asymmetric C-H stretching, which is present in bare PVP, is also found in the non-cured sample. This peak is significantly weaker in all other spectra. Oven curing at  $400\text{ }^{\circ}\text{C}$  resulted in a complete removal of PVP as expected (**Figure 3-8c**, blue), because PVP thermally degrades at  $400\text{ }^{\circ}\text{C}$  into volatile pyrrolidone that further decomposes into hydrocarbons<sup>207</sup>. The spectrum of the inkjet-printed PVP- Co<sub>3</sub>O<sub>4</sub>/N-rGO CL after photonic curing with the med pulse shows that PVP has not been removed (**Figure 3-8d**, green). However, the characteristic peaks at  $1660\text{ cm}^{-1}$ ,  $1420\text{ cm}^{-1}$  and  $1280\text{ cm}^{-1}$  shifted to  $1740\text{ cm}^{-1}$  ( $+80\text{ cm}^{-1}$ ),  $1370\text{ cm}^{-1}$  ( $-50\text{ cm}^{-1}$ ) and  $1220\text{ cm}^{-1}$  ( $-50\text{ cm}^{-1}$ ), respectively. This can be correlated to degradation products of PVP<sup>208</sup>. In addition, two peaks at  $2350\text{ cm}^{-1}$  and  $2320\text{ cm}^{-1}$  increased significantly compared to bare PVP and can be correlated to CO<sub>2</sub> (antisymmetric stretching modes of O=C-O)<sup>209,210</sup>. CO<sub>2</sub> from the atmosphere or generated during the thermal decomposition of PVP could either be adsorbed or entrapped in hollow spheres. Importantly, all peaks that can be correlated to PVP disappeared in the printed CL after photonic curing with the high pulse, which suggests its complete removal (**Figure 3-8e**, orange).

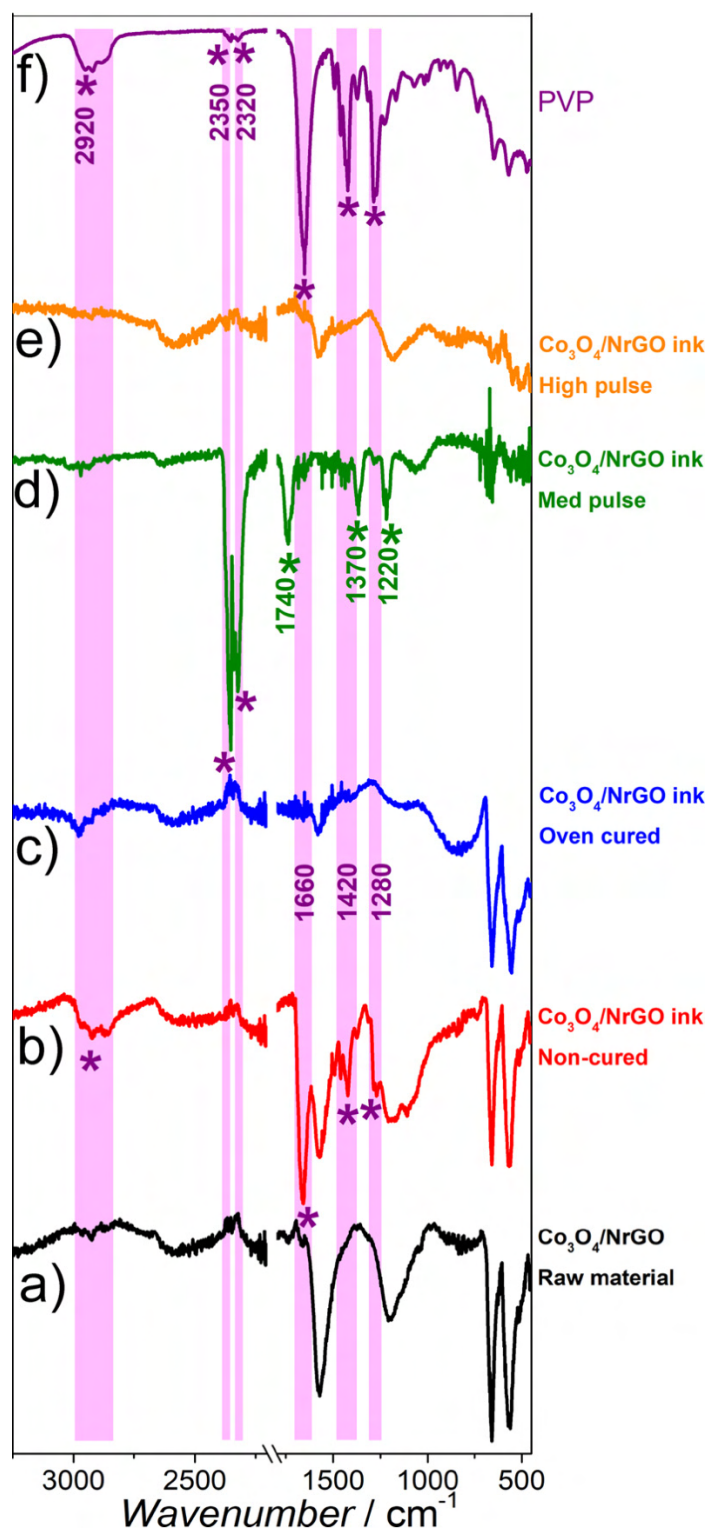


**Figure 3-8.** Removal of PVP through thermal post-processing. FT-IR spectra of a) raw  $\text{Co}_3\text{O}_4/\text{N-rGO}$  (black), b) non-cured inkjet-printed PVP-  $\text{Co}_3\text{O}_4/\text{N-rGO}$  pattern (red), c) oven-cured inkjet-printed PVP- $\text{Co}_3\text{O}_4/\text{N-rGO}$  pattern (blue), d) med pulse photonic-cured inkjet-printed PVP-  $\text{Co}_3\text{O}_4/\text{N-rGO}$  pattern (green), e) high pulse photonic-cured inkjet-printed PVP-  $\text{Co}_3\text{O}_4/\text{N-rGO}$  pattern (orange) and f) PVP (purple). Asterisks and colored rectangles in the background indicate recognizable peaks throughout all spectra. Peaks marked by purple asterisks and rectangles correlated with selected peaks in bare PVP. Green asterisks correlate with degradation products of PVP.

The activity of the CLs for the ORR was evaluated by linear sweep voltammetry in O<sub>2</sub>-saturated 0.1 M KOH. The printed electrodes were placed faced-up at the bottom of the electrochemical cell. The electrolyte solution and the electrode were stationary during all measurements. Therefore, the measurements were mass-transport controlled, and the data were not corrected for it, impeding kinetic analysis. As a result, the interpretation of the electrochemical data from different CLs can only be carried out on a relative basis. **Figure 3-9a** shows the effect of different post-processing conditions using identically inkjet-printed CLs. The electrochemical response of the oven- and photonic-cured samples were significantly different. Herein, oven curing resulted in the lowest absolute onset potential, but with the largest peak current ( $-30 \text{ mA} \cdot \text{mg}^{-1}$ ), highest peak potential (0.6 V) and more pronounced slope, therefore higher kinetics. The low pulse- Co<sub>3</sub>O<sub>4</sub> resulted in the highest onset potential and in a peak current of  $-22 \text{ mA} \cdot \text{mg}^{-1}$  at 0.56 V. Among the photonic-cured samples, the high pulse resulted in the lowest absolute onset potential and less pronounced slope. The LSV of the medium pulse-Co<sub>3</sub>O<sub>4</sub>-CoO is located in between. Generally, it is known that spinel Co<sub>3</sub>O<sub>4</sub> on graphene derivatives shows activity for the ORR<sup>211</sup>, however the reaction mechanism is still under debate. On the one hand, it is believed that the catalytic activity in alkaline media is associated with Co<sup>3+</sup> ions as active sites, which is affected by the catalyst morphology<sup>212</sup>. On the other hand, in a different study it was demonstrated that Co<sup>2+</sup> could be the active site for the electron transfer to one adsorbed oxygen molecule, which favours O–O bond breaking while the Co<sup>2+</sup> is oxidized to Co<sup>3+</sup><sup>213,214</sup>. Supporting this view, it was recently found that CoO showed better catalytic activity for the ORR than Co<sub>3</sub>O<sub>4</sub><sup>72,215</sup>. However, synergistic effects between Co<sub>3</sub>O<sub>4</sub> nano-sized particles and graphene improved the ORR activity, presumed due to the formation of Co–O–C bonds, which increases the electron density at the O and decreases the electron density at the Co, most likely improving the electron transfer<sup>176</sup>. N-doping of graphene derivatives have shown to strengthen the coupling between Co<sub>3</sub>O<sub>4</sub>

and the graphene derivative while being a nucleation site for the catalyst formation<sup>176</sup>. Another essential factor for the catalyst activity is the conductivity of the support material, which for instance has been shown to be higher for N-doped CNTs than for N-rGO and resulting in a higher activity with the former support<sup>72</sup>. Therefore, the results of the photonic-cured samples could be explained by the change in the particle size and morphology of cobalt oxide, cobalt oxidation state and the interaction of the cobalt oxide with the N-rGO support material, which affects active surface area and the electron density. The crystal structure of the Co<sub>3</sub>O<sub>4</sub>/N-rGO using the lowest photonic curing pulse resembled closest that of the catalyst raw material (*vide supra*). Lower onset potentials could be attributed to the larger size of the catalyst NCs. The larger slope could be the result of faster kinetics. The mass-transport is controlled by semi-infinite linear diffusion and should be similar for each electrode surface. However, minor variations of the surface roughness cannot be excluded. Photonic curing of PVP-Co<sub>3</sub>O<sub>4</sub>/N-rGO films was supposed to decompose the PVP resulting only in gaseous and evaporated compounds. However, PVP residues or the formation of carbonaceous side products in the CLs could have slowed down the kinetics of the catalyst. In fact, recent studies show the effects of adsorbed PVP on platinum NPs, where PVP inhibited the hydrogen underpotential deposition in acidic solution. The electro-oxidation of PVP with adsorption of the reaction products on Pt above 0.4 V *vs.* RHE was reported<sup>216</sup>. It was further suggested to perform electrochemical cleaning to remove PVP from carbon supported Pd NPs, which in turn caused structural modifications and agglomeration of the Pd NPs<sup>217</sup>. The presence of low quantities of carbonaceous residues on Co<sub>3</sub>O<sub>4</sub>/N-rGO and an oxidation of the N-rGO sheets is difficult to be analyzed due to the large background signals from carbon in the material itself and in the support layers.

One of the major advantages of IJP is the possibility to print reproducible features with highly controlled loadings. **Figure 3-9b** shows the LSVs for the ORR of three examples CLs generated with the same printing and photonic curing parameters. The onset potentials are identical, the slopes nearly the same and the peak currents and potentials vary only by 3% and 4%, respectively. In



**Figure 3-9c**, the catalytic activities of the  $\text{Co}_3\text{O}_4/\text{N-rGO}$  CLs cured with the medium pulse and oven are compared with a state-of-the-art ORR catalyst, which was carbon black supported Pt with two Pt loadings (10% and 40%). For the Pt/C CLs, Nafion was used as a binder and curing temperatures were moderate ( $80\text{ }^\circ\text{C}$ ). As expected, the catalytic activity for the ORR for 40% Pt/C was superior. The 10% Pt/C-based CL showed the highest overpotential, most likely due to the four times lower Pt loading. The slopes of both Pt/C-based CLs and the peak currents were quite comparable and similar to the oven-cured  $\text{Co}_3\text{O}_4/\text{N-rGO}$  CL. These slopes were more pronounced than that from the photonic-cured  $\text{Co}_3\text{O}_4/\text{N-rGO}$  CL. The half-peak potentials indicate a larger overpotential for the oven-cured  $\text{Co}_3\text{O}_4/\text{N-rGO}$  CL ( $0.67\text{ V}$ ) compared to in photonic-cured samples. Generally, it is known that spinel  $\text{Co}_3\text{O}_4$  on graphene derivatives shows activity for the ORR<sup>211</sup>, however the reaction mechanism is still under debate<sup>214</sup>. On the one hand, it is believed that the catalytic activity in alkaline media is associated with  $\text{Co}^{3+}$  ions as the low pulse photonic-cured  $\text{Co}_3\text{O}_4/\text{N-rGO}$  CL ( $0.7\text{ V}$ ). As it is well known, the oxygen reduction mechanism can follow a  $4\text{-}e^-$  or  $2\text{-}e^-$  pathway, wherein the latter results in the formation of hydrogen peroxide ( $\text{H}_2\text{O}_2$ ) as a side product. This should be avoided, since this strongly oxidizing compound can degrade for instance polymeric materials, such as Nafion, in fuel cells<sup>218</sup>.

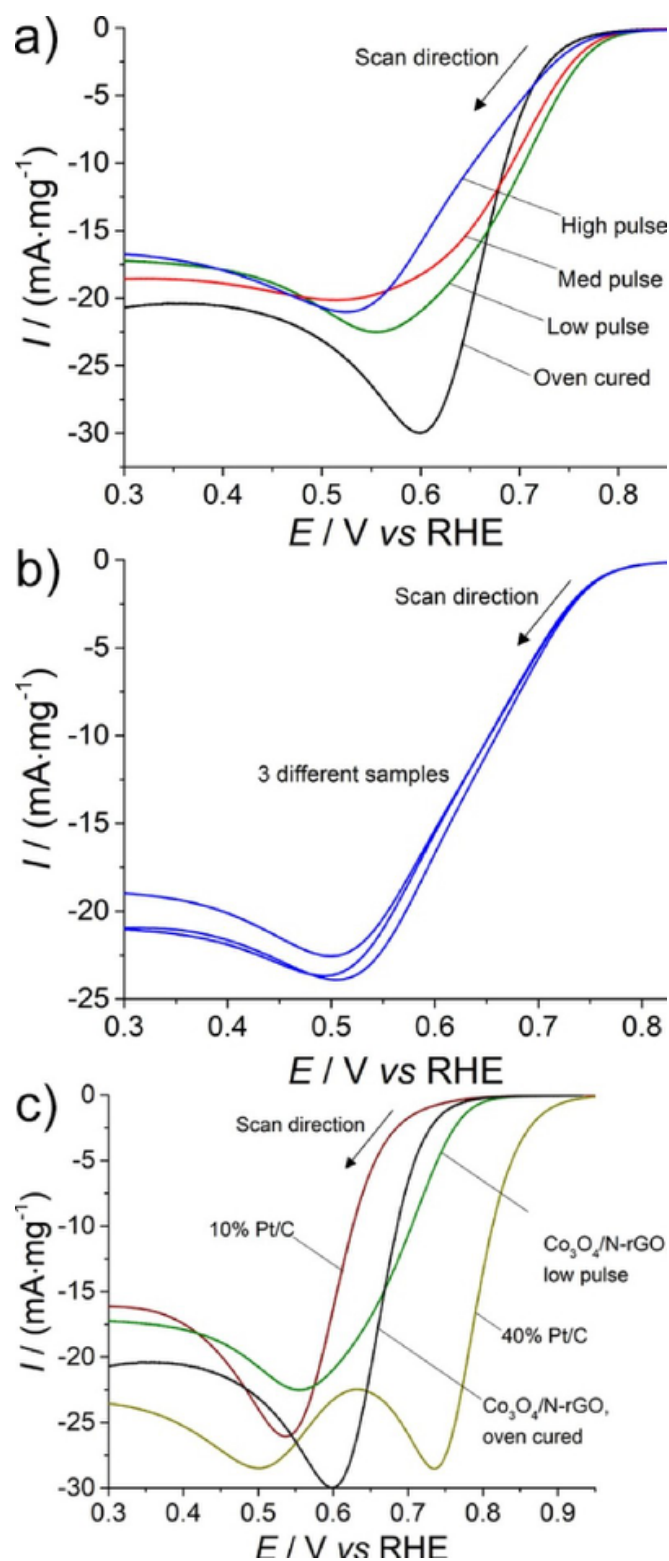


**Figure 3-9.** Stationary LSVs for the ORR of inkjet-printed and post-processed CLs of  $\text{Co}_3\text{O}_4/\text{N-rGO}$  (LSVs not  $iR$ -corrected). a) Comparison of oven-cured and photonic-cured CLs using different pulses. b) Reproducibility of three different CLs that were identically printed and post-processed (high pulse) on three GC substrates. c) Comparison of the ORR performance of a typical  $\text{Co}_3\text{O}_4/\text{N-rGO}$  CL (low pulse) with two Pt/C-based CLs made with different Pt content. Experimental conditions: Oxygen-saturated 0.1 M KOH, scan rate  $5 \text{ mV s}^{-1}$

Previous studies with the present material had indicated an electron transfer number close to 4.<sup>152</sup> In order to investigate the effects of material processing, from ink formulation to pattern curing a study was conducted in order to determine the electron transfer number according to the Koutecky-Levich equation (Eq. 55)<sup>152</sup>:

$$\frac{1}{j} = \frac{1}{j_k} + \left( \frac{1}{0.620nFAD^{2/3}\nu^{-1/6}C} \right) \omega^{-1/2} \quad (55)$$

where  $j$  is the measured current density,  $j_k$  are diffusion-limited current densities at a constant potential,  $n$  is the number of electrons transferred per O<sub>2</sub> molecule,  $F$  is the Faraday constant (96 485 C mol<sup>-1</sup>),  $D$  is the diffusion coefficient of oxygen ( $1.9 \times 10^{-5}$  cm<sup>2</sup> s<sup>-1</sup>),  $\nu$  is the kinematic viscosity of the solution (0.01 cm<sup>2</sup> s<sup>-1</sup>);  $C$  is the bulk concentration of oxygen ( $1.2 \times 10^{-6}$  mol cm<sup>-3</sup>), and  $\omega$  is the electrode rotating speed expressed in rps. The values for  $n$  are presented in **Table 3-2** and small shifts in the electron transfer value from literature, considering the same material as utilized herein, can be seen, indicating a concomitant production of H<sub>2</sub>O<sub>2</sub>.

Under hydrodynamic control, the low pulse cured sample does not behave according to the Koutecky-Levich conditions. Hence, it is not possible to estimate the number of electrons transferred for this sample. It is possible to see in **Figure 3-10** (green curve and right inset) that, at higher rotation rates, the current is smaller than at lower rotation rates. This could indicate that the cured layer has still polymer embedded leading to a lower mechanical attachment to the electrode during rotation and material is lost.

**Table 3-2** Transfer electron number for different electrode preparation methods.

<i>Co<sub>3</sub>O<sub>4</sub>/N-rGO/GC electrode</i>	<i>Electron number</i>
<i>oven cured</i>	3.89
<i>low pulse</i>	N/A
<i>medium pulse</i>	3.34
<i>high pulse</i>	3.46

It could be caused by the processing route utilized to obtain the CL. The Koutecky-Levich plots obtained for the studied CL can be found in **Figure 3-10**. It is possible to see that under hydrodynamic control the behavior of the CL is different from static conditions (**Figure 3-10** left inset). Despite the good mechanical adhesion during static conditions, for measurements utilizing rotation the electrodes have some material lixiviated. The chosen potential for extracting the values was 450 mV vs. RHE.

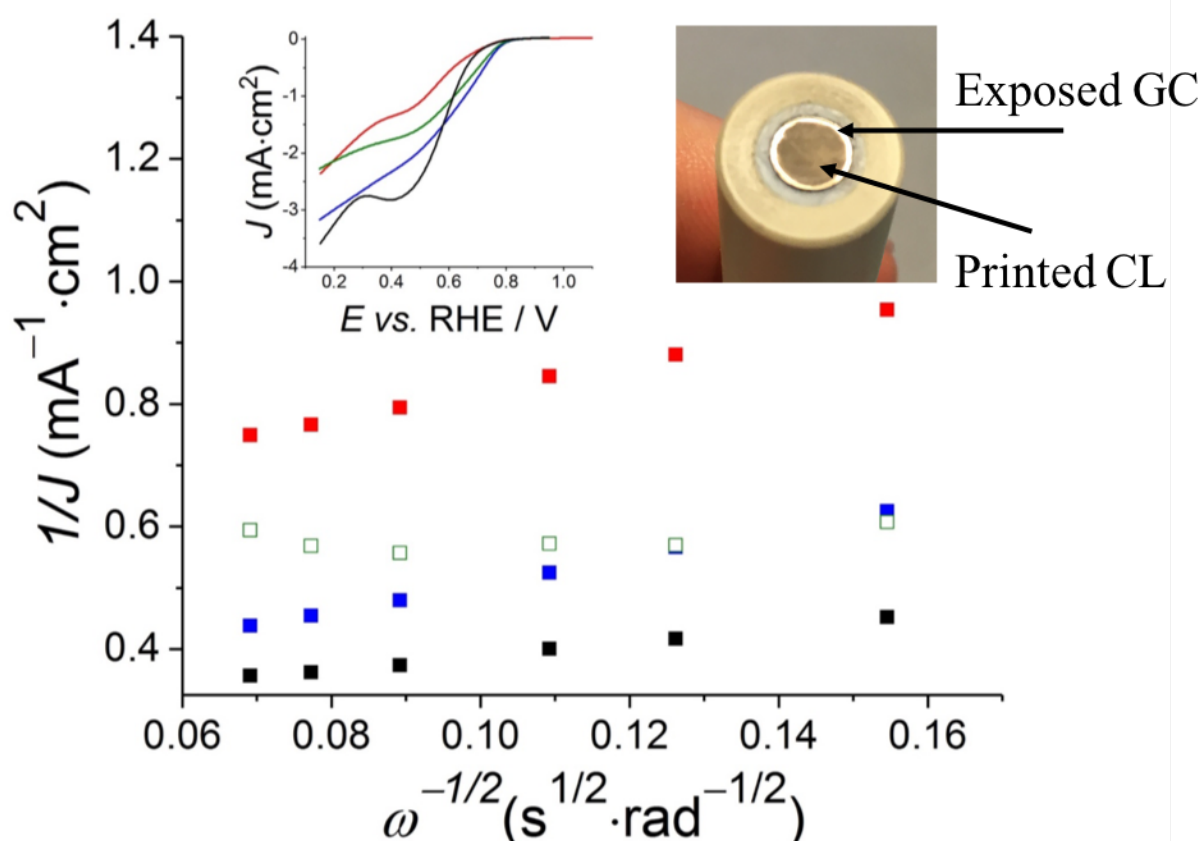


**Figure 3-10.** Koutecky-Levich plots for oven-cured and photonic-cured CLs. Left inset LSVs at 1600 rpm for the ORR of inkjet-printed and post-processed CLs of  $\text{Co}_3\text{O}_4/\text{N-rGO}$  (LSVs not  $iR$ -corrected). Right inset, RDE after measurement with the low pulse CL, demonstrating material removal. Oven cured (black), low pulse (green), medium pulse (red) and high pulse (blue). Experimental conditions: Oxygen-saturated 0.1 M KOH, scan rate  $5 \text{ mV}\cdot\text{s}^{-1}$

### 3.4 Conclusions

In conclusion, combined inkjet printing and photonic curing as potential large-scale platform for the fabrication of  $\text{Co}_3\text{O}_4/\text{N-rGO}$ -based catalyst layers was applied. Inkjet printing allowed the accurate deposition of a formulated catalyst ink resulting in precise catalyst loadings on glassy carbon substrates. In order to get a printable  $\text{Co}_3\text{O}_4/\text{N-rGO}$  dispersion, polyvinylpyrrolidone and ethyl cellulose were added to the ink as stabilizers. In order to remove the stabilizers, the ink solvents were evaporated, generating well-adhered CLs.

Thermal post-processing was performed using traditional oven curing and photonic curing. The duration of the photonic curing process was only 75 s compared to 3 h that was applied for oven curing. The CLs after oven curing and photonic curing with three different flash light intensities were analyzed spectroscopically and electrochemically. The  $\text{Co}_3\text{O}_4$  nanocrystals grew from  $\sim 7$  nm to nearly  $\sim 15$  nm, independently of the applied curing tool. While during oven curing the oxidation states of Co were kept at (II,III), photonic curing above  $\sim 2 \text{ J}\cdot\text{cm}^{-2}$  resulted in the reduction of  $\text{Co}_3\text{O}_4$  to CoO. CoO/N-rGO showed a lower activity for the ORR than  $\text{Co}_3\text{O}_4$ /N-rGO. Photonic curing below  $\sim 10 \text{ J}\cdot\text{cm}^{-2}$  did not remove all the stabilizers, from which the catalytic activity suffered.

This work shows that ink formulation, printing and photonic curing processes need to be well adjusted to each other in order to fulfill the requirements of fast printing, fast post-processing and high catalytic activity of new electrocatalyst materials in mesoporous catalyst layers. The present printing concept can be extended to further catalyst materials deposited on graphene sheets and its derivatives, as long as they can be dispersed into an ink. In order to achieve multi-layers for sufficient catalyst loadings, the number of printing passes can be increased. Furthermore, ion conducting materials, such as Nafion, can be printed subsequently to approach a catalyst layer closer to the ones applied in fuel cells<sup>219</sup>.



# Chapter 4 Print-Light-Synthesis of noble metal nano-electrocatalysts

This chapter is based on the work adapted from *Adv. Mater. Technol.* **2018**, 3 (2), 1700201, by A. Lesch. The work was herein extended to glassy carbon substrates as alternatives to the transparent but less conductive indium-tin oxide coated glass slides. Victor Costa Bassetto contributed with the development of applying the technique Print-Light-Synthesis on glassy carbon electrodes.

## 4.1 Abstract

In this chapter, Pt nanoparticles were synthesized on glassy carbon (GC) substrates as an extension of the work done previously in the group on ITO substrates. The utilization of GC substrates was done in order to develop further the range of suitable substrates and electrochemical characterization possibilities. The GC substrate has several different characteristics than ITO, however the most relevant is the higher thermal dissipation coefficient. ITO substrates are a thin layer of ITO deposited over glass, therefore, over high energy irradiation, such as the ones utilized in PLS, the ITO substrate can crack as presented by Lesch.<sup>116</sup> Therefore, the utilization of GC can be crucial for further developments of PLS for nanostructured catalysts. GC plates are further cheaper for long-term studies, because they are simpler to prepare and renew, e.g. by mechanical polishing, for reuse. For the fabrication, a combined inkjet printer and photonic curing platform was utilized. The process took place under ambient conditions, *i.e.* at air and under room temperature, without the necessity to work in a reactor as wet synthesis methods require. A platinum containing salt (chloroplatinic acid) was dissolved in a water alcohol mixture to adequately meet the physicochemical properties of the solution



to the printing process. By the ink preparation and by modifying the printing parameters, the loading of the Pt precursor on the substrate was controlled. The fast evaporation of the main ink solvents left thin liquid films of the precursors on the substrate. Photonic curing, here in form of light pulses as short as 330  $\mu\text{s}$  was applied to induce the thermal reduction of the Pt precursor into metallic Pt nanoparticles. The precursor coverage was only 1  $\mu\text{g}/\text{mm}^2$  with an ink volume in the lower nanoliter range. The synthesized nanoparticles were spectroscopically and electrochemically characterized, which confirmed the complete conversion of the Pt precursor into Pt metal and the electrochemical activity of the fabricated electrodes was investigated.

## 4.2 Introduction

Through this thesis the utilization of inkjet printing in order to fabricate catalyst materials of interests in energy conversion devices was explored. In this chapter we describe the fabrication of metal nanostructures on diverse substrates through the recently developed Print-Light-Synthesis method. As presented in Chapter I, Pt is one of the most studied electrocatalysts in the field of energy conversion. Pt based materials play a central role in technologies for electrical mobility based on hydrogen, which are Polymer Electrolyte Membrane Fuel Cells (PEMFCs). Pt-based electrocatalysts are utilized to overcome the sluggish kinetics of the oxygen reduction reaction (ORR).<sup>29,53,220–225</sup> Due to high relevance in future economy, Pt based electrocatalyst synthesis methods have extensively been investigated and many methods have been described, similarly to the ones presented in Chapter 5 for the fabrication of NiFe nanostructures. The majority of the proposed methods share the thermal reduction of the catalyst particles under well controlled conditions to obtain the desired nanomaterial.<sup>226,227</sup> In addition, due to the high degree of control required for the synthesis process, scaling up the fabrication of the desired nanostructure is challenging, especially when considering contaminants and capping agents utilized in the synthetic process interfering with the further application of the electrocatalyst.<sup>18,91,228–230</sup>

Besides all the particularities in nanoparticles synthesis and scaling up another point of concern is the fabrication of the catalyst layer containing the nanoparticulated electrocatalyst. The transfer of the nanocatalyst material from the as-synthesized-form to an active catalyst layer normally involves a dispersion step. For instance, as discussed in Chapter 3 the adequate dispersion of catalyst particles in an ink is necessary prior to the fabrication of the CL. However, the downside of this methodology is the undesired particle modification with the components utilized to stabilize the dispersion.<sup>121,123,231</sup> Therefore, a suitable alternative is the utilization of hyphenated technologies, such as inkjet printing with photonic curing for both synthesis of new electrocatalyst materials and the production of catalyst layers in a single step. In order to achieve such conditions, it is necessary to utilize inks that do not contain nanoparticulate materials, but dissolved precursor salts. The substitution of nanoparticles by metal salts eliminate the undesired effects of working with nanoparticulated inks that can block the nozzles of the printheads. Hence, it is possible to obtain the major advantage on making a two-step device fabrication simpler, by eliminating the initial and time-consuming nanoparticle synthesis. With advanced printers and the possibility of parallel printheads, also combinatorial electrocatalyst libraries can be printed, facilitating the screening for their catalytic performance using various established electrochemical and spectroscopic analytical techniques.<sup>126,127,232,233</sup>

The conversion of Pt precursors salts into Pt metal is achieved by thermal decomposition, *i.e.* the thermally induced reduction of the Pt precursors and gaseous side products. In the case of the presented chapter the reduction is obtained with light pulses from a Xenon flash lamp, a process known as flash light sintering or photonic curing. This methodology is based on a Xenon flash lamp that can irradiate light with energy densities of several J/cm<sup>2</sup>. When the substrate is coated with a thin layer of nanoparticles, molecules or precursor salts that will absorb light of different wavelengths, the layer can heat up to several hundred degrees within a fraction of a second causing a rapid thermally induced process, such as sintering or thermal decomposition. Photonic curing is mainly used with the goal to create homogeneous and compact conductive films from nanoparticles and precursors, such

as Cu<sup>134,173</sup> or Ag,<sup>234</sup> but is rarely applied for the fabrication of separate nanoparticles as applied for analytical and catalytic applications.

In addition to the direct heating of the precursor salts, solid nanostructures, such as carbon nanotubes or metallic nanoparticles, can absorb the light, increasing the surface temperature and, by conduction, will heat up the surrounding precursors. In this way these particles act as absorber-to-heat converters. Recently, Kim and co-workers used metal, metal alloy and metal oxide precursors on carbonaceous substrates.<sup>205,235</sup>

In this chapter, the rapid fabrication of Pt nano- and microstructures on glassy carbon by combining efficiently inkjet printing and photonic curing of a chloroplatinic acid-based ink is presented (**Figure 4-1**). The objective is to prepare two-dimensional electrode patterns that can potentially be used for catalyst screening or in devices requiring Pt nanoparticle-decorated electrodes.

The conversion was obtained by the selective light absorption of the precursor film and subsequent conversion into metal. Inkjet printing has been chosen to deposit various precursor loadings with high precision in order to identify the film properties for a successful photonic curing process. Glassy carbon has been selected because of its well-known electrochemical response and has been widely used as support in electrocatalysis for material studies.

The ink volumes applied, in this work, for square millimeter sized areas were in the lower nL range.

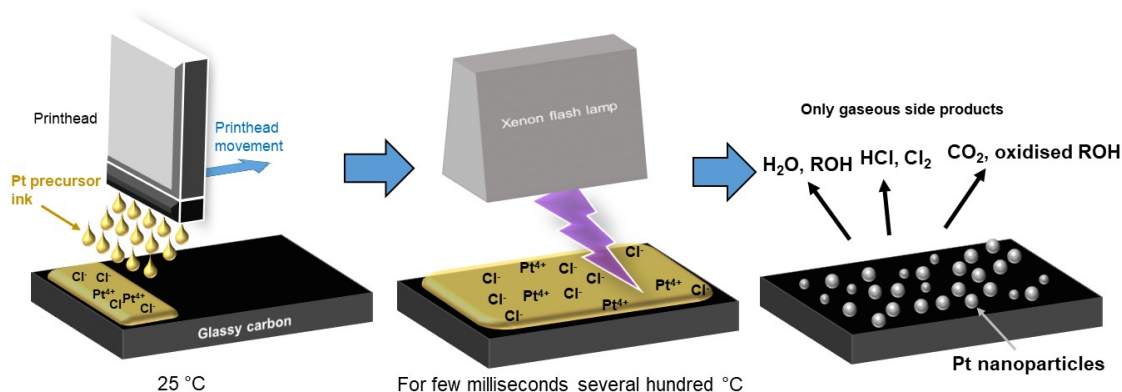


**Figure 4-1** Schematic representation of Print-Light-Synthesis of Pt nanoparticles and nanostructures on a glassy carbon electrode.

### 4.3 Results and Discussion

A successful inkjet printing process is linked to the proper adjustment of the ink as discussed in Chapter II. In the work presented in this chapter a mixture of water, isopropanol and 1,2-propanediol in equal parts was utilized as ink media. This specific solvent mixture was utilized for the following: control ink drying time and  $\eta$  with the utilization of 1,2 propanediol, adjust  $\gamma$  with the addition of isopropanol and increase the precursor salt solubility in the ink with water. The printable range is between  $1 < Z < 10$  as described in Chapter II, and this solvent mixture had a  $Z$  value of 5.6, which is almost in the center of ideal value for printing.<sup>155</sup> In fact, stable jetting of  $\sim 17.3$  pL droplets was obtained (**Figure 4-2 a**) by applying a custom designed voltage signal to the piezoelectric actuators of the printhead. The picture shows the stability of jetting for seven consecutive nozzles, characterized by the nearly perfect parallel falling of the droplets and their similar falling speed (*i.e.* similar height of the droplets in the picture). In fact, 50 mg of the Pt precursor  $\text{H}_2\text{PtCl}_6 \cdot x\text{H}_2\text{O}$  could be easily dissolved in 1 mL of the ink (**Figure 4-2 b**) resulting a slightly yellowish colored solution. After printing, a wet film of Pt precursor was formed on GC (**Figure 4-2c**). The inhomogeneity arose due to the previously not sufficiently polished GC plate, leaving a shiny surface to the eye, but with inhomogeneous wetting ability. The location of a circular Pt precursor pattern is shown in white in **Figure 4-2c**. By photonic curing, the wet film transformed into a solid structure (**Figure 4-2c**) due to the decomposition of  $\text{H}_2\text{Pt}^{\text{IV}}\text{Cl}_6 \cdot x\text{H}_2\text{O}$  into  $\text{Pt}^0$  and gaseous side products. The film was well adhered and could not be removed by rinsing with DI water. On ITO it was reported that the Pt patterns were composed of nanoparticles and their aggregates.<sup>116</sup> A laser scanning microscope image of a drop-casted and photonic cured pattern (**Figure 4-2d**) shows the bare GC surface (right part) and a mix of smaller particles with larger, *i.e.*, micrometer aggregates, suggesting similar nanostructures on the GC substrate compared to ITO.<sup>116</sup>

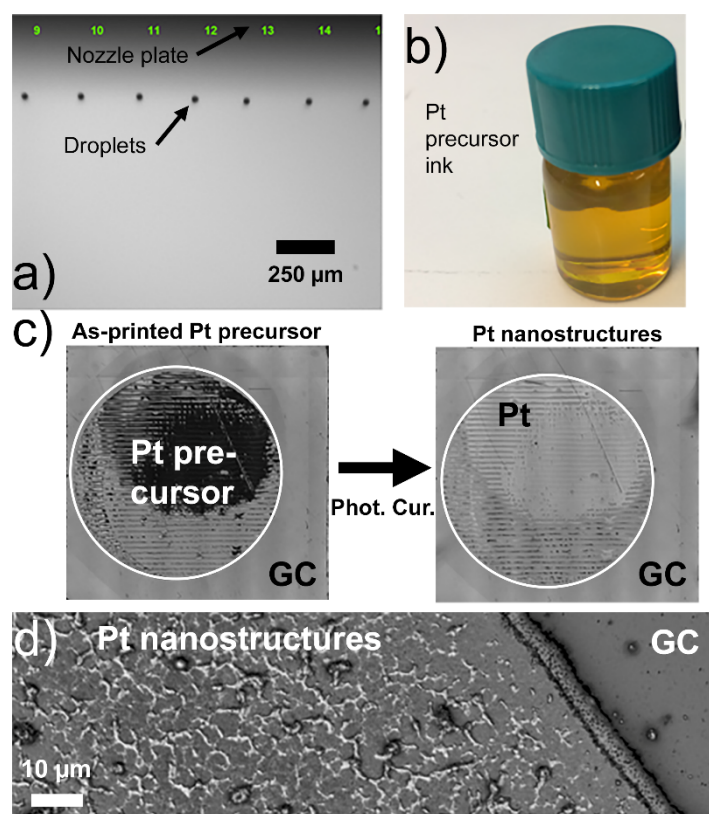


**Figure 4-2** a) Droplets of the Pt precursor ink generated from seven exemplary parallel nozzles. b) Photograph of the Pt precursor ink. c) Printed Pt precursor ink in the shape of a circle (5 mm diameter) on a GC plate before (left) and after (right) a 330  $\mu\text{s}$  flash lamp pulse with  $(3.52 \pm 0.03) \text{ J/cm}^2$ . Please note that heterogeneity in the layer appearance is due to the GC plate surface. d) Laser scanning micrograph of a Pt nanostructure on GC, obtained by drop casting and photonic curing (330  $\mu\text{s}$  pulse,  $(3.52 \pm 0.03) \text{ J/cm}^2$ ).

The characterization of the Pt precursor conversion into chloride-free Pt nanoparticles was executed utilizing the ITO substrates. Patterns of  $1 \text{ mm}^2$  were printed each with 3'050 droplets. The fabrication of the particles was executed through the procedure described by Lesch<sup>116</sup>. The printed patterns consumed 52.8 nL of ink, leading to a loading of  $1.03 \mu\text{g}$  of Pt and took 60 seconds to fabricate. Directly after printing on the ITO glass, the printed pattern liquid film appeared almost transparent (**Figure 4-3**). To avoid fast drying, precipitation of the salt and formation of regions with high concentration of Pt precursor, the ink formulation included a low vapor pressure solvent (1-2-propenodiol) therefore it was possible to control the pattern drying. The pattern achieved a homogeneous thin film of liquid after 10 minutes (**Figure 4-2, middle**). After drying, the printed film revealed a strong yellow colour and the delimiting borders of the patterns appeared more defined. The thin

film thickness is a relevant factor for the conversion of the precursor to nanoparticles. In case of a thick layer less light would be absorbed and the liquid would have a quenching effect on the temperature of the precursor layer.

Chloroplatinic acid in standard methods for thermal decomposition (*i.e.* furnace with temperature ramp) decomposes at temperatures above 500 °C. The decomposition leads to the formation of metallic platinum, water and chlorine.<sup>236,237</sup> Therefore, one can only assume that if the precursor salt is decomposed to metallic particles, the pattern has reached at least 500°C during the light sintering process. This process consisted in a single pulse of  $3.52\pm 0.03 \text{ J}\cdot\text{cm}^{-2}$  during 330  $\mu\text{s}$  (**Figure 4-3 a, right**).

In order to reach the decomposing conditions, the energy emitted during the flash is absorbed by the thin film containing the Pt precursor salt. This is demonstrated in **Figure 4-3b** where the overlap of the emission and absorption spectra is given between 300 and 500 nm. In contrast, the substrate utilized in this case was ITO (transparent substrates allow analysis in the UV/Vis spectrophotometer) has very low overlap between the absorption and emission spectra. For this reason, it is suggested that the decomposition of the Pt precursor is given by the direct absorption of the energy irradiated from the broad spectrum Xenon flash lamp. The same applies to the substrate of borosilicate glass, as the low absorption beyond 300 nm would not lead to any significant heat induced by the lamp emission.

The obtained Pt patterns appeared homogeneous and mainly as well-defined squares. ITO is a challenging surface for printing and can result in lateral pattern shrinkage during ink drying, this phenomenon will be discussed further in this chapter. In such case, the flat and squared ink pattern contracts towards the center of the printed pattern in case of a mismatch of ink surface tension and surface free energy of the substrate.

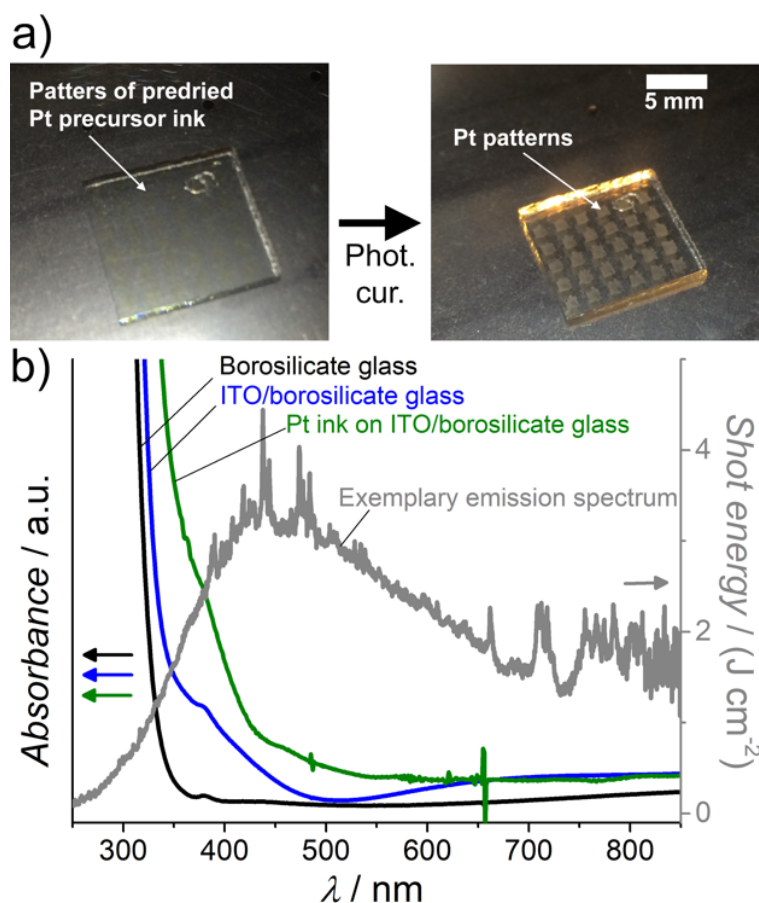


**Figure 4-3** a) 30 inkjet-printed squares of Pt precursor salt ( $1 \text{ mm}^2$ ) on indium-coated borosilicate glass after printing with 5 min drying time at  $54 \text{ }^\circ\text{C}$  (left) and after photonic curing using a  $330 \text{ }\mu\text{s}$  short light pulse with  $(3.52 \pm 0.03) \text{ J/cm}^2$  shot energy density (right). b) Absorption spectra of bare borosilicate glass slide (black), ITO-coated borosilicate glass slide (blue) and Pt ink on ITO-coated borosilicate glass slide (green) prior to photonic curing. Photographs and data kindly provided by Dr. Andreas Lesch.

In order to study the decomposition of the chloroplatinic acid energy dispersive x-ray (EDX) spectroscopy was initially used. Pt and Cl were clearly present in the sample not subjected to irradiation in contrast to the sample after irradiation, where the almost absence of the Cl peak indicated the almost full conversion of chloroplatinic acid to Pt (**Figure 4-4a left and right respectively**). Further in spectroscopy characterization the converted patterns were analyzed with X-ray diffraction (XRD) and the four characteristic Pt peaks, corresponding to the Pt facets are present (**Figure 4-4b**). The encountered diffraction angles were:  $39.87^\circ$  (111),  $46.37^\circ$  (200),  $67.61^\circ$  (200) and  $81.46^\circ$  (311). The last spectroscopy technique employed in the characterization was X-ray photoelectron spectroscopy (XPS) and the spectrum is presented in **Figure 4-4c**. The XPS analysis confirmed the absence of Cl

with no distinguished peaks of Cl in the typical position of Cl 2p<sub>3/2</sub> (Cl 2p<sub>1/2</sub>) 198.5 eV (+ 1.6 eV for spin split).<sup>[28]</sup> Pt peaks are well defined and show in the Pt 4f region a clear peak for Pt 4f<sub>7/2</sub> (Pt 4f<sub>5/2</sub>) at 70.4 eV (73.69 eV,  $\Delta = 3.29$  eV). This confirms the conversion to Pt in consequence of irradiation. Moreover, the shift of the peak in relation to literature indicated that not only the conversion occurred, but the Pt is in metal form.

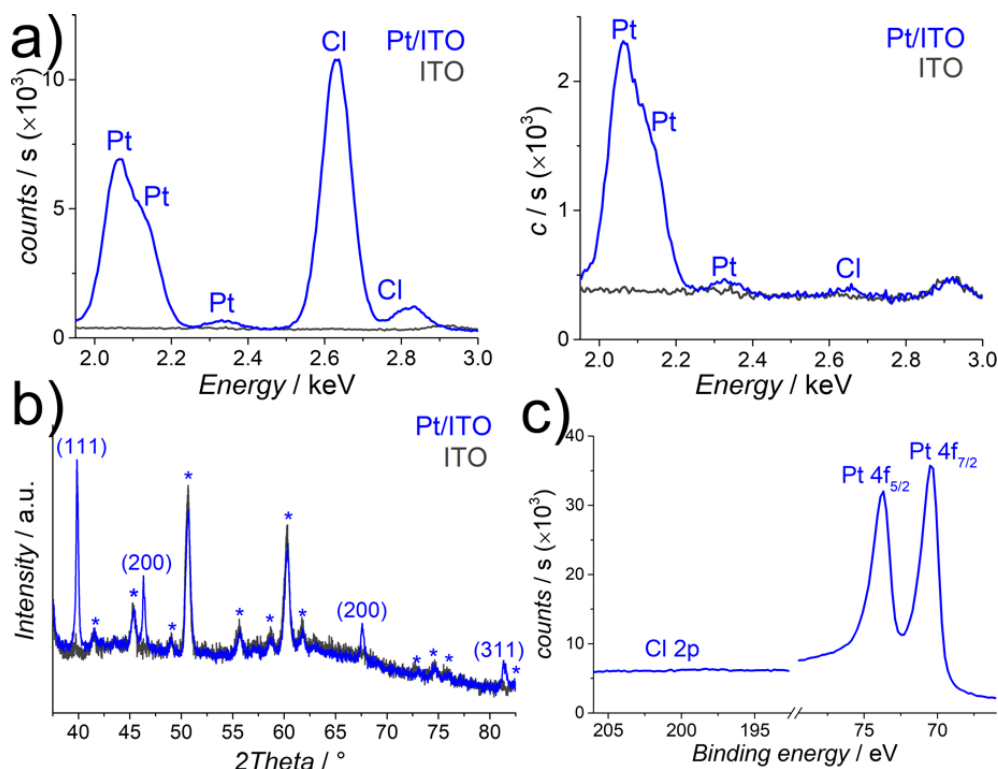


**Figure 4-4** a) Scanning electron microscopy – energy dispersive x-ray (SEM-EDX) spectroscopy analysis of inkjet-printed Pt precursor ink before (left) and after (right) photonic curing. Substrate: Indium tin oxide-coated glass slide. b) Bragg Brentano X-ray diffractometry (BBXRD) patterns of bare ITO glass substrate (grey) and the Pt nanostructures (blue) on the ITO-coated glass. Peaks marked with an asterisk correspond to ITO. c) X-ray photoelectron spectroscopy (XPS) spectra of the Pt nanostructures on the ITO-coated glass slide, focus is on Cl 2p and Pt 4f. Data were kindly provided by Dr. Andreas Lesch and published in reference <sup>116</sup>.

Continuing the characterization of the Pt/ITO electrodes, scanning electrochemical microscopy (SECM) with soft probes was used to investigate the conversion of the Pt precursor salt into a Pt nanoparticle-coated thin film. The Pt coated areas should provide faster redox mediator regeneration kinetics and thus higher feedback mode currents. SECM is an electrochemical scanning probe



microscopy technique that is applied to investigate the surface activity of a given sample by scanning a microelectrode in close proximity (several  $\mu\text{m}$  distance) to the sample surface that is immersed in an electrolyte solution.<sup>238</sup> Redox active species in the solution are reduced or oxidized at the microelectrode and sample allowing the identification of local variations in the reaction kinetics at the sample. The redox active species diffuse between microelectrode and substrate, which as a result requires a constant working distance.<sup>239</sup> The SECM tips are typically metal or carbon disc microelectrodes, embedded in an insulating mantle. Measurements are then normally carried out in constant height mode on flat and smooth surfaces guaranteeing a constant working distance.<sup>239</sup> In case of tilted and curved surfaces, the microelectrodes can contact the substrate surface and damage the sample under investigation or, even more problematic, break themselves.<sup>201</sup>

Therefore, for samples which are topographically challenging, soft microelectrodes have been developed by Girault and co-workers.<sup>240</sup> In this case, the glass insulated electrode is substituted by a thin ( $<100\ \mu\text{m}$ ) polymer-based probe with embedded carbon paste microelectrode that can slightly bend and be operated in contact with the surface, thus sliding on the surface with a constant working distance. Contact mode SECM is well described in literature and demonstrates the possibility of imaging various kind of samples from solid conductive and well defined to biological samples of diverse stiffness and topography.

The principle underlying the measurement in **Figure 4-5** is that, for each chosen point (step), a signal is sampled (for the current corresponding to the oxidation of FcMeOH at the microelectrode), and the combination of the results are reconstructed to form an image that describes the surface reactivity towards the electrochemical reaction used as a probe. The SECM measurement mode employed in this measurement is the feedback mode. This mode is characterized by the differential feedback response to the oxidation/reduction of the redox mediator utilized (FcMeOH) over an unbiased substrate immersed in solution. When the microelectrode is placed in close proximity above nonconductive/insulating surfaces the FcMeOH oxidized in the microelectrode tip is not reduced. In addition,

as the electrode is in close proximity of the substrate the diffusion of FcMeOH from the bulk is hindered. Therefore, the currents read are very low, limited to the oxidation of FcMeOH in the diffusion layer in the vicinity of the electrode. However, over conductive substrates, the FcMeOH<sup>+</sup> is reduced back to FcMeOH and a feedback condition is established. As high is the conductivity of the substrate, more FcMeOH will be regenerated at the sample and available in the diffusion layer of the microelectrode to be oxidized, leading to higher current values to be measured at the microelectrode.

For the Pt/ITO sample, it was investigated the contrast of the electrochemical reactivity of Pt and ITO in the redox cycle of FcMeOH (redox probe). The reactivity contrast (current contrast) originates from the fact that Pt has a higher capacity to reduce the oxidized FcMeOH than the ITO surface, which can be seen in the figure with the higher intensity of current over the regions where the Pt pattern was located, proving the higher conductivity of the printed pattern. This is one indicative of the conversion of the Pt salts to Pt nanostructures over the ITO surface. In addition, it is possible to discuss the effects of the shrinkage of the printed pattern before the conversion. Despite the low coverage of material in the surrounding areas of the printed pattern, due to pattern shrinking, it was still possible to analyse the remaining material, and observe it is converted. Proving that Pt patterns are bigger than what is possible to measure with the optical microscope. Such information is useful for understanding the effects in resolution of the printed pattern and reactivity. Analyzing one printed pattern, it is possible to see that in the surrounding areas of the pattern the conductivity is higher than the bare ITO substrate. The peak reactivity is reached on the Pt surface. The roughness, in contrast, can be attributed to a variation in the Pt loading through the printed pattern. The use of carbon soft probes, similarly to the finding in Chapter III, opened the possibility for further developments in the Soft Probe SECM scanning of catalyst layers. At the current stage it is possible to scan printed sensitive electrodes.

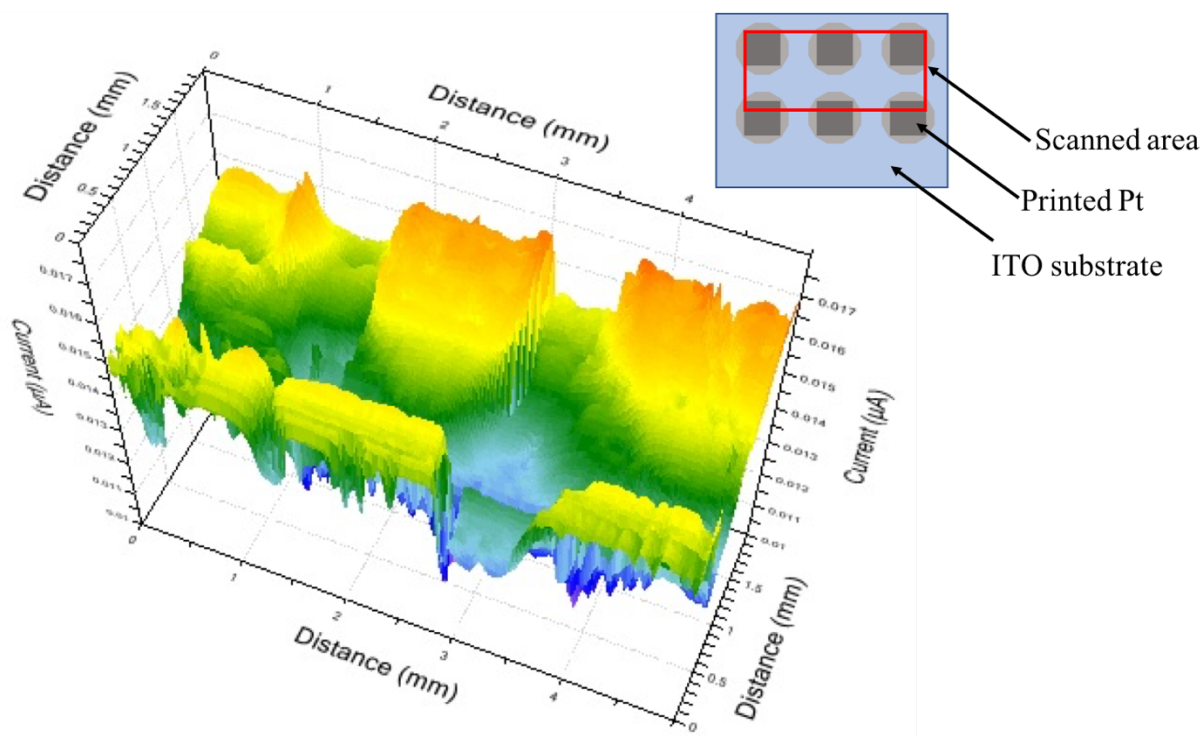


**Figure 4-5.** Soft-Probe-SECM feedback mode image of the catalyst patterns using a soft carbon microelectrode in contact mode. Experimental conditions: 2mM FeMeOH and 0.1 M KNO<sub>3</sub>, Potential at microelectrode: 0.4 V, sample was un-biased, step size in *x*- and *y*-direction 25 µm, probe translation rate 25 µm·s<sup>-1</sup>, scan direction from right to left.

As discussed above, two substrates were chosen, GC and ITO. GC is one of the most used electrode support material, which can be attributed to the wide potential window (both in acidic and alkaline electrolyte), stability and cost. Present below in **Figure 4-6a** we have the evolution the cyclic voltammograms during the activation procedure. First, in the region of Pt oxidation (1.0 V vs Ag/AgCl), the vertex current decreases with cycling and a wave corresponding to Pt oxidation becomes more pronounced. This fact can be attributed to the final conversion (reduction) of the precursor salt to Pt, leading to an increase conductivity on the pattern. In the anodic scan, observed at 0.5 V (vs. Ag/AgCl) is the formation and increasing with cycling of the peak corresponding to Pt oxides reduction. With cycling, as for the oxidation, the overpotential decreases, as a consequence of the increasing in conductivity of the pattern. In the region between 0 and -0.25 V (vs Ag/AgCl) we have the region of hydrogen atoms adsorption (cathodic) and desorption (anodic). **Figure 4-6b** presents

the 20<sup>th</sup> potential cycle of the Pt/GC electrode. Due to the cycle characteristics it is possible to conclude the after cycling the Pt nanoparticles deposition in the GC Print-Light sintered electrode has the same activity and traditional CV as normal polycrystalline Pt.

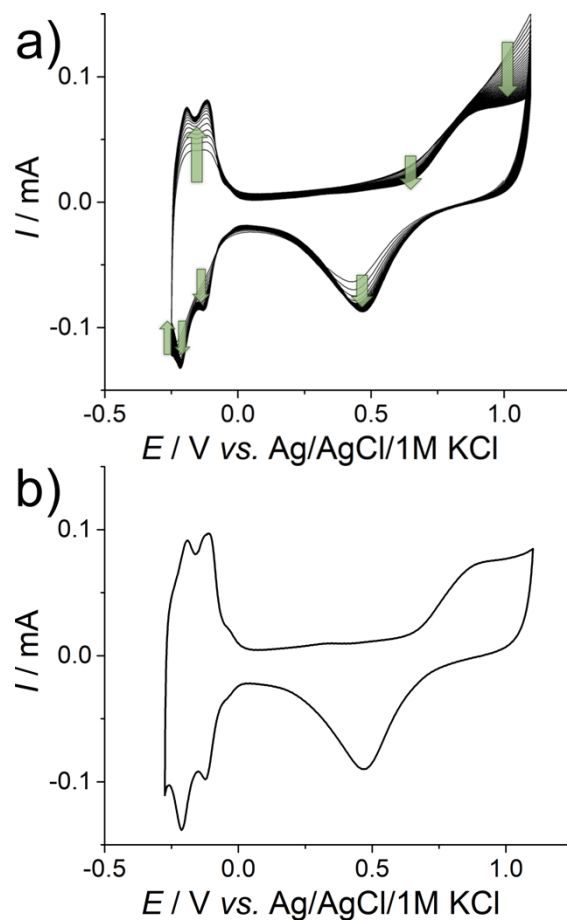


**Figure 4-6.** Electrochemical characterization of the Pt/GC electrode obtained by Print-Light-Synthesis. a) 42 activation cycles, 50 mV/s. b) Activated Pt/GC electrode, 50 mV/s. All experiments were carried out in 0.1 M HClO<sub>4</sub>.

## 4.4 Conclusion

Print-Light-Synthesis has been successfully applied for the fabrication of noble metal electrocatalysts. It was possible to obtain Pt decorated GC substrates in a fast process, less than 10 minutes which principally can be reproduced from mm<sup>2</sup> to m<sup>2</sup> without any process alteration. The fact that the ink contains no nanoparticles simplified the printing step of the process and decreased the material waste. The simplification is attributed to the fact that no purging and cleaning steps were necessary and no nozzle clogged during the fabrication process. Therefore, all the utilized ink was recovered in

the printed patterns. The obtained loading on the substrate was of  $1 \mu\text{g}/\text{mm}^2$  with just few nL printed. The results presented in this chapter sum to previous results indicating the viability of employing inkjet printing as a fabrication tool from electrocatalyst screening to catalyst layers development. The simplified synthesis and fabrication procedure needs further developments to achieve a higher degree of control in particle size and shape. Yet, the promising results presented so far indicates the viability to explore this technique.



# Chapter 5 Print-Light-Synthesis of Ni and NiFe-nanoscaled electrodes for oxygen evolution reaction

This chapter is based on the work adapted from: : Victor Costa Bassetto, Mounir Mensi, Emad Oveisi, Hubert H Girault, Andreas Lesch – ACS Appl. Energy Mater. (2019), 2, 6322 - 6331 in which Victor Costa Bassetto contributed with the ink formulation, inkjet printing and curing procedures. He further conducted the TGA experiments and electrochemical characterization. Together with Dr. Emad Oveisi, was responsible for the STEM characterization.

## 5.1 Abstract

Ni- and NiFe-based nanocatalyst coated electrodes are prepared as oxygen evolution catalysts by merging large-scale electrode fabrication and nanoparticle synthesis into one process. This is realized by a hyphenated inkjet printing and flash light irradiation platform. Inkjet inks, containing Ni and Fe chloride in adjustable ratios, are printed leading after light-induced thermal decomposition to Ni and NiFe-based nanoparticles of less than 2.5 nm in diameter. The role of a light absorbing support layer, here carbon nanotubes, and the synergistic role of mixing Fe and Ni precursors for the complete light-induced precursor conversion are discussed. The entire fabrication process based on the reproducible deposition of nanoliter ink volumes (reaching  $<2 \mu\text{g}\cdot\text{cm}^{-2}$  metal precursor salt) is operated under ambient conditions, requires only few minutes and is up-scalable to the industrial fabrication level. After Print-Light-Synthesis, electrochemical activation, *e.g.*, by potential cycling, leads to catalytically active Ni- and NiFe-based nanoelectrocatalysts with onset potentials as low as 240 mV (at  $0.1 \text{ mA}\cdot\text{cm}^{-2}$ ), overpotentials of 334 mV (at  $10 \text{ mA}\cdot\text{cm}^{-2}$ ), Tafel slopes of  $41 \text{ mV}\cdot\text{dec}^{-1}$  and high turnover frequencies of up to  $6.53 \text{ s}^{-1}$  for the oxygen evolution reaction.

## 5.2 Introduction

The low-cost, large-scale production of two-dimensional and three-dimensional electrodes containing functional nanomaterials finds important applications in numerous fields ranging from biosensing<sup>138,241,242</sup> to energy conversion and storage<sup>130,219,243</sup>. The nanomaterials act often as electrocatalysts to increase the rate of chemical reactions for sensing as well as energy conversion. The nanocatalysts are generally supported on carbonaceous materials for reasons of (electro)chemical stability of the nanoparticles (NPs), mechanical stability as well as electronic conductivity of the electrode structure, and provision of sufficiently large surface area of the electrocatalyst.

For instance, nanostructured catalysts on nanocarbon supports play an important role in energy conversion devices, such as polymer electrolyte membrane (PEM) electrolyzers, in which they are implemented into two mesoporous, three-dimensional catalyst layers, separated by the PEM, to promote water splitting<sup>244</sup>. Two half reactions, known as hydrogen evolution reaction and oxygen evolution reaction (OER), are involved. For the latter, IrO<sub>2</sub> and RuO<sub>2</sub> are the state-of-the-art electrocatalyst materials<sup>245</sup> but their long-term implementation is impeded by their high costs and scarcity. As the demand for electrochemical hydrogen generating systems, with OER on the counter electrode, is continuously raising in the growing hydrogen economy, tremendous efforts have been made to either increase the efficiency of the utilized catalyst amounts or to replace Ir and Ru by abundant materials, such as Ni, Co, Fe and their alloys<sup>243,246–249</sup>.

Oxygen evolution is based on the formation of an oxygen-oxygen bond due to a four-proton electron transfer process, which represents a kinetically sluggish reaction.<sup>250</sup> NiFe-based nanocomposites have been shown to be a promising candidate for the OER<sup>251,252</sup> and a wide range of metal ratios, shapes, sizes and catalyst supports have been reported<sup>253–257</sup>. Especially layered double hydroxides of Fe and Ni found recent attention<sup>258</sup>. NiFe-based materials are synthesized by reducing their precursor salts in chemical and thermally driven processes. Chemical reduction is achieved by the sol-gel method<sup>259</sup> or by electrochemical<sup>40</sup> and electroless deposition<sup>260</sup>. The latter can require



that the 2D or 3D catalyst supports have already been prepared. Further, these methods do not provide high throughput, as the process is limited to the active support area and deposition time. The thermal route can be realized using solvothermal synthesis in solution or thermal decomposition under gas atmosphere, which can produce larger amounts of material in the form of dispersed NPs or powders. Many of the corresponding chemical reactions require the accurate control of process conditions, such as temperature, pressure and atmosphere<sup>261</sup>.

The growth of NPs in solution is further controlled by the use of capping agents that functionalize the NPs and block their further growth as well as their agglomeration<sup>262</sup>. The capping agents should be removed after the synthesis, as they can adsorb strongly on the electrocatalyst surface altering the catalytic activity<sup>263</sup>. Such procedure can require harsh chemical and temperature conditions affecting the initial electrocatalyst properties. After the synthesis, the materials need to be transferred onto electrode supports by drop casting or pasting for electrochemical and spectroscopic characterization, which generally requires the addition of binders, such as Nafion, for the adhesion of the layer to the support. For the implementation into electrochemical reactors, as-synthesized catalyst powders need to be dispersed to form processable inks and pastes for spraying and printing-based methods. These standard methods can allow flexibility, but are often limited to low throughput, require advanced reaction conditions or are based on multi-process steps, which together make the industrialization complex.

We have recently introduced a combination of device fabrication and nanoparticle synthesis by hyphenating inkjet printing and flash light irradiation<sup>116</sup>. Inkjet printing allows the precise and rapid deposition of low concentrated inks achieving nL/mm<sup>2</sup> ink coatings while the use of a flash lamp can heat thin layers up to several hundred degrees within a fraction of a second, notably being operated under ambient conditions and decomposing metal precursors into nanoparticles<sup>135</sup>. This concept, called Print-Light-Synthesis, enabled for instance the large-scale production of Pt-nanostructured indium-tin oxide electrodes for energy research<sup>116</sup>. The use of printheads that contain hundreds

of parallel nozzles and eject droplets with kHz frequency allows both printing of small test samples for characterization purposes and, by using the same parameters, producing devices on the industrial scale. Furthermore, the use of parallel printheads and digital droplet deposition software enables the accurate mixing of precursors generating multi-functional material composites and gradients of those.

Flash light sintering, also known as photonic curing or pulsed light irradiation, delivers within a fraction of a second onto a closely positioned substrate up to several Joules per cm<sup>2</sup> of light energy. The wavelength range is from approximately 300 to above 800 nm, enabling many light absorbing materials to be sufficiently heated up. Flash light irradiation is generally applied in printed electronics to form conductive traces from nanoparticulate films by removing ink solvents, degrading polymeric and ink stabilizing additives and sintering the NPs. The rapid generation of several hundred degrees in thin films has further enabled the thermally induced reduction of metal oxides into metals, such as Cu from CuO<sup>171</sup>, but also the thermal decomposition of metal salts into metallic and alloyed nanoparticles, such as Co<sup>264</sup>, Pt<sup>116</sup>, PtRu<sup>235</sup> or Cu<sup>134</sup>. The mechanism is based on the thermally induced reduction of metal cations while the anions, such as chloride, evaporate as gaseous side products (*e.g.* HCl and chlorine), making it unnecessary to use capping agents and other additives. Light absorbers, such as carbon nanotubes (CNTs) can be added to facilitate the process and to achieve high conductivity of metal/CNT composites<sup>134</sup>. Indeed, CNTs have been reported to be good light-to-heat converters<sup>265</sup>.

Herein, we present Print-Light-Synthesis of Ni and Ni<sub>x</sub>Fe<sub>(1-x)</sub>-based nanostructures on carbon nanotube-coated as well as bare glassy carbon substrates (**Figure 5-1**). Importantly, the goal was to create nano-sized features for electrocatalysis rather than conductive films as aimed in printed electronics. Ni and Fe chloride salts were dissolved in specifically designed inks to enable rapid printing, drying and flash light-induced thermal decomposition. A combined inkjet printer and photonic curing apparatus was employed for flexible and rapid processing. Print-Light-Synthesis requires that the printed precursor ink or the substrate underneath absorb the light

emitted from the flash lamp and heat up. In the former case, the ink heats up and decomposes as a direct process while in the latter case the heat transfer from a light absorbing substrate to the precursor film on top represents an indirect route. Both concepts were addressed herein by using a layer of CNTs that was strongly light absorbing and placed between the substrate and the precursor ink. The Ni- and Ni<sub>x</sub>Fe<sub>(1-x)</sub>-nanocatalyst on CNT/GC as well as on GC were characterized by scanning electron microscopy (SEM), scanning transmission microscopy (STEM), X-ray photoelectron spectroscopy (XPS) and voltammetry to analyse the fabrication process itself and the electrochemical activity of the printed layers towards the OER.

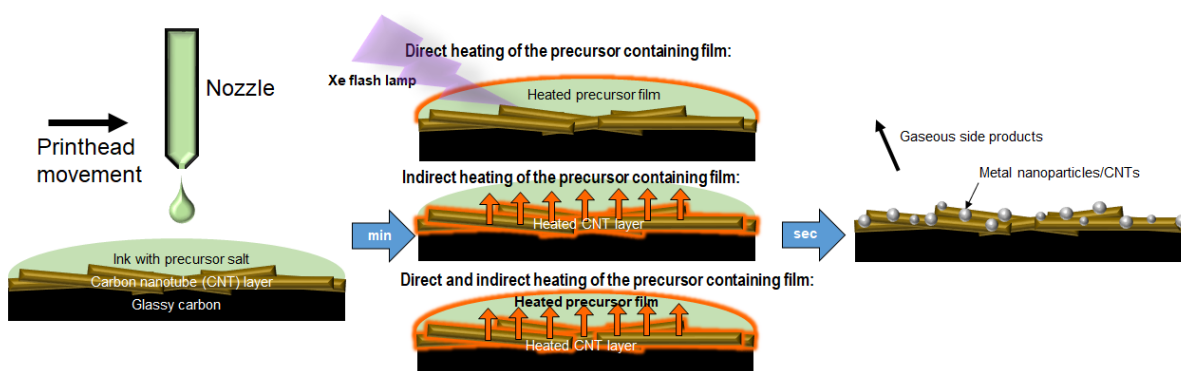


**Figure 5-1** Schematic representation of Print-Light-Synthesis to create nanostructured electrodes with a combined inkjet-printing and flash light irradiation step to induce the thermal decomposition of electrocatalyst precursors following either a direct and indirect precursor heating mechanism. A layer of CNTs act, as light absorber and local heat generator.

### 5.3 Results and discussion

The ink was designed in order to fulfil the following four major properties that are required for Print-Light-Synthesis: *i*) solubility of the metal precursor salts in the desired concentrations, *ii*) stable jetting with the piezoelectric driven printheads, *iii*) covering the substrate homogeneously, and *iv*) allowing fast drying of the printed metal precursor layer to form a thin wet film with still dissolved salt and being immediately ready for its flash light-induced thermal composition. A dissolved salt is assumed to result in homogeneously distributed particles. Adapting a previous work from the labor-

atory,<sup>116</sup> the ink solvent herein was composed of isopropanol and 1,2-propanediol. Isopropanol majorly controlled the surface tension  $\gamma$  and 1,2-propanediol the viscosity  $\eta$ , *i.e.*,  $\gamma = (24.24 \pm 1.12)$  m·Nm<sup>-1</sup> and  $\eta = 9.96$  mPa·s<sup>-1</sup>, respectively, with a density  $\rho = 0.9$  g/mL (at room temperature). The ink was notably stable allowing long-term printing without the need of performing frequent nozzle-cleaning steps, *e.g.*, by pressure-based nozzle purging. Calculating the printability parameter  $Z = (\gamma \cdot \rho \cdot a)^{0.5} \cdot \eta^{-1}$  where  $a$  represents a characteristic length (here the nozzle diameter with  $a = 21.5$   $\mu$ m) leads to a value of  $Z = 2.2$  that according to Derby<sup>155</sup> is within the printability range of  $1 < Z < 10$ . Indeed, stable jetting of  $\sim 15.3$  pL droplet was obtained (**Figure 5-2a**)<sup>155,263</sup>. An array of separate droplets of Ni<sub>0.45</sub>Fe<sub>0.55</sub> (molar ratio) precursor ink was printed on a CNT/GC electrode to evaluate the accuracy and precision of the droplets positioning and to measure the diameter of the droplet ( $85.2 \pm 3.5$   $\mu$ m) after spreading on the CNT/GC substrate (**Figure 5-2b**). The bluish and brownish spots at the rim of each individual droplet indicate larger material aggregation as result of a minor coffee ring effect<sup>266</sup>. Notably, these precipitates were absent in the internal part of larger patterns that were created by printing overlapping droplets, *e.g.*, with 5  $\mu$ m penetration of adjacent droplets to each other (*i.e.*,  $\sim 80$   $\mu$ m droplet separation, **Figure 5-2c**).

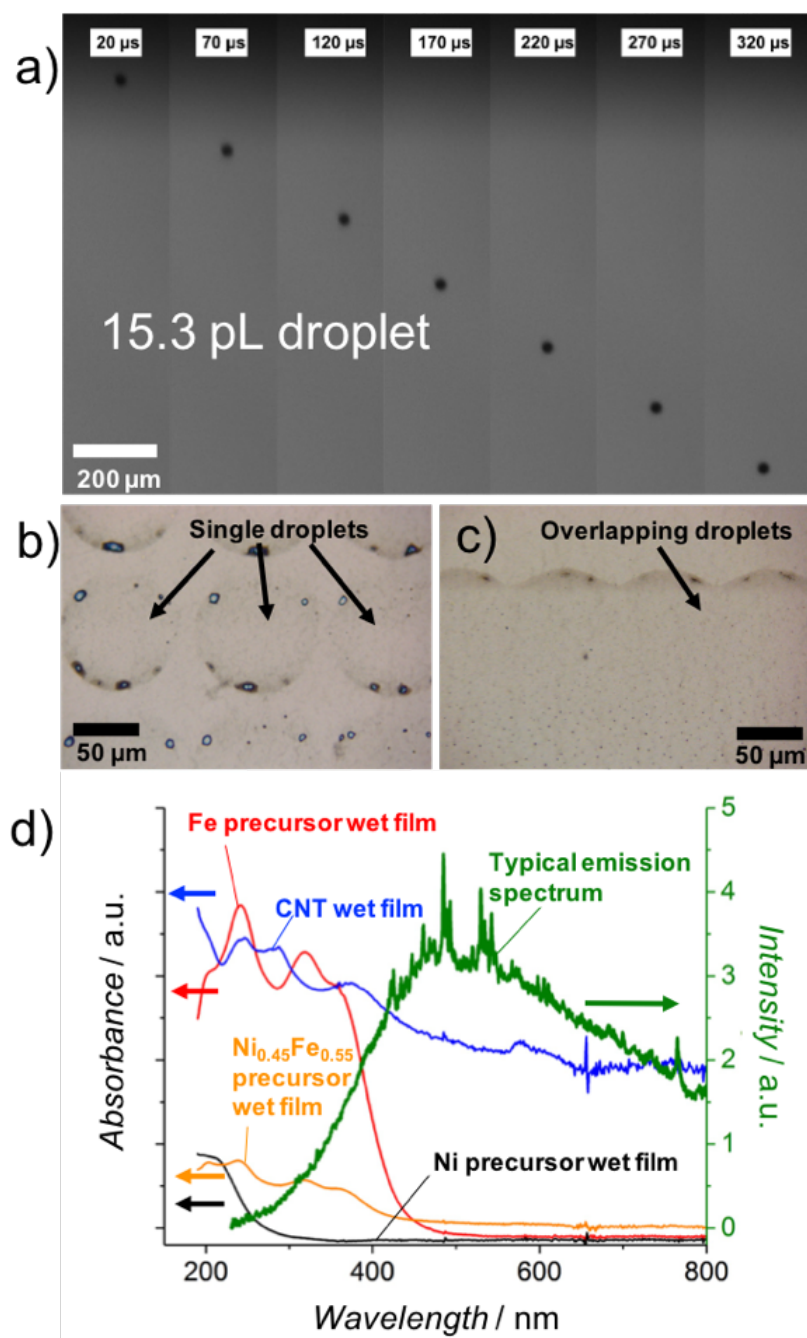


**Figure 5-2** Single droplet development during different periods after droplet ejection. Micrographs of inkjet-printed and flash light-irradiated separated (b) and overlapping (c)  $\text{Ni}_{0.45}\text{Fe}_{0.55}$  precursor ink droplets on a CNT layer on GC. d) Absorption spectra of Fe (red),  $\text{Ni}_{0.45}\text{Fe}_{0.55}$  (orange) and Ni precursor wet films and CNT ink wet film (blue) on a quartz glass slide. Emission spectrum of the Xe flash lamp (pulse condition 750 V, 200  $\mu\text{s}$ , green).

For the thermal decomposition of  $\text{NiCl}_2 \cdot 6\text{H}_2\text{O}$  in air to form Ni and/or NiO, *i.e.*, the evaporation of the entire crystal water and the removal of chloride as  $\text{Cl}_2$  and HCl, the requirement of exceeding 590  $^\circ\text{C}$ <sup>267</sup> or even 820  $^\circ\text{C}$  was reported<sup>268</sup>. For  $\text{FeCl}_2 \cdot 4\text{H}_2\text{O}$ , the thermal decomposition to

$\text{Fe}_2\text{O}_3$  occurs in air at temperatures exceeding  $400\text{ }^\circ\text{C}$ <sup>269</sup>. For the complete thermal decomposition under equilibrium conditions, *i.e.*, at constant temperature, more than 1 h equilibrium heating is required.<sup>268</sup> The stepwise equilibrium-driven thermal decomposition of the hydrated chloride precursor salts used herein was measured by thermogravimetric analysis providing thermal decomposition temperature ranges of  $200\text{-}455\text{ }^\circ\text{C}$  for the pure Fe (**Table 5-1**),  $420\text{-}650\text{ }^\circ\text{C}$  for Ni (**Table 5-2**) and  $400\text{-}680\text{ }^\circ\text{C}$  for the Ni-Fe mixed precursor inks (**Figure 5-3**).

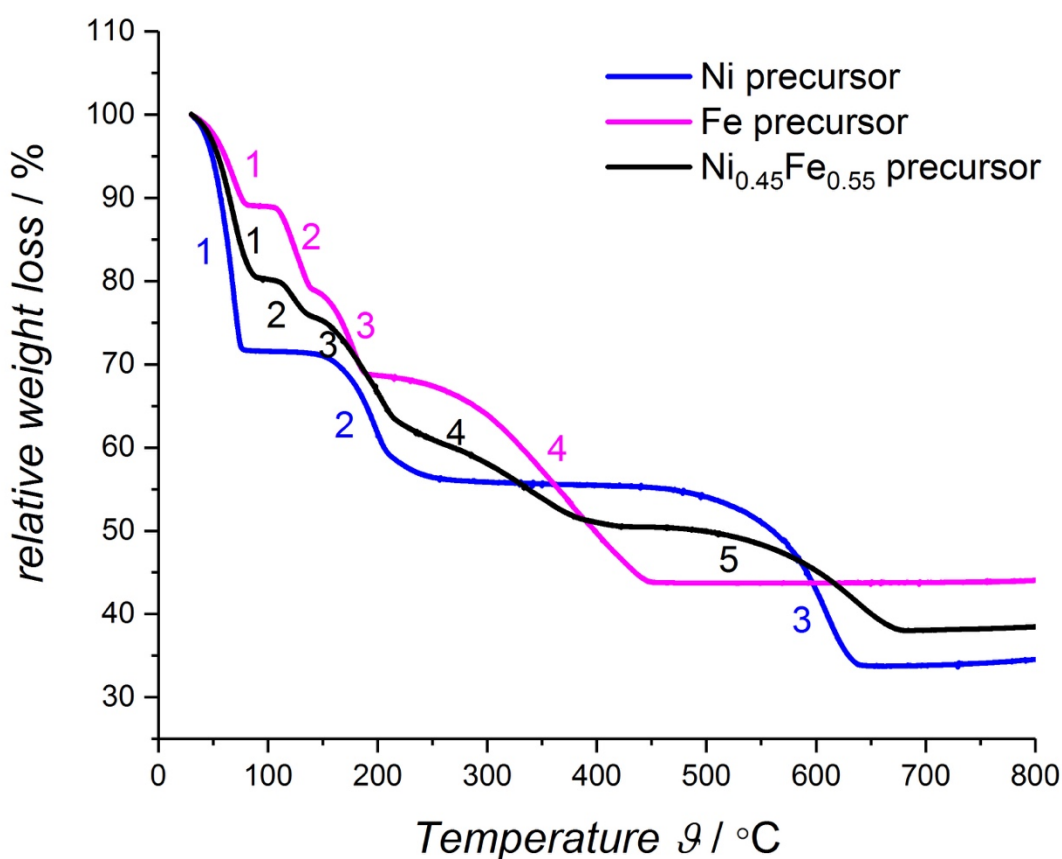


**Figure 5-3** Thermogravimetric analysis (TGA) of the iron, nickel and iron:nickel 0.45:0.55 molar ratio salts. Temperature scan with  $10\text{ }^\circ\text{C}/\text{min}$  heating ramp at air. Number in the plot indicate the number of the decomposition reaction steps for each compound.

**Table 5-1** Assumed steps for the thermal decomposition of  $\text{FeCl}_2 \cdot 4\text{H}_2\text{O}$  in air following references<sup>269,270</sup>.

$T / ^\circ\text{C}$	Composition
30	$\text{FeCl}_2 \cdot 4\text{H}_2\text{O}_{(s)}$
30 – 85	$\text{FeCl}_2 \cdot 4\text{H}_2\text{O}_{(s)} \rightarrow \text{FeCl}_2 \cdot 2\text{H}_2\text{O}_{(s)} + 2\text{H}_2\text{O}_{(g)}$
100 – 135	$\text{FeCl}_2 \cdot 2\text{H}_2\text{O}_{(s)} \rightarrow \text{FeCl}_{2(s)} + 2\text{H}_2\text{O}_{(g)}$
135 – 190	$3\text{FeCl}_{2(s)} + 3\text{O}_{2(g)} \rightarrow 3\text{FeClO}_{(s)} + 3/2\text{O}_{2(g)} + 3/2\text{Cl}_{2(g)}$
200 – 455	$2\text{FeCl}_2 + 3/2\text{O}_2 \rightarrow \text{Fe}_2\text{O}_3 + 2\text{Cl}_2$ $2\text{FeClO} + 1/2\text{O}_2 \rightarrow \text{Fe}_2\text{O}_3 + \text{Cl}_2$

**Table 5-2** Assumed steps for the thermal decomposition of  $\text{NiCl}_2 \cdot 6\text{H}_2\text{O}$  in air following references<sup>270,271</sup>.

$T / ^\circ\text{C}$	Composition
30	$\text{NiCl}_2 \cdot 6\text{H}_2\text{O}_{(s)}$
30 – 80	$\text{NiCl}_2 \cdot 6\text{H}_2\text{O}_{(s)} \rightarrow \text{NiCl}_2 \cdot x\text{H}_2\text{O}_{(s)} + (1-x)\text{H}_2\text{O}_{(g)}$
130 – 275	$\text{NiCl}_2 \cdot x\text{H}_2\text{O}_{(s)} \rightarrow \text{NiCl}_{2(s)} + x\text{H}_2\text{O}_{(g)}$
420 – 650	$\text{NiCl}_{2(s)} + 1/2\text{O}_{2(g)} \rightarrow \text{NiO}_{(s)} + \text{Cl}_{2(g)}$

In order to realize Print-Light-Synthesis, either the ink or the substrate, needs to absorb the light emitted from the flash lamp and generate the required temperatures for the thermal decomposition. The absorption spectra of thin wet precursor films on fully transparent quartz glass after drying were recorded and showed film absorbance until 300 nm (Ni precursor ink) and 450 nm (Fe precursor ink), **Figure 5-2d**. The typical light emission from the flash lamp (Pulse parameters: 750 V, 200  $\mu\text{s}$ ) starts above 250 nm. Consequently, the wet film of pure Ni precursor ink provides very little overlap with the lamp emission, while the pure Fe precursor ink overlapped over a broader wavelength range. The temperature of the precursor films during light exposure was not measurable due to the short

process time. A light absorbing substrate could be bare glassy carbon or a layer of CNTs, the latter absorbing from 200 nm to 800 nm (**Figure 5-2d**). Therefore, heating of the CNT layer with potential transfer of this heat into the wet precursor film on top was aimed as an indirect route for the decomposition<sup>134</sup>. Obviously, the direct and indirect flash light-induced heating of precursors may take place in parallel.

In **Figure 5-2**, five layers of Ni<sub>0.45</sub>Fe<sub>0.55</sub> precursor ink were inkjet-printed with a total ink volume of only 3.15  $\mu\text{L}/\text{cm}^2$ , equal to a total Ni and Fe loading of only 1.58  $\mu\text{g}/\text{cm}^2$ , the latter being low compared to literature<sup>253</sup>. The printing was performed at 60°C substrate temperature to accelerate the evaporation of the ink solvents. The lower evaporating ink solvent (1,2-propanediol) remained after few minutes of drying creating a thin homogeneous wet film rather than letting the precursor crystallize<sup>116</sup>. Two different pulse series were then applied. The first pulse resulted in a total shot energy density of  $10.60 \pm 0.19 \text{ J}\cdot\text{cm}^{-2}$  with estimated peak temperature at the GC surface of 275 °C (Fig. 4-4). The second pulse gave an entire shot energy density of  $3.52 \pm 0.03 \text{ J}\cdot\text{cm}^{-2}$  with 450 °C estimated peak temperature.<sup>116</sup> The first pulse was intended to dry the ink completely (solvent boiling points were 83 °C and 188 °C, respectively) and to remove remaining water of the crystal lattices in the precursor salts. The second pulse was supposed to remove the chlorine (**Figure 5-4**).



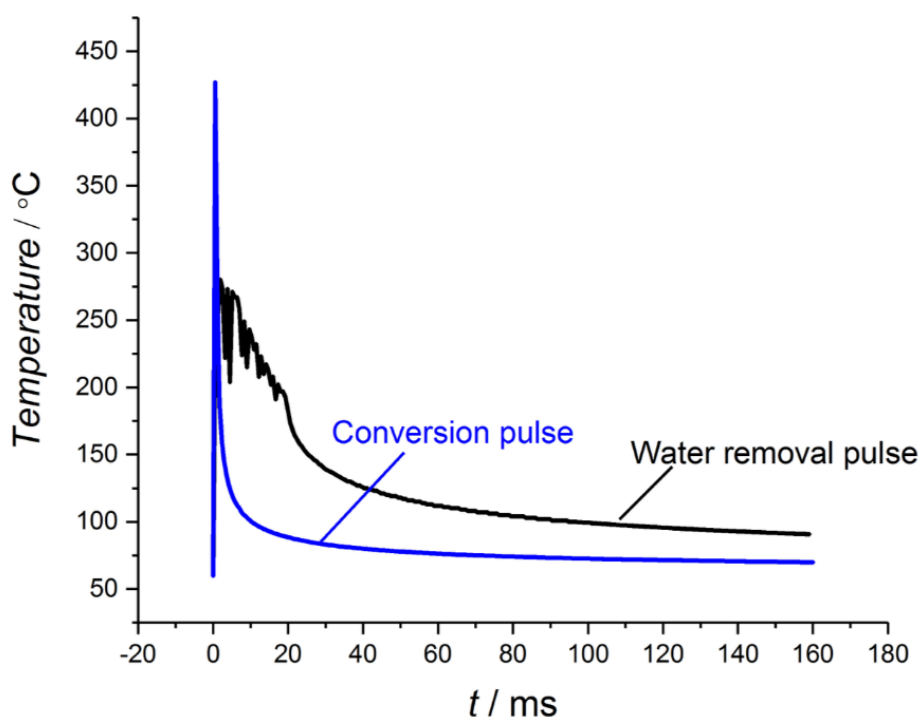


**Figure 5-4** Simulated temporal temperature profiles of the two applied flash light pulses for the water removal/complete solvent evaporation ("water removal pulse") and material conversion ("conversion pulse") on the GC surface. The effect of the presence of a CNT layer could not be simulated due to a lack of known physical constants required for the simulation. The measured shot energy densities given in the main text consider the entire pulse duration.

Print-Light-Synthesis is followed by a washing step to remove any non-converted precursor material, but also converted precursor material that instead of being well adhered to the electrode support is present as loose particles. For particle size analysis by STEM, the  $\text{Ni}_{0.45}\text{Fe}_{0.55}/\text{CNT}$  layer was scratched away from the GC support after washing and drying (**Figure 5-5 a,b**). NPs were smaller than 2.5 nm in diameter assuming spherical particles (**Figure 5-5c**). Due to the limited resolution of the images, the software-based particle size determination was performed with a lower cut-off limit of 0.5 nm. However, assuming a Gaussian size distribution suggests that particles of also less than 0.5 nm diameter could have been present on the CNTs.

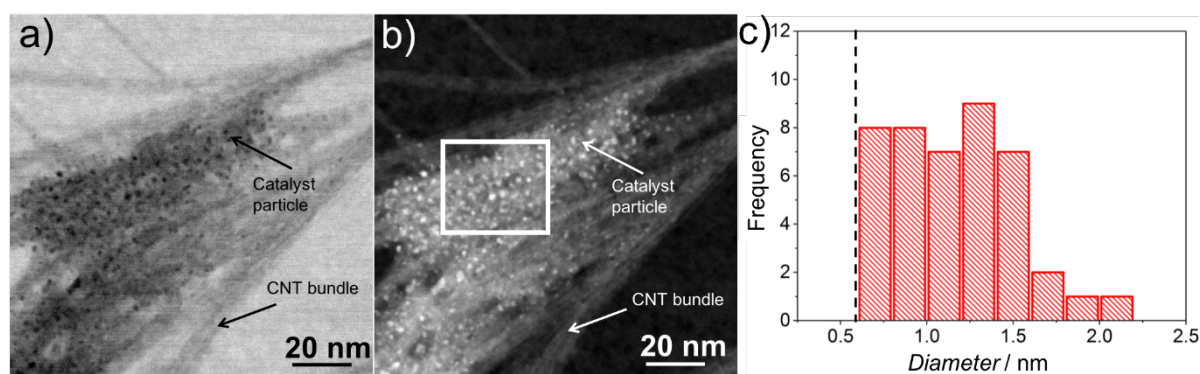


**Figure 5-5** Bright field (a) and dark field (b) STEM of  $\text{Ni}_{0.45}\text{Fe}_{0.55}$  NPs formed on CNTs. The area indicated in (b) by the white rectangle was used for particle size distribution analysis (c). The dashed line in (c) indicates the lower cut-off value that was set for the image-based particle size analysis.

X-ray photoelectron spectroscopy (XPS) of Fe (left panels a-c) and Ni (right panels d-f) precursor ink patterns on CNT/GC substrates before (black curves) and after flash light-irradiation (red curves) are shown in **Figure 5-6**. Print-Light-Synthesis is operated under ambient atmosphere and samples are stored at air, which could lead to an oxidation of the materials immediately after the process. In the XPS spectrum of Fe, peaks at 712.5 eV ( $\text{Fe}2p_{3/2}$ ) and 725 eV ( $\text{Fe}2p_{1/2}$ ) can be seen before and after the flash light irradiation (**Figure 5-6a**). A peak at 720 eV (satellite  $\text{Fe}2p_{3/2}$ ) evolved due to the flash light process indicating iron oxide formation. The Cl XPS spectrum of the non-irradiated Fe/CNT/GC sample shows three peaks, which are the result of two "metallic" Cl peaks allocated to  $\text{FeCl}_2$  and two "organic" Cl peaks that we have been able to associate to the CNT ink (**Figure 5-6b** and **Figure 5-7**). The peak at 198.5 eV corresponds to metallic  $\text{Cl}2p_{3/2}$ , the one at 201.6 eV to organic Cl ( $\text{Cl}2p_{1/2}$ ) and the central peak at 201.1 eV is a superposition of metallic  $\text{Cl}2p_{1/2}$  and organic  $\text{Cl}2p_{3/2}$ . The organic Cl peaks were not affected by the photonic curing. Incomplete precursor conversion was indicated by a remaining metallic Cl peak at 198.5 eV ( $\text{Cl}2p_{3/2}$ ). The O 1s spectrum is dominated by the peak at 532 eV corresponding to organic C-O bonds (from the CNTs and GC support), but a shoulder at 530.5 eV appears after photonic curing indicating iron oxide formation (**Figure 5-6c**).<sup>272</sup> A conversion of the Ni precursor is not visible in the XPS spectra, as the Ni (**Figure**

5-6d), Cl (Figure 5-6e) and O (Figure 5-6f) peaks remained nearly the same after the process. According to the TGA data (Figure 5-3), anhydrous NiCl<sub>2</sub> could have been formed. Notably, the washing step did not remove the light-treated Ni precursor salt, which was clearly the case for non-flashed samples (*vide infra*). This could be explained by the lower solubility of anhydrous NiCl<sub>2</sub><sup>273</sup>.

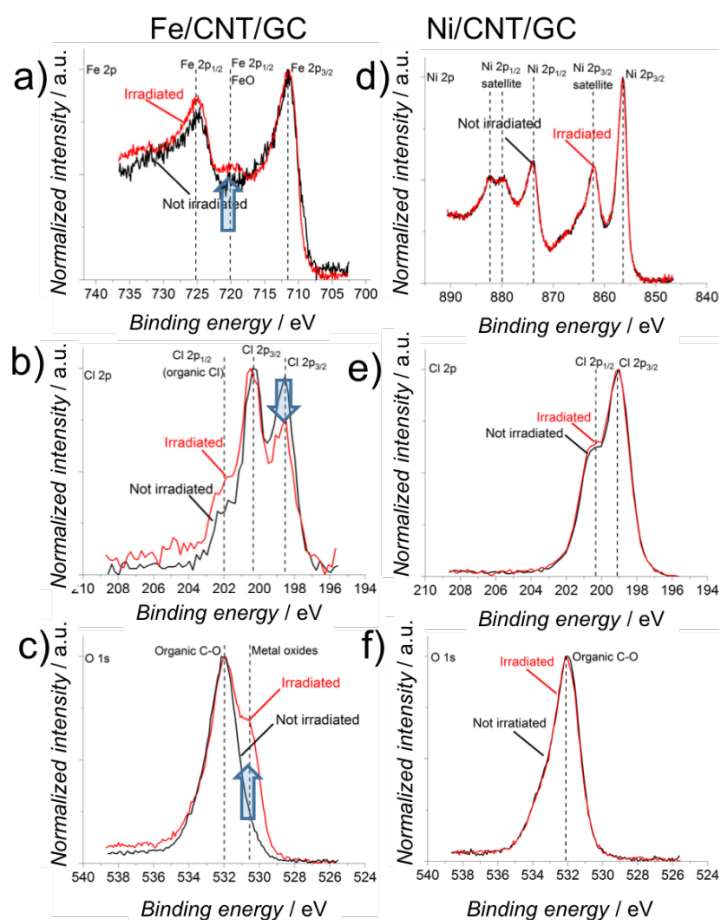


**Figure 5-6** X-ray photoelectron spectroscopy (XPS) characterization of Fe (a-c) and Ni (d-f) precursor patterns, printed on CNT/GC substrates, before (black) and after flash light irradiation (red). Lines for Ni2p (a), Fe2p (b), Cl2p (b, e) and O1s (c, f) are shown. Note: all spectra were normalized considering the base line and the main peak height, thus the spectra before and after flash light irradiation do not represent quantitative comparisons.

Thereafter, the XPS spectra of mixed precursor films (left panels in Figure 5-7a-c) and the role of the intermediate CNT layer (right panels in Figure 5-7d-f) were investigated. While no significant changes in the Ni spectra can be observed on both substrates (Figure 5-7a,d), iron oxide

formation (720 eV) took place on both CNT/GC and GC substrates (**Figure 5-7b,e**). A high removal efficiency of the metallic Cl  $2p_{3/2}$  peak at 198.5 eV can be seen on both substrates, but only on the CNT layer with 100% chlorine removal (**Figure 5-7c,f**). While the pure precursor inks resulted in insufficient Cl removal, the flash light irradiation of the Fe-Ni precursor mixture resulted in the disappearance of Cl. This synergistic effect could be explained by the higher light absorption properties of the Fe precursor leading to Fe(0) sites. Ni cations could then be absorbed by these Fe(0) nucleation sites and reduced similarly to Ni(II) sequestration in water treatments<sup>274</sup>. The application of repetitive pulses could lead to higher temperatures in the solid particles and generated sufficient temperatures for the stepwise thermal decomposition.

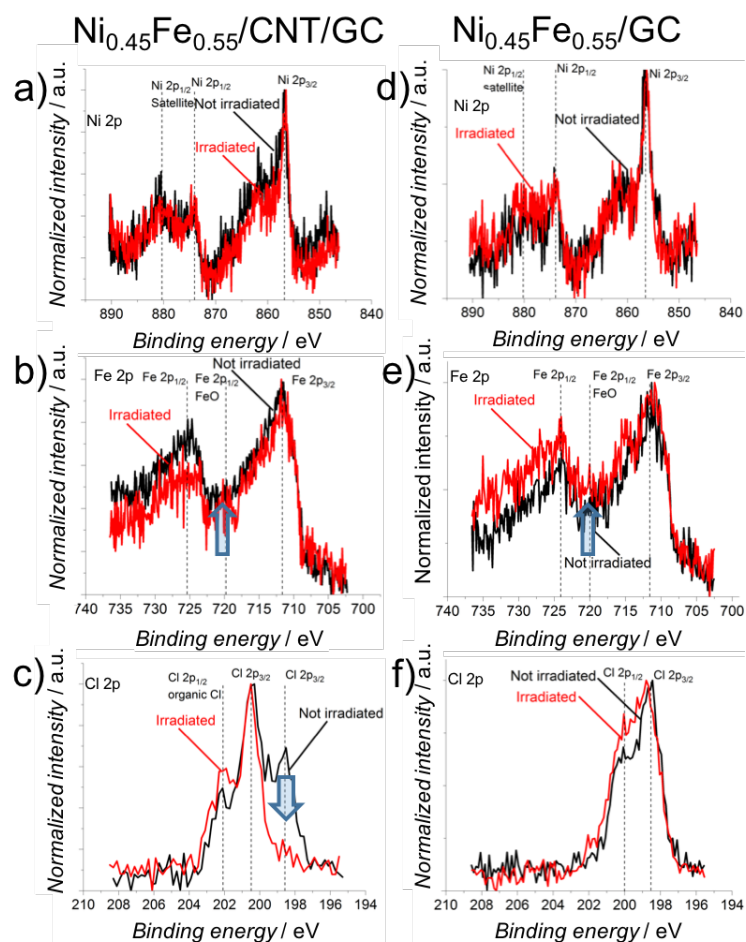
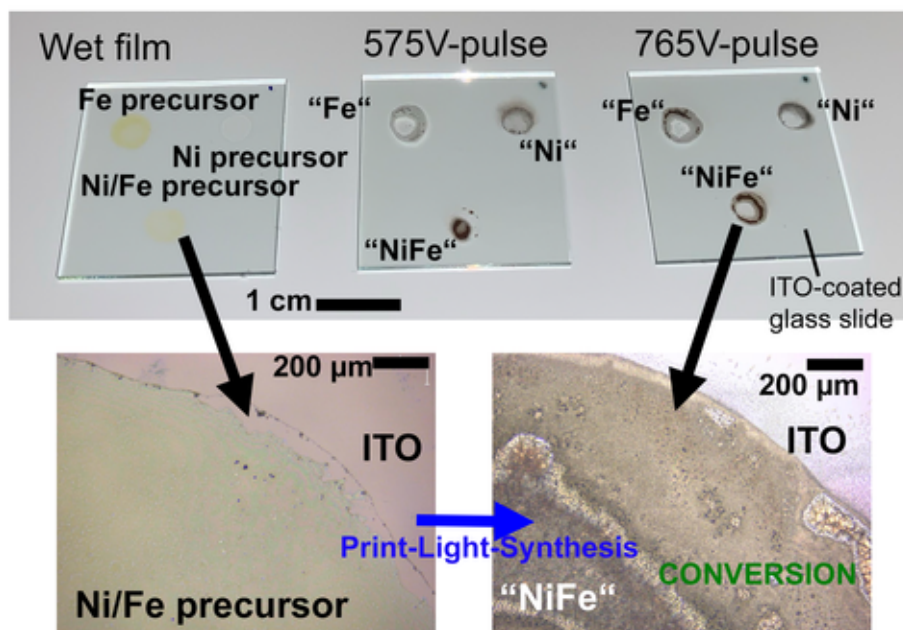


**Figure 5-7** Normalized XPS spectra of mixed  $\text{Ni}_{0.45}\text{Fe}_{0.55}$  precursor ink printed on CNT/GC (left) and GC (right) substrates before (black) and after flash light irradiation (red). Lines for Ni 2p (a,d), Fe 2p (b,e) and Cl 2p (c,f) are shown. Note: all spectra were normalized considering the base line and the main peak height, thus the spectra before and after flash light irradiation do not represent quantitative comparisons.

Ni, Fe and NiFe chloride inks made of alcohols (1,2-propanediol and isopropanol) and DI water were prepared. The water-based ink was not inkjet printable due to a too high surface tension and too low viscosity. Therefore, 0.5  $\mu\text{L}$  of all inks were drop casted rather than inkjet printed. Two indium tin oxide (ITO)-coated glass slides served as substrates, because of their transparency to identify ink changes, such as color, and low surface energy to limit spreading of the inks (**Figure 5-8**). One substrate was used for the alcohol-based inks and one substrate for the aqueous inks. Using 0.5  $\mu\text{L}$  droplets, the precursor concentrations in this test were notably higher than achieved by inkjet-printing. The ink droplets were dried at 60  $^{\circ}\text{C}$  for several minutes as in the printing protocol and flash light-irradiated in the same way as the CNT/GC substrates.

The drying led to thin wet layers that were transparent for the aqueous inks, strongly yellow for the Fe precursor alcoholic wet film, nearly transparent for the Ni precursor alcoholic wet film and slightly yellowish for the mixed Ni and Fe precursor alcoholic ink. Looking first at the alcoholic inks, after the 575V-based pulse the Fe- and Ni-based patterns appeared mainly whitish/greyish, while the NiFe-mixture appeared much darker indicating a more efficient conversion. This effect was even more pronounced after the second flashing. As shown by Lesch<sup>116</sup>, ITO does not generate much heat thus requiring the direct mechanism for the thermal decomposition. In addition, the films were much higher concentrated than the inkjet-printed and flash light-irradiated wet films on CNT/GC and GC, creating thus a process that was not representing completely the combined inkjet printing and flash light irradiation protocol. The ink was also not optimized to reach a homogeneous wetting of the ITO (coffee ring formation). Nevertheless, the higher conversion efficiency of the mixed precursor ink is obvious, even without the CNT layer. In contrast, nearly no conversion took place for the aqueous wet films of identical concentration and identically processed to the alcoholic inks. This clearly demonstrates the effect of the alcohols as electron donor.

## Alcoholic ink:



## Alcohol-free ink:

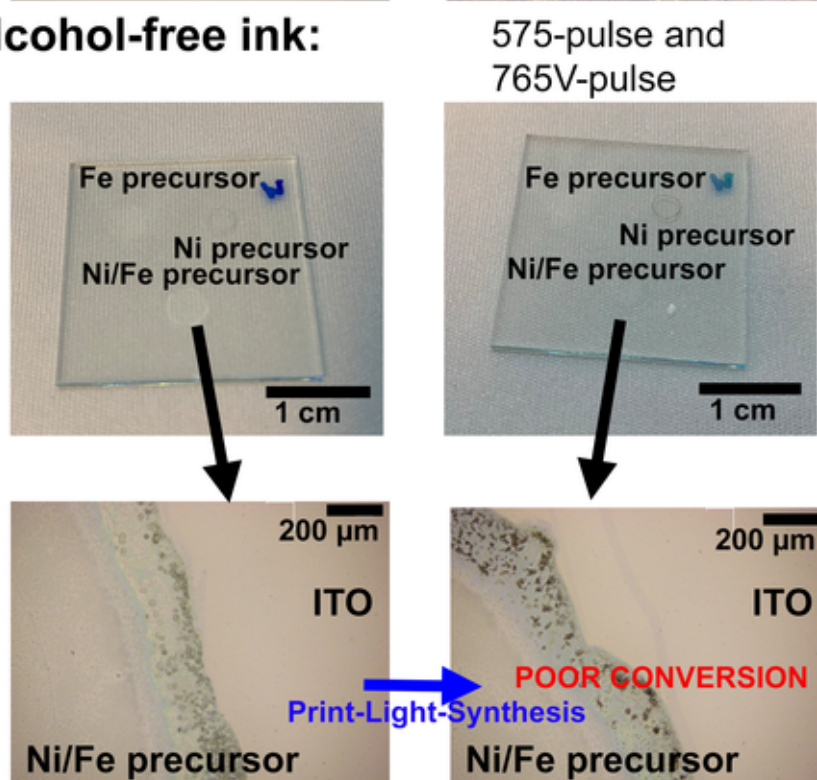


**Figure 5-8** Flash light irradiation of Ni, Fe and NiFe-precursor salt wet layers with (top) and without (bottom) sacrificial electron donor, *i.e.*, alcohol.

Still, an additional advantage of using the CNT support layer is related to the wetting of its surface by the precursor ink, which is more homogeneous on the CNTs than on the bare GC. Due to the differences in the surface free energy of the two substrates, the wettability varies. Indeed, while a

nearly homogeneous precursor layer is formed on CNTs with overlapping adjacent droplets (**Figure 5-9**), individual, non-overlapping droplets were created on GC that shrunk during drying and curing (**Figure 5-10**). The latter resulted in a locally higher precursor loading, where the evaporation of ink solvents and decomposition products resulted in bubble-shaped features at the rim of the created nano-/micro-structures.

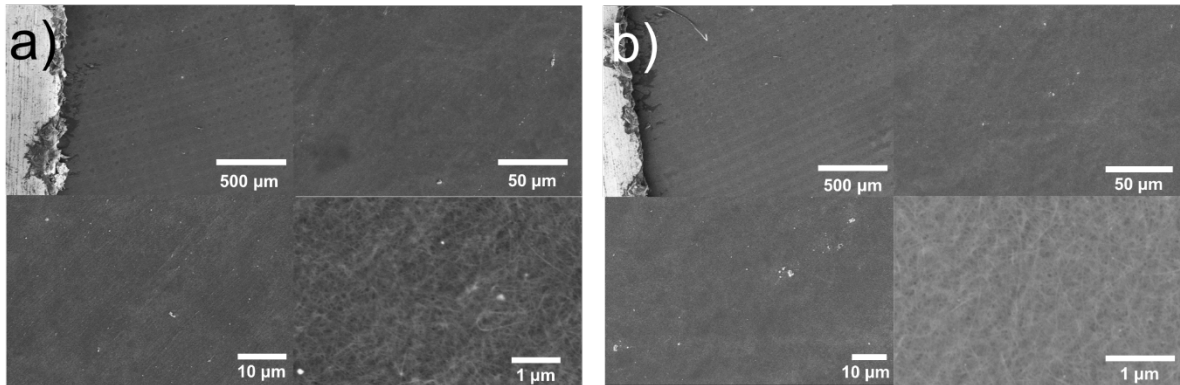


**Figure 5-9** Scanning electron micrographs with four different magnifications of Ni/CNT/GC substrates before (a) and after (b) flash light sintering.



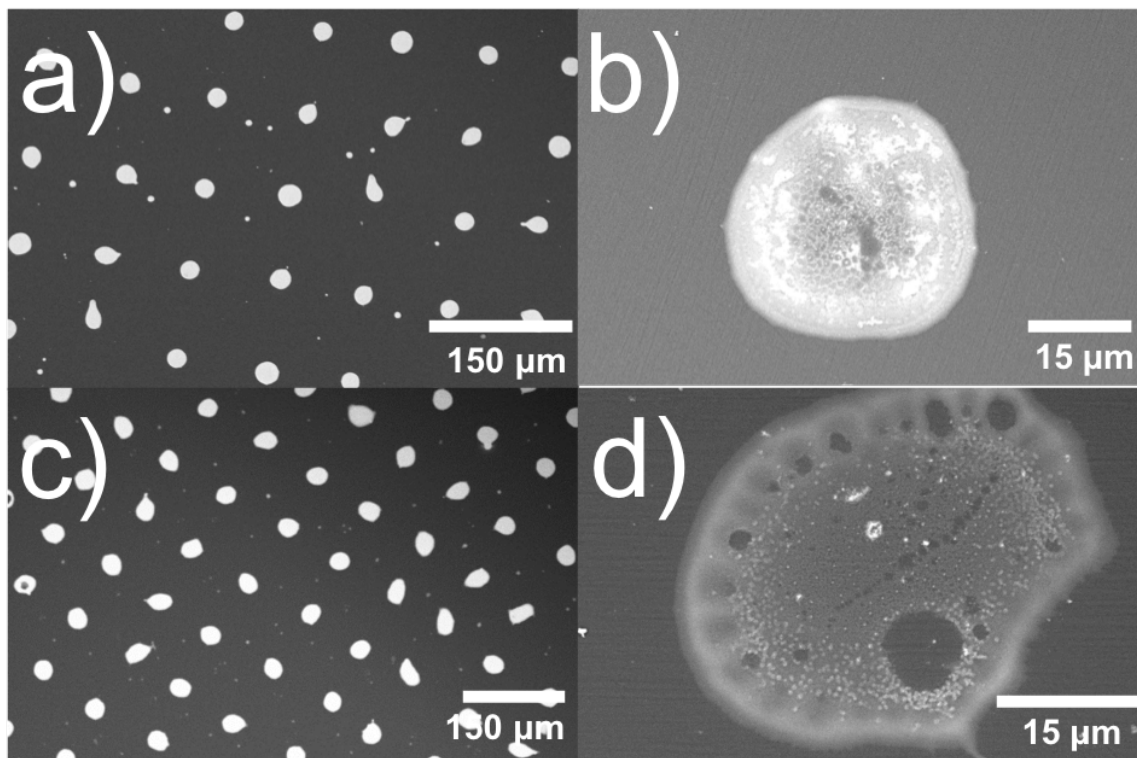


**Figure 5-10.** Scanning electron microscopy of Ni/GC before (a) and after (c) flash light sintering and of Fe/GC before (b) and after (d) flash light sintering.

After 20 cycles, the CVs were reproducible. The alkaline pH and cathodic cycling could have contributed to the conversion efficiency of nickel chlorides into the according hydroxides (*vide infra*)<sup>275</sup>. **Figure 5-11a** shows the excerpts of the twentieth cycles between 1 V and 1.6 V for Ni/CNT/GC (solid line), Ni<sub>0.45</sub>Fe<sub>0.55</sub>/CNT/GC (dashed line) and Fe/CNT/GC (dotted line). For Ni/CNT/GC, after (oxy)hydroxide layer growth (**Figure 5-12a**), typical peaks for Ni(II/III) oxidation and reduction can be seen<sup>276,277</sup>. Two overlapping oxidation peaks are most likely related to the oxidation of hydrous  $\alpha$ -Ni(OH)<sub>2</sub> (~1.45 V) and  $\beta$ -NiOOH, respectively<sup>278–280</sup>. In contrast to the  $\alpha$ -phase,  $\beta$ -Ni(OH)<sub>2</sub> was increasingly formed during cycling (**Figure 5-12a**). The broad oxidation wave at around 1.2 V was a result of the low cathodic vertex potential (*i.e.*, 0.25 V) and not present when more positive lower vertex potentials were chosen (*e.g.*, 0.9 V). Deep cathodic scanning can reduce the Ni oxide species to Ni(0), which during subsequent anodic scanning generates  $\alpha$ -Ni(OH)<sub>2</sub> that converts slowly into  $\beta$ -Ni(OH)<sub>2</sub>, a process generally described as ageing<sup>281,282</sup>. A single reduction

peak was present ( $E = \sim 1.35$  V) possibly due to an overlap of the  $\alpha$ - and  $\beta$ -phase reductions. The apparent lower charge for the reduction compared to the oxidation ( $Q_{\text{ox}}/Q_{\text{red}} = 1.7$ ) could be due to NiOOH species that catalytically oxidise adsorbed  $\text{OH}^-$  to  $\text{O}_2$  under reduction of NiOOH to  $\text{Ni}(\text{OH})_2$ <sup>283</sup>. The CV of Fe/CNT/GC does not show any relevant feature in this potential range. The electrochemical behaviour of  $\text{Ni}_{0.45}\text{Fe}_{0.55}/\text{CNT}/\text{GC}$  was clearly different from pure Ni/CNT/GC and Fe/CNT/GC as indicated by the single oxidation wave at  $\sim 1.5$  V prior to the increase of the current due to oxygen evolution. This suggests that a NiFe composite was formed during Print-Light-Synthesis with different properties compared to the pure metals. As for the Ni/CNT/GC electrode, the charge for the reduction in this potential region was smaller than for the oxidation (**Figure 5-12**).

Without the CNT layer, the peak currents for Ni oxidation and reduction were lower indicating either less converted Ni material (non-converted precursor washed away) or less active Ni surface area (*e.g.*, through larger NPs, **Figure 5-11b**). This on the one hand could be the result of a lower conversion rate for the Ni precursor decomposition without CNT layer or, on the other hand, it could mean that a different Ni morphology was obtained, for instance by less efficient wetting of the bare GC substrates by the precursor inks (**Figure 5-11b**, **Figure 5-13b**). The oxidation wave for  $\text{Ni}_{0.45}\text{Fe}_{0.55}/\text{GC}$  directly prior to oxygen evolution is not visible. In addition, the oxidation wave around 1.2 V ( $\alpha\text{-Ni}(\text{OH})_2 = \beta\text{-Ni}(\text{OH})_2$ ) and the oxidation peak related to  $\text{Ni}(\text{OH})_2$  are absent for the CNT free Ni-coated electrode, which could suggest a synergistic effect of the Ni/CNT layer on the  $\beta\text{-Ni}(\text{OH})_2$  formation.

The ratio of Ni and Fe had a clear effect on the shape of the CVs of  $\text{Ni}_x\text{Fe}_{(x-1)}/\text{CNT}/\text{GC}$  (**Figure 5-11c**). An increasing oxidation wave at  $\sim 1.5$  V before the OER was observed in the order  $\text{Ni}_{0.22}\text{Fe}_{0.78}$ ,  $\text{Ni}_{0.45}\text{Fe}_{0.55}$  and  $\text{Ni}_{0.71}\text{Fe}_{0.29}$ . On the contrary,  $\text{Ni}_{0.88}\text{Fe}_{0.12}$  on CNTs behaved almost like pure Ni indicating that the desired NiFe composite formation might not have taken place or did not have a visible effect on the CVs.

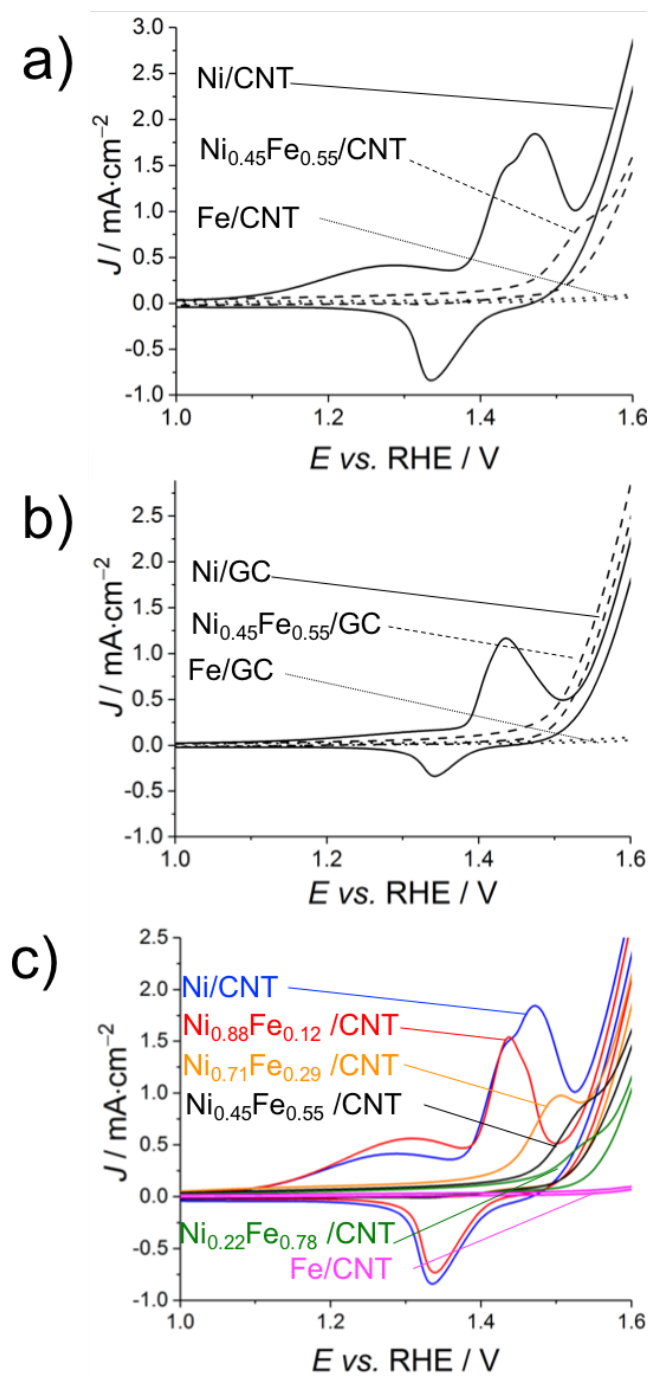


**Figure 5-11** Excerpts of cyclic voltammograms of  $\text{Ni}_x\text{Fe}_{(1-x)}$  on CNT/GC and on GC. a)  $\text{Ni}_{0.50}\text{Fe}_{0.50}/\text{CNT}/\text{GC}$  (dashed line),  $\text{Ni}/\text{CNT}/\text{GC}$  (solid line) and  $\text{Fe}/\text{CNT}/\text{GC}$  (point line). b)  $\text{Ni}_{0.45}\text{Fe}_{0.55}/\text{GC}$  (dashed line),  $\text{Ni}/\text{GC}$  (full line) and  $\text{Fe}/\text{GC}$  (point line). c) Comparison between different  $\text{Ni}_x\text{Fe}_{(1-x)}/\text{CNT}/\text{GC}$ . Electrolyte 0.1 M KOH, scan rate 50 mV/s, cycle number 20, vertex potentials 0.25 and 1.70 V. Not  $iR$ -corrected.

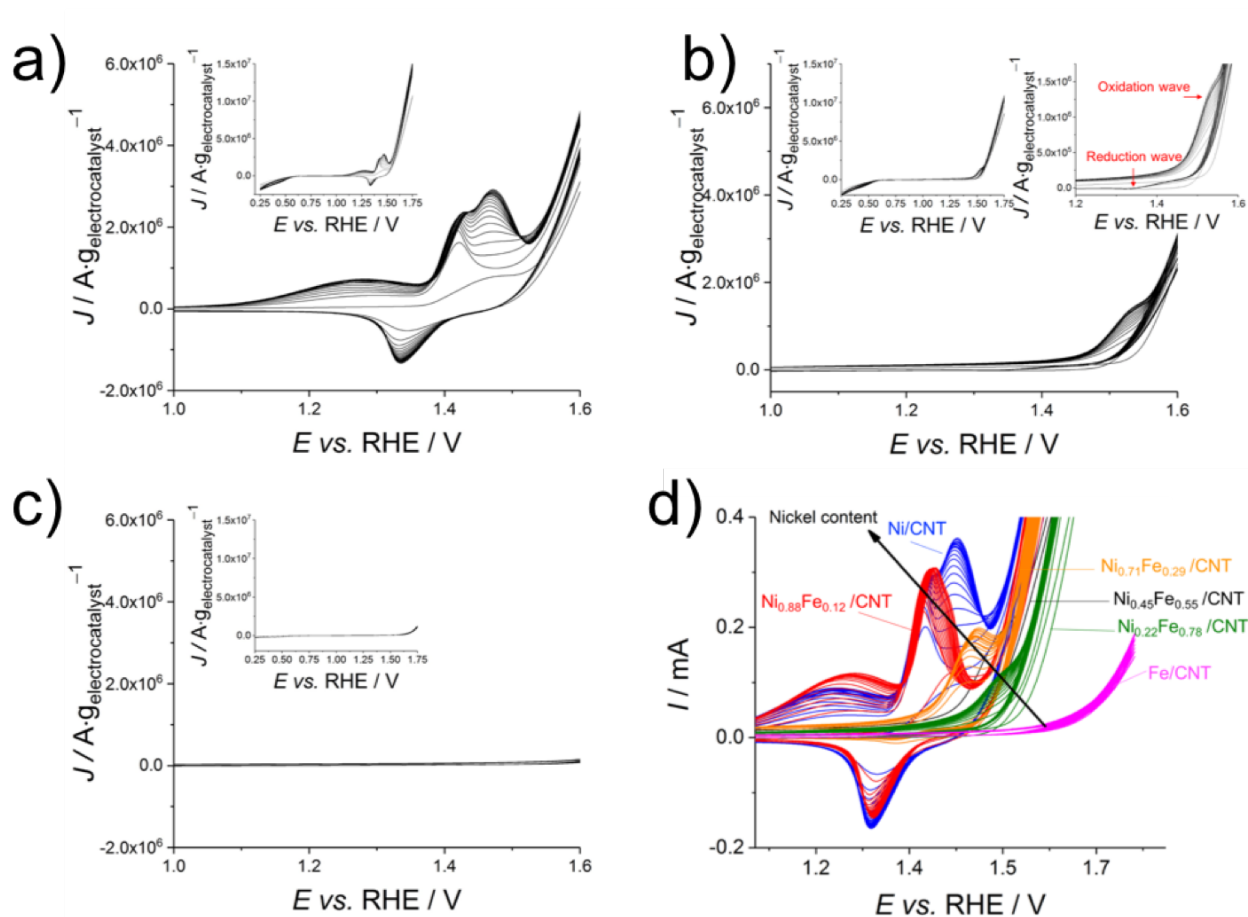


**Figure 5-12** 20 cyclic voltammograms of a) Ni/CNT/GC, b)  $\text{Ni}_{0.45}\text{Fe}_{0.55}/\text{CNT}/\text{GC}$ , c) Fe/CNT/GC and d) excerpts of Ni,  $\text{Ni}_{0.88}\text{Fe}_{0.12}$ ,  $\text{Ni}_{0.71}\text{Fe}_{0.29}$ ,  $\text{Ni}_{0.45}\text{Fe}_{0.55}$ ,  $\text{Ni}_{0.22}\text{Fe}_{0.78}$ , Fe. a) Main figure shows the CV excerpt between 1.0 and 1.6 V while the insert shows the full potential range. With cycling, the peak currents increased until reaching a stable behaviour. b) Main figure shows the CV excerpt between 1.0 and 1.6 V while the left insert shows the full potential range. Right insert presents a zoomed view of the oxidation reduction wave. With cycling, the peak currents increased until reaching a stable behaviour. c) Main figure shows the CV excerpt between 1.0 and 1.6 V while the insert shows the full potential range. d) Excerpts of cyclic voltammograms of Ni,  $\text{Ni}_{0.88}\text{Fe}_{0.12}$ ,  $\text{Ni}_{0.71}\text{Fe}_{0.29}$ ,  $\text{Ni}_{0.45}\text{Fe}_{0.55}$ ,  $\text{Ni}_{0.22}\text{Fe}_{0.78}$ , Fe printed on CNT/GC. Electrolyte 0.1 M KOH, scan rate 50 mV/s.

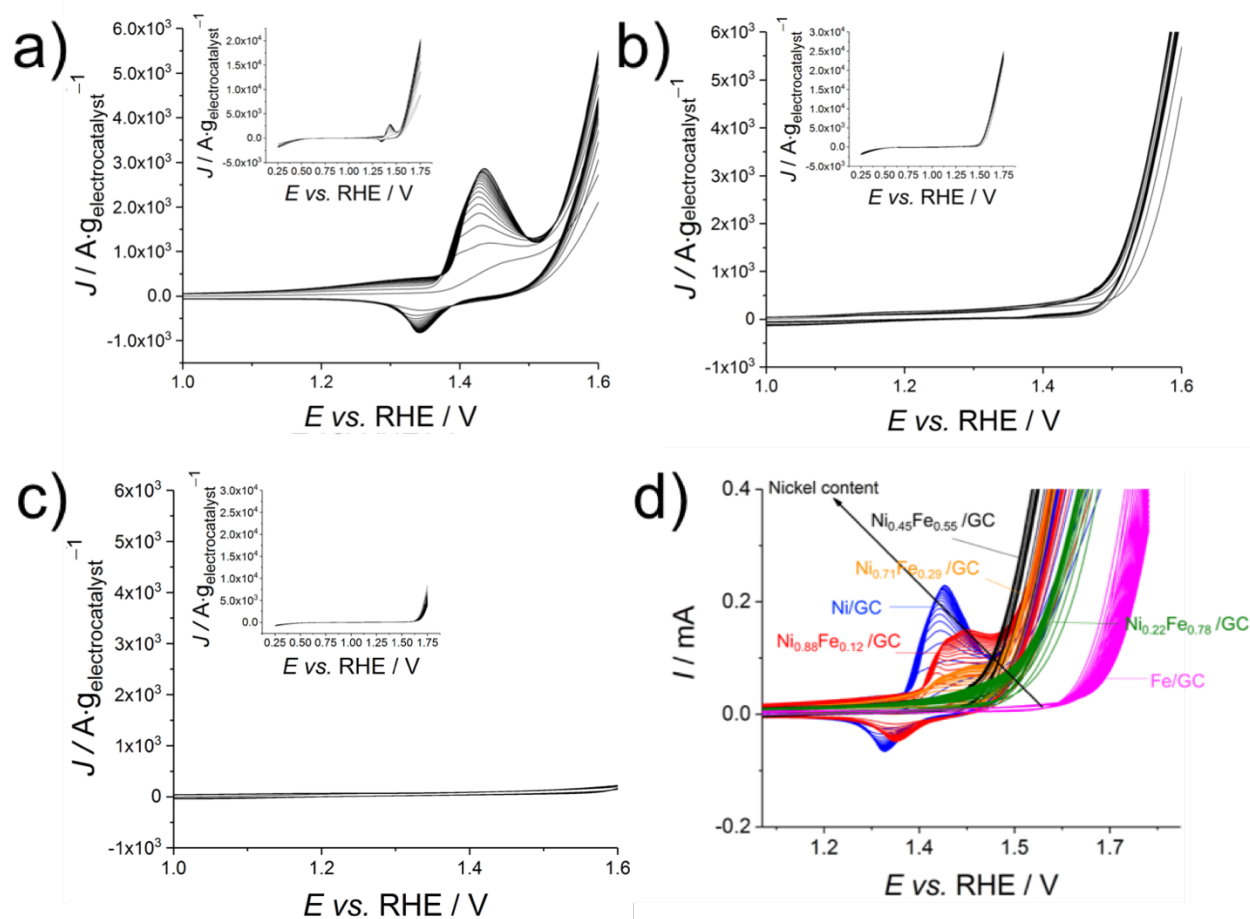


**Figure 5-13** 20 cyclic voltammograms of a) Ni/GC, b) Ni<sub>0.45</sub>Fe<sub>0.55</sub>/GC, c) Fe/GC and d) excerpts of Ni, Ni<sub>0.88</sub>Fe<sub>0.12</sub>, Ni<sub>0.71</sub>Fe<sub>0.29</sub>, Ni<sub>0.45</sub>Fe<sub>0.55</sub>, Ni<sub>0.22</sub>Fe<sub>0.78</sub>, Fe. a) Main figure shows the CV excerpt between 1.0 and 1.6 V while the insert shows the full potential range. With cycling, the peak currents increased until reaching a stable behaviour. b) Main figure shows the CV excerpt between 1.0 and 1.6 V while the left insert shows the full potential range. Right insert presents a zoomed view of the oxidation reduction wave. With cycling, the peak currents increased until reaching a stable behaviour. c) Main figure shows the CV excerpt between 1.0 and 1.6 V while the insert shows the full potential range. d) Excerpts of cyclic voltammograms of Ni, Ni<sub>0.88</sub>Fe<sub>0.12</sub>, Ni<sub>0.71</sub>Fe<sub>0.29</sub>, Ni<sub>0.45</sub>Fe<sub>0.55</sub>, Ni<sub>0.22</sub>Fe<sub>0.78</sub>, Fe printed on GC. Electrolyte 0.1 M KOH, scan rate 50 mV/s.<sup>284</sup>

The activity towards the OER was investigated by comparing the first and twentieth forward half cycles of the CVs (**Figure 5-14**). The Ni<sub>x</sub>Fe<sub>(1-x)</sub> nanostructures on bare GC showed clearly inferior activity compared to the CNT/GC-based counterparts (**Figure 5-14c**). Further, Ni<sub>0.71</sub>Fe<sub>0.29</sub>/CNT and Ni<sub>0.88</sub>Fe<sub>0.12</sub>/CNT showed the highest initial OER activity (*i.e.*, the recorded current density at a given potential, **Figure 5-14d,e**) while in particular Ni/CNT (**Figure 5-14f**) showed initially poor activity. However, with cycling both Ni<sub>0.71</sub>Fe<sub>0.29</sub>/CNT and Ni<sub>0.88</sub>Fe<sub>0.12</sub>/CNT decayed in activity, while Ni<sub>0.22</sub>Fe<sub>0.78</sub> (**Figure 5-14b**), Ni<sub>0.45</sub>Fe<sub>0.55</sub> (**Figure 5-14c**) and Ni (**Figure 5-14c**) gained in activity.

Ni/CNT gained substantially in activity during the cycling protocol approaching the curves of Ni<sub>0.71</sub>Fe<sub>0.28</sub> and Ni<sub>0.88</sub>Fe<sub>0.12</sub>, while Fe/CNT showed poor activity for the OER (**Figure 5-14a**). Indeed, it is reported in literature that cycling of Ni enhances the OER activity<sup>85</sup>. In literature, the positive effect of the presence of Fe, also added as minor impurities, on the OER has been discussed for a long time, but varying amounts of Fe for maximum activity are reported<sup>253,285–287</sup>. This is often related to the large variety of NiFe-composites and the related syntheses and process conditions.

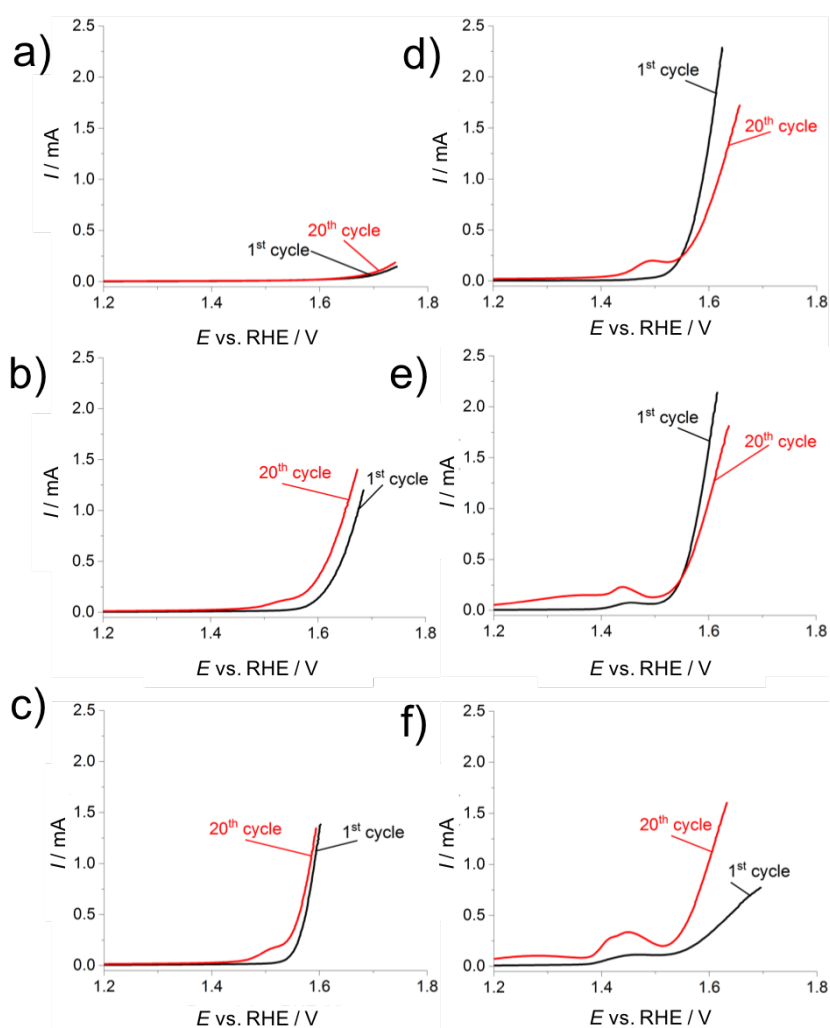


**Figure 5-14** *iR*-corrected first (black) and twentieth (red) forward half cycles of CVs of Ni<sub>x</sub>Fe<sub>(1-x)</sub>/CNT/GC with x = 0 (a), 0.22 (b), 0.45 (c), 0.71 (d), 0.88 (e) and 1 (f) (red). Electrolyte 0.1 M KOH, scan rate 50 mV/s.

Polarization curves of the Ni- and NiFe-nanostructured CNT/GC (left panels a, c, e) and GC (right panels b, d, f) were carried out after the 20 CV cycles discussed above (**Figure 5-15**). All the curves were individually *iR*-corrected. In fact, the values of the solution resistance varied between 40

$\Omega$  and  $100 \Omega$ . Ni showed the highest OER activity, which was determined as the onset potential necessary to achieve  $0.1 \text{ mA}\cdot\text{cm}^{-2}$  (**Table 5-3**). Further, the OER activity increased inversely to the Fe content with onset potentials 0.24 V for Ni/CNT, 0.28 V for  $\text{Ni}_{0.88}\text{Fe}_{0.12}/\text{CNT}$  to 0.31 V for  $\text{Ni}_{0.22}\text{Fe}_{0.78}/\text{CNT}$  (1.53 V, **Figure 5-15a,b**). The polarization curves of Ni- and all NiFe-nanostructured GC substrates show clearly lower activity compared to their CNT-supported counterparts (**Table 5-3**). The onset potentials for all NiFe ratios on GC are nearly identical (except for the highest Fe content, **Figure 5-15**), while a clear shift is observed for the CNT-supported NiFe layers (**Figure 5-15a**).

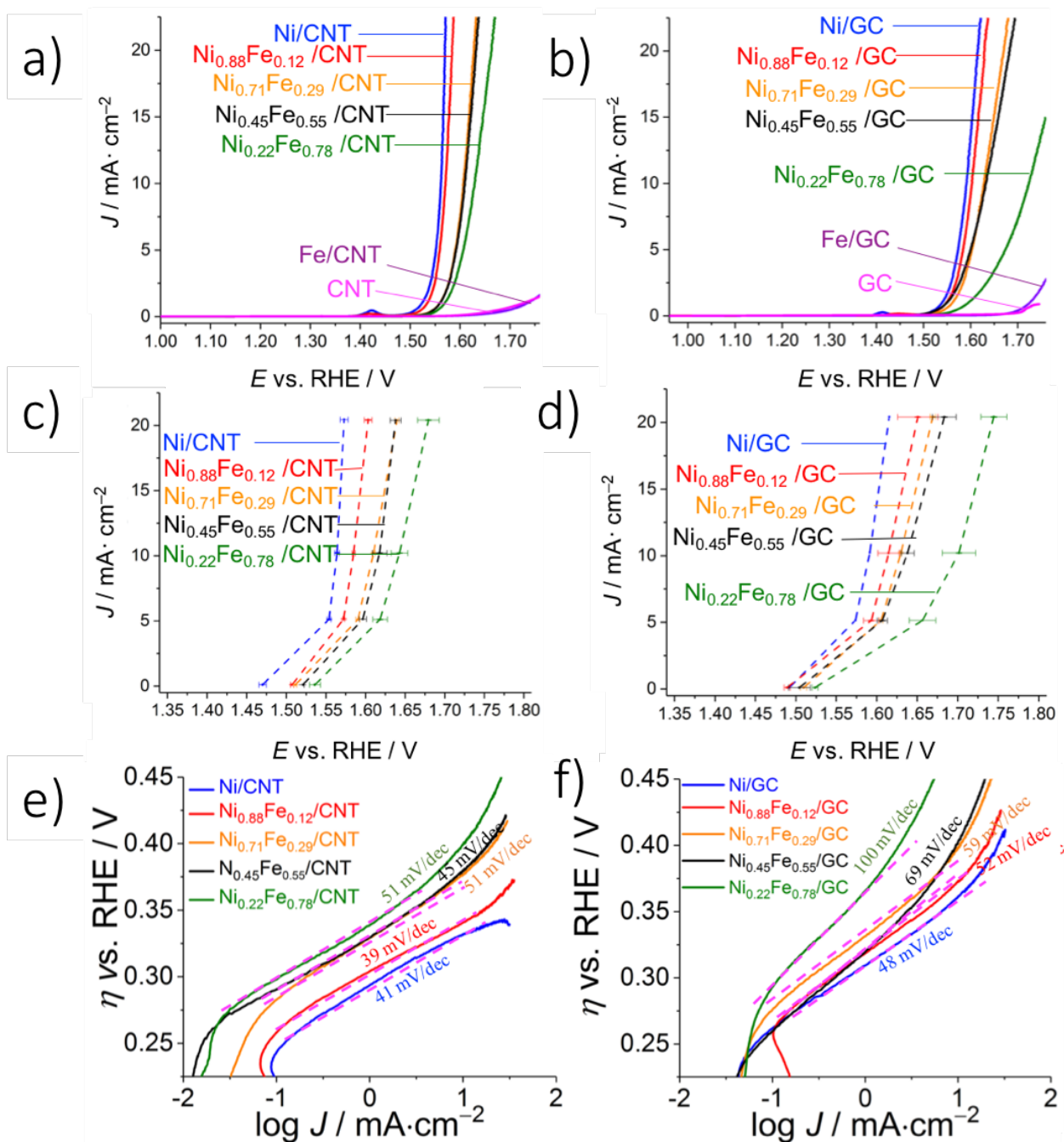


**Figure 5-15** *iR*-corrected polarization curves (a, b), average overpotentials at 0.1, 5, 10 and 20 mA/cm<sup>2</sup> (N = 3; c, d) with dashed connection lines as guides to the eye and Tafel slopes (e, f) of Ni<sub>x</sub>Fe<sub>(1-x)</sub> on CNT/GC (left) and GC (right) with x = 0, 0.22, 0.45, 0.71, 0.88 and 1. Electrolyte 0.1 M KOH, scan rate 5 mV/s and rotation rate 3200 rpm.

While in **Figure 5-15a,b**, each curve was recorded with a single printed electrode, **Figure 5-15c,d** shows the overpotentials at 0.1, 5, 10 and 20 mA/cm<sup>2</sup> of three different, but identically printed electrodes to demonstrate the repeatability of electrode production. Notably, the nanostructures with



CNT layer showed more than five times lower variation between electrodes (**Table 5-3**), *e.g.*, 0.3% versus 2% for Ni<sub>0.88</sub>Fe<sub>0.12</sub> at 10 mA/cm<sup>2</sup>. The overpotentials for 10 mA/cm<sup>2</sup> were slightly higher than what is generally reported in literature for state-of-the-art catalysts, such as NiFe@NC<sup>257</sup>, NiFe-NS<sup>258</sup>, CS-NiFeCU<sup>288</sup>. The Tafel slopes for the Ni and Ni<sub>x</sub>Fe<sub>(1-x)</sub>-based nanostructures on CNT/GC increased with iron content from 41 mV/decade to 51 mV/decade (**Figure 5-15e,f, Table 5-3**), which were similar or lower than the ones typically reported for various nanostructured NiO and Ni(OH)<sub>2</sub> on carbonaceous nanomaterials, *i.e.*, 42-87 mV/decade<sup>87,289</sup>. This suggests fast reaction kinetics due to surface-adsorbed species produced in the early stage of the OER, *i.e.*, OH<sup>-</sup>.<sup>290</sup> Similar Tafel slopes have been reported for NiFe-composites on carbonaceous supports<sup>291-293</sup>, which were partially outperformed by certain NiFe-LDH/CNTs with 30 mV/decade<sup>256</sup> and Ni(OH)<sub>2</sub>/CNTs with 32 mV/decade.<sup>294</sup> For GC-supported NiFe-based nanostructures herein, the Tafel slopes were slightly larger and increased from 48 mV/decade to 100 mV/decade with increasing iron content (**Table 5-3**), which confirmed the positive effect of the CNT sublayer on the OER activity of the NiFe nanostructures. Turn-over-frequency (TOF) numbers at  $\eta = 340$  mV, such value was obtained considering that all moles of printed precursor have been transformed into active sites, were  $\sim 4\times$  higher for the Ni/CNT composites with  $x=1$  and  $x=0.88$  compared to the CNT-free case (*i.e.*, 6.53 s<sup>-1</sup> and 3.31 s<sup>-1</sup> vs. 1.75 s<sup>-1</sup> and 0.83 s<sup>-1</sup>, respectively, **Table 5-3**). Compared to literature<sup>289,293</sup> only few cases can be found with higher reported values<sup>294-296</sup>.

**Table 5-3.** Onset potential, overpotential, Tafel slope and TOF numbers after 20 CV cycles.

<b>Electrode</b>	<b>Onset poten- tial@0.1 mA·cm<sup>-2</sup> / mV vs. E° (O<sub>2</sub>,H<sub>2</sub>O) = 1.23 V</b>	<b>Overpoten- tial@10 mA·cm<sup>-2</sup> / mV vs. E° (O<sub>2</sub>,H<sub>2</sub>O) = 1.23 V</b>	<b>Tafel slope / mV·dec<sup>-1</sup></b>	<b>TOF / s<sup>-1</sup> (total metals)</b>
Ni/CNT/GC	240.1 ± 4.7	334.0 ± 2.8	41	6.53
Ni <sub>0.88</sub> Fe <sub>0.12</sub> /CNT/GC	277.1 ± 2.0	354.9 ± 2.0	39	3.31
Ni <sub>0.71</sub> Fe <sub>0.29</sub> /CNT/GC	281.3 ± 2.0	360.2 ± 2.1	45	0.75
Ni <sub>0.45</sub> Fe <sub>0.55</sub> /CNT/GC	291.1 ± 1.3	367.8 ± 9.3	45	0.63
Ni <sub>0.22</sub> Fe <sub>0.78</sub> /CNT/GC	306.1 ± 6.9	392.8 ± 10.5	51	0.26
Ni/GC	262	361.4	48	1.75
Ni <sub>0.88</sub> Fe <sub>0.12</sub> /GC	259.1 ± 3.6	363.6 ± 13.0	52	0.83
Ni <sub>0.71</sub> Fe <sub>0.29</sub> /GC	269.3 ± 4.0	378.8 ± 10.1	59	0.75
Ni <sub>0.45</sub> Fe <sub>0.55</sub> /GC	264.2 ± 13.3	387.1 ± 8.1	69	0.50
Ni <sub>0.22</sub> Fe <sub>0.78</sub> /GC	283.5 ± 3.5	450.5 ± 20.4	100	0.20

In addition, the Ni precursor ink was inkjet-printed on the CNT layer without subsequent flash light irradiation. Indeed, the washing step removed the non-irradiated precursor salts completely and linear sweep voltammograms showed, as expected, negligible activity for the OER (**Figure 5-16c**). As discussed, cathodic cycling until the lower vertex potential of 0.25 V seemed to be necessary to a) form a nickel hydroxide structure that promotes the OER<sup>85</sup>, and/or b) reduced electrochemically incompletely converted Ni<sub>x</sub>Cl<sub>y</sub> residues. Indeed, CVs with more positive lower vertex potential (*i.e.*, 0.9 V) resulted in less active layers for the OER (**Figure 5-16**).

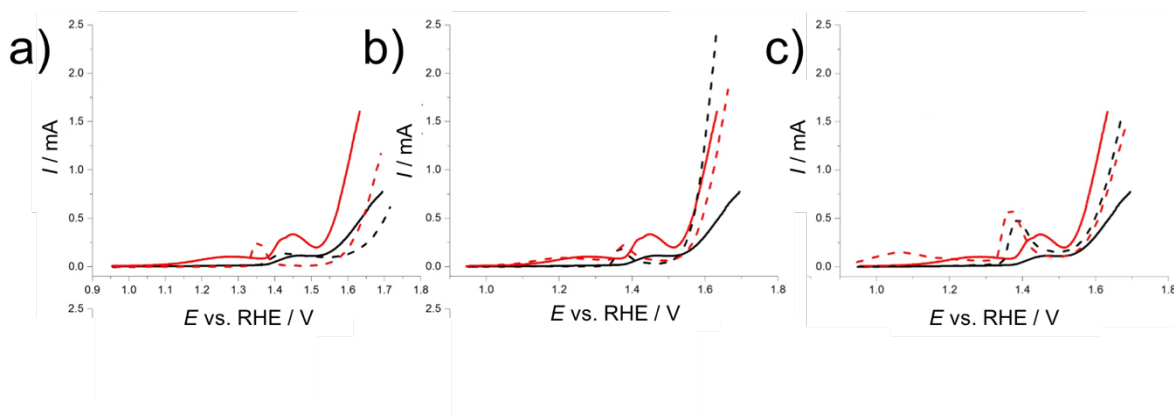


**Figure 5-16.** Comparison of the iR-corrected first (black) and twentieth (red) forward half cycles of CVs of Ni/CNT/GC electrode, prepared using Print-Light-Synthesis and using the CV vertex potentials 0.25 V and 1.70 V (solid lines in all plots) with a) Ni/CNT/GC (Print-Light-Synthesis) and lower CV vertex potential (0.9 V) avoiding cathodic currents (dashed), b) Ni/CNT/GC (Print-Light-Synthesis), lower CV vertex potential (0.9 V) for 20 cycles and then 20 CV cycles with vertex potentials 0.25 and 1.70 V (dashed) and c) Ni/CNT/GC (electrodeposited).

The electrochemical deposition of Ni from a precursor solution following a standard protocol<sup>283</sup> resulted in a more stable, but less active Ni/CNT/GC electrode. Furthermore, metallic chloride, which was present after Print-Light-Synthesis, disappeared by immersion and KOH solution and cycling (**Figure 5-16**).

## 5.4 Conclusion

Ni- and NiFe-based nanostructures, supported on carbon nanotubes or directly synthesized on bare glassy carbon electrodes, were fabricated as electrocatalysts for the oxygen evolution reaction using Print-Light-Synthesis. The process was based on the rapid inkjet printing of Ni and Fe chloride containing thin wet layers, which was followed by their immediate thermal decomposition through (sub)millisecond pulses from a Xe flash lamp under atmospheric conditions.

We demonstrated a synergistic effect of mixing Fe and Ni precursor inks for a complete thermal decomposition of the precursors forming a NiFe-composite. The positive influence of an intermediate CNT layer in-between substrate and precursor film as a light absorber and process enhancer was

demonstrated. The entire fabrication process was finished within few minutes offering new opportunities for low cost and easily up-scalable electrode production. Drop-on-demand inkjet printing enabled high precursor utilization and the use of parallel printheads allowed synthesizing flexibly nanostructures of various Ni-Fe ratios. The ink volumes and precursor salt mass deposited on the substrate were in the nL and  $\mu\text{g per cm}^2$  range. Material ratios and loadings can be precisely adjusted by the printing parameters like the number of printed layers. The catalyst layers prepared herein were electrochemically conditioned and showed high activity for the OER, which was confirmed by low Tafel slopes, considerably low overpotentials and high turnover frequency numbers. Under the fabrication and electrochemical operation conditions applied herein, pure Ni-based nanostructures constructed the most stable and active electrodes, while Fe inclusions provided electrocatalysts with higher initial activity.

This work showed further that the recently developed Print-Light-Synthesis provides a rapid and facile tool to create ultrathin nanocatalyst loadings for energy research with expanding capabilities in terms of substrate size, catalyst amount and materials. For the production of mesoporous micro-three-dimensional catalyst layers in fuel cells and electrolyzers, we envisage to re-disperse the CNT-supported nanostructures in suitable solvents and using complementary deposition methods.



# Chapter 6 Conclusions and Perspectives

## 6.1 Conclusions

Throughout the presented thesis an overview of the application of digital microfabrication techniques to develop and produce nano-electrocatalysts and catalyst layers, was presented. Initially, in Chapter III, a deep understanding on the effects of processing advanced electrocatalysts was discussed. In such work, a state-of-the-art non-commercial catalyst was processed (*i.e.* dispersed, excess dispersant removal and ink formulation), achieving an ink within the physicochemical requirements for printing. Afterwards it was possible to proceed the fabrication of a CL through drop-on-demand inkjet printing, using piezoelectric printheads. Initially, a stable dispersion was obtained by capping the catalyst particle with a polymer. Ink formulation involves increasing the viscosity of the media to stabilize particles and to enable printability. However, functional inks require more than just maintaining the printability, it is necessary to keep the desired activity of the material when printed. In the presented case, the capping agent affects the catalytic activity negatively. Such fact was then overcome utilizing a multistep approach on the ink formulation, minimizing the use of additives and processing the printed patterns with photonic curing to remove the capping agents. Photonic curing is a non-thermal equilibrium technique based on intense light pulses that generate selective light absorption of materials as fundament. Therefore, the materials with higher absorption of the emitted radiation heat up while the other materials remain in the initial state. In the case of the results presented in Chapter III, such feature was used to degrade selectively the capping polymer at elevated temperature without affecting the substrate. The degradation of the polymer and catalyst, depending on the amount of energy irradiated, were studied and optimum parameters were found.

In Chapter IV a different approach was utilized to create electrodes that were decorated with nano-electrocatalysts by synthesizing Pt nanoparticles *in situ*. Such approach allowed a straightforward ink formulation containing a dissolved Pt precursor salt whose thermal decomposition upon light

irradiation was obtained by simple, but highly energetic flash light pulses. This method is known as Print-Light-Synthesis and was further utilized to convert Ni and Fe precursor inks into mixed nanocomposites. A carbon nanotube support layer on glassy carbon was used to absorb the light and to generate more heat than what the thin precursor films did on their own. Alcohols in the ink acted as sacrificial electron donors to improve the efficiency of metal precursor reduction. NiFe nanocomposites were created with activity towards the OER and compared with pure Ni nanocatalysts made in the same way. The use of particle-free inks has the advantage of controlling the metal ratios and loadings in a simple way. Further, such refined approach is able to deviate one of the critical limitations on printing, which is the necessity of low particle size and exclusion of excessive nanoparticle aggregation. Moreover, the intrinsic development of Print-Light-Synthesis opens possibilities for the development of inks and fabrication processes with higher degree of control on reactant consumption and are more flexible (in terms of fabricated nanostructures and supports).

From the technological point of view this thesis introduces a range of novel paths that could be followed in the area of energy conversion device fabrication and catalyst synthesis. From the fabrication of CLs with high degree of control in dimension, loading and shape to fast, flexible and tunable catalyst synthesis the possibilities here presented agree with industrial process requirements. In addition, the high flexibility of inkjet printing and Pulse-Light-Synthesis allow a smart fabrication process design, utilizing better the resources available with lower wastage.

## 6.2 Perspectives

Throughout this thesis, the importance of nanostructured electrocatalysts in electrochemistry was discussed. Much attention was devoted to discuss the importance in exploiting advanced fabrication methods, utilizing resources in a smarter and careful way. Nonetheless, there is a vast field to be explored. Distinctively, in the field of Print-Light-Synthesis much can still be explored. For such explorations DSAs are an interesting model system. This particular kind of electrodes is fabricated on resistant materials such as Ti mesh and foils, therefore a vast range of energy can be irradiated

without degrading the substrate. In addition, many researches are devoted to synthesize new electrocatalysts, alloys and oxides in these electrodes.

Therefore, to identify materials that overcome in activity and stability, some state-of-the-art electrocatalysts are of a great challenge, such as platinum and platinum alloys for the oxygen reduction reaction<sup>56</sup>, iridium oxide for the oxygen evolution reaction and titanium/ruthenium oxides for chlorine evolution. Moreover, the possibility to develop such new synthesis protocols in order to control the catalyst properties is of great interest. Besides addressing the material properties, challenges are typically faced in the transfer from a small-scale laboratory synthesis into a large-scale industrial level process, using tanks and large meshes with high-throughput. The latter should ideally be fast and reproducible, operate at ambient conditions, rely in efficient material consumption, and be environmentally friendly and flexible in terms of the targeted materials. Currently, the coating of support materials, *e.g.* carbonaceous materials or titanium meshes, with metal structures of different dimensions, is generally performed by the thermal decomposition of metal precursor coatings in a furnace.

The support materials are coated with thin films of inks or pastes through dip coating, roller, brushing or spraying, before they remain for a certain amount of time in a furnace at several hundred degrees. A reducing atmosphere, such as hydrogen gas, favors the formation of pure metals while air or oxygen leads to oxide formation. Examples are the thermal decomposition of hexachloroplatinic acid into Pt, H<sub>2</sub>O, Cl<sub>2</sub> and HCl or of hexachloroiridate into IrO<sub>x</sub>, H<sub>2</sub>O, Cl<sub>2</sub> and HCl, respectively. Besides the metals or metal oxides, only gaseous side products are formed under the above process conditions. Furthermore, due to high temperature and prolonged heating of the sample, the substrate will react to the thermal treatment. Such fact can accelerate the degradation or form unwanted side products, such as the case of Ti substrates with titanium oxide formed. Denser or higher loading coatings can be achieved by performing the procedure of coating and thermal treatment repetitively or by increasing the precursor concentration in the solution. The continuation of the work carried out during the



thesis pursue interest in the investigation of the possibility to generate thicker catalyst coatings with defined morphology for DSAs.



## References

- (1) Armaroli, N.; Balzani, V. The Future of Energy Supply: Challenges and Opportunities. *Angew. Chemie Int. Ed.* **2007**, *46* (1–2), 52–66. <https://doi.org/10.1002/anie.200602373>.
- (2) Mwasilu, F.; Justo, J. J.; Kim, E.-K.; Do, T. D.; Jung, J.-W. Electric Vehicles and Smart Grid Interaction: A Review on Vehicle to Grid and Renewable Energy Sources Integration. *Renew. Sustain. Energy Rev.* **2014**, *34*, 501–516. <https://doi.org/http://dx.doi.org/10.1016/j.rser.2014.03.031>.
- (3) Chourabi, H.; Nam, T.; Walker, S.; Gil-Garcia, J. R.; Mellouli, S.; Nahon, K.; Pardo, T. A.; Scholl, H. J. Understanding Smart Cities: An Integrative Framework. *Proceedings of the 2012 45th Hawaii International Conference on System Sciences*. IEEE Computer Society 2012, pp 2289–2297. <https://doi.org/10.1109/hicss.2012.615>.
- (4) Bolund, B.; Bernhoff, H.; Leijon, M. Flywheel Energy and Power Storage Systems. *Renew. Sustain. Energy Rev.* **2007**, *11* (2), 235–258. <https://doi.org/http://dx.doi.org/10.1016/j.rser.2005.01.004>.
- (5) Denholm, P.; Kulcinski, G. L. Life Cycle Energy Requirements and Greenhouse Gas Emissions from Large Scale Energy Storage Systems. *Energy Convers. Manag.* **2004**, *45* (13–14), 2153–2172. <https://doi.org/http://dx.doi.org/10.1016/j.enconman.2003.10.014>.
- (6) Kazempour, S. J.; Moghaddam, M. P.; Haghifam, M. R.; Yousefi, G. R. Electric Energy Storage Systems in a Market-Based Economy: Comparison of Emerging and Traditional Technologies. *Renew. Energy* **2009**, *34* (12), 2630–2639. <https://doi.org/http://dx.doi.org/10.1016/j.renene.2009.04.027>.
- (7) Divya, K. C.; Østergaard, J. Battery Energy Storage Technology for Power Systems—An

Overview. *Electr. Power Syst. Res.* **2009**, *79* (4), 511–520.  
<https://doi.org/http://dx.doi.org/10.1016/j.epsr.2008.09.017>.

- (8) Gualous, H.; Bouquain, D.; Berthon, A.; Kauffmann, J. M. Experimental Study of Supercapacitor Serial Resistance and Capacitance Variations with Temperature. *J. Power Sources* **2003**, *123* (1), 86–93. [https://doi.org/http://dx.doi.org/10.1016/S0378-7753\(03\)00527-5](https://doi.org/http://dx.doi.org/10.1016/S0378-7753(03)00527-5).
- (9) Amstutz, V.; Toghiani, K. E.; Powlesland, F.; Vruble, H.; Comninellis, C.; Hu, X.; Girault, H. H. Renewable Hydrogen Generation from a Dual-Circuit Redox Flow Battery. *Energy Environ. Sci.* **2014**, *7* (7), 2350–2358. <https://doi.org/10.1039/C4EE00098F>.
- (10) Alotto, P.; Guarnieri, M.; Moro, F. Redox Flow Batteries for the Storage of Renewable Energy: A Review. *Renew. Sustain. Energy Rev.* **2014**, *29*, 325–335. <https://doi.org/http://dx.doi.org/10.1016/j.rser.2013.08.001>.
- (11) Cho, J.; Jeong, S.; Kim, Y. Commercial and Research Battery Technologies for Electrical Energy Storage Applications. *Prog. Energy Combust. Sci.* **2015**, *48*, 84–101. <https://doi.org/http://dx.doi.org/10.1016/j.pecs.2015.01.002>.
- (12) Economie, D. Perspectives énergétiques 2050 Résumé  
<http://www.bfe.admin.ch/themen/00526/00527/?lang=en>.
- (13) Fraunhofer. Energy Charts <https://www.energy-charts.de/power.htm>.
- (14) Hart, D.; Lewis, J.; Lehner, F.; Klippenstein, M.; Rose, R. *The Fuel Cell Industry Review 2017; 2017*. <https://doi.org/10.1595/147106712X657535>.
- (15) Kurzweil, P. Gaston Planté and His Invention of the Lead-Acid Battery-The Genesis of the First

- Practical Rechargeable Battery. *J. Power Sources* **2010**, *195* (14), 4424–4434. <https://doi.org/10.1016/j.jpowsour.2009.12.126>.
- (16) Ligen, Y.; Vrabel, H.; Girault, H. H. Mobility from Renewable Electricity: Infrastructure Comparison for Battery and Hydrogen Fuel Cell Vehicles. *World Electr. Veh. J.* **2018**, *9* (1). <https://doi.org/10.3390/wevj9010003>.
- (17) Rahman, M. A.; Wang, X.; Wen, C. A Review of High Energy Density Lithium-Air Battery Technology. *J. Appl. Electrochem.* **2014**, *44* (1), 5–22. <https://doi.org/10.1007/s10800-013-0620-8>.
- (18) Zhang, J.; Vukmirovic, M. B. M. B.; Xu, Y. Y.; Mavrikakis, M.; Adzic, R. R. R. Controlling the Catalytic Activity of Platinum-Monolayer Electrocatalysts for Oxygen Reduction with Different Substrates. *Angew. Chemie Int. Ed.* **2005**, *44* (14), 2132–2135. <https://doi.org/10.1002/anie.200462335>.
- (19) Fabbri, E.; Schmidt, T. J. Oxygen Evolution Reaction—The Enigma in Water Electrolysis. *ACS Catal.* **2018**, *8* (10), 9765–9774. <https://doi.org/10.1021/acscatal.8b02712>.
- (20) Martini Pasqualetti, A. Eletrocatalisadores Formados Por Nitretos, Carbetos e Óxidos Metálicos Para o Eletrodo de Oxigênio, 2017. [https://doi.org/10.1016/S0301-0082\(00\)00043-5](https://doi.org/10.1016/S0301-0082(00)00043-5)  
T4 - Transport across cell membranes, fluxes from neurons to glial cells, and role in signalling  
M4 - Citavi.
- (21) Debe, M. K. Electrocatalyst Approaches and Challenges for Automotive Fuel Cells. *Nature* **2012**, *486* (7401), 43–51.
- (22) Wroblowa, H. S.; Yen-Chi-Pan; Razumney, G. Electroreduction of Oxygen. A New Mechanistic Criterion. *J. Electroanal. Chem.* **1976**, *69* (2), 195–201. <https://doi.org/10.1016/S0022->

0728(76)80250-1.

- (23) Mittal, V. O.; Russell Kunz, H.; Fenton, J. M. Is H<sub>2</sub>O<sub>2</sub> Involved in the Membrane Degradation Mechanism in PEMFC? *Electrochem. Solid-State Lett.* **2006**, *9* (6), A299. <https://doi.org/10.1149/1.2192696>.
- (24) Zhao, S.; Wangstrom, A. E.; Liu, Y.; Rigdon, W. A.; Mustain, W. E. Stability and Activity of Pt/ITO Electrocatalyst for Oxygen Reduction Reaction in Alkaline Media. *Electrochim. Acta* **2015**, *157*, 175–182. <https://doi.org/10.1016/j.electacta.2015.01.030>.
- (25) Darab, M.; Barnett, A. O.; Lindbergh, G.; Thomassen, M. S.; Sunde, S. The Influence of Catalyst Layer Thickness on the Performance and Degradation of PEM Fuel Cell Cathodes with Constant Catalyst Loading. *Electrochim. Acta* **2017**, *232*, 505–516. <https://doi.org/10.1016/j.electacta.2017.02.101>.
- (26) Maass, S.; Finsterwalder, F.; Frank, G.; Hartmann, R.; Merten, C. Carbon Support Oxidation in PEM Fuel Cell Cathodes. *J. Power Sources* **2008**, *176* (2), 444–451. <https://doi.org/10.1016/j.jpowsour.2007.08.053>.
- (27) Reier, T.; Oezaslan, M.; Strasser, P. Electrocatalytic Oxygen Evolution Reaction (OER) on Ru, Ir, and Pt Catalysts: A Comparative Study of Nanoparticles and Bulk Materials. *ACS Catal.* **2012**, *2* (8), 1765–1772. <https://doi.org/10.1021/cs3003098>.
- (28) Wu, J.; Yuan, X. Z.; Martin, J. J.; Wang, H.; Zhang, J.; Shen, J.; Wu, S.; Merida, W. A Review of PEM Fuel Cell Durability: Degradation Mechanisms and Mitigation Strategies. *J. Power Sources* **2008**, *184*, 104–119. <https://doi.org/10.1016/j.jpowsour.2008.06.006>.
- (29) Wang, Y. J.; Fang, B.; Li, H.; Bi, X. T.; Wang, H. Progress in Modified Carbon Support Materials for Pt and Pt-Alloy Cathode Catalysts in Polymer Electrolyte Membrane Fuel Cells. *Progress in*

*Materials Science*. 2016, pp 445–498. <https://doi.org/10.1016/j.pmatsci.2016.06.002>.

- (30) Noël, J.-M. M.; Latus, A.; Lagrost, C.; Volanschi, E.; Hapiot, P.; Noël, J.-M.; Latus, A.; Lagrost, C.; Volanschi, E.; Hapiot, P. Evidence for OH Radical Production during Electrocatalysis of Oxygen Reduction on Pt Surfaces: Consequences and Application. *J. Am. Chem. Soc.* **2012**, *134* (5), 2835–2841. <https://doi.org/10.1021/ja211663t>.
- (31) Nilekar, A. U.; Mavrikakis, M. Improved Oxygen Reduction Reactivity of Platinum Monolayers on Transition Metal Surfaces. *Surf. Sci.* **2008**, *602* (14), L89–L94. <https://doi.org/http://dx.doi.org/10.1016/j.susc.2008.05.036>.
- (32) Duan, Z.; Wang, G. A First Principles Study of Oxygen Reduction Reaction on a Pt(111) Surface Modified by a Subsurface Transition Metal M (M = Ni, Co, or Fe). *Phys. Chem. Chem. Phys.* **2011**, *13* (45), 20178–20187. <https://doi.org/10.1039/C1CP21687B>.
- (33) Nørskov, J. K.; Rossmeisl, J.; Logadottir, A.; Lindqvist, L.; Kitchin, J. R.; Bligaard, T.; Jónsson, H. Origin of the Overpotential for Oxygen Reduction at a Fuel-Cell Cathode. *J. Phys. Chem. B* **2004**, *108* (46), 17886–17892. <https://doi.org/10.1021/jp047349j>.
- (34) Stephens, I. E. L.; Bondarenko, A. S.; Grønbjerg, U.; Rossmeisl, J.; Chorkendorff, I. Understanding the Electrocatalysis of Oxygen Reduction on Platinum and Its Alloys. *Energy Environ. Sci.* **2012**, *5* (5), 6744–6762. <https://doi.org/10.1039/c2ee03590a>.
- (35) Hansen, H. A.; Viswanathan, V.; Nørskov, J. K. Unifying Kinetic and Thermodynamic Analysis of 2 e<sup>−</sup> and 4 e<sup>−</sup> Reduction of Oxygen on Metal Surfaces. *J. Phys. Chem. C* **2014**, *118* (13), 6706–6718. <https://doi.org/10.1021/jp4100608>.
- (36) Wang, C.; Daimon, H.; Onodera, T.; Koda, T.; Sun, S. A General Approach to the Size- and Shape-Controlled Synthesis of Platinum Nanoparticles and Their Catalytic Reduction of

Oxygen. *Angew. Chemie Int. Ed.* **2008**, *47* (19), 3588–3591.  
<https://doi.org/10.1002/anie.200800073>.

- (37) Shao, M.; Peles, A.; Shoemaker, K. Electrocatalysis on Platinum Nanoparticles: Particle Size Effect on Oxygen Reduction Reaction Activity. *Nano Lett.* **2011**, *11* (9), 3714–3719.  
<https://doi.org/10.1021/nl2017459>.
- (38) Zhang, K.; Han, X.; Hu, Z.; Zhang, X.; Tao, Z.; Chen, J. Nanostructured Mn-Based Oxides for Electrochemical Energy Storage and Conversion. *Chem. Soc. Rev.* **2015**, *44* (3), 699–728.  
<https://doi.org/10.1039/C4CS00218K>.
- (39) Li, M. F.; Liao, L. W.; Yuan, D. F.; Mei, D.; Chen, Y.-X. PH Effect on Oxygen Reduction Reaction at Pt(1 1 1) Electrode. *Electrochim. Acta* **2013**, *110*, 780–789.  
<https://doi.org/10.1016/j.electacta.2013.04.096>.
- (40) Shao, M.; Chang, Q.; Dodelet, J.-P.; Chenitz, R. Recent Advances in Electrocatalysts for Oxygen Reduction Reaction. *Chem. Rev.* **2016**, *116* (6), 3594–3657.  
<https://doi.org/10.1021/acs.chemrev.5b00462>.
- (41) Stellman, J. M. *Encyclopaedia of Occupational Health and Safety: Chemical, Industries and Occupations*; 1998.
- (42) Exchange, F. S. ETFS Physical Platinum [http://www.boerse-frankfurt.de/en/etc\\_etn/etc+commodities/etfs+physical+platinum+DE000A0N62D7](http://www.boerse-frankfurt.de/en/etc_etn/etc+commodities/etfs+physical+platinum+DE000A0N62D7).
- (43) Morozan, A.; Josselme, B.; Palacin, S. Low-Platinum and Platinum-Free Catalysts for the Oxygen Reduction Reaction at Fuel Cell Cathodes. *Energy Environ. Sci.* **2011**, *4* (4), 1238–1254.  
<https://doi.org/10.1039/C0EE00601G>.



- (44) Carter, D. The Cost of Platinum in Fuel Cell Electric Vehicles. *Fuel Cell Today* **2013**, *Analyst* vi.
- (45) Endoh, E.; Honmura, S.; Terazono, S.; Widjaja, H.; Takimoto, Y. Degradation Study of MEA for PEMFC under Low Humidity Conditions. *ECS Proc. Vol.* **2019**, *2004–21*, 363–369. <https://doi.org/10.1149/200421.0363pv>.
- (46) Li, H.; Bai, Y.; Wu, F.; Li, Y.; Wu, C. Budding Willow Branches Shaped Na<sub>3</sub>V<sub>2</sub>(PO<sub>4</sub>)<sub>3</sub>/C Nanofibers Synthesized via an Electrospinning Technique and Used as Cathode Material for Sodium Ion Batteries. *J. Power Sources* **2015**, *273* (0), 784–792. <https://doi.org/http://dx.doi.org/10.1016/j.jpowsour.2014.09.153>.
- (47) Yazdanpour, M.; Esmaeilifar, A.; Rowshanzamir, S. Effects of Hot Pressing Conditions on the Performance of Nafion Membranes Coated by Ink-Jet Printing of Pt/MWCNTs Electrocatalyst for PEMFCs. *Int. J. Hydrogen Energy* **2012**, *37* (15), 11290–11298. <https://doi.org/http://dx.doi.org/10.1016/j.ijhydene.2012.04.139>.
- (48) Xu, Y.; Zhu, X.; Zhou, X.; Liu, X.; Liu, Y.; Dai, Z.; Bao, J. Ge Nanoparticles Encapsulated in Nitrogen-Doped Reduced Graphene Oxide as an Advanced Anode Material for Lithium-Ion Batteries. *J. Phys. Chem. C* **2014**, *118* (49), 28502–28508. <https://doi.org/10.1021/jp509783h>.
- (49) Kanan, M. W.; Surendranath, Y.; Nocera, D. G. Cobalt-Phosphate Oxygen-Evolving Compound. *Chem. Soc. Rev.* **2009**, *38* (1), 109–114. <https://doi.org/10.1039/b802885k>.
- (50) Zhao, Z.-G.; Zhang, J.; Yuan, Y.; Lv, H.; Tian, Y.; Wu, D.; Li, Q.-W. In-Situ Formation of Cobalt-Phosphate Oxygen-Evolving Complex-Anchored Reduced Graphene Oxide Nanosheets for Oxygen Reduction Reaction. *Sci. Rep.* **2013**, *3*, 2263. <https://doi.org/10.1038/srep02263http://www.nature.com/articles/srep02263#supplementary-information>.

- (51) Doan-Nguyen, V. V. T.; Zhang, S.; Trigg, E. B.; Agarwal, R.; Li, J.; Su, D.; Winey, K. I.; Murray, C. B. Synthesis and X-Ray Characterization of Cobalt Phosphide (Co<sub>2</sub>P) Nanorods for the Oxygen Reduction Reaction. *ACS Nano* **2015**, *9* (8), 8108–8115. <https://doi.org/10.1021/acsnano.5b02191>.
- (52) Jackson, C. SiC AND B4C AS ELECTROCATALYST SUPPORT MATERIALS FOR LOW TEMPERATURE FUEL CELLS, University of Cape Town (UCT), 2017.
- (53) Jackson, C.; Smith, G. T.; Inwood, D. W.; Leach, A. S.; Whalley, P. S.; Callisti, M.; Polcar, T.; Russell, A. E.; Levecque, P.; Kramer, D. Electronic Metal-Support Interaction Enhanced Oxygen Reduction Activity and Stability of Boron Carbide Supported Platinum. *Nat. Commun.* **2017**, *8*. <https://doi.org/10.1038/ncomms15802>.
- (54) Perry, S. C.; Denuault, G. Transient Study of the Oxygen Reduction Reaction on Reduced Pt and Pt Alloys Microelectrodes: Evidence for the Reduction of Pre-Adsorbed Oxygen Species Linked to Dissolved Oxygen. *Phys. Chem. Chem. Phys.* **2015**, *17* (44), 30005–30012. <https://doi.org/10.1039/C5CP04667J>.
- (55) Porter, D. A.; Easterling, K. E. *Phase Transformations in Metals and Alloys*, 2nd ed.; Chapman & Hall, 1992.
- (56) Stephens, I. E. L.; Bondarenko, A. S.; Perez-Alonso, F. J.; Calle-Vallejo, F.; Bech, L.; Johansson, T. P.; Jepsen, A. K.; Frydendal, R.; Knudsen, B. P.; Rossmeisl, J.; et al. Tuning the Activity of Pt(111) for Oxygen Electroreduction by Subsurface Alloying. *J. Am. Chem. Soc.* **2011**, *133* (14), 5485–5491. <https://doi.org/10.1021/ja111690g>.
- (57) Jalan, V.; Taylor, E. J. Importance of Interatomic Spacing in Catalytic Reduction of Oxygen in Phosphoric Acid. *J. Electrochem. Soc.* **1983**, *130* (11), 2299–2302.

<https://doi.org/10.1149/1.2119574>.

- (58) Gasteiger, H. A.; Kocha, S. S.; Sompalli, B.; Wagner, F. T. Activity Benchmarks and Requirements for Pt, Pt-Alloy, and Non-Pt Oxygen Reduction Catalysts for PEMFCs. *Appl. Catal. B Environ.* **2005**, *56* (1–2), 9–35. <https://doi.org/http://dx.doi.org/10.1016/j.apcatb.2004.06.021>.
- (59) Peng, Z.; Yang, H. Designer Platinum Nanoparticles: Control of Shape, Composition in Alloy, Nanostructure and Electrocatalytic Property. *Nano Today* **2009**, *4* (2), 143–164. <https://doi.org/http://dx.doi.org/10.1016/j.nantod.2008.10.010>.
- (60) Luo, Y.; Alonso-Vante, N. The Effect of Support on Advanced Pt-Based Cathodes towards the Oxygen Reduction Reaction. State of the Art. *Electrochim. Acta* **2015**, *179*, 108–118. <https://doi.org/http://dx.doi.org/10.1016/j.electacta.2015.04.098>.
- (61) Zhou, S.; Varughese, B.; Eichhorn, B.; Jackson, G.; McIlwrath, K. Pt–Cu Core–Shell and Alloy Nanoparticles for Heterogeneous NO<sub>x</sub> Reduction: Anomalous Stability and Reactivity of a Core–Shell Nanostructure. *Angew. Chemie Int. Ed.* **2005**, *44* (29), 4539–4543. <https://doi.org/10.1002/anie.200500919>.
- (62) Teng, X.; Black, D.; Watkins, N. J.; Gao, Y.; Yang, H. Platinum-Maghemite Core–Shell Nanoparticles Using a Sequential Synthesis. *Nano Lett.* **2003**, *3* (2), 261–264. <https://doi.org/10.1021/nl025918y>.
- (63) Wang, Y.; Toshima, N. Preparation of Pd–Pt Bimetallic Colloids with Controllable Core/Shell Structures. *J. Phys. Chem. B* **1997**, *101* (27), 5301–5306. <https://doi.org/10.1021/jp9704224>.
- (64) Oezaslan, M.; Hasché, F.; Strasser, P. Pt-Based Core-Shell Catalyst Architectures for Oxygen Fuel Cell Electrodes. *J. Phys. Chem. Lett.* **2013**, *4* (19), 3273–3291.

<https://doi.org/10.1021/jz4014135>.

- (65) Jasinski, R. A New Fuel Cell Cathode Catalyst. *Nature* **1964**, *201* (4925), 1212–1213.
- (66) Jiang, S.; Zhu, C.; Dong, S. Cobalt and Nitrogen-Cofunctionalized Graphene as a Durable Non-Precious Metal Catalyst with Enhanced ORR Activity. *J. Mater. Chem. A* **2013**, *1* (11), 3593–3599. <https://doi.org/10.1039/C3TA01682J>.
- (67) Bezerra, C. W. B.; Zhang, L.; Lee, K.; Liu, H.; Marques, A. L. B.; Marques, E. P.; Wang, H.; Zhang, J. A Review of Fe–N/C and Co–N/C Catalysts for the Oxygen Reduction Reaction. *Electrochim. Acta* **2008**, *53* (15), 4937–4951. <https://doi.org/http://dx.doi.org/10.1016/j.electacta.2008.02.012>.
- (68) Matter, P. H.; Zhang, L.; Ozkan, U. S. The Role of Nanostructure in Nitrogen-Containing Carbon Catalysts for the Oxygen Reduction Reaction. *J. Catal.* **2006**, *239* (1), 83–96. <https://doi.org/http://dx.doi.org/10.1016/j.jcat.2006.01.022>.
- (69) Yuasa, M.; Yamaguchi, A.; Itsuki, H.; Tanaka, K.; Yamamoto, M.; Oyaizu, K. Modifying Carbon Particles with Polypyrrole for Adsorption of Cobalt Ions as Electrocatalytic Site for Oxygen Reduction. *Chem. Mater.* **2005**, *17* (17), 4278–4281. <https://doi.org/10.1021/cm050958z>.
- (70) Chu, D.; Jiang, R. Novel Electrocatalysts for Direct Methanol Fuel Cells. *Solid State Ionics* **2002**, *148* (3–4), 591–599. [https://doi.org/http://dx.doi.org/10.1016/S0167-2738\(02\)00124-8](https://doi.org/http://dx.doi.org/10.1016/S0167-2738(02)00124-8).
- (71) Sawai, K.; Suzuki, N. Heat-Treated Transition Metal Hexacyanometallates as Electrocatalysts for Oxygen Reduction Insensitive to Methanol. *J. Electrochem. Soc.* **2004**, *151* (5), A682. <https://doi.org/10.1149/1.1690287>.
- (72) Liang, Y.; Wang, H.; Diao, P.; Chang, W.; Hong, G.; Li, Y.; Gong, M.; Xie, L.; Zhou, J.; Wang, J.;

et al. Oxygen Reduction Electrocatalyst Based on Strongly Coupled Cobalt Oxide Nanocrystals and Carbon Nanotubes. *J. Am. Chem. Soc.* **2012**, *134* (38), 15849–15857. <https://doi.org/10.1021/ja305623m>.

- (73) Cheng, H.; Scott, K. Carbon-Supported Manganese Oxide Nanocatalysts for Rechargeable Lithium–Air Batteries. *J. Power Sources* **2010**, *195* (5), 1370–1374. <https://doi.org/http://dx.doi.org/10.1016/j.jpowsour.2009.09.030>.
- (74) Gong, K.; Du, F.; Xia, Z.; Durstock, M.; Dai, L. Nitrogen-Doped Carbon Nanotube Arrays with High Electrocatalytic Activity for Oxygen Reduction. *Science (80-. )*. **2009**, *323* (5915), 760–764. <https://doi.org/10.1126/science.1168049>.
- (75) Qu, L.; Liu, Y.; Baek, J.-B.; Dai, L. Nitrogen-Doped Graphene as Efficient Metal-Free Electrocatalyst for Oxygen Reduction in Fuel Cells. *ACS Nano* **2010**, *4* (3), 1321–1326. <https://doi.org/10.1021/nn901850u>.
- (76) Liu, R.; Wu, D.; Feng, X.; Müllen, K. Nitrogen-Doped Ordered Mesoporous Graphitic Arrays with High Electrocatalytic Activity for Oxygen Reduction. *Angew. Chemie Int. Ed.* **2010**, *49* (14), 2565–2569. <https://doi.org/10.1002/anie.200907289>.
- (77) Jaouen, F.; Lefèvre, M.; Dodelet, J. P.; Cai, M. Heat-Treated Fe/N/C Catalysts for O<sub>2</sub> Electroreduction: Are Active Sites Hosted in Micropores? *J. Phys. Chem. B* **2006**, *110* (11), 5553–5558. <https://doi.org/10.1021/jp057135h>.
- (78) Galiote, N. A.; Oliveira, F. E. R.; Lima, F. H. B. FeCo-N-C Oxygen Reduction Electrocatalysts: Activity of the Different Compounds Produced during the Synthesis via Pyrolysis. *Appl. Catal. B Environ.* **2019**, *253* (October 2018), 300–308. <https://doi.org/10.1016/j.apcatb.2019.04.057>.

- (79) Petitto, S. C.; Marsh, E. M.; Carson, G. A.; Langell, M. A. Cobalt Oxide Surface Chemistry: The Interaction of CoO(1 0 0), Co<sub>3</sub>O<sub>4</sub>(1 1 0) and Co<sub>3</sub>O<sub>4</sub>(1 1 1) with Oxygen and Water. *J. Mol. Catal. A Chem.* **2008**, *281* (1–2), 49–58. <https://doi.org/http://dx.doi.org/10.1016/j.molcata.2007.08.023>.
- (80) Wang, Y.-J.; Wilkinson, D. P.; Zhang, J. Noncarbon Support Materials for Polymer Electrolyte Membrane Fuel Cell Electrocatalysts. *Chem. Rev.* **2011**, *111* (12), 7625–7651. <https://doi.org/10.1021/cr100060r>.
- (81) Katsounaros, I.; Cherevko, S.; Zeradjanin, A. R.; Mayrhofer, K. J. J. Oxygen Electrochemistry as a Cornerstone for Sustainable Energy Conversion. *Angew. Chemie - Int. Ed.* **2014**, *53* (1), 102–121. <https://doi.org/10.1002/anie.201306588>.
- (82) Siracusano, S.; Van Dijk, N.; Payne-Johnson, E.; Baglio, V.; Aricò, A. S. Nanosized IrO<sub>x</sub> and IrRuO<sub>x</sub> Electrocatalysts for the O<sub>2</sub> Evolution Reaction in PEM Water Electrolysers. *Appl. Catal. B Environ.* **2015**, *164*, 488–495. <https://doi.org/http://dx.doi.org/10.1016/j.apcatb.2014.09.005>.
- (83) OSAKA, T.; ISHIBASHI, H.; ENDO, T.; YOSHIDA, T. ChemInform Abstract: OXYGEN EVOLUTION REACTION ON TRANSITION METAL BORIDES. *Chem. Informationsd.* **2016**, *12* (20). <https://doi.org/10.1002/chin.198120022>.
- (84) Yin, S.; Tu, W.; Sheng, Y.; Du, Y.; Kraft, M.; Borgna, A.; Xu, R. A Highly Efficient Oxygen Evolution Catalyst Consisting of Interconnected Nickel–Iron-Layered Double Hydroxide and Carbon Nanodomains. *Adv. Mater.* **2018**, *30* (5), 1–9. <https://doi.org/10.1002/adma.201705106>.
- (85) Godwin, I. J.; Lyons, M. E. G. Enhanced Oxygen Evolution at Hydrous Nickel Oxide Electrodes

via Electrochemical Ageing in Alkaline Solution. *Electrochem. commun.* **2013**, *32*, 39–42.  
<https://doi.org/10.1016/j.elecom.2013.03.040>.

- (86) Wang, X.; Han, X.; Lim, M.; Singh, N.; Chee, †; Gan, L.; Jan, M.; Lee, P. S. Nickel Cobalt Oxide-Single Wall Carbon Nanotube Composite Material for Superior Cycling Stability and High-Performance Supercapacitor Application. **2012**. <https://doi.org/10.1021/jp3028353>.
- (87) Roy, A.; Ray, A.; Saha, S.; Ghosh, M.; Das, T.; Satpati, B.; Nandi, M.; Das, S. NiO-CNT Composite for High Performance Supercapacitor Electrode and Oxygen Evolution Reaction. *Electrochim. Acta* **2018**, *283*, 327–337. <https://doi.org/10.1016/j.electacta.2018.06.154>.
- (88) Frydendal, R. ; Chorkendorff, I. ;; Stephens, I. E. L. General Rights Improving Performance of Catalysts for Water Electrolysis The MnO<sub>x</sub> Case.
- (89) Man, I. C. General Rights Theoretical Study of Electro-Catalysts for Oxygen Evolution.
- (90) Pasqualetti, A. M.; Olu, P.-Y.; Chatenet, M.; Lima, F. H. B. Borohydride Electrooxidation on Carbon-Supported Noble Metal Nanoparticles: Insights into Hydrogen and Hydroxyborane Formation. **2015**. <https://doi.org/10.1021/acscatal.5b00107>.
- (91) Wei Seh, Z.; Kibsgaard, J.; Dickens, C. F.; Chorkendorff, I.; Nørskov, J. K.; Jaramillo, T. F.; She, Z. W.; Kibsgaard, J.; Dickens, C. F.; Chorkendorff, I.; et al. Combining Theory and Experiment in Electrocatalysis: Insights into Materials Design. *Science (80-. )*. **2017**, *355* (6321).  
<https://doi.org/10.1126/science.aad4998>.
- (92) Bockris, J. O. M. Kinetics of Activation Controlled Consecutive Electrochemical Reactions: Anodic Evolution of Oxygen. *J. Chem. Phys.* **1956**, *24* (4), 817–827.  
<https://doi.org/10.1063/1.1742616>.

- (93) Fabbri, E.; Haberer, A.; Waltar, K.; Kötz, R.; Schmidt, T. J. Developments and Perspectives of Oxide-Based Catalysts for the Oxygen Evolution Reaction. *Catal. Sci. Technol.* **2014**, *4* (11), 3800–3821. <https://doi.org/10.1039/c4cy00669k>.
- (94) Otagawa, T.; Bockris, J. O. Oxygen Evolution on Perovskites. *J. Phys. Chem* **1983**, *87* (15), 2960–2971. <https://doi.org/10.1021/j100238a048>.
- (95) Wade, W. H.; Hackerman, N. Anodic Phenomena at an Iron Electrode. *Trans. Faraday Soc.* **1957**, *53*, 1636–1647. <https://doi.org/10.1039/tf9575301636>.
- (96) Zhu, C.; Fu, S.; Shi, Q.; Du, D.; Lin, Y. Single-Atom Electrocatalysts. *Angew. Chemie - Int. Ed.* **2017**, *56* (45), 13944–13960. <https://doi.org/10.1002/anie.201703864>.
- (97) Gandía, L. M.; Oroz, R.; Ursúa, A.; Sanchis, P.; Diéguez, P. M. Renewable Hydrogen Production: Performance of an Alkaline Water Electrolyzer Working under Emulated Wind Conditions. *Energy and Fuels* **2007**, *21* (3), 1699–1706. <https://doi.org/10.1021/ef060491u>.
- (98) Oh, H. S.; Nong, H. N.; Reier, T.; Gliech, M.; Strasser, P. Oxide-Supported Ir Nanodendrites with High Activity and Durability for the Oxygen Evolution Reaction in Acid PEM Water Electrolyzers. *Chem. Sci.* **2015**, *6* (6), 3321–3328. <https://doi.org/10.1039/c5sc00518c>.
- (99) Zheng, Y.; Jiao, Y.; Zhu, Y.; Cai, Q.; Li, L. H.; Han, Y.; Chen, Y.; Qiao, S. Molecule-Level G-C<sub>3</sub>N<sub>4</sub> Coordinated Transition Metals as a New Class of Electrocatalysts for Oxygen Electrode Reactions. **2017**, 4–7. <https://doi.org/10.1021/jacs.6b13100>.
- (100) Kocha, S. S. Electrochemical Degradation: Electrocatalyst and Support Durability. In *Polymer Electrolyte Fuel Cell Degradation*; 2011; pp 89–214. <https://doi.org/10.1016/B978-0-12-386936-4.10003-X>.



- (101) Barbir, F. *Fuel Cell Basics - Overview*; 2008.
- (102) Adler, S. B. Factors Governing Oxygen Reduction in Solid Oxide Fuel Cell Cathodes †. *Chem. Rev.* **2004**, *104* (10), 4791–4844. <https://doi.org/10.1021/cr020724o>.
- (103) Yoon, Y. G.; Park, G. G.; Yang, T. H.; Han, J. N.; Lee, W. Y.; Kim, C. S. Effect of Pore Structure of Catalyst Layer in a PEMFC on Its Performance. *Int. J. Hydrogen Energy* **2003**, *28* (6), 657–662. [https://doi.org/http://dx.doi.org/10.1016/S0360-3199\(02\)00156-8](https://doi.org/http://dx.doi.org/10.1016/S0360-3199(02)00156-8).
- (104) Xie, J.; More, K. L.; Zawodzinski, T. A.; Smith, W. H. Porosimetry of MEAs Made by “Thin Film Decal” Method and Its Effect on Performance of PEFCs. *J. Electrochem. Soc.* **2004**, *151* (11), A1841–A1846. <https://doi.org/10.1149/1.1796991>.
- (105) Uchida, M.; Aoyama, Y.; Eda, N.; Ohta, A. New Preparation Method for Polymer-Electrolyte Fuel Cells. *J. Electrochem. Soc.* **1995**, *142* (2), 463–468. <https://doi.org/10.1149/1.2044068>.
- (106) Wilson, M. S.; Gottesfeld, S. Thin-Film Catalyst Layers for Polymer Electrolyte Fuel Cell Electrodes. *J. Appl. Electrochem.* **1992**, *22* (1), 1–7. <https://doi.org/10.1007/BF01093004>.
- (107) Rajalakshmi, N.; Dhathathreyan, K. S. Catalyst Layer in PEMFC Electrodes—Fabrication, Characterisation and Analysis. *Chem. Eng. J.* **2007**, *129* (1–3), 31–40. <https://doi.org/http://dx.doi.org/10.1016/j.cej.2006.10.035>.
- (108) Lesch, A.; Cortés-Salazar, F.; Bassetto, V. C.; Amstutz, V.; Girault, H. H. Inkjet Printing Meets Electrochemical Energy Conversion. *Chimia (Aarau)*. **2015**, *69* (5), 284–289. <https://doi.org/10.2533/chimia.2015.284>.
- (109) Bladergroen, B.; Su, H.; Pasupathi, S.; Linkov, V. *Overview of Membrane Electrode Assembly Preparation Methods for Solid Polymer Electrolyte Electrolyzer*; 2012. <https://doi.org/40146>.

- (110) Ismagilov, Z. R.; Podyacheva, O. Y.; Solonenko, O. P.; Pushkarev, V. V.; Kuz'min, V. I.; Ushakov, V. A.; Rudina, N. A. Application of Plasma Spraying in the Preparation of Metal-Supported Catalysts. *Catal. Today* **1999**, *51* (3–4), 411–417. [https://doi.org/http://dx.doi.org/10.1016/S0920-5861\(99\)00030-9](https://doi.org/http://dx.doi.org/10.1016/S0920-5861(99)00030-9).
- (111) Wan, C.-H.; Lin, M.-T.; Zhuang, Q.-H.; Lin, C.-H. Preparation and Performance of Novel MEA with Multi Catalyst Layer Structure for PEFC by Magnetron Sputter Deposition Technique. *Surf. Coatings Technol.* **2006**, *201* (1–2), 214–222. <https://doi.org/http://dx.doi.org/10.1016/j.surfcoat.2005.11.119>.
- (112) Wang, C.; Waje, M.; Wang, X.; Tang, J. M.; Haddon, R. C.; Yan, Y. Proton Exchange Membrane Fuel Cells with Carbon Nanotube Based Electrodes. *Nano Lett.* **2004**, *4* (2), 345–348. <https://doi.org/10.1021/nl034952p>.
- (113) Thompson, S. D.; Jordan, L. R.; Forsyth, M. Platinum Electrodeposition for Polymer Electrolyte Membrane Fuel Cells. *Electrochim. Acta* **2001**, *46* (10–11), 1657–1663. [https://doi.org/http://dx.doi.org/10.1016/S0013-4686\(00\)00767-2](https://doi.org/http://dx.doi.org/10.1016/S0013-4686(00)00767-2).
- (114) Martin, S.; Garcia-Ybarra, P. L.; Castillo, J. L. Electrospray Deposition of Catalyst Layers with Ultra-Low Pt Loadings for PEM Fuel Cells Cathodes. *J. Power Sources* **2010**, *195* (9), 2443–2449. <https://doi.org/http://dx.doi.org/10.1016/j.jpowsour.2009.11.092>.
- (115) Morikawa, H.; Tsuihiji, N.; Mitsui, T.; Kanamura, K. Preparation of Membrane Electrode Assembly for Fuel Cell by Using Electrophoretic Deposition Process. *J. Electrochem. Soc.* **2004**, *151* (10), A1733–A1737. <https://doi.org/10.1149/1.1793195>.
- (116) Lesch, A. Print-Light-Synthesis of Platinum Nanostructured Indium-Tin-Oxide Electrodes for Energy Research. *Adv. Mater. Technol.* **2018**, *3* (2).

<https://doi.org/10.1002/admt.201700201>.

- (117) Sasi Kumar, G.; Raja, M.; Parthasarathy, S.; Kumar, G. S.; Raja, M.; Parthasarathy, S. High Performance Electrodes with Very Low Platinum Loading for Polymer Electrolyte Fuel Cells. *Electrochim. Acta* **1995**, *40* (3), 285–290. [https://doi.org/http://dx.doi.org/10.1016/0013-4686\(94\)00270-B](https://doi.org/http://dx.doi.org/10.1016/0013-4686(94)00270-B).
- (118) Tseng, H.-Y.; Subramanian, V. All Inkjet-Printed, Fully Self-Aligned Transistors for Low-Cost Circuit Applications. *Org. Electron.* **2011**, *12* (2), 249–256. <https://doi.org/http://dx.doi.org/10.1016/j.orgel.2010.11.013>.
- (119) Briand, D.; Molina-Lopez, F.; Quintero, A. V.; Ataman, C.; Courbat, J.; de Rooij, N. F. Why Going Towards Plastic and Flexible Sensors? *Procedia Eng.* **2011**, *25*, 8–15. <https://doi.org/http://dx.doi.org/10.1016/j.proeng.2011.12.004>.
- (120) Molina-Lopez, F.; Briand, D.; de Rooij, N. F. All Additive Inkjet Printed Humidity Sensors on Plastic Substrate. *Sensors Actuators B Chem.* **2012**, *166–167*, 212–222. <https://doi.org/http://dx.doi.org/10.1016/j.snb.2012.02.042>.
- (121) Briand, D.; Molina-Lopez, F.; Quintero, A. V.; Mattana, G.; de Rooij, N. F. Printed Sensors on Smart RFID Labels for Logistics. In *New Circuits and Systems Conference (NEWCAS), 2012 IEEE 10th International*; 2012; pp 449–452. <https://doi.org/10.1109/NEWCAS.2012.6329053>.
- (122) Hoath, S. D.; Vadiillo, D. C.; Harlen, O. G.; McIlroy, C.; Morrison, N. F.; Hsiao, W.-K.; Tuladhar, T. R.; Jung, S.; Martin, G. D.; Hutchings, I. M. Inkjet Printing of Weakly Elastic Polymer Solutions. *J. Nonnewton. Fluid Mech.* **2014**, *205* (0), 1–10. <https://doi.org/http://dx.doi.org/10.1016/j.jnnfm.2014.01.002>.
- (123) Deiner, L. J.; Reitz, T. L. Inkjet and Aerosol Jet Printing of Electrochemical Devices for Energy

Conversion and Storage. *Adv. Eng. Mater.* **2017**, *19* (7).  
<https://doi.org/10.1002/adem.201600878>.

(124) Lesch, A.; Maye, S.; Jović, M.; Gumy, F.; Tacchini, P.; Girault, H. H. Analytical Sensing Platforms with Inkjet Printed Electrodes. In *Advanced Materials - TechConnect Briefs 2016*; 2016; Vol. 3, pp 121–124.

(125) Öhlund, T.; Schuppert, A. K.; Hummelgård, M.; Bäckström, J.; Nilsson, H. E.; Olin, H. Inkjet Fabrication of Copper Patterns for Flexible Electronics: Using Paper with Active Precoatings. *ACS Appl. Mater. Interfaces* **2015**, *7* (33), 18273–18282.  
<https://doi.org/10.1021/acsami.5b03061>.

(126) Liu, X.; Shen, Y.; Yang, R.; Zou, S.; Ji, X.; Shi, L.; Zhang, Y.; Liu, D.; Xiao, L.; Zheng, X.; et al. Inkjet Printing Assisted Synthesis of Multicomponent Mesoporous Metal Oxides for Ultrafast Catalyst Exploration. *Nano Lett.* **2012**, *12* (11), 5733–5739.  
<https://doi.org/10.1021/nl302992q>.

(127) Reddington, E.; Sapienza, A.; Gurau, B.; Viswanathan, R.; Sarangapani, S.; Smotkin, E. S.; Mallouk, T. E. Combinatorial Electrochemistry: A Highly Parallel, Optical Screening Method for Discovery of Better Electrocatalysts. *Science* (80-. ). **1998**, *280* (5370), 1735–1737.  
<https://doi.org/10.1126/science.280.5370.1735>.

(128) Fernández, J. L.; Bard, A. J. Scanning Electrochemical Microscopy. 47. Imaging Electrocatalytic Activity for Oxygen Reduction in an Acidic Medium by the Tip Generation–Substrate Collection Mode. *Anal. Chem.* **2003**, *75* (13), 2967–2974. <https://doi.org/10.1021/ac0340354>.

(129) Seley, D.; Ayers, K.; Parkinson, B. A. Combinatorial Search for Improved Metal Oxide Oxygen Evolution Electrocatalysts in Acidic Electrolytes. *ACS Comb. Sci.* **2013**, *15* (2), 82–89.

<https://doi.org/10.1021/co300086h>.

- (130) Hurt, C.; Brandt, M.; Priya, S. S.; Bhatelia, T.; Patel, J.; Selvakannan, P. R.; Bhargava, S. Combining Additive Manufacturing and Catalysis: A Review. *Catal. Sci. Technol.* **2017**, *7* (16), 3421–3439. <https://doi.org/10.1039/c7cy00615b>.
- (131) Saha, M. S.; Malevich, D.; Halliop, E.; Pharoah, J. G.; Peppley, B. A.; Karan, K. Electrochemical Activity and Catalyst Utilization of Low Pt and Thickness Controlled Membrane Electrode Assemblies. *J. Electrochem. Soc.* **2011**, *158* (5), B562–B567. <https://doi.org/10.1149/1.3559188>.
- (132) Shukla, S.; Domican, K.; Karan, K.; Bhattacharjee, S.; Secanell, M. Analysis of Low Platinum Loading Thin Polymer Electrolyte Fuel Cell Electrodes Prepared by Inkjet Printing. *Electrochim. Acta* **2015**, *156*, 289–300. <https://doi.org/http://dx.doi.org/10.1016/j.electacta.2015.01.028>.
- (133) Taylor, A. D.; Kim, E. Y.; Humes, V. P.; Kizuka, J.; Thompson, L. T. Inkjet Printing of Carbon Supported Platinum 3-D Catalyst Layers for Use in Fuel Cells. *J. Power Sources* **2007**, *171* (1), 101–106. <https://doi.org/http://dx.doi.org/10.1016/j.jpowsour.2007.01.024>.
- (134) Rosen, Y. S.; Yakushenko, A.; Offenhäusser, A.; Magdassi, S. Self-Reducing Copper Precursor Inks and Photonic Additive Yield Conductive Patterns under Intense Pulsed Light. *ACS Omega* **2017**, *2* (2), 573–581. <https://doi.org/10.1021/acsomega.6b00478>.
- (135) Tetzner, K.; Schroder, K. A.; Bock, K. Photonic Curing of Sol-Gel Derived HfO<sub>2</sub>dielectrics for Organic Field-Effect Transistors. *Ceram. Int.* **2014**, *40* (10), 15753–15761. <https://doi.org/10.1016/j.ceramint.2014.07.099>.
- (136) Joo, S. J.; Park, S. H.; Moon, C. J.; Kim, H. S. A Highly Reliable Copper Nanowire/Nanoparticle Ink Pattern with High Conductivity on Flexible Substrate Prepared via a Flash Light-Sintering

Technique. *ACS Appl. Mater. Interfaces* **2015**, *7* (10), 5674–5684.  
<https://doi.org/10.1021/am506765p>.

- (137) Kim, H. S.; Dhage, S. R.; Shim, D. E.; Hahn, H. T. Intense Pulsed Light Sintering of Copper Nanoink for Printed Electronics. *Appl. Phys. A Mater. Sci. Process.* **2009**, *97* (4), 791–798.  
<https://doi.org/10.1007/s00339-009-5360-6>.
- (138) Jović, M.; Zhu, Y.; Lesch, A.; Bondarenko, A.; Cortés-Salazar, F.; Gumy, F.; Girault, H. H. Inkjet-Printed Microtiter Plates for Portable Electrochemical Immunoassays. *J. Electroanal. Chem.* **2017**, *786*, 69–76. <https://doi.org/10.1016/j.jelechem.2016.12.051>.
- (139) Cui, H.-W.; Jiu, J.-T.; Nagao, S.; Sugahara, T.; Suganuma, K.; Uchida, H.; Schroder, K. A. Ultra-Fast Photonic Curing of Electrically Conductive Adhesives Fabricated from Vinyl Ester Resin and Silver Micro-Flakes for Printed Electronics. *RSC Adv.* **2014**, *4* (31), 15914–15922.  
<https://doi.org/10.1039/C4RA00292J>.
- (140) Safo, I. A.; Oezaslan, M. Electrochemical Cleaning of Polyvinylpyrrolidone-Capped Pt Nanocubes for the Oxygen Reduction Reaction. *Electrochim. Acta* **2017**, *241*, 544–552.  
<https://doi.org/10.1016/j.electacta.2017.04.118>.
- (141) Schroder, K. A.; McCool, S. C.; Furlan, W. F. Broadcast Photonic Curing of Metallic Nanoparticle Films. In *2006 NSTI Nanotechnology Conference and Trade Show - NSTI Nanotech 2006 Technical Proceedings*; 2006; Vol. 3, pp 198–201.
- (142) Ryu, J.; Kim, H.-S. S.; Hahn, H. T. Reactive Sintering of Copper Nanoparticles Using Intense Pulsed Light for Printed Electronics. *J. Electron. Mater.* **2011**, *40* (1), 42–50.  
<https://doi.org/10.1007/s11664-010-1384-0>.
- (143) Dharmadasa, R.; Jha, M.; Amos, D. A.; Druffel, T. Room Temperature Synthesis of a Copper

- Ink for the Intense Pulsed Light Sintering of Conductive Copper Films. *ACS Appl. Mater. Interfaces* **2013**, 5 (24), 13227–13234. <https://doi.org/10.1021/am404226e>.
- (144) Druffel, T.; Dharmadasa, R.; Lavery, B. W.; Ankireddy, K. Intense Pulsed Light Processing for Photovoltaic Manufacturing. *Sol. Energy Mater. Sol. Cells* **2018**, 174, 359–369. <https://doi.org/10.1016/j.solmat.2017.09.010>.
- (145) Pierret, R. F.; Neudeck, G. W. *Advanced Semiconductor Fundamentals*; 1987; Vol. 6. <https://doi.org/10.1017/CBO9781107415324.004>.
- (146) Chung, W. H.; Hwang, H. J.; Lee, S. H.; Kim, H. S. In Situ Monitoring of a Flash Light Sintering Process Using Silver Nano-Ink for Producing Flexible Electronics. *Nanotechnology* **2013**, 24 (3), 35202–35210. <https://doi.org/10.1088/0957-4484/24/3/035202>.
- (147) Bauer, C.; Abid, J. P.; Girault, H. H. Role of Adsorbates on Dynamics of Hot-Electron (Type I and II) Thermalization within Gold Nanoparticles. *Comptes Rendus Chim.* **2006**, 9 (2), 261–267. <https://doi.org/10.1016/j.crci.2005.03.030>.
- (148) Bauer, C.; Abid, J. P.; Girault, H. H. Size Dependence Investigations of Hot Electron Cooling Dynamics in Metal/Adsorbates Nanoparticles. *Chem. Phys.* **2005**, 319 (1–3), 409–421. <https://doi.org/10.1016/j.chemphys.2005.06.040>.
- (149) Clavero, C. Plasmon-Induced Hot-Electron Generation at Nanoparticle/Metal-Oxide Interfaces for Photovoltaic and Photocatalytic Devices. **2014**. <https://doi.org/10.1038/NPHOTON.2013.238>.
- (150) Hwang, H.-J.; Oh, K.-H.; Kim, H.-S. All-Photonic Drying and Sintering Process via Flash White Light Combined with Deep-UV and near-Infrared Irradiation for Highly Conductive Copper Nano-Ink. *Sci. Rep.* **2016**, 6. <https://doi.org/10.1038/srep19696>.

- (151) Lesch, A.; Cortés-Salazar, F.; Prudent, M.; Delobel, J.; Rastgar, S.; Lion, N.; Tissot, J.-D.; Tacchini, P.; Girault, H. H. Large Scale Inkjet-Printing of Carbon Nanotubes Electrodes for Antioxidant Assays in Blood Bags. *J. Electroanal. Chem.* **2014**, *717–718* (0), 61–68. <https://doi.org/http://dx.doi.org/10.1016/j.jelechem.2013.12.027>.
- (152) Xiao, J.; Bian, X.; Liao, L.; Zhang, S.; Ji, C.; Liu, B. Nitrogen-Doped Mesoporous Graphene as a Synergistic Electrocatalyst Matrix for High-Performance Oxygen Reduction Reaction. *ACS Appl. Mater. Interfaces* **2014**, *6* (20), 17654–17660. <https://doi.org/10.1021/am503895w>.
- (153) Nallan, H. C.; Sadie, J. A.; Kitsomboonloha, R.; Volkman, S. K.; Subramanian, V. Systematic Design of Jettable Nanoparticle-Based Inkjet Inks: Rheology, Acoustics, and Jettable. *Langmuir* **2014**, *30* (44), 13470–13477. <https://doi.org/10.1021/la502903y>.
- (154) Reis, N.; Ainsley, C.; Derby, B. Viscosity and Acoustic Behavior of Ceramic Suspensions Optimized for Phase-Change Ink-Jet Printing. *J. Am. Ceram. Soc.* **2005**, *88* (4), 802–808. <https://doi.org/10.1111/j.1551-2916.2005.00138.x>.
- (155) Derby, B. Inkjet Printing of Functional and Structural Materials: Fluid Property Requirements, Feature Stability, and Resolution. *Annu. Rev. Mater. Res.* **2010**, *40* (1), 395–414. <https://doi.org/10.1146/annurev-matsci-070909-104502>.
- (156) Momand, H. The Effect of Ultrasound on Nafion® Polymer in Proton Exchange Membrane Fuel Cells (PEMFCs), University of Birmingham, 2013.
- (157) Gao, M.; Li, L.; Song, Y. Inkjet Printing Wearable Electronic Devices. *J. Mater. Chem. C* **2017**, *5* (12), 2971–2993. <https://doi.org/10.1039/c7tc00038c>.
- (158) Liu, X.; Tarn, T.-J.; Huang, F.; Fan, J. Recent Advances in Inkjet Printing Synthesis of Functional Metal Oxides. *Particuology* **2015**, *19*, 1–13. <https://doi.org/10.1016/j.partic.2014.05.001>.



- (159) Özkan, M.; Hashmi, S. G.; Halme, J.; Karakoç, A.; Sarikka, T.; Paltakari, J.; Lund, P. D. Inkjet-Printed Platinum Counter Electrodes for Dye-Sensitized Solar Cells. *Org. Electron. physics, Mater. Appl.* **2017**, *44*, 159–167. <https://doi.org/10.1016/j.orgel.2017.02.015>.
- (160) Kimmich, D.; Taffa, D. H.; Dosche, C.; Wark, M.; Wittstock, G. Combinatorial Screening of Photoanode Materials - Uniform Platform for Compositional Arrays and Macroscopic Electrodes. *Electrochim. Acta* **2018**, *259*, 204–212. <https://doi.org/10.1016/j.electacta.2017.10.147>.
- (161) Niu, W.; Li, L.; Liu, X.; Wang, N.; Liu, J.; Zhou, W.; Tang, Z.; Chen, S. Mesoporous N-Doped Carbons Prepared with Thermally Removable Nanoparticle Templates: An Efficient Electrocatalyst for Oxygen Reduction Reaction. *J. Am. Chem. Soc.* **2015**, *137* (16), 5555–5562. <https://doi.org/10.1021/jacs.5b02027>.
- (162) Neyerlin, K. C.; Bugosh, G.; Forgie, R.; Liu, Z.; Strasser, P. Combinatorial Study of High-Surface-Area Binary and Ternary Electrocatalysts for the Oxygen Evolution Reaction. *J. Electrochem. Soc.* **2009**, *156* (3), B363–B369. <https://doi.org/10.1149/1.3049820>.
- (163) McCrory, C. C. L.; Jung, S.; Ferrer, I. M.; Chatman, S. M.; Peters, J. C.; Jaramillo, T. F. Benchmarking Hydrogen Evolving Reaction and Oxygen Evolving Reaction Electrocatalysts for Solar Water Splitting Devices. *J. Am. Chem. Soc.* **2015**, *137* (13), 4347–4357. <https://doi.org/10.1021/ja510442p>.
- (164) Li, J.; Stein, H. S.; Sliozberg, K.; Liu, J.; Liu, Y.; Sertic, G.; Scanley, E.; Ludwig, A.; Schroers, J.; Schuhmann, W.; et al. Combinatorial Screening of Pd-Based Quaternary Electrocatalysts for Oxygen Reduction Reaction in Alkaline Media. *J. Mater. Chem. A* **2017**, *5* (1), 67–72. <https://doi.org/10.1039/C6TA08088J>.

- (165) Osgood, H.; Devaguptapu, S. V.; Xu, H.; Cho, J.; Wu, G. Transition Metal (Fe, Co, Ni, and Mn) Oxides for Oxygen Reduction and Evolution Bifunctional Catalysts in Alkaline Media. *Nano Today* **2016**, *11* (5), 601–625. <https://doi.org/10.1016/j.nantod.2016.09.001>.
- (166) Kang, H.; Sowade, E.; Baumann, R. R. Direct Intense Pulsed Light Sintering of Inkjet-Printed Copper Oxide Layers within Six Milliseconds. *ACS Appl. Mater. Interfaces* **2014**, *6* (3), 1682–1687. <https://doi.org/10.1021/am404581b>.
- (167) Secor, E. B.; Ahn, B. Y.; Gao, T. Z.; Lewis, J. A.; Hersam, M. C. Rapid and Versatile Photonic Annealing of Graphene Inks for Flexible Printed Electronics. *Adv. Mater.* **2015**, *27* (42), 6683–6688. <https://doi.org/10.1002/adma.201502866>.
- (168) Hwang, H.; Oh, K.-H.; Kim, H.-S. All-Photonic Drying and Sintering Process via Flash White Light Combined with Deep-UV and near- Infrared Irradiation for Highly Conductive Copper Nano-Ink. *Nat. Publ. Gr.* **2016**, No. January, 1–10. <https://doi.org/10.1038/srep19696>.
- (169) Perelaer, J.; Abbel, R.; Wünscher, S.; Jani, R.; Van Lammeren, T.; Schubert, U. S. Roll-to-Roll Compatible Sintering of Inkjet Printed Features by Photonic and Microwave Exposure: From Non-Conductive Ink to 40% Bulk Silver Conductivity in Less than 15 Seconds. *Adv. Mater.* **2012**, *24* (19), 2620–2625. <https://doi.org/10.1002/adma.201104417>.
- (170) Park, S.-H.; Kim, H.-S. Flash Light Sintering of Nickel Nanoparticles for Printed Electronics. *Thin Solid Films* **2014**, *550*, 575–581. <https://doi.org/10.1016/j.tsf.2013.11.075>.
- (171) Paglia, F.; Vak, D.; Van Embden, J.; Chesman, A. S. R.; Martucci, A.; Jasieniak, J. J.; Della Gaspera, E. Photonic Sintering of Copper through the Controlled Reduction of Printed CuO Nanocrystals. *ACS Appl. Mater. Interfaces* **2015**, *7* (45), 25473–25478. <https://doi.org/10.1021/acsami.5b08430>.

- (172) Rager, M. S.; Aytug, T.; Veith, G. M.; Joshi, P. Low-Thermal-Budget Photonic Processing of Highly Conductive Cu Interconnects Based on CuO Nanoinks: Potential for Flexible Printed Electronics. *ACS Appl. Mater. Interfaces* **2016**, *8* (3), 2441–2448. <https://doi.org/10.1021/acsami.5b12156>.
- (173) Chung, W.-H. W.-H. H.; Hwang, H.-J. J. H.-J.; Kim, H.-S. S. H.-S. H.-S. S. H.-S. Flash Light Sintered Copper Precursor/Nanoparticle Pattern with High Electrical Conductivity and Low Porosity for Printed Electronics. *Thin Solid Films* **2015**, *580*, 61–70. <https://doi.org/10.1016/j.tsf.2015.03.004>.
- (174) Zhao, Q.; Yan, Z.; Chen, C.; Chen, J. Spinel: Controlled Preparation, Oxygen Reduction/Evolution Reaction Application, and Beyond. *Chem. Rev.* **2017**, *117* (15), 10121–10211. <https://doi.org/10.1021/acs.chemrev.7b00051>.
- (175) Tahir, M.; Pan, L.; Idrees, F.; Zhang, X.; Wang, L.; Zou, J.-J.; Wang, Z. L. Electrocatalytic Oxygen Evolution Reaction for Energy Conversion and Storage: A Comprehensive Review. *Nano Energy* **2017**, *37*, 136–157. <https://doi.org/10.1016/j.nanoen.2017.05.022>.
- (176) Liang, Y.; Li, Y.; Wang, H.; Zhou, J.; Wang, J.; Regier, T.; Dai, H. Co<sub>3</sub>O<sub>4</sub> Nanocrystals on Graphene as a Synergistic Catalyst for Oxygen Reduction Reaction. *Nat Mater* **2011**, *10* (10), 780–786. <https://doi.org/http://www.nature.com/nmat/journal/v10/n10/abs/nmat3087.html#supplementary-information>.
- (177) Pletcher, D.; Li, X.; Price, S. W. T.; Russell, A. E.; Sönmez, T.; Thompson, S. J. Comparison of the Spinel Co<sub>3</sub>O<sub>4</sub> and NiCo<sub>2</sub>O<sub>4</sub> as Bifunctional Oxygen Catalysts in Alkaline Media. *Electrochim. Acta* **2016**, *188*, 286–293. <https://doi.org/10.1016/j.electacta.2015.10.020>.

- (178) Zhang, H.; Li, H.; Wang, H.; He, K.; Wang, S.; Tang, Y.; Chen, J. NiCo<sub>2</sub>O<sub>4</sub>/N-Doped Graphene as an Advanced Electrocatalyst for Oxygen Reduction Reaction. *J. Power Sources* **2015**, *280*, 640–648. <https://doi.org/10.1016/j.jpowsour.2015.01.147>.
- (179) Liu, X.; Liu, W.; Ko, M.; Park, M.; Kim, M. G.; Oh, P.; Chae, S.; Park, S.; Casimir, A.; Wu, G.; et al. Metal (Ni, Co)-Metal Oxides/Graphene Nanocomposites as Multifunctional Electrocatalysts. *Adv. Funct. Mater.* **2015**, *25* (36), 5799–5808. <https://doi.org/10.1002/adfm.201502217>.
- (180) Ge, X.; Liu, Y.; Goh, F. W. T.; Hor, T. S. A.; Zong, Y.; Xiao, P.; Zhang, Z.; Lim, S. H.; Li, B.; Wang, X.; et al. Dual-Phase Spinel MnCo<sub>2</sub>O<sub>4</sub> and Spinel MnCo<sub>2</sub>O<sub>4</sub> /Nanocarbon Hybrids for Electrocatalytic Oxygen Reduction and Evolution. *ACS Appl. Mater. Interfaces* **2014**, *6* (15), 12684–12691. <https://doi.org/10.1021/am502675c>.
- (181) Wang, M.; Huang, J.; Wang, M.; Zhang, D.; Zhang, W.; Li, W.; Chen, J. Co<sub>3</sub>O<sub>4</sub> Nanorods Decorated Reduced Graphene Oxide Composite for Oxygen Reduction Reaction in Alkaline Electrolyte. *Electrochem. commun.* **2013**, *34*, 299–303. <https://doi.org/10.1016/j.elecom.2013.07.017>.
- (182) Zhang, T.; He, C.; Sun, F.; Ding, Y.; Wang, M.; Peng, L.; Wang, J.; Lin, Y. Co<sub>3</sub>O<sub>4</sub> Nanoparticles Anchored on Nitrogen-Doped Reduced Graphene Oxide as a Multifunctional Catalyst for H<sub>2</sub>O<sub>2</sub> Reduction, Oxygen Reduction and Evolution Reaction. *Sci. Rep.* **2017**, *7*. <https://doi.org/10.1038/srep43638>.
- (183) Tong, Y.; Chen, P.; Zhou, T.; Xu, K.; Chu, W.; Wu, C.; Xie, Y. A Bifunctional Hybrid Electrocatalyst for Oxygen Reduction and Evolution: Cobalt Oxide Nanoparticles Strongly Coupled to B,N-Decorated Graphene. *Angew. Chemie - Int. Ed.* **2017**, *56* (25), 7121–7125.

<https://doi.org/10.1002/anie.201702430>.

- (184) Li, Y.; Yang, J.; Zhao, N.; Huang, J.; Zhou, Y.; Xu, K.; Zhao, N. Facile Fabrication of N-Doped Three-Dimensional Reduced Graphene Oxide as a Superior Electrocatalyst for Oxygen Reduction Reaction. *Appl. Catal. A Gen.* **2017**, *534*, 30–39. <https://doi.org/10.1016/j.apcata.2017.01.014>.
- (185) Molina-García, M. A.; Rees, N. V. “Metal-Free” Electrocatalysis: Quaternary-Doped Graphene and the Alkaline Oxygen Reduction Reaction. *Appl. Catal. A Gen.* **2018**, *553*, 107–116. <https://doi.org/10.1016/j.apcata.2017.12.014>.
- (186) Torrisi, F.; Hasan, T.; Wu, W.; Sun, Z.; Lombardo, A.; Kulmala, T. S.; Hsieh, G.-W.; Jung, S.; Bonaccorso, F.; Paul, P. J.; et al. Inkjet-Printed Graphene Electronics. *ACS Nano* **2012**, *6* (4), 2992–3006. <https://doi.org/10.1021/nn2044609>.
- (187) Secor, E. B.; Prabhumirashi, P. L.; Puntambekar, K.; Geier, M. L.; Hersam, M. C. Inkjet Printing of High Conductivity, Flexible Graphene Patterns. *J. Phys. Chem. Lett.* **2013**, *4* (8), 1347–1351. <https://doi.org/10.1021/jz400644c>.
- (188) Fang, Y.; Hester, J. G. D.; Deglee, B. M.; Tuan, C.-C.; Brooke, P. D.; Le, T.; Wong, C.-P.; Tentzeris, M. M.; Sandhage, K. H. A Novel, Facile, Layer-by-Layer Substrate Surface Modification for the Fabrication of All-Inkjet-Printed Flexible Electronic Devices on Kapton. *J. Mater. Chem. C* **2016**, *4* (29), 7052–7060. <https://doi.org/10.1039/c6tc01066k>.
- (189) McManus, D.; Vranic, S.; Withers, F.; Sanchez-Romaguera, V.; Macucci, M.; Yang, H.; Sorrentino, R.; Parvez, K.; Son, S.-K.; Iannaccone, G.; et al. Water-Based and Biocompatible 2D Crystal Inks for All-Inkjet-Printed Heterostructures. *Nat. Nanotechnol.* **2017**, *12* (4), 343–350. <https://doi.org/10.1038/nnano.2016.281>.

- (190) Ervin, M. H.; Le, L. T.; Lee, W. Y. Inkjet-Printed Flexible Graphene-Based Supercapacitor. *Electrochim. Acta* **2014**, *147*, 610–616. <https://doi.org/10.1016/j.electacta.2014.10.006>.
- (191) Pang, H.; Zhang, Y.; Lai, W.-Y.; Hu, Z.; Huang, W. Lamellar  $\text{K}_2\text{Co}(\text{PO}_3)_2 \cdot 2\text{H}_2\text{O}$  Nanocrystal Whiskers: High-Performance Flexible All-Solid-State Asymmetric Micro-Supercapacitors via Inkjet Printing. *Nano Energy* **2015**, *15*, 303–312. <https://doi.org/10.1016/j.nanoen.2015.04.034>.
- (192) Dodoo-Arhin, D.; Howe, R. C. T.; Hu, G.; Zhang, Y.; Hiralal, P.; Bello, A.; Amaratunga, G.; Hasan, T. Inkjet-Printed Graphene Electrodes for Dye-Sensitized Solar Cells. *Carbon N. Y.* **2016**, *105*, 33–41. <https://doi.org/10.1016/j.carbon.2016.04.012>.
- (193) Dong, S.; Wang, Z.; Asif, M.; Wang, H.; Yu, Y.; Hu, Y.; Liu, H.; Xiao, F. Inkjet Printing Synthesis of Sandwiched Structured Ionic Liquid-Carbon Nanotube-Graphene Film: Toward Disposable Electrode for Sensitive Heavy Metal Detection in Environmental Water Samples. *Ind. Eng. Chem. Res.* **2017**, *56* (7), 1696–1703. <https://doi.org/10.1021/acs.iecr.6b04251>.
- (194) Schneider, C. A.; Rasband, W. S.; Eliceiri, K. W. NIH Image to ImageJ: 25 Years of Image Analysis. *Nat. Methods* **2012**, *9* (7), 671–675. <https://doi.org/10.1038/nmeth.2089>.
- (195) Izquierdo, J.; Knittel, P.; Kranz, C. Scanning Electrochemical Microscopy: An Analytical Perspective. *Anal. Bioanal. Chem.* **2018**, *410* (2), 307–324. <https://doi.org/10.1007/s00216-017-0742-7>.
- (196) Bertocello, P. Advances on Scanning Electrochemical Microscopy (SECM) for Energy. <https://doi.org/10.1039/c0ee00046a>.
- (197) Güell, A. G.; Cuharuc, A. S.; Kim, Y.-R.; Zhang, G.; Tan, S.; Ebejer, N.; Unwin, P. R. Redox-

- Dependent Spatially Resolved Electrochemistry at Graphene and Graphite Step Edges. *ACS Nano* **2015**, *9* (4), 3558–3571. <https://doi.org/10.1021/acsnano.5b00550>.
- (198) Kang, M.; Perry, D.; Kim, Y. R.; Colburn, A. W.; Lazenby, R. A.; Unwin, P. R. Time-Resolved Detection and Analysis of Single Nanoparticle Electrocatalytic Impacts. *J. Am. Chem. Soc.* **2015**, *137* (34), 10902–10905. <https://doi.org/10.1021/jacs.5b05856>.
- (199) Bondarenko, A.; Cortés-Salazar, F.; Gheorghiu, M.; Gáspár, S.; Gáspár, G.; Momotenko, D.; Stanica, L.; Lesch, A.; Gheorghiu, E.; Girault, H. H. Electrochemical Push–Pull Probe: From Scanning Electrochemical Microscopy to Multimodal Altering of Cell Microenvironment. *Anal. Chem.* **2015**, *87*, 4479–4486. <https://doi.org/10.1021/acs.analchem.5b00455>.
- (200) Lesch, A.; Momotenko, D.; Cortés-Salazar, F.; Roelfs, F.; Girault, H. H.; Wittstock, G. High-Throughput Scanning Electrochemical Microscopy Brushing of Strongly Tilted and Curved Surfaces. *Electrochim. Acta* **2013**, *110*, 30–41. <https://doi.org/10.1016/j.electacta.2013.03.101>.
- (201) Lin, T. E. T.-E.; Bondarenko, A.; Lesch, A.; Pick, H.; Cortés-Salazar, F.; Girault, H. H. Monitoring Tyrosinase Expression in Non-Metastatic and Metastatic Melanoma Tissues by Scanning Electrochemical Microscopy. *Angew. Chemie - Int. Ed.* **2016**, *55* (11), 3813–3816. <https://doi.org/10.1002/anie.201509397>.
- (202) Lin, T.-E.; Lu, Y.-J.; Sun, C.-L.; Pick, H.; Chen, J.-P.; Lesch, A.; Girault, H. H. Soft Electrochemical Probes for Mapping the Distribution of Biomarkers and Injected Nanomaterials in Animal and Human Tissues. *Angew. Chemie - Int. Ed.* **2017**, *56* (52), 16498–16502. <https://doi.org/10.1002/anie.201709271>.
- (203) Gokuladeepan, P.; Karthigeyan, A. Effect of Annealing Temperature on Oxygen Reduction

Reaction of Reduced Graphene Oxide Incorporated Cobalt Oxide Nanocomposites for Fuel Cell Applications. *Appl. Surf. Sci.* **2018**, *449*, 705–711. <https://doi.org/10.1016/j.apsusc.2017.12.153>.

(204) Navrotsky, A.; Ma, C.; Lilova, K.; Birkner, N. Nanophase Transition Metal Oxides Show Large Thermodynamically Driven Shifts in Oxidation-Reduction Equilibria. *Science (80-. )*. **2010**, *330* (6001), 199–201. <https://doi.org/10.1126/science.1195875>.

(205) Lee, S.; Park, S. H. S.-H.; Jang, K.; Yu, S.; Song, C.; Kim, H. S. H.-S.; Ahn, H. Simple, Ultra-Rapid, Versatile Method to Synthesize Cobalt/Cobalt Oxide Nanostructures on Carbon Fiber Paper via Intense Pulsed White Light (IPWL) Photothermal Reduction for Energy Storage Applications. *J. Alloys Compd.* **2017**, *724*, 684–694. <https://doi.org/10.1016/j.jallcom.2017.07.069>.

(206) Kim, Y.-J.; Ryu, C.-H.; Park, S.-H.; Kim, H.-S. The Effect of Poly (N-Vinylpyrrolidone) Molecular Weight on Flash Light Sintering of Copper Nanopaste. *Thin Solid Films* **2014**, *570* (PartA), 114–122. <https://doi.org/10.1016/j.tsf.2014.09.035>.

(207) Peniche, C.; Zaldívar, D.; Pazos, M.; Páz, S.; Bulay, A.; Román, J. S. Study of the Thermal Degradation of Poly(N-vinyl-2-pyrrolidone) by Thermogravimetry–FTIR. *J. Appl. Polym. Sci.* **1993**, *50* (3), 485–493. <https://doi.org/10.1002/app.1993.070500312>.

(208) Loría-Bastarrachea, M. I.; Herrera-Kao, W.; Cauch-Rodríguez, J. V; Cervantes-Uc, J. M.; Vázquez-Torres, H.; Ávila-Ortega, A. A TG/FTIR Study on the Thermal Degradation of Poly(Vinyl Pyrrolidone). *J. Therm. Anal. Calorim.* **2011**, *104* (2), 737–742. <https://doi.org/10.1007/s10973-010-1061-9>.

(209) He, X.; Yang, C.; Wang, D.; Gilliland S.E., I. I. I.; Chen, D.-R.; Wang, W.-N. Facile Synthesis of



ZnO@ZIF Core-Shell Nanofibers: Crystal Growth and Gas Adsorption. *CrystEngComm* **2017**, *19* (18), 2445–2450. <https://doi.org/10.1039/c7ce00368d>.

- (210) Liu, Q.; MacE, A.; Bacsik, Z.; Sun, J.; Laaksonen, A.; Hedin, N. NaKA Sorbents with High CO<sub>2</sub>-over-N<sub>2</sub> Selectivity and High Capacity to Adsorb CO<sub>2</sub>. *Chem. Commun.* **2010**, *46* (25), 4502–4504. <https://doi.org/10.1039/c000900h>.
- (211) Zhao, S.; Yan, L.; Luo, H.; Mustain, W.; Xu, H. Recent Progress and Perspectives of Bifunctional Oxygen Reduction/Evolution Catalyst Development for Regenerative Anion Exchange Membrane Fuel Cells. *Nano Energy* **2018**, *47*, 172–198. <https://doi.org/10.1016/j.nanoen.2018.02.015>.
- (212) Xu, J.; Gao, P.; Zhao, T. S. Non-Precious Co<sub>3</sub>O<sub>4</sub> Nano-Rod Electrocatalyst for Oxygen Reduction Reaction in Anion-Exchange Membrane Fuel Cells. *Energy Environ. Sci.* **2012**, *5* (1), 5333–5339. <https://doi.org/10.1039/c1ee01431e>.
- (213) Xiao, J.; Kuang, Q.; Yang, S.; Xiao, F.; Wang, S.; Guo, L. Surface Structure Dependent Electrocatalytic Activity of Co<sub>3</sub>O<sub>4</sub> Anchored on Graphene Sheets toward Oxygen Reduction Reaction. **2013**, 1–8. <https://doi.org/10.1038/srep02300>.
- (214) Zhao, S.; Rasimick, B.; Mustain, W.; Xu, H. Highly Durable and Active Co<sub>3</sub>O<sub>4</sub> Nanocrystals Supported on Carbon Nanotubes as Bifunctional Electrocatalysts in Alkaline Media. *Appl. Catal. B Environ.* **2017**, *203*, 138–145. <https://doi.org/10.1016/j.apcatb.2016.09.048>.
- (215) Guo, S.; Zhang, S.; Wu, L.; Sun, S. Co/CoO Nanoparticles Assembled on Graphene for Electrochemical Reduction of Oxygen. *Angew. Chemie - Int. Ed.* **2012**, *51* (47), 11770–11773. <https://doi.org/10.1002/anie.201206152>.
- (216) Gasparotto, L. H. S.; Gomes, J. F.; Tremiliosi-Filho, G. Cyclic-Voltammetry Characteristics of

Poly(Vinyl Pyrrolidone) (PVP) on Single-Crystal Pt Surfaces in Aqueous H<sub>2</sub>SO<sub>4</sub>. *J. Electroanal. Chem.* **2011**, *663* (1), 48–51. <https://doi.org/10.1016/j.jelechem.2011.09.025>.

- (217) Martins, C. A.; Fernández, P. S.; Troiani, H. E.; Martins, M. E.; Arenillas, A.; Camara, G. A. Agglomeration and Cleaning of Carbon Supported Palladium Nanoparticles in Electrochemical Environment. *Electrocatalysis* **2014**, *5* (2), 204–212. <https://doi.org/10.1007/s12678-014-0184-3>.
- (218) Tsuneda, T.; Singh, R. K.; Iiyama, A.; Miyatake, K. Theoretical Investigation of the H<sub>2</sub>O<sub>2</sub>-Induced Degradation Mechanism of Hydrated Nafion Membrane via Ether-Linkage Dissociation. *ACS Omega* **2017**, *2* (7), 4053–4064. <https://doi.org/10.1021/acsomega.7b00594>.
- (219) Wang, Z.; Nagao, Y. Effects of Nafion Impregnation Using Inkjet Printing for Membrane Electrode Assemblies in Polymer Electrolyte Membrane Fuel Cells. *Electrochim. Acta* **2014**, *129*, 343–347. <https://doi.org/10.1016/j.electacta.2014.02.133>.
- (220) Lee, K.-S.; Park, I.-S.; Cho, Y.-H.; Jung, D.-S.; Jung, N.; Park, H.-Y.; Sung, Y.-E. Electrocatalytic Activity and Stability of Pt Supported on Sb-Doped SnO<sub>2</sub> nanoparticles for Direct Alcohol Fuel Cells. *J. Catal.* **2008**, *258* (1), 143–152. <https://doi.org/10.1016/j.jcat.2008.06.007>.
- (221) Liu, Y.; Mustain, W. E. High Stability, High Activity Pt/ITO Oxygen Reduction Electrocatalysts. *J. Am. Chem. Soc.* **2013**, *135* (2), 530–533. <https://doi.org/10.1021/ja307635r>.
- (222) Zhao, L.; Wang, Z.-B.; Liu, J.; Zhang, J.-J.; Sui, X.-L.; Zhang, L.-M.; Gu, D.-M. Facile One-Pot Synthesis of Pt/Graphene-TiO<sub>2</sub> hybrid Catalyst with Enhanced Methanol Electrooxidation Performance. *J. Power Sources* **2015**, *279*, 210–217.

<https://doi.org/10.1016/j.jpowsour.2015.01.023>.

- (223) Lv, H.; Li, D.; Strmcnik, D.; Paulikas, A. P.; Markovic, N. M.; Stamenkovic, V. R. Recent Advances in the Design of Tailored Nanomaterials for Efficient Oxygen Reduction Reaction. *Nano Energy* **2016**, *29*, 149–165. <https://doi.org/10.1016/j.nanoen.2016.04.008>.
- (224) Wang, Y.; Chen, K. S.; Mishler, J.; Cho, S. C.; Adroher, X. C. A Review of Polymer Electrolyte Membrane Fuel Cells: Technology, Applications, and Needs on Fundamental Research. *Appl. Energy* **2011**, *88* (4), 981–1007. <https://doi.org/10.1016/j.apenergy.2010.09.030>.
- (225) Carmo, M.; Fritz, D. L.; Mergel, J.; Stolten, D. A Comprehensive Review on PEM Water Electrolysis. *Int. J. Hydrogen Energy* **2013**, *38* (12), 4901–4934. <https://doi.org/10.1016/j.ijhydene.2013.01.151>.
- (226) Chen, A.; Holt-Hindle, P. Platinum-Based Nanostructured Materials: Synthesis, Properties, and Applications. *Chem. Rev.* **2010**, *110* (6), 3767–3804. <https://doi.org/10.1021/cr9003902>.
- (227) Liu, P.; Zhao, Y.; Qin, R.; Mo, S.; Chen, G.; Gu, L.; Chevrier, D. M.; Zhang, P.; Guo, Q.; Zang, D.; et al. Catalysis: Photochemical Route for Synthesizing Atomically Dispersed Palladium Catalysts. *Science* (80-. ). **2016**, *352* (6287), 797–801. <https://doi.org/10.1126/science.aaf5251>.
- (228) Stamenkovic, V.; Mun, B. S.; Mayrhofer, K. J. J.; Ross, P. N.; Markovic, N. M.; Rossmeisl, J.; Greeley, J.; Nørskov, J. K. Changing the Activity of Electrocatalysts for Oxygen Reduction by Tuning the Surface Electronic Structure. *Angew. Chemie - Int. Ed.* **2006**, *45* (18), 2897–2901. <https://doi.org/10.1002/anie.200504386>.
- (229) Guo, S.; Zhang, S.; Sun, S. Tuning Nanoparticle Catalysis for the Oxygen Reduction Reaction. *Angew. Chemie - Int. Ed.* **2013**, *52* (33), 8526–8544. <https://doi.org/10.1002/anie.201207186>.

- (230) Kang, Y.; Yang, P.; Markovic, N. M.; Stamenkovic, V. R. Shaping Electrocatalysis through Tailored Nanomaterials. *Nano Today*. 2016, pp 587–600. <https://doi.org/10.1016/j.nantod.2016.08.008>.
- (231) Calvert, P. Inkjet Printing for Materials and Devices. *Chem. Mater.* **2001**, *13* (10), 3299–3305. <https://doi.org/10.1021/cm0101632>.
- (232) Grote, J.-P.; Zeradhanin, A. R.; Cherevko, S.; Mayrhofer, K. J. J. Coupling of a Scanning Flow Cell with Online Electrochemical Mass Spectrometry for Screening of Reaction Selectivity. *Rev. Sci. Instrum.* **2014**, *85* (10). <https://doi.org/10.1063/1.4896755>.
- (233) Newhouse, P. F. P. F. P. F.; Parkinson, B. A. A. Combinatorial Optimization of Spinel  $\text{Co}_{3-x}\text{M}_x\text{O}_4$  M = (Al, Ga, In) Alloyed Thin Films Prepared by Ink Jet Printing: Photoelectrochemical, Optical, and Structural Properties. *J. Mater. Chem. A* **2015**, *3* (11), 5901–5907. <https://doi.org/10.1039/c4ta05671j>.
- (234) Yim, C.; Sandwell, A.; Park, S. S. S. S. S. Hybrid Copper-Silver Conductive Tracks for Enhanced Oxidation Resistance under Flash Light Sintering. *ACS Appl. Mater. Interfaces* **2016**, *8* (34), 22369–22373. <https://doi.org/10.1021/acsami.6b07826>.
- (235) Park, S.-H.; Kim, H.-S. Flash Light-Assisted Facile and Eco-Friendly Synthesis of Platinum-Based Alloy Nanoparticle/Carbon Nano-Tube Catalysts for a Direct Methanol Fuel Cell. *J. Electrochem. Soc.* **2014**, *162* (1), F204–F210. <https://doi.org/10.1149/2.0711501jes>.
- (236) Hernandez, J. O.; Choren, E. A. Thermal Stability of Some Platinum Complexes. *Thermochim. Acta* **1983**, *71* (3), 265–272. [https://doi.org/10.1016/0040-6031\(83\)80059-8](https://doi.org/10.1016/0040-6031(83)80059-8).
- (237) Schweizer, A. E.; Kerr, G. T. Thermal Decomposition of Hexachloroplatinic Acid. *Inorg. Chem.* **1978**, *17* (8), 2326–2327. <https://doi.org/10.1021/ic50186a067>.

- (238) Bard, A. J. .; Mirkin, M. V. *Scanning Electrochemical Microscopy*, 2nd Editio.; 2012.
- (239) Cortés-Salazar, F.; Momotenko, D.; Lesch, A.; Wittstock, G.; Girault, H. H. Soft Microelectrode Linear Array for Scanning Electrochemical Microscopy. *Anal. Chem.* **2010**, *82* (24), 10037–10044. <https://doi.org/10.1021/ac1019304>.
- (240) Cortés-Salazar, F.; Träuble, M.; Li, F.; Busnel, J. M.; Gassner, A. L.; Hojeij, M.; Wittstock, G.; Girault, H. H. Soft Stylus Probes for Scanning Electrochemical Microscopy. *Anal. Chem.* **2009**, *81* (16), 6889–6896. <https://doi.org/10.1021/ac900887u>.
- (241) Lesch, A.; Cortés-Salazar, F.; Amstutz, V.; Tacchini, P.; Girault, H. H. Inkjet Printed Nanohydrogel Coated Carbon Nanotubes Electrodes for Matrix Independent Sensing. *Anal. Chem.* **2015**, *87* (2), 1026–1033. <https://doi.org/10.1021/ac503748g>.
- (242) Santhiago, M.; Corrêa, C. C.; Bernardes, J. S.; Pereira, M. P.; Oliveira, L. J. M.; Strauss, M.; Bufon, C. C. B. Flexible and Foldable Fully-Printed Carbon Black Conductive Nanostructures on Paper for High-Performance Electronic, Electrochemical, and Wearable Devices. *ACS Appl. Mater. Interfaces* **2017**, *9* (28), 24365–24372. <https://doi.org/10.1021/acsami.7b06598>.
- (243) Zou, L.; Jiang, Y.; Cheng, J.; Chen, Y.; Chi, B.; Pu, J.; Jian, L. Bifunctional Catalyst of Well-Dispersed RuO<sub>2</sub> on NiCo<sub>2</sub>O<sub>4</sub> Nanosheets as Enhanced Cathode for Lithium-Oxygen Batteries. *Electrochim. Acta* **2018**, *262*, 97–106. <https://doi.org/10.1016/j.electacta.2018.01.005>.
- (244) Grigoriev, S. A.; Millet, P.; Fateev, V. N. Evaluation of Carbon-Supported Pt and Pd Nanoparticles for the Hydrogen Evolution Reaction in PEM Water Electrolysers. *J. Power Sources* **2008**, *177*, 281–285. <https://doi.org/10.1016/j.jpowsour.2007.11.072>.
- (245) Lee, Y.; Suntivich, J.; May, K. J.; Perry, E. E.; Shao-Horn, Y. Synthesis and Activities of Rutile IrO<sub>2</sub> and RuO<sub>2</sub> Nanoparticles for Oxygen Evolution in Acid and Alkaline Solutions. *Journal of*

*Physical Chemistry Letters*. 2012, pp 399–404. <https://doi.org/10.1021/jz2016507>.

- (246) Corrigan, D. A. *The Catalysis of the Oxygen Evolution Reaction by Iron Impurities in Thin Film Nickel Oxide Electrodes*; Cambridge University Press, 1983; Vol. 134.
- (247) Jeerage, K. M.; Candelaria, S. L.; Stavis, S. M. Rapid Synthesis and Correlative Measurements of Electrocatalytic Nickel/Iron Oxide Nanoparticles. *Sci. Rep.* **2018**, *8* (1). <https://doi.org/10.1038/s41598-018-22609-x>.
- (248) Jin, J.; Xia, J.; Qian, X.; Wu, T.; Ling, H.; Hu, A.; Li, M.; Hang, T. Exceptional Electrocatalytic Oxygen Evolution Efficiency and Stability from Electrodeposited NiFe Alloy on Ni Foam. *Electrochim. Acta* **2019**, *299*, 567–574. <https://doi.org/10.1016/j.electacta.2019.01.026>.
- (249) Greenlee, L. F.; Acharya, P.; Nelson, Z. Compositional Optimization of Alloy Fe<sub>x</sub>Ni<sub>y</sub>(OH)<sub>2</sub> Nanoparticles for Alkaline Electrochemical Oxygen Evolution. *ECS Trans.* **2017**, *77* (9), 25–38. <https://doi.org/10.1149/07709.0025ecst>.
- (250) Suen, N. T.; Hung, S. F.; Quan, Q.; Zhang, N.; Xu, Y. J.; Chen, H. M. Electrocatalysis for the Oxygen Evolution Reaction: Recent Development and Future Perspectives. *Chemical Society Reviews*. 2017, pp 337–365. <https://doi.org/10.1039/c6cs00328a>.
- (251) Zhu, K.; Zhu, X.; Yang, W. Application of In Situ Techniques for the Characterization of NiFe-Based Oxygen Evolution Reaction (OER) Electrocatalysts. *Angew. Chemie - Int. Ed.* **2019**, *58* (5), 1252–1265. <https://doi.org/10.1002/anie.201802923>.
- (252) Song, F.; Busch, M. M.; Lassalle-Kaiser, B.; Hsu, C.-S.; Petkucheva, E.; Bensimon, M.; Chen, H. M.; Corminboeuf, C.; Hu, X. An Unconventional Iron Nickel Catalyst for the Oxygen Evolution Reaction. *ACS Cent. Sci.* **2019**. <https://doi.org/10.1021/acscentsci.9b00053>.

- (253) Dionigi, F.; Strasser, P. NiFe-Based (Oxy)Hydroxide Catalysts for Oxygen Evolution Reaction in Non-Acidic Electrolytes. *Adv. Energy Mater.* **2016**, *6* (23). <https://doi.org/10.1002/aenm.201600621>.
- (254) Baur, J.; Le Goff, A.; Dementin, S.; Holzinger, M.; Rousset, M.; Cosnier, S. Three-Dimensional Carbon Nanotube-Polypyrrole-[NiFe] Hydrogenase Electrodes for the Efficient Electrocatalytic Oxidation of H<sub>2</sub>. *Int. J. Hydrogen Energy* **2011**, *36* (19), 12096–12101. <https://doi.org/10.1016/j.ijhydene.2011.06.122>.
- (255) Feng, Y.; Yu, X. Y.; Paik, U. N-Doped Graphene Layers Encapsulated NiFe Alloy Nanoparticles Derived from MOFs with Superior Electrochemical Performance for Oxygen Evolution Reaction. *Sci. Rep.* **2016**, *6*. <https://doi.org/10.1038/srep34004>.
- (256) Gong, M.; Li, Y.; Wang, H.; Liang, Y.; Wu, J. Z.; Zhou, J.; Wang, J.; Regier, T.; Wei, F.; Dai, H. An Advanced Ni-Fe Layered Double Hydroxide Electrocatalyst for Water Oxidation. *J. Am. Chem. Soc.* **2013**, *135* (23), 8452–8455. <https://doi.org/10.1021/ja4027715>.
- (257) Zhang, Z.; Qin, Y.; Dou, M.; Ji, J.; Wang, F. One-Step Conversion from Ni/Fe Polyphthalocyanine to N-Doped Carbon Supported Ni-Fe Nanoparticles for Highly Efficient Water Splitting. *Nano Energy* **2016**, *30*, 426–433. <https://doi.org/10.1016/j.nanoen.2016.10.035>.
- (258) Song, F.; Hu, X. Exfoliation of Layered Double Hydroxides for Enhanced Oxygen Evolution Catalysis. *Nat. Commun.* **2014**, *5*. <https://doi.org/10.1038/ncomms5477>.
- (259) Han, B.; Risch, M.; Belden, S.; Lee, S.; Bayer, D.; Mutoro, E.; Shao-Horn, Y. Screening Oxide Support Materials for OER Catalysts in Acid. *J. Electrochem. Soc.* **2018**, *165* (10), F813–F820. <https://doi.org/10.1149/2.0921810jes>.

- (260) Batchellor, A. S.; Boettcher, S. W. Pulse-Electrodeposited Ni-Fe (Oxy)Hydroxide Oxygen Evolution Electrocatalysts with High Geometric and Intrinsic Activities at Large Mass Loadings. **2015**. <https://doi.org/10.1021/acscatal.5b01551>.
- (261) Rosa, M.; Zielke, P.; Kiebach, R.; Costa Bassetto, V.; Lesch, A.; Esposito, V. Printing of NiO-YSZ Nanocomposites: From Continuous Synthesis to Inkjet Deposition. *J. Eur. Ceram. Soc.* **2019**, *39* (4), 1279–1286. <https://doi.org/10.1016/j.jeurceramsoc.2018.12.030>.
- (262) Tanner, E. E. L.; Tschulik, K.; Tahany, R.; Jurkschat, K.; Batchelor-McAuley, C.; Compton, R. G. Nanoparticle Capping Agent Dynamics and Electron Transfer: Polymer-Gated Oxidation of Silver Nanoparticles. *J. Phys. Chem. C* **2015**, *119* (32), 18808–18815. <https://doi.org/10.1021/acs.jpcc.5b05789>.
- (263) Costa Bassetto, V.; Xiao, J.; Oveisi, E.; Amstutz, V.; Liu, B.; Girault, H. H.; Lesch, A. Rapid Inkjet Printing of High Catalytic Activity Co<sub>3</sub>O<sub>4</sub>/N-RGO Layers for Oxygen Reduction Reaction. *Appl. Catal. A Gen.* **2018**, *563*, 9–17. <https://doi.org/10.1016/j.apcata.2018.06.026>.
- (264) Park, C.; Hwang, J.; Hwang, Y.-T. T.; Song, C.; Ahn, S.; Kim, H.-S. S.; Ahn, H. Intense Pulsed White Light Assisted Fabrication of Co-CoO<sub>x</sub> Core-Shell Nanoflakes on Graphite Felt for Flexible Hybrid Supercapacitors. *Electrochim. Acta* **2017**, *246*, 757–765. <https://doi.org/10.1016/j.electacta.2017.06.087>.
- (265) Dao, V.-D.; Choi, H.-S. Carbon-Based Sunlight Absorbers in Solar-Driven Steam Generation Devices. *Glob. Challenges* **2018**, *2* (2), 1700094. <https://doi.org/10.1002/gch2.201700094>.
- (266) Gadea, C.; Hanniet, Q.; Lesch, A.; Marani, D.; Jensen, S. H.; Esposito, V. Aqueous Metal-Organic Solutions for YSZ Thin Film Inkjet Deposition. *J. Mater. Chem. C* **2017**, *5* (24), 6021–6029. <https://doi.org/10.1039/c7tc01879g>.



- (267) Patil, P. S.; Kadam, L. D. *Preparation and Characterization of Spray Pyrolyzed Nickel Oxide (NiO) Thin Films*; 2002; Vol. 199. [https://doi.org/10.1016/S0169-4332\(02\)00839-5](https://doi.org/10.1016/S0169-4332(02)00839-5).
- (268) Mishra, S. K.; Kanungo, S. B. *THERMAL DEHYDRATION AND DECOMPOSITION OF NICKEL CHLORIDE HYDRATE (NiCl<sub>2</sub>.XH<sub>2</sub>O)*; 1992; Vol. 38.
- (269) Suganuma, K.; Yagi, T. Thermal Decomposition of Iron(II) Chloride. *Nippon KAGAKU KAISHI* **1978**, No. 3, 319–325. <https://doi.org/10.1246/nikkashi.1978.319>.
- (270) Gadalla, A. M.; Livingston, T. W. *Thermal Behavior of Oxides and Hydroxides of Iron and Nickel*; 1989; Vol. 145. [https://doi.org/10.1016/0040-6031\(89\)85121-4](https://doi.org/10.1016/0040-6031(89)85121-4).
- (271) Patil, P. S.; Kadam, L. D.; Lokhande, C. D. Preparation and Characterization of Spray Pyrolysed Cobalt Oxide Thin Films. **1996**, 272, 29–32.
- (272) Biesinger, M. C.; Payne, B. P.; Grosvenor, A. P.; Lau, L. W. M. W.; Gerson, A. R.; StC Smart, R.; Smart, R. S. C. Resolving Surface Chemical States in XPS Analysis of First Row Transition Metals, Oxides and Hydroxides: Cr, Mn, Fe, Co and Ni. *Appl. Surf. Sci.* **2011**, 257 (7), 2717–2730. <https://doi.org/10.1016/j.apsusc.2010.10.051>.
- (273) Prager, J. . *Environmental Contaminant Reference Databook Volume 1*; Van Nostrand Reinhold: New York, NY, 1995.
- (274) Li, X. Q.; Zhang, W. X. Iron Nanoparticles: The Core-Shell Structure and Unique Properties for Ni(II) Sequestration. *Langmuir* **2006**, 22 (10), 4638–4642. <https://doi.org/10.1021/la060057k>.
- (275) Hutton, L. A.; Vidotti, M.; Patel, A. N.; Newton, M. E.; Unwin, P. R.; Macpherson, J. V. Electrodeposition of Nickel Hydroxide Nanoparticles on Boron-Doped Diamond Electrodes for Oxidative Electrocatalysis. *J. Phys. Chem. C* **2011**, 115, 1649–1658.

<https://doi.org/10.1021/jp109526b>.

- (276) Swierk, J. R.; Klaus, S.; Trotochaud, L.; Bell, A. T.; Tilley, T. D. Electrochemical Study of the Energetics of the Oxygen Evolution Reaction at Nickel Iron (Oxy)Hydroxide Catalysts. *J. Phys. Chem. C* **2015**, *119* (33), 19022–19029. <https://doi.org/10.1021/acs.jpcc.5b05861>.
- (277) Trotochaud, L.; Ranney, J. K.; Williams, K. N.; Boettcher, S. W. Solution-Cast Metal Oxide Thin Film Electrocatalysts for Oxygen Evolution. *J. Am. Chem. Soc.* **2012**, *134* (41), 17253–17261. <https://doi.org/10.1021/ja307507a>.
- (278) Burke, L. Voltammetric Behaviour of Nickel in Base with Particular Reference to Thick Oxide Growth. *J. Electroanal. Chem.* **2002**, *162* (1–2), 101–119. [https://doi.org/10.1016/0368-1874\(84\)83324-9](https://doi.org/10.1016/0368-1874(84)83324-9).
- (279) Garnett, E. C.; Cai, W.; Cha, J. J.; Mahmood, F.; Connor, S. T.; Greyson Christoforo, M.; Cui, Y.; McGehee, M. D.; Brongersma, M. L. Self-Limited Plasmonic Welding of Silver Nanowire Junctions. *Nat. Mater.* **2012**, *11*. <https://doi.org/10.1038/NMAT3238>.
- (280) Bode, H.; Dehmelt, K.; Witte, J. Zur Kenntnis Der Nickelhydroxidelektrode—I.Über Das Nickel (II)-Hydroxidhydrat. *Electrochim. Acta* **1966**, *11* (8), 1079-IN1. [https://doi.org/10.1016/0013-4686\(66\)80045-2](https://doi.org/10.1016/0013-4686(66)80045-2).
- (281) Cheshideh, H.; Nasirpouri, F. Cyclic Voltammetry Deposition of Nickel Nanoparticles on TiO<sub>2</sub> Nanotubes and Their Enhanced Properties for Electro-Oxidation of Methanol. *J. Electroanal. Chem.* **2017**, *797*, 121–133. <https://doi.org/10.1016/j.jelechem.2017.05.024>.
- (282) Hahn, F.; Beden, B.; Croissant, M. J.; Lamy, C. In Situ Uv Visible Reflectance Spectroscopic Investigation of the Nickel Electrode-Alkaline Solution Interface. *Electrochim. Acta* **1986**, *31* (3), 335–342. [https://doi.org/10.1016/0013-4686\(86\)80087-1](https://doi.org/10.1016/0013-4686(86)80087-1).

- (283) Sharel, P. E.; Liu, D.; Lazenby, R. A.; Sloan, J.; Vidotti, M.; Unwin, P. R.; Macpherson, J. V. Electrodeposition of Nickel Hydroxide Nanoparticles on Carbon Nanotube Electrodes: Correlation of Particle Crystallography with Electrocatalytic Properties. *J. Phys. Chem. C* **2016**, *120* (29), 16059–16068. <https://doi.org/10.1021/acs.jpcc.5b12741>.
- (284) Vidotti, M.; Torresi, R.; De Torresi, S. I. C. Eletrodos Modificados Por Hidróxido de Níquel: Um Estudo de Revisão Sobre Suas Propriedades Estruturais e Eletroquímicas Visando Suas Aplicações Em Eletrocatalise, Eletrocromismo e Baterias Secundárias. *Quim. Nova* **2010**, *33* (10), 2176–2186. <https://doi.org/10.1590/S0100-40422010001000030>.
- (285) Trotochaud, L.; Young, S. L.; Ranney, J. K.; Boettcher, S. W. Nickel-Iron Oxyhydroxide Oxygen-Evolution Electrocatalysts: The Role of Intentional and Incidental Iron Incorporation. *J. Am. Chem. Soc.* **2014**, *136* (18), 6744–6753. <https://doi.org/10.1021/ja502379c>.
- (286) Li, Y.; Zhao, C. Iron-Doped Nickel Phosphate as Synergistic Electrocatalyst for Water Oxidation. *Chem. Mater.* **2016**, *28* (16), 5659–5666. <https://doi.org/10.1021/acs.chemmater.6b01522>.
- (287) Liu, G.; Gao, X.; Wang, K.; He, D.; Li, J. Mesoporous Nickel–Iron Binary Oxide Nanorods for Efficient Electrocatalytic Water Oxidation. *Nano Res.* **2017**, *10* (6), 2096–2105. <https://doi.org/10.1007/s12274-016-1398-x>.
- (288) Zhang, P.; Li, L.; Nordlund, D.; Chen, H.; Fan, L.; Zhang, B.; Sheng, X.; Daniel, Q.; Sun, L. Dendritic Core-Shell Nickel-Iron-Copper Metal/Metal Oxide Electrode for Efficient Electrocatalytic Water Oxidation. *Nat. Commun.* **2018**, *9* (1). <https://doi.org/10.1038/s41467-017-02429-9>.
- (289) Luan, C.; Liu, G.; Liu, Y.; Yu, L.; Wang, Y.; Xiao, Y.; Qiao, H.; Dai, X.; Zhang, X. Structure Effects

of 2D Materials on  $\alpha$ -Nickel Hydroxide for Oxygen Evolution Reaction. *ACS Nano* **2018**, *12* (4), 3875–3885. <https://doi.org/10.1021/acsnano.8b01296>.

- (290) Shinagawa, T.; Garcia-Esparza, A. T.; Takanabe, K. Insight on Tafel Slopes from a Microkinetic Analysis of Aqueous Electrocatalysis for Energy Conversion OPEN. **2015**, 23955–26900. <https://doi.org/10.1038/srep13801>.
- (291) Zhang, X.; Xu, H.; Li, X.; Li, Y.; Yang, T.; Liang, Y. Facile Synthesis of Nickel-Iron/Nanocarbon Hybrids as Advanced Electrocatalysts for Efficient Water Splitting. *ACS Catal.* **2016**, *6* (2), 580–588. <https://doi.org/10.1021/acscatal.5b02291>.
- (292) Zhu, X.; Tang, C.; Wang, H. F.; Zhang, Q.; Yang, C.; Wei, F. Dual-Sized NiFe Layered Double Hydroxides in Situ Grown on Oxygen-Decorated Self-Dispersal Nanocarbon as Enhanced Water Oxidation Catalysts. *J. Mater. Chem. A* **2015**, *3* (48), 24540–24546. <https://doi.org/10.1039/c5ta08019c>.
- (293) Wang, A.-L.; Dong, Y.-T.; Li, M.; Liang, C.; Li, G.-R. In Situ Derived Ni<sub>x</sub>Fe<sub>1-x</sub>OOH/NiFe/Ni<sub>x</sub>Fe<sub>1-x</sub>OOH Nanotube Arrays from NiFe Alloys as Efficient Electrocatalysts for Oxygen Evolution. **2017**. <https://doi.org/10.1021/acscami.7b10609>.
- (294) Wang, L.; Chen, H.; Daniel, Q.; Duan, L.; Philippe, B.; Yang, Y.; Rensmo, H.; Sun, L. Promoting the Water Oxidation Catalysis by Synergistic Interactions between Ni(OH)<sub>2</sub> and Carbon Nanotubes. *Adv. Energy Mater.* **2016**, *6* (15), 1600516. <https://doi.org/10.1002/aenm.201600516>.
- (295) Zou, S.; Burke, M. S.; Kast, M. G.; Fan, J.; Danilovic, N.; Boettcher, S. W. Fe (Oxy)Hydroxide Oxygen Evolution Reaction Electrocatalysis: Intrinsic Activity and the Roles of Electrical Conductivity, Substrate, and Dissolution. *Chem. Mater.* **2015**, *27* (23), 8011–8020.

<https://doi.org/10.1021/acs.chemmater.5b03404>.

- (296) Nardi, K. L.; Yang, N.; Dickens, C. F.; Strickler, A. L.; Bent, S. F. Creating Highly Active Atomic Layer Deposited NiO Electrocatalysts for the Oxygen Evolution Reaction. *Adv. Energy Mater.* **2015**, *5* (17), 1–10. <https://doi.org/10.1002/aenm.201500412>.

## CURRICULUM VITAE

Victor Costa Bassetto

May 2<sup>nd</sup> 1986, Brazil

E-mail: [victor.costabassetto@epfl.ch](mailto:victor.costabassetto@epfl.ch)

Tel: +41 79 942 5977

Chemin des Vendanges 5, CH-3960 – Sierre, Valais, Switzerland

### Education

---

#### **03.2005- 07.2009 Bachelor degree in Pharmacy and Biochemistry**

Universidade Estadual Paulista, Júlio de Mesquita Filho, UNESP – São Paulo – Brazil.

#### **2011-2014 Master in Analytical Chemistry**

Laboratory of Electrochemistry, Electroanalytics and Sensor Development (LEEDS).

Chemistry Institute, Universidade Estadual de Campinas, Campinas, São Paulo – Brazil.

Dissertation: Utilization of copper alloys as work electrode for electrochemical of amino acids in ion chromatography.

Dissertation director: Prof. Dr. Lauro Tatsuo Kubota.

#### **12.2014 – 08.2019 PhD in Chemistry**

Laboratory of Physical and Analytical Electrochemistry

Institute of Chemistry and Chemical Engineering

École Polytechnique Fédérale de Lausanne, Switzerland

Thesis: Inkjet printing and electrocatalysis

Thesis directors: Prof. Hubert H. Girault and Dr. Andreas Lesch.

### Scientific Research Experience

---

Preparation of nanotemplated electrodes for spectroelectrochemistry coupled to surface enhanced Raman spectroscopy (SERS);

Ion chromatography instrumental and methodological development aimed to samples from food industry;

Scanning electron microscopy application for electrode surface characterization;

Nanoparticulated functional ink formulation, from raw material to stable dispersion;

Inkjet printing of functional and conductive inks for the fabrication of electrodes and catalyst layers;

Nanostructured electrocatalysts synthesis utilizing thermal decomposition based on selective energy absorption.

## Awards and Honors

---

Year 2012 – 2014	Fapesp Master Thesis Scholarship – Fapesp 11/04043-0
Year 2013	Fapesp International Exchange Grant – Fapesp 13/02849-3
Year 2013	Best Poster Award – XIX SIBEE
Year 2015	Best Poster Award – ISE 16 <sup>th</sup> Topical Meeting
Year 2016	Best Case Study Award – 3DCamp Summer School - EPFL
Year 2018	Fondazione Oronzio e Niccolò De Nora Fellowship in Applied electrochemistry.

## Patent Application

---

**Costa Bassetto, Victor**; Timm, Ronaldo A.; Toma, Mario S.; Kubota, Lauro T. Closed cell for spectroelectrochemistry. Register number: BR1020140268413. Brazilian Institute of Industrial Property. Filing date: 27.10.2014.

## Publications

---

“Print-Light-Synthesis of Ni and NiFe-nanoscale catalyst for oxygen evolution” **Costa Bassetto, Victor**; Mensi, Mounir; Oveisi, Emad; Girault, Hubert H; Lesch, Andreas. – ACS Appl. Energy Mater. **2**, 2019, 6322 – 6331. DOI: 10.1021/acsaem.9b00957

“A Self-Assembled Organic/Metal Junction for Water Photo-Oxidation.” Olaya, Astrid J.; Omatsu, Terumasa; Hidalgo-Acosta, Jonnathan C.; Riva, Julieta S.; **Costa Bassetto, Victor**; Gasilova, Natalia; Girault, Hubert H. *Journal of the American Chemical Society* (2019) DOI: 10.1021/jacs.9b02693 .

“Printing of NiO-YSZ nanocomposites: from continuous synthesis to inkjet deposition.” Rosa, Massimo; Zielke, Philippe; Kiebach, Ragnar; **Costa Bassetto, Victor**; Lesch, Andreas; Esposito, Vincenzo. *Journal of the European Ceramic Society* **39** (2019) 1279 – 1286.

“Inkjet-Printed Mesoporous TiO<sub>2</sub> and Perovskite Layers for High Efficiency Perovskite Solar Cells.” Huckaba, Aron J.; Lee, Yonghui; Xia, Rui; Paek, Sanghyun; **Bassetto, Victor Costa**; Oveisi, Emad; Lesch, Andreas; Kinge, Sachin; Dyson, Paul J.; Girault, Hubert; Nazeeruddin, Mohammad Kaja. *Energy Technology* **7** (2019) 317 – 324.

“Standard ion transfer potential at the water|butyronitrile interface.” Riva, J.S.; **Bassetto, V.C.**; Girault, H.H.; Olaya, A.J. *Journal of Electroanalytical Chemistry* **835** (2019) 192 – 196.

“Rapid inkjet printing of high catalytic activity Co<sub>3</sub>O<sub>4</sub>/N-rGO layers for oxygen reduction reaction.” **Costa Bassetto, Victor**; Xiao, Jingjing; Oveisi, Emad; Amstutz, Véronique; Liu, Baohong; Girault, Hubert; Lesch, Andreas. *Applied Catalysis A: General* **563** (2018) 9 – 17.

“Large-scale layer-by-layer inkjet printing of flexible iridium-oxide based pH sensors.” Jovic, Milica; Hidalgo-Costa, Jonnathan; Lesch, Andreas; **Bassetto, Victor Costa**; Smirnov, Evgeny; Cortés-Salazar, Fernando; Girault, Hubert. *Electroanalytical Chemistry* **819** (2018) 384 – 390.

“Electrochemical Reduction of Protic Supercritical CO<sub>2</sub> on Copper Electrodes” Melcheva, Olga; Voyame Patrick; **Costa Bassetto, Victor**; Prokein, Michael; Renner, Manfred; Weidner, Eckhard; Petermann, Marcus and Battistel, Alberto. *ChemSusChem* **18** (2017) 3660 – 3670.

“Versatile and low cost spectroelectrochemical cell for *in situ* study of electrode surfaces” Timm, Ronaldo A.; Da Silva, Everson T.S.G.; **Bassetto, Victor C.** Abruña, Héctor; Kubota, Lauro Tatsuo. *Electrochim. Acta* **232** (2017) 150 – 155.

“Inkjet Printing Meets Energy Conversion” Lesch, Andreas; Cortés-Salazar, Fernando; **Bassetto, Victor Costa**; Amstutz, Véronique and H.H. Girault. *Chimia* **69** (2015) 284-289.

“Preparation of copper sphere segment void templates for electrochemical SERS and their use to study the interaction of amino acids with copper under potentiostatic control” **Bassetto, Victor Costa**; Russell, Andrea; Kubota, Lauro Tatsuo; Bartlett, Philip N. *Electrochim. Acta* **144** (2014) 400 - 405.

“Critical View on Graphene Oxide Production and Its Transfer to Surfaces Aiming Electrochemical Applications” Timm, Ronaldo A.; Kisner Alexandre; **Bassetto, Victor Costa**; Kubota, Lauro Tatsuo. *Journal of Nanoscience and Nanotechnology* **14** (2014) 6478-6496

“Electrochemical Approaches Employed for Sensing the Antioxidant Capacity Exhibited by Vegetal Extracts: A Review.” Hilgemann, Mauricio; **Bassetto, Victor**; Kubota, Lauro. *Combinatorial Chemistry & High Throughput Screening*. **16** (2013) 98-10





